Università di Pisa

Scuola di Dottorato
Scienze di base "Galileo Galilei"

Corso di Dottorato in Fisica XXVI ciclo

SSD FIS/01

PhD thesis

Trigger for rare kaon decays searches at the CERN NA62 experiment

Candidate
Bruno Angelucci

Supervisor
Prof. Marco Sozzi

Abstract

The work reported in this thesis has been carried out within the Trigger and Data Acquisition (TDAQ) working group of the CERN NA62 experiment, and focused on the development of a trigger strategy for collecting rare kaon decays.
The main aim of the NA62 experiment is the study of the ultra rare decay $K^+ \to \pi^+\nu\bar{\nu}$ in order to provide a stringent test of the Standard Model. The theoretical framework of the $K^+ \to \pi^+\nu\bar{\nu}$ decay, the present experimental status of the measurement of the Branching Ratio and the NA62 experimental strategy are described in chapter 1.
Chapter 2 provides a description of the NA62 experimental setup.
The first part of the work concerned the design, development and assessment of the common Trigger and Data Acquisition system for the majority of detectors in NA62, a high-speed integrated data acquisition and trigger generation system based on digital high resolution time measurements. The architecture of the boards, a detailed description of the developed firmwares and some results obtained during the NA62 TDAQ commissioning phase are presented in chapter 3.
The second part of the work focused on Monte Carlo studies of hardware low-level (L0) trigger schemes with the purpose of selecting interesting decays. The dependence of the L0 output trigger rate and of the trigger efficiency upon the variation of several trigger parameters has been studied.
The optimization of the L0 trigger scheme for the selection of $K^+ \to \pi^+\nu\bar{\nu}$ decays is described in chapter 4. In addition, a L0 trigger selection for the search for a hypothetical dark photon (U) in π^0 decays is discussed in chapter 5. After a general introduction about the searches for rare and forbidden kaon decays at NA62, the physics motivations and the experimental status are described. Finally, the NA62 expected upper limits on the Branching Ratio of the $\pi^0 \to \gamma U, U \to e^+e^-$ decay are computed and compared with present limits.

Contents

List of Tables

List of Figures

Chapter 1

The NA62 physics goal

1.1 Introduction

The main aim of the NA62 experiment is the study of the ultra rare decay $K^+ \to \pi^+\nu\bar{\nu}$. The final goal is to measure the Branching Ratio of this process with a 10% accuracy, in order to provide a stringent test of the Standard Model (SM) predictions or lead to a discovery of deviations from the SM which turns into evidence of new physics.
The theoretical framework of the $K^+ \to \pi^+\nu\bar{\nu}$ decay is described in section 1.2. Among the many rare flavour changing neutral current (FCNC) K and B decays, the ultra rare decays $K \to \pi\nu\bar{\nu}$ play a key role in the search for new physics through underlying mechanisms of flavour mixing. The Branching Ratio can be computed to an exceptionally high degree of precision: the prediction for the $K^+ \to \pi^+\nu\bar{\nu}$ channel is $(7.81 \pm 0.75 \pm 0.29) \times 10^{-11}$ [1]. The first error comes from the uncertainty on the CKM matrix elements, the second one is the intrinsic theoretical uncertainty.
This decay is one of the best probes for new physics effects complementary to direct searches, especially within non Minimal Flavour Violation models [2][3]. Since the theoretical cleanness of these decays holds also in these scenarios, even deviations from the SM value at the level of 20% can be considered signals of new physics.
Within the SM, the Branching Ratio value provides a measurement of $|V_{td}|$ free from hadronic uncertainties and independent from that obtained from B meson decays.
The present experimental status is reported in section 1.3. The decay $K^+ \to \pi^+\nu\bar{\nu}$ has been observed by the dedicated experiments E787 and E949 at the Brookhaven National Laboratory and the measured Branching Ratio is $\left(1.73^{+1.15}_{-1.05}\right) \times 10^{-10}$ [4]. However only a measurement of the Branching Ratio with at least 10% accuracy can be a significant test of new physics.
Section 1.4 gives the details of the NA62 experimental strategy. The goal is collecting about 100 events of the $K^+ \to \pi^+\nu\bar{\nu}$ decay, with a Signal over Background ratio (S/B) of 10/1, in two to three years of data taking. 10^{13} K^+ decays are required, assuming a 10%

signal acceptance and a $K^+ \to \pi^+\nu\bar{\nu}$ Branching Ratio of 10^{-10}. The need of reducing the systematic uncertainty, requires a rejection factor for generic kaon decays of the order of 10^{12} and the possibility to measure efficiencies and background suppression factors directly from data.

1.2 $K^+ \to \pi^+\nu\bar{\nu}$ theoretical framework

1.2.1 CKM matrix and unitarity triangle

The Cabibbo-Kobayashi-Maskawa (CKM) matrix describes the quark flavour-mixing in weak decays within the Standard Model [5]. It is a unitary 3×3 matrix and is a generalisation of the 2×2 Cabibbo matrix, with the extension to the third quark family (t, b).

$$\begin{pmatrix} d' \\ s' \\ b' \end{pmatrix} = \begin{pmatrix} V_{ud} & V_{us} & V_{ub} \\ V_{cd} & V_{cs} & V_{cb} \\ V_{td} & V_{ts} & V_{tb} \end{pmatrix} \begin{pmatrix} d \\ s \\ b \end{pmatrix} \tag{1.1}$$

A common and useful way of expressing the matrix is through the Wolfenstein parametrisation [6]

$$V = \begin{pmatrix} 1-\lambda^2/2 & \lambda & A\lambda^3(\rho - i\eta) \\ -\lambda & 1-\lambda^2/2 & A\lambda^2 \\ A\lambda^3(1-\rho-i\eta) & -A\lambda^2 & 1 \end{pmatrix} + O(\lambda^4) \tag{1.2}$$

where λ is used as an expansion parameter.
The four free parameters of the CKM matrix satisfy the following relations:

$$\lambda = \sin\theta_{12}, \qquad A\lambda^2 = \sin\theta_{23}, \qquad A\lambda^3(\rho - i\eta) = \sin\theta_{13}e^{-i\phi} \tag{1.3}$$

Alternative parameters are

$$\bar{\rho} = \rho\left(1 - \frac{\lambda^2}{2}\right), \qquad \bar{\eta} = \eta\left(1 - \frac{\lambda^2}{2}\right) \tag{1.4}$$

In the relations (1.3) θ_{ij} are three real angles expressing a rotation (Cabibbo-like angles), while ϕ is a phase factor encoding the CP violation.
The current experimental values of the matrix elements are [7]:

$$\begin{pmatrix} |V_{ud}| = 0.97425 \pm 0.00022 & |V_{us}| = 0.2252 \pm 0.0009 & |V_{ub}| = (4.15 \pm 0.49) \times 10^{-3} \\ |V_{cd}| = 0.230 \pm 0.011 & |V_{cs}| = 1.006 \pm 0.023 & |V_{cb}| = (40.9 \pm 1.1) \times 10^{-3} \\ |V_{td}| = (8.4 \pm 0.6) \times 10^{-3} & |V_{ts}| = (42.9 \pm 2.6) \times 10^{-3} & |V_{tb}| = 0.89 \pm 0.07 \end{pmatrix} \tag{1.5}$$

It is evident that diagonal elements are dominant and represent the most favoured quark transitions, while off-diagonal elements describe suppressed transitions.
In particular, the $|V_{td}|$ and $|V_{ts}|$ elements are not likely to be precisely measurable in tree-level processes involving top quarks, which are suppressed. The alternative is to study $B^0 - \bar{B^0}$ oscillations mediated by box diagrams and loop-mediated rare decays in K and B meson sectors. A theoretically clean determination of $|V_{td}||V_{ts}^*|$ is possible from the $K^+ \to \pi^+ \nu\bar{\nu}$ decay [8].
The current measurements of $|V_{td}|$ and $|V_{ts}|$ are obtained from the mass difference of two neutral B^0 meson mass eigenstates, which has been measured by CDF [9] and LHCb [10] experiments.

The CKM matrix unitarity gives nine conditions on the CKM matrix elements: three equations on the diagonal elements and six other vanishing combinations for the off-diagonal terms.
One of the combinations is e.g.

$$V_{ud}V_{ub}^* + V_{cd}V_{cb}^* + V_{td}V_{tb}^* = 0 \tag{1.6}$$

and can be interpreted as the sum of three vectors in a complex plane. This is represented by the triangle of figure 1.1.

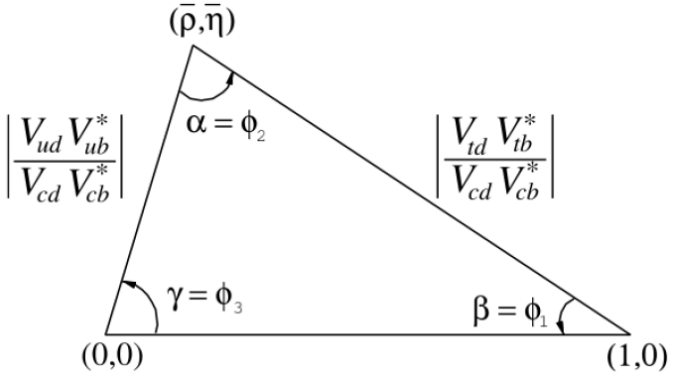

Figure 1.1: Unitarity triangle for equation 1.6.

The angles of the unitarity triangle are related to the CKM matrix elements by the following relations:

$$\beta = \arg\left(-\frac{V_{cd}V_{cb}^*}{V_{td}V_{tb}^*}\right) \qquad \alpha = \arg\left(-\frac{V_{td}V_{tb}^*}{V_{ud}V_{ub}^*}\right) \qquad \gamma = \arg\left(-\frac{V_{ud}V_{ub}^*}{V_{cd}V_{cb}^*}\right) \tag{1.7}$$

The vertexes of the triangle are $(0,0), (1,0), (\bar{\rho}, \bar{\eta})$ (defined in equation 1.4).

Measurements of CP asymmetries in $B_d \to J/\Psi K_s$ and $B_d \to \pi\pi$ processes allow to extract the angles $\sin 2\beta$ and $\sin 2\alpha$, while $K \to \pi\nu\bar{\nu}$ processes offer a complementary and independent tool to test the Standard Model consistency.

1.2.2 Branching Ratio of the $K^+ \to \pi^+\nu\bar{\nu}$ decay

The $K^+ \to \pi^+\nu\bar{\nu}$ decay and its neutral partner $K_L \to \pi^0\nu\bar{\nu}$ are Flavour Changing Neutral Current (FCNC) processes which are strongly suppressed in the Standard Model by a quadratic GIM mechanism.
At the quark level the $K \to \pi\nu\bar{\nu}$ processes arise from the flavour changing quark transition $s \to d\nu\bar{\nu}$, which in the SM receives one-loop contributions from Z-penguin and electroweak W-box diagrams, as shown in figure 1.2.

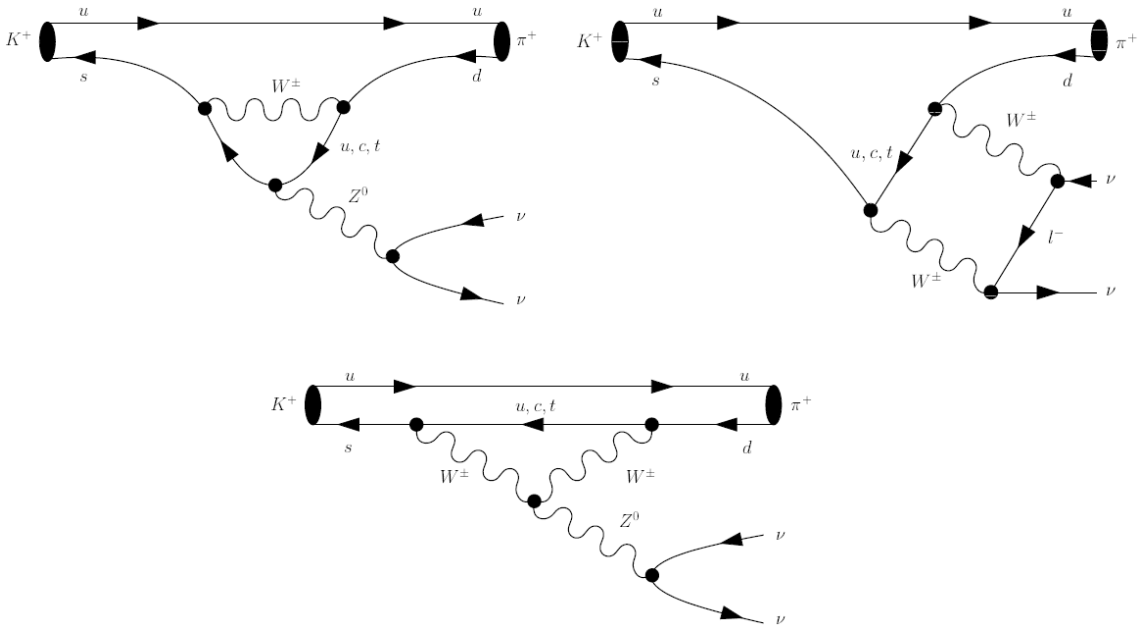

Figure 1.2: The penguin and box diagrams contributing to $K^+ \to \pi^+\nu\bar{\nu}$. For $K_L \to \pi^0\nu\bar{\nu}$ the spectator quark is changed from u to d.

The effective Hamiltonian relevant for $K^+ \to \pi^+\nu\bar{\nu}$ and $K_L \to \pi^0\nu\bar{\nu}$ decays can be written in the SM as follows [11]

$$\mathcal{H}_{\text{eff}}^{\text{SM}} = \frac{G_F}{\sqrt{2}} \frac{\alpha}{2\pi \sin^2\theta_W} \sum_{l=e,\mu,\tau} \left(V_{cs}^* V_{cd} X^l + V_{ts}^* V_{td} X(x_t) \right) (\bar{s}d)_{V-A} (\bar{\nu}_l \nu_l)_{V-A} \tag{1.8}$$

where

- G_F is the Fermi coupling constant,

- α is the fine-structure constant,
- θ_W is the Weinberg angle,
- V_{ij} are the CKM matrix elements (see section 1.2.1),
- $x_t = m_t^2/M_W^2$ where m_t is the top-quark mass and M_W is the W boson mass,
- X^l with $l = e, \mu, \tau$ are three functions describing the charm-quark contribution in the loop,
- $X(x_t)$ is a function encoding the dominant (unique) top-quark loop contribution to the charged (neutral) $K \to \pi\nu\bar{\nu}$ decay mode,
- $(\bar{s}d)_{V-A}$ and $(\bar{\nu}_l\nu_l)_{V-A}$ are the quark and lepton neutral weak currents with vector - axial vector $(V-A)$ structure: $[\bar{s}\gamma_\mu(1-\gamma_5)d][\bar{\nu}\gamma_\mu(1-\gamma_5)\nu]$.

The presence of the up quark contribution is needed for the GIM mechanism to work, but its quantitative effect is negligible. Considering the magnitude of CKM matrix elements, up and charm quark contributions should be favoured. However, as flavour-changing transitions such as $s \to d$ are forbidden at tree-level, quantum loops contribute at the leading order, and the amplitude is written in terms of $(m_q^2/M_W^2)^a$, with $a > 0$. Because of its mass, the top-quark contribution is dominant and the transition $s \to d$ is described by short-distance quark dynamics.
The Branching Ratio extracted from equation 1.8 can be written as follows, summing over three neutrino flavours [11]:

$$\mathrm{BR}(K^+ \to \pi^+\nu\bar{\nu}) = \kappa_+(1+\Delta_{\mathrm{EM}})\left[\left(\frac{\mathrm{Im}\lambda_t}{\lambda^5}X(x_t)\right)^2 + \left(\frac{\mathrm{Re}\lambda_c}{\lambda}P_c(X) + \frac{\mathrm{Re}\lambda_t}{\lambda^5}X(x_t)\right)^2\right] \tag{1.9}$$

where $\lambda = |V_{us}|$ and $\lambda_q = V_{qs}^* V_{qd}$ contain the parameters of the CKM matrix (see section 1.2.1).
The hadronic matrix element of the low-energy effective Hamiltonian can be extracted from the well-measured semi-leptonic $K \to \pi l\nu$ (K_{l3}) decays, including isospin breaking and long-distance QED radiative corrections. These contributions are contained in the parameters κ_+, including NLO and partially NNLO corrections in chiral perturbation theory, and Δ_{EM} respectively.
The κ_+ parameter also includes the remaining factors of the effective Hamiltonian in equation 1.8 and can be written as:

$$\kappa_+ = r_{K^+}\frac{3\alpha^2\mathrm{BR}(K^+ \to \pi^0 e^+\nu_e)}{2\pi^2\sin^4\theta_W}\lambda^8 \tag{1.10}$$

The parameter $r_{K^+} = 0.901$ describes three isospin breaking corrections in relating $K^+ \to \pi^+\nu\bar{\nu}$ to $K^+ \to \pi^0 e^+\nu_e$) (a 0.9614 phase-space reduction factor due to the $\pi^+ - \pi^0$ mass

difference; a factor of 0.9575 which comes primarily from $\pi^0-\eta$ mixing; a relative reduction factor of 0.979 because there are no leading logarithmic short-distance electroweak radiative corrections in $K^+ \to \pi^+\nu\bar{\nu}$) [12].
Other numerical parameters are $\mathrm{BR}(K^+ \to \pi^0 e^+ \nu_e) = (5.07 \pm 0.04)\%$ which contributes mostly to the uncertainty of κ_+, $\alpha = \frac{1}{127.9}$, $\sin^2\theta_W = 0.231$.
The final numerical value is [13]

$$\kappa_+ = (5.173 \pm 0.025) \cdot 10^{-11} \left[\frac{\lambda}{0.225}\right]^8$$

Details of the calculation of the long-distance QED radiative corrections can be found in [13]: the fully inclusive correction is $\Delta_{\mathrm{EM}} = -0.15\%$.
Square brackets in equation 1.9 enclose the charm and top quark contributions.
The top quark term can be expanded as

$$X(x_t) = X^{(0)}(x_t) + \frac{\alpha_s(m_t)}{4\pi} X^{(1)}(x_t) + \frac{\alpha}{4\pi} X^{(EW)}(x_t) \tag{1.11}$$

with α_s the strong coupling constant, where $X^{(0)}$ represents the leading-order (LO) contribution [14], $X^{(1)}$ is the next-to-leading order (NLO) QCD correction [15], and the last term corresponds to the recently computed two-loop electroweak correction [1].
The current value for the function relevant for the top quark is

$$X(x_t) = 1.469 \pm 0.017 \pm 0.002$$

where the first error quantifies the remaining scale uncertainty of the QCD corrections, and the second error corresponds to the uncertainty of the electroweak corrections. The dominant contribution to the error comes from the experimental error on the top quark mass ($\sim$3%).
The charm quark contribution is summarised through the parameter $P_c(X)$ which is written as

$$P_c(X) = P_c^{\mathrm{SD}}(X) + \delta P_{c,u} \tag{1.12}$$

The short-distance part is given by

$$P_c^{\mathrm{SD}}(X) = \frac{1}{\lambda^4}\left[\frac{2}{3}X^e + \frac{1}{3}X^\tau\right] \tag{1.13}$$

The distinction between charged lepton flavours in the box diagrams is irrelevant in the top contribution since $m_t \gg m_l$, but is relevant in the charm contribution as $m_\tau > m_c$.
The QCD part of the short distance charm contribution has been calculated at LO [16], NLO [11] and NNLO [8], with a progressive reduction of the uncertainty from $\pm$26% to $\pm$2.5%.

QED electroweak corrections have been more recently included, calculating the LO and logarithmic NLO [17]: this contribution gives an increase of 2%.
The current value for the short-distance contribution is

$$P_c^{\mathrm{SD}}(X) = 0.372 \pm 0.015$$

where 42% of the error is due to the intrinsic theoretical uncertainty and 58% to the uncertainties in the parameters m_c and $\alpha_s(M_Z)$.
The long distance contributions are calculated in [18] to be

$$\delta P_{c,u} = 0.04 \pm 0.02$$

Using all the above numerical inputs, the current theoretical prediction for the Branching Ratio of the charged mode $K^+ \to \pi^+ \nu\bar{\nu}$ is [1]

$$\mathrm{BR}(K^+ \to \pi^+ \nu\bar{\nu}) = (7.81^{+0.80}_{-0.71} \pm 0.29) \times 10^{-11} \tag{1.14}$$

The first error is related to the uncertainties in the input parameters. The main contributions are V_{cb} (56%), $\bar{\rho}$ (21%), m_c (8%), m_t (6%), $\bar{\eta}$ (4%), α_s (3%), $\sin^2\theta_W$ (1%) (for $\bar{\rho}$ and $\bar{\eta}$ see section 1.2.1).
The second error quantifies the remaining intrinsic theoretical uncertainties. In detail the contributions are $\delta P_{c,u}$ (46%), X_t(QCD) (24%), P_c (20%), κ_+ (7%), X_t(EW) (3%).

The Branching Ratio of the CP-violating neutral mode involves the top-quark contribution only and can be written as

$$\mathrm{BR}(K_L \to \pi^0 \nu\bar{\nu}) = \kappa_L \left(\frac{\mathrm{Im}\lambda_t}{\lambda^5} X(x_t) \right)^2 \tag{1.15}$$

The hadronic matrix element can be extracted from K_{l3} decays and is parametrised by κ_L. No other long-distance contributions are present, making this channel exceptionally clean from the theoretical side.
The indirect CP-violating contribution to this decay is of the order of 1% with respect to the direct contribution, and must be included at the current level of accuracy. This corresponds to multiplying the Branching Ratio by a factor

$$1 - \sqrt{2}|\epsilon_K| \frac{1 + P_C(X)/(A^2 X_t) - \rho}{\eta} \tag{1.16}$$

where η and ρ come from the parametrisation of the CKM matrix (section 1.2.1). $A = V_{cb}/\lambda^2$ and ϵ_K describe indirect CP violation in the neutral kaon system. Taking this factor into account, the result for the Branching Ratio of the neutral mode $K_L \to \pi^0 \nu\bar{\nu}$ is

[1]

$$\mathrm{BR}(K_L \to \pi^0 \nu\bar{\nu}) = (2.43^{+0.40}_{-0.37} \pm 0.06) \times 10^{-11} \tag{1.17}$$

1.2.3 Unitarity triangle from $K \to \pi\nu\bar{\nu}$ decays

The $K \to \pi\nu\bar{\nu}$ processes offer a complementary and independent tool to test the Standard Model consistency.
The measured value of $\mathrm{BR}(K^+ \to \pi^+\nu\bar{\nu})$ determines an ellipse in the $(\bar{\rho}, \bar{\eta})$ plane (figure 1.4) centred at $(\rho_c, 0)$. The departure of ρ_c from unity measures the relative importance of the internal charm contribution (it contains the $P_c(X)$ charm term from the Branching Ratio) and is shown in the triangle of figure 1.3.
The Branching Ratio of the neutral mode $K_L \to \pi^0\nu\bar{\nu}$ determines the height of the triangle, being directly related to the parameter $\bar{\eta}$ (horizontal lines shown in figure 1.4).
The use of both Branching Ratios simultaneously allows to eliminate $|V_{ub}/V_{cb}|$, thus removing a considerable uncertainty, and can determine the unitarity triangle completely.
In addition, measurements from both $K \to \pi\nu\bar{\nu}$ decays offer a clean determination of the β and γ angles in the unitarity triangle.

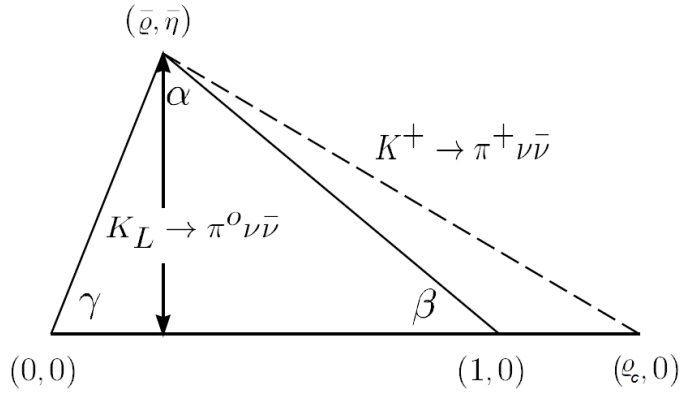

Figure 1.3: Unitarity triangle corresponding to the unitary condition $V_{ud}V_{us}^* + V_{cd}V_{cs}^* + V_{td}V_{ts}^* = 0$. The $K^+ \to \pi^+\nu\bar{\nu}$ decay determines the dashed side and the displacement of the right down vertex due to the charm-quark contribution; the neutral mode $K_L \to \pi^0\nu\bar{\nu}$ gives the $\bar{\eta}$ parameter, the triangle height.

1.2.4 $K \to \pi\nu\bar{\nu}$ beyond the Standard Model

In the case of most K and B meson decays the effective Hamiltonian in extensions of the SM becomes generally much more complex than in the SM in that new operators, new complex phases, and new one-loop short distance functions and generally new flavour

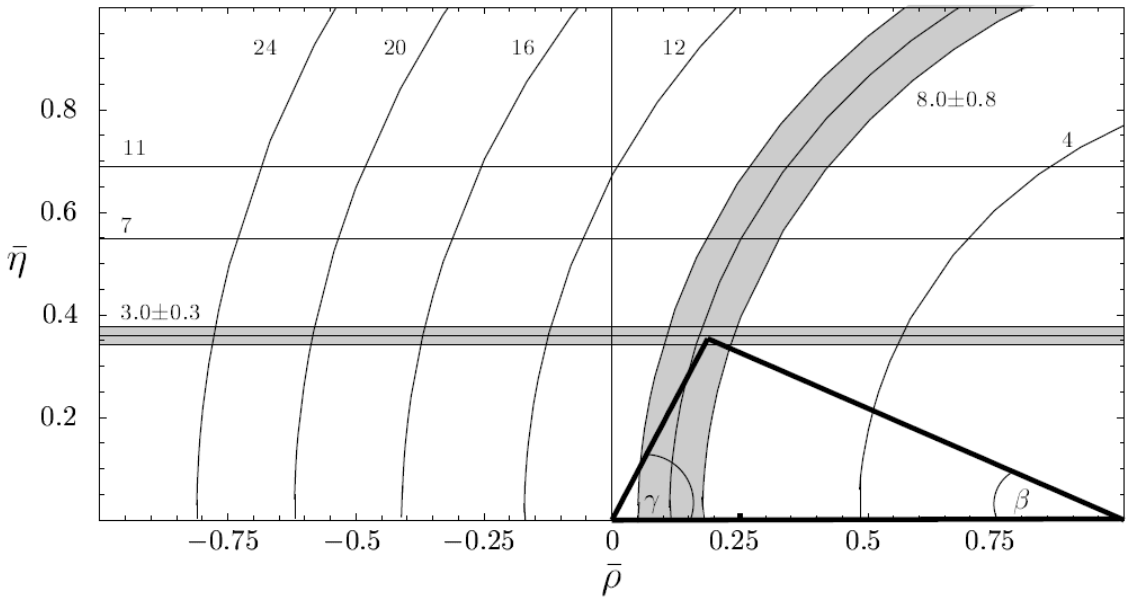

Figure 1.4: The unitarity triangle as defined with current predictions for the two Branching Ratios of $K \to \pi\nu\bar{\nu}$ modes. Lines corresponding to several values (in units of 10^{-11}) for the charged (ellipses) and neutral (horizontal lines) modes are shown.

violating couplings can be present.

For what concerns the $K \to \pi\nu\bar{\nu}$ processes, the effective Hamiltonian in essentially all extensions of the SM is obtained simply from equation 1.8 by replacing $X(x_t)$ as

$$X(x_t) \to X = |X|e^{i\theta_X} \tag{1.18}$$

Thus, the only effect of new physics is to modify the magnitude of the SM function $X(x_t)$ and/or introduce a new complex phase θ_X that vanishes in the SM.

The simplest class of extensions are models with Minimal Flavour Violation (MFV) in which $\theta_X = 0, \pi$ and $|X|$ is only modified by loop diagrams with new particles exchanges but the driving mechanism of flavour and CP violation remains the CKM matrix. As in this class of models the basic structure of effective Hamiltonians in other decays is unchanged relative to the SM and only modifications in the one-loop functions, analogous to X, are allowed, the correlations between $K \to \pi\nu\bar{\nu}$ and other K and B decays which are valid in the SM remain true.

However, the recently improved bounds on rare B decays, combined with the above correlations, do not allow for a large departure of $K \to \pi\nu\bar{\nu}$ from the SM within this simplest class of new physics.

More deviations from the SM in $K \to \pi\nu\bar{\nu}$ are possible in models beyond MFV. Examples are Minimal Supersymmetric extension of the Standard Model (MSSM) [2] and Littlest Higgs model with T-parity (LHT) [3].

1.3 Experimental status

The searches for the $K^+ \to \pi^+\nu\bar{\nu}$ decay started in 1969; the early experiments used stopped-kaon beams.
The first result was published by a heavy-liquid bubble chamber experiment at the Argonne Zero Gradient Synchrotron [19]: a 90% confidence level (CL) upper limit $\mathrm{BR}(K^+ \to \pi^+\nu\bar{\nu}) < 10^{-4}$ was obtained.
In 1973 a spark chamber experiment at the Berkeley Bevatron improved the limit down to $\mathrm{BR}(K^+ \to \pi^+\nu\bar{\nu}) < 5.6 \times 10^{-7}$ [20]. The collaboration performed a combined search in two kinematic regions, above and below that of the potential background $K^+ \to \pi^+\pi^0$, called region I and region II.
In 1981 the limit was further improved down to $\mathrm{BR}(K^+ \to \pi^+\nu\bar{\nu}) < 1.4 \times 10^{-7}$ by an experiment at the KEK Proton Synchrotron [21], for which the region I was the only accessible kinematic region.
The first observation of the $K^+ \to \pi^+\nu\bar{\nu}$ decay and the best measurement currently available of its Branching Ratio have been performed in two experiments at Brookhaven National Laboratory (BNL), E787 and its upgrade E949, which obtained first results at the end of 1990s.
The adopted technique is to study $K^+ \to \pi^+\nu\bar{\nu}$ decay from kaons at rest. The signature for the decay is a pion of momentum $P < 227\,\mathrm{MeV}/c$ and no other particles. The observation of this signal requires suppression of all backgrounds with a reliable estimate of residual events. Main background sources are $K^+ \to \mu^+\nu_\mu$ ($K_{\mu 2}$) with a 64% Branching Ratio and $P = 236\,\mathrm{MeV}/c$, $K^+ \to \pi^+\pi^0$ ($K_{\pi 2}$) with a 21% Branching Ratio and $P = 205\,\mathrm{MeV}/c$, scattering of residual pions in the beam and K^+ charge exchange processes resulting in decays of the K_L.
Figure 1.5 shows the two $\pi\nu\bar{\nu}$ regions in the spectrum of the $K^+ \to \pi^+\nu\bar{\nu}$ decay together with the spectra of main kaon decay channels (not normalised to the Branching Ratio which is indicated in parentheses).

In E787 kaons are produced at momenta between $710\,\mathrm{MeV}/c$ and $790\,\mathrm{MeV}/c$ (in different runs) at a rate of 7×10^6 per 1.6 s-spill of the Alternating Gradient Synchrotron (AGS), identified by Čerenkov, tracking and energy loss counters. 20% of the kaons reach a stopping target of plastic scintillating fibres. Measurements of the momentum (P), range (R) and kinetic energy (E) of charged decay products were made using the target, a central drift chamber, and a cylindrical range stack made of layers of plastic scintillator counters and double-layer straw chambers. Pions were distinguished from muons by kinematics and by observing the pion decay sequence into muon and electron in the range stack. Photons

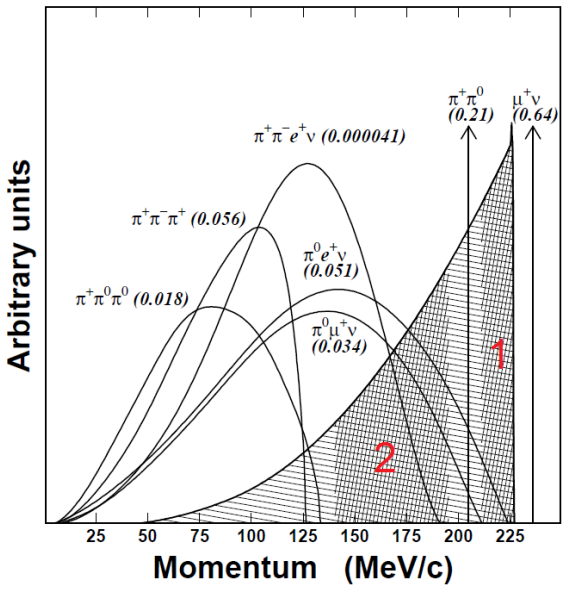

Figure 1.5: Momentum spectra of charged particles from K^+ decays in the rest frame. The values in parentheses represent the Branching Ratios of the decay modes. The hatched area represents the π^+ spectrum from $K^+ \to \pi^+\nu\bar{\nu}$ decays. The densely hatched regions are the signal region I and region II (E949).

were detected in a hermetic calorimeter, including detectors in the extreme forward and backward regions. A magnetic field was used for momentum measurements.
The search was performed requiring an identified kaon stopping in the target followed by a single charged particle track unaccompanied by other decay products. This particle must have been identified as a π^+ with P, R and E; in addition to the kinematics, the measurement of the $\pi \to \mu \to e$ decay sequence provided a further rejection factor against $K_{\mu 2}$ events. $K_{\pi 2}$ events were efficiently eliminated by exploiting the full calorimeter coverage, with an inefficiency of 10^{-6} for photon energies above 1 MeV. A scattered beam pion could result from a mis-identification as a K^+. Charge exchange background survived if K_L were produced at low enough energy to remain in the target for the required time and if the charged lepton decay product went unobserved.
The experiment used a blind data analysis strategy, and the background sources were identified and estimated with data-driven techniques. The major results of the E787 experiment are shown in figure 1.7:

- Two observed events in region I, with a pion momentum between 211 MeV/c and 229 MeV/c (between the peaks corresponding to the two body background decays $K_{\mu 2}$ and $K_{\pi 2}$). The events are identified by red circle markers in figure 1.7. This observation leads to BR($K^+ \to \pi^+\nu\bar{\nu}$)=$1.57^{+1.75}_{-0.82} \times 10^{-10}$, with an estimated background of 0.15 ± 0.05 in a total sample of 5.9×10^{12} stopped kaons [22] [23].

- One candidate event in region II, with a pion momentum 140 MeV/c < P < 195 MeV/c

(below the peak of the $K_{\pi 2}$). The event is indicated with a green triangle in figure 1.7. This region has larger potential acceptance because of the larger phase space, but is affected by additional sources of background: the most important is due to $K_{\pi 2}$ event in which the pion had a nuclear interaction near the kaon vertex decay, resulting in less kinetic energy of the outgoing particle. The observation performed on a sample of 1.12×10^{12} kaons is consistent with the expected background of 0.73 ± 0.18, giving a 90% CL upper limit of BR($K^+ \to \pi^+ \nu\bar{\nu}$)$< 42 \times 10^{-10}$ [24].

E949 is an upgrade of the E787 experiment: the expected sensitivity increased by a factor 5. The improvements regarded an upgrade of the photon veto calorimeter, replacement of one third of the Range Stack for the tracking, improvement of the trigger system and data analysis, which enabled to achieve a comparable acceptance even with twice the rate of E787. The layout of the E949 detector is shown in figure 1.6.

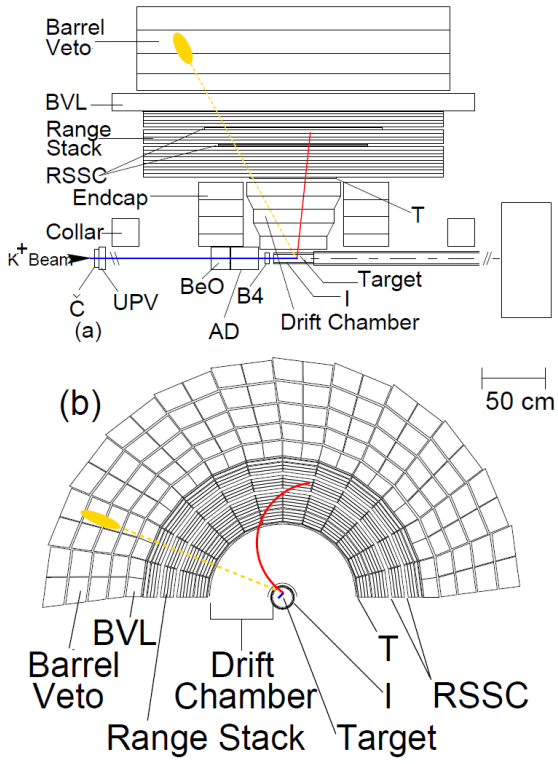

Figure 1.6: Schematic side(a) and end(b) views of the upgraded E949 detector. A $K^+ \to \pi^+\pi^0$ event is shown.

The complete data analysis of E949 was performed as for E787 in the two different kinematic regions leading to the results included in figure 1.7:

- One event was observed in region I near the upper kinematic limit (blue triangle in figure 1.7), over an expected background of 0.30 ± 0.03. The number of kaons

stopped in the target was 1.8×10^{12}. The combined E787+E949 result in this region was BR($K^+ \to \pi^+\nu\bar{\nu}$)=$1.47^{+1.30}_{-0.89} \times 10^{-10}$ based on three events [25].

- Three events observed in region II (black square markers in figure 1.7) in an exposure of 1.71×10^{12} stopped kaons with an estimated total background of $0.93 \pm 0.17(\text{stat.})^{+0.32}_{-0.24}(\text{syst.})$ events. The Branching Ratio determined with these three events is BR($K^+ \to \pi^+\nu\bar{\nu}$)=$7.89^{+9.26}_{-5.10} \times 10^{-10}$ [4].

The combined final measurements of E787+E949 is BR($K^+ \to \pi^+\nu\bar{\nu}$)=$1.73^{+1.15}_{-1.05} \times 10^{-10}$, based on 7 observed candidate $K^+ \to \pi^+\nu\bar{\nu}$ events [4].
This result is consistent with the SM theoretical prediction reported in section 1.2.2. However a measurement of the Branching Ratio with at least 10% accuracy is needed for a significant test of new physics.

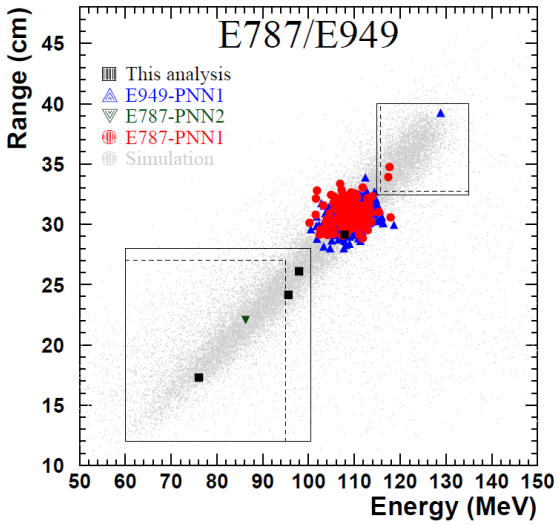

Figure 1.7: Range (R) vs. Kinetic energy (E) of all events passing analysis selection in E787 and E949 experiments. The squares represent the events observed by the E949 region II analysis. The circles and upward-pointing triangles represent the events observed by the E787 and E949 region I analyses, respectively. The downward-pointing triangle represent the events observed by the E787 region II analysis. The solid (dashed) lines represent the limits of the signal region I and region II for the E949 (E787) analyses. The points near E_π = 108 MeV were $K_{\pi 2}$ decays that survived the photon veto cuts and were predominantly from the region I analyses due to the higher sensitivity and the less stringent photon veto cuts. The light grey points are simulated $K^+ \to \pi^+\nu\bar{\nu}$ events that passed the trigger conditions.

A recap of all the experimental measurements of the Branching Ratio of the $K^+ \to \pi^+\nu\bar{\nu}$ decay reported in this section is presented in figure 1.8, where the results are shown along a time line indicating the year of publication.

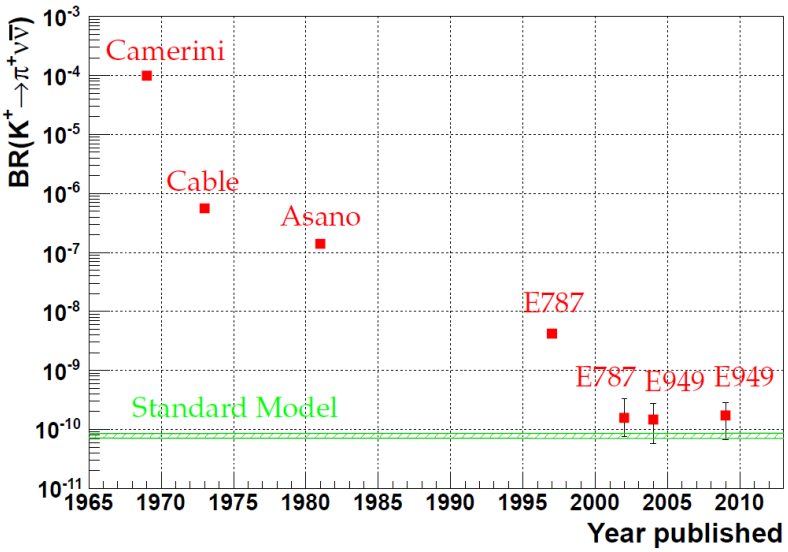

Figure 1.8: Experimental upper limits and measurements of the Branching Ratio of the $K^+ \to \pi^+\nu\bar{\nu}$ shown along a time line indicating the year of publication. The different measurements are described in this section (1.3). Squares with no errors are upper limits at 90% confidence level.

1.4 NA62 experimental strategy

NA62 uses a decay-in-flight technique, differently from the kaon decay at rest approach which was at the basis of the previous experiments.
The experimental setup consists of a 100 m long beam line to select the appropriate secondary beam component produced by protons from the SPS CERN accelerator, followed by a 80 m long evacuated volume which defines the decay region. The detectors are designed to measure the K^+ and the secondary particles from kaon decays occurring in the decay volume. The integrated rate downstream is about 10 MHz, mainly coming from K^+ decays. A detailed description of the NA62 experimental setup is given in chapter 2.
The signature of the signal is one track in the final state matched with one K^+ track in the beam. The kinematics of the $K^+ \to \pi^+\nu\bar{\nu}$ decay is shown in figure 1.9: the measurable quantities are $\vec{p}_K$ (kaon momentum), $\vec{p}_\pi$ (pion momentum) and the angle $\theta_{\pi K}$ (angle between the pion and the kaon).

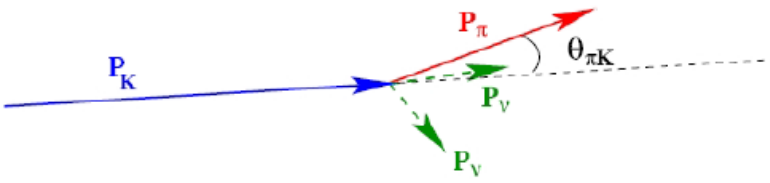

Figure 1.9: Kinematics of the $K^+ \to \pi^+\nu\bar{\nu}$ decay.

The squared missing mass describes the kinematics of the decay. It is defined as follows:

$$m^2_{\text{miss}} = (P_K - P_\pi)^2 = (E_K - E_\pi)^2 - (|\vec{p}_K|^2 + |\vec{p}_\pi|^2 - 2|\vec{p}_K||\vec{p}_\pi|\cos\theta_{\pi K}) \tag{1.19}$$

where

$$(E_K - E_\pi)^2 = m^2_K + |\vec{p}_K|^2 + m^2_\pi + |\vec{p}_\pi|^2 - 2\vec{p}_K||\vec{p}_\pi|\sqrt{\left(1 + \frac{m^2_K}{|\vec{p}_K|^2}\right)\left(1 + \frac{m^2_\pi}{|\vec{p}_\pi|^2}\right)} \tag{1.20}$$

Given the characteristics of the experiment, with relativistic particles ($mc^2 \ll pc$) and small angles (order of mrad), a good approximation for the missing mass is:

$$m^2_{\text{miss}} \simeq m^2_K\left(1 - \frac{|\vec{p}_\pi|}{|\vec{p}_K|}\right) + m^2_\pi\left(1 - \frac{|\vec{p}_K|}{|\vec{p}_\pi|}\right) - |\vec{p}_K||\vec{p}_\pi|\theta^2_{\pi K} \tag{1.21}$$

The absolute values of the kaon and pion momenta, together with their relative directions, are measured by a beam spectrometer (see section 2.1.3) and a spectrometer placed downstream of the decay region (see section 2.2.1).
The distribution of m^2_{miss} (with the hypothesis that the charged decay product is a pion) allows a separation of the signal from the main K^+ decay modes by defining two signal regions where a limited background coming from the kinematically constrained decays is expected (figure 1.10):

- region I: $0 < m^2_{\text{miss}} < m^2_{\pi^0} - (\Delta m)^2$
- region II: $m^2_{\pi^0} + (\Delta m)^2 < m^2_{\text{miss}} < \min[m^2_{\text{miss}}(K^+ \to \pi^+\pi^+\pi^-)] - (\Delta m)^2$

where $(\Delta m)^2$ represents the resolution on the squared missing mass.
Nevertheless, the total background in these regions is still several order of magnitude larger than the $K^+ \to \pi^+\nu\bar{\nu}$ signal, as a consequence of the main decay modes leaking there via resolution effects and radiative tails, semi-leptonic decays and even rare decays like $K^+ \to \pi^+\pi^-e^+\nu_e$, whose kinematics cannot be constrained by the m^2_{miss} variable (figure 1.11). Possible interactions of the beam with the material along the beam line and in the residual gas in the vacuum region are the main sources for accidental single track background.

The presence of one track reconstructed in the downstream spectrometer matched in space and time with one track reconstructed in the beam spectrometer is the first requirement for a signal selection. A set of criteria for pion identification allows the suppression of the decay modes with muons and positrons, by means of a RICH (section 2.2.2) and hadronic calorimeters (sections 2.2.3). The same requirements are also effective for controlling the backgrounds with more than one charged track in the final state.
A hermetic photon veto system (section 2.3) is also important to suppress decay modes

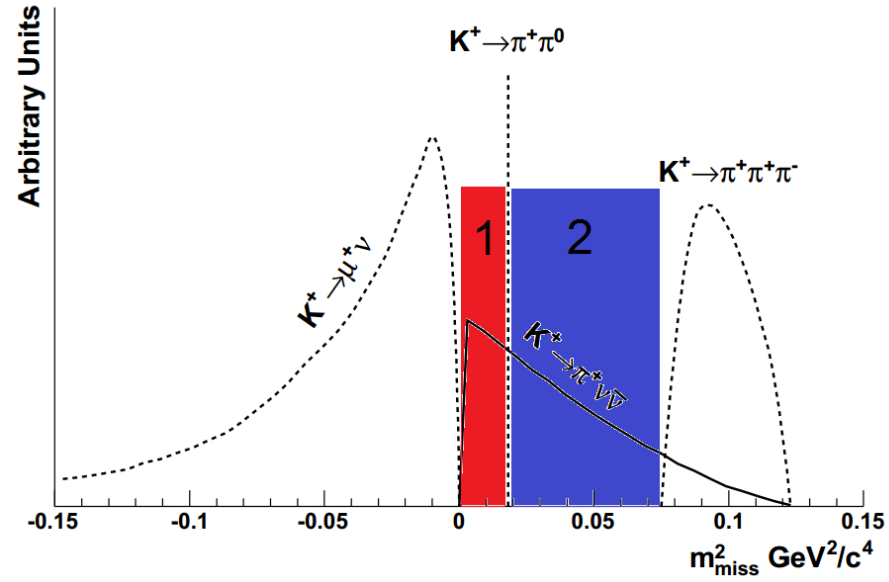

Figure 1.10: Distributions of the $m^2_{\rm miss}$ variable under the hypothesis that the detected charged particle in the final state is a pion, for the signal (solid curve) and the kaon kinematically constrained decays (dotted curves). The spectra are plotted in arbitrary units, not weighted with the Branching Ratios, and neglecting resolution effects. The $K^+ \to \pi^+\pi^0$ background forces the analysis region to be split into two regions: region I (in red) and region II (in blue).

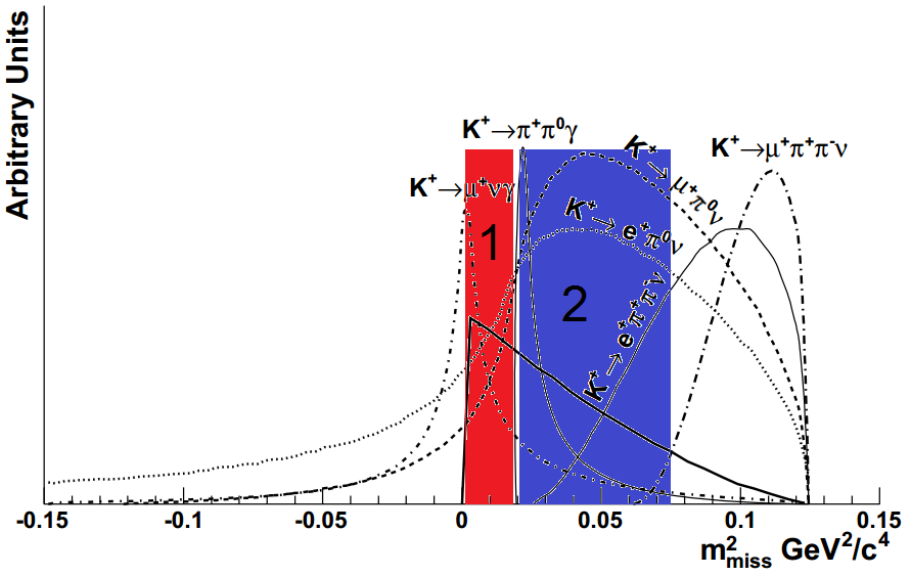

Figure 1.11: Distributions of the $m^2_{\rm miss}$ variable under the hypothesis that the detected charged particle in the final state is a pion, for the signal (solid curve) and the kaon not kinematically constrained decays (dashed curves). The spectra are plotted in arbitrary units, not weighted with the Branching Ratios, and neglecting resolution effects. The two analysis regions are indicated in red (I) and blue (II).

with photons in the final state, by vetoing events compatible with the presence of photons. A signal in the Čerenkov counter on the beam line (section 2.1.2) ensures the presence of a kaon in time with the tracks in beam spectrometer and in the downstream spectrometer. This allows the suppression of most of the accidental tracks coming from the interactions of the pions in the beam with the material along the beam line.
Finally two global requirements are applied: the kaon decay has to take place in the first 60 m of the decay volume; the measured momentum of the downstream π^+ must be between 15 GeV/c and 35 GeV/c.
Table 1.1 lists the dominant K^+ decay modes, together with the techniques that will be used to reject them.

Decay	BR	Rejection mode
$K^+ \to \mu^+\nu$	63%	μ-ID + kinematics
$K^+ \to \pi^+\pi^0$	21%	γ-veto + kinematics
$K^+ \to \pi^+\pi^+\pi^-$	6%	multi-track + π^--ID + kinematics
$K^+ \to \pi^+\pi^0\pi^0$	2%	γ-veto + kinematics
$K^+ \to \pi^0\mu^+\nu_\mu$	3%	μ-ID + γ-veto
$K^+ \to \pi^0 e^+\nu_e$	5%	e-ID + γ-veto

Table 1.1: Main kaon decays (98% of the total Branching Ratio), their Branching Ratios and corresponding rejection methods. The first 4 rows correspond to kinematically constrained channels, while last two list the largest not kinematically constrained decays.

The $K^+ \to \pi^+\pi^0$ is primarily rejected by selecting the two signal regions defined above. The tracking system allows a 10^{-3} GeV$^2/c^4$ resolution on $m^2_{\rm miss}$. The rejection factor from kinematics is about 5×10^3. The non Gaussian tails due to multiple scattering and pileup in the beam spectrometer are the main limiting factors to the kinematic rejection power. For what concerns the pileup, the precise timing between the upstream and downstream track is the key ingredient to reduce the mismatch probability below the percent level, which corresponds to about one half of the total kinematic rejection inefficiency.
The photon rejection must guarantee a π^0 suppression by 8 orders of magnitude. Nevertheless the π^0 has at least an energy of 40 GeV, after requiring that the π^+ momentum should not exceed 35 GeV/c. The system of electromagnetic calorimeters and photon vetoes of NA62 ensures a geometrical coverage for photons with polar angles up to 50 mrad and with an energy down to 100 MeV. About 0.2% of the $K^+ \to \pi^+\pi^0$ decays have one photon outside the detection region, but the other photon has always an energy of the order of 10 GeV or even more and travels in the forward direction.

Because of the pion track hypothesis, the $m^2_{\rm miss}$ spectrum of the $K^+ \to \mu^+\nu_\mu$ is negative and momentum dependent, approaching zero at increasing pion momenta. As a consequence, the cuts on $m^2_{\rm miss}$ defining the signal regions allow a strong suppression of

this background. Also, the cut at $35\,\mathrm{GeV}/c$ on the maximum track momentum enhances the kinematic rejection factor. The situation is similar to that of $K^+ \to \pi^+\pi^0$, with the difference that the $K^+ \to \mu^+\nu_\mu$ background affects mainly region I and the muon does not suffer from hadronic elastic scattering. The overall rejection factor is 1.5×10^4 with the limiting factors coming from multiple scattering non Gaussian tails and pileup.
The muon suppression comes from the pion identification which uses calorimetric and Čerenkov information. These inputs are combined with those from the hadronic calorimeter subdetectors. The ultimate inefficiency of the muon-pion separation is 10^{-5} and comes from the absorption of muons due to the energy loss via Bremsstrahlung. The RICH of NA62 allows a muon-pion separation with an inefficiency below a percent, for tracks momenta between $15\,\mathrm{GeV}/c$ (about 20% above the Čerenkov threshold for pions) and $35\,\mathrm{GeV}/c$.

The requirement of having only one track in the downstream spectrometer rejects about 99% of the $K^+ \to \pi^+\pi^+\pi^-$. The m^2_{miss} spectrum is crucial to strongly suppress the contribution from those $K^+ \to \pi^+\pi^+\pi^-$ with one π^+ and the π^- not reconstructed in the spectrometer. Also the cut at $15\,\mathrm{GeV}/c$ on the minimum track momentum is effective to this goal. The overall rejection factor from kinematics is 1.5×10^6. The residual background comes from events entering in region II, because of the tails of the reconstructed m^2_{miss} due to the non Gaussian multiple scattering.
The largest part of the remaining events have one good π^+ reconstructed and the other two charged pions pointing to the central beam hole which allows the passage of undecayed beam particles throughout the downstream detectors. Nevertheless, the strength of the magnetic field of the spectrometer magnet and the distance between this magnet and the detectors downstream ensure a full geometrical coverage downstream of the magnet for the detection of π^- up to $65\,\mathrm{GeV}/c$. The rejection factor is of the order of 10^6.

The table of figure 1.12 summarises the expected results on the sensitivity of NA62 for the measurement of the $K^+ \to \pi^+\nu\bar{\nu}$, combining all the rejection factors coming from kinematics, particle identification and vetoes [26]. The total number of events is normalised to the expected number of kaons per year of data taking (4.5×10^{12}). The Standard Model Branching Ratio is assumed for the signal.

Decay	event/year
$K^+ \to \pi^+ \nu\bar{\nu}$	45
$K^+ \to \pi^+ \pi^0$	5
$K^+ \to \pi^+ \pi^+ \pi^-$	1
$K^+ \to \pi^+ \pi^- e^+ \nu$	<1
$K^+ \to \pi^+ \pi^0 \gamma$	<1
$K^+ \to \mu^+ \nu\gamma$	1.5
other rare decays	0.5
Total backgrounds	<10

Figure 1.12: Expected signal and background from K^+ decays estimated from NA62 sensitivity studies [26]. The numbers are normalised to 4.5×10^{12} kaon decays per year of data taking. The SM Branching Ratio is assumed for the signal.

Chapter 2

The NA62 experimental setup

The NA62 experiment is housed in the CERN North Area High Intensity Facility and uses the SPS extraction line already used by the previous NA48 experiment in the same area. A schematic view (not in scale) of the CERN accelerator complex is shown in figure 2.1.

The use of a decay-in-flight technique to study kaon decays is the experimental principle of NA62 and it is well matched to the characteristics of the CERN SPS. The main elements for the detection of the K^+ decay products are spread along a 170 m long region starting about 100 m downstream of the target. Useful kaon decays are detected within a 60 m long fiducial region. The largest detectors have an approximately cylindrical shape around the beam axis with a diameter up to about 2 m and down to 10 cm in order to let the very intense flux of undecayed beam particles pass through without affecting the active area.
Since the neutrino-antineutrino pair is undetectable, the signature of the signal consists of a single π^+ track reconstructed downstream of the decay volume and matched to a K^+ track upstream. Timing, spatial and angular information are needed to match these two tracks.
The experimental setup consists in tracking devices for both K^+ and π^+ (sections 2.1 and 2.2), and calorimeters to veto photons, positrons and muons (section 2.3). Furthermore, a powerful particle identification system to identify the incident kaons (section 2.1) and distinguish π^+ from μ^+ and e^+ (section 2.2) complements the tracking and veto detectors to reach the required sensitivity and to guarantee redundancy.
The schematic layout of the NA62 experiment including the target, the beam line, the decay fiducial region and all detectors is shown in figure 2.2.

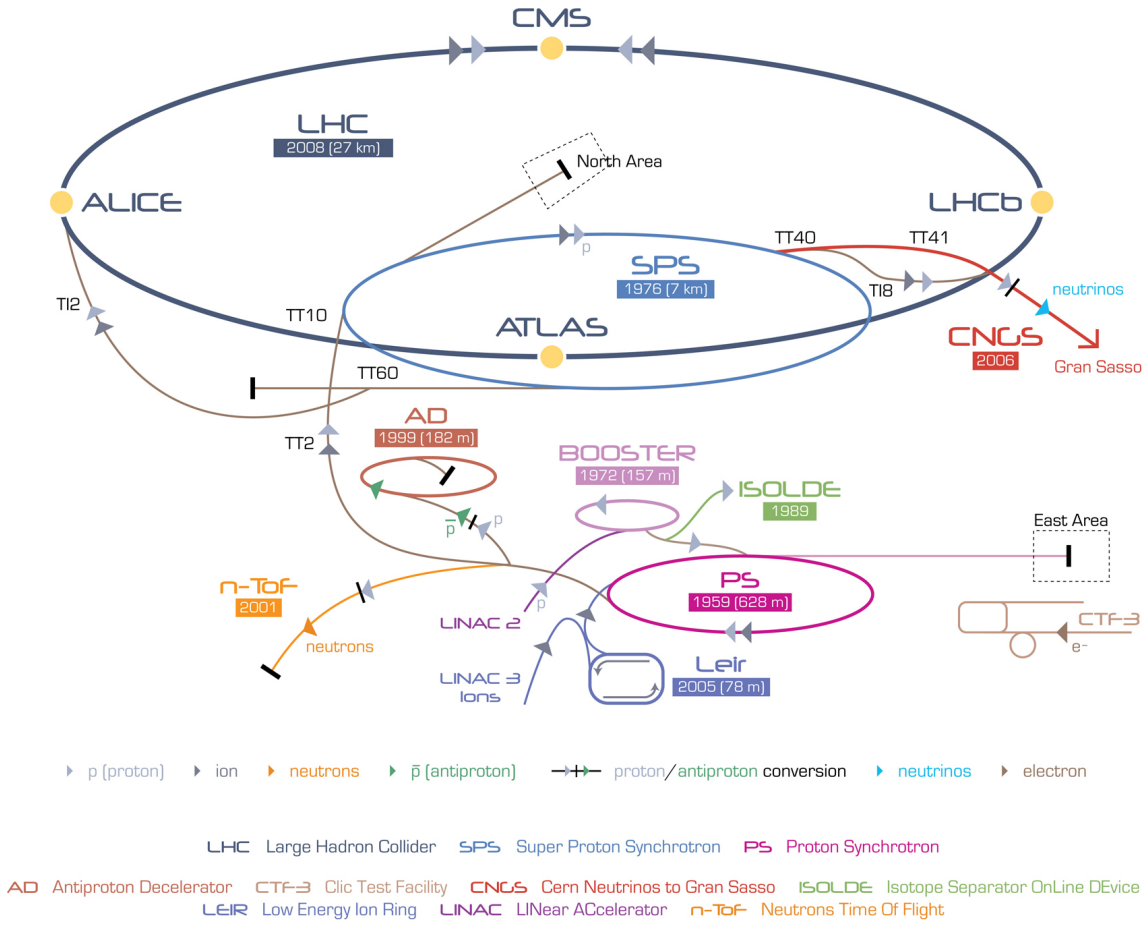

Figure 2.1: Schematic view of the CERN accelerator complex (not to scale). The NA62 experiment is located in the North Area SPS extraction line.

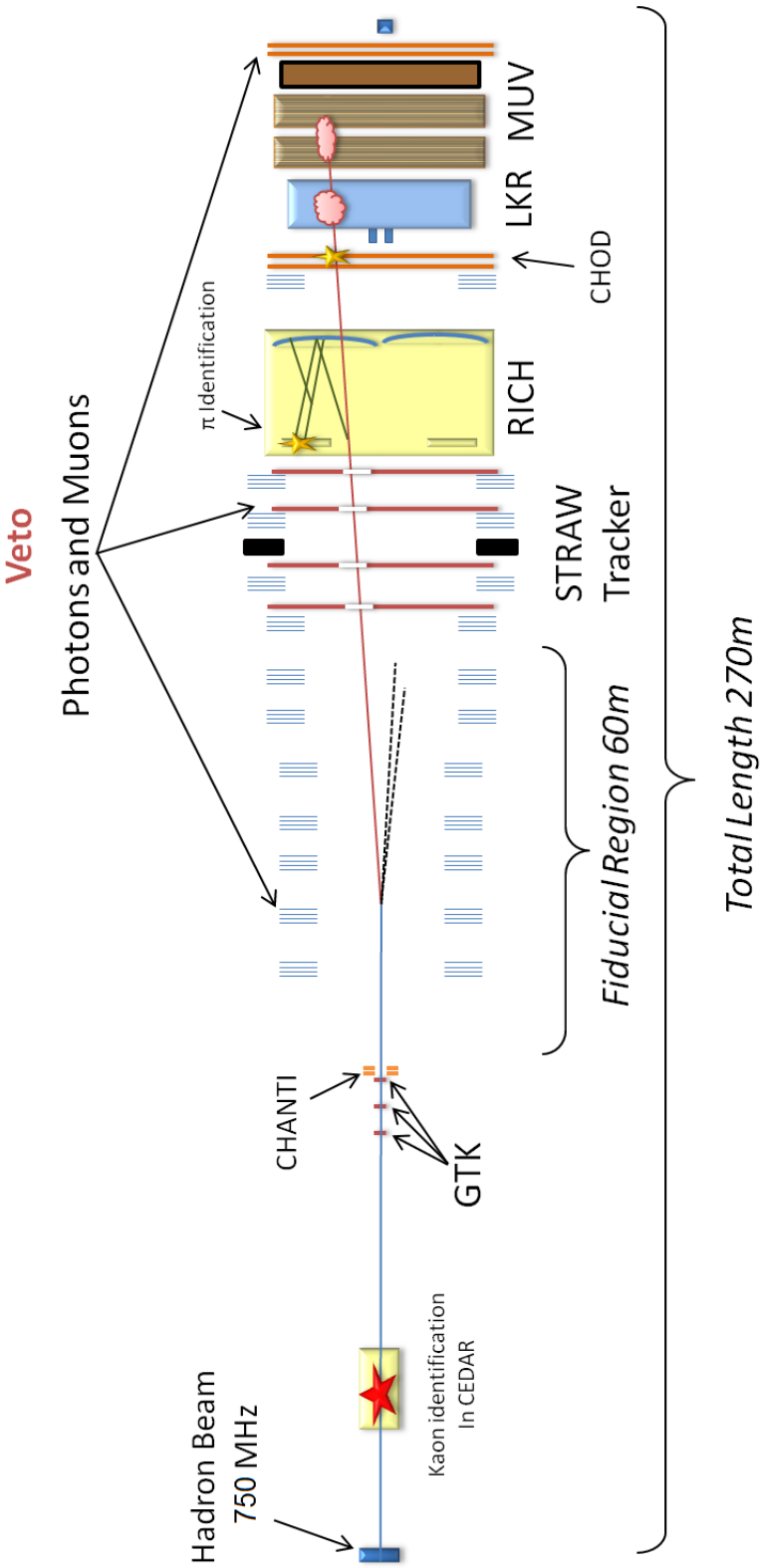

Figure 2.2: Layout of the NA62 experimental setup (not to scale).

2.1 The beam line: Kaon tagging and tracking

This section describes the kaon beam properties, and the detectors placed along the beam line for kaon identification and tracking.

2.1.1 Beam line

The beam feeding the NA62 experiment is a secondary hadron beam produced from primary protons extracted from the SPS with a momentum of 400 GeV/c and impinging on a beryllium target located at the beginning of the NA62 experimental hall.
The major advantage of using a high energy proton machine is that the cross-section for the production of kaons increases with the proton energy: to achieve a given kaon flux a lower proton flux is needed and this results in an effective reduction of the non-kaon related accidental activity. A simple empirical formula fitting the measured particle production data [27] shows that the maximum K^+ (K^-) yield in a given momentum and solid angle range, per primary proton of fixed momentum p_0, occurs at a kaon momentum $p_K \sim 0.35p_0$ ($\sim 0.23p_0$).
The choice of a positive hadron beam is motivated by the fact that the ratio of production rates $K^+/K^- \sim 2.1$ for 400 GeV/c primary protons, and the ratio $\frac{K^+/\pi^+}{K^-/\pi^-} \sim 1.2$.
The choice of a central momentum of 75 GeV/c is driven by several factors, and is the result of a compromise between particle flux at production and fraction of kaons decaying within the 60 m long fiducial region. In addition, this value fits well with the characteristics of the detectors for particle identification: the useful range of momenta for a π^+ decay product to be distinguished from a background μ^+ is between 15 GeV/c and 35 GeV/c, and this means that other particles associated with an accepted pion must carry an energy above 40 GeV, for which the veto system has an adequate efficiency. Finally, it is the maximum momentum for which the required stages of the beam optics can fit in the available length of about 102 m from the production target to the beginning of the decay fiducial region.
The principal disadvantage of performing the experiment at high momentum is that kaons cannot be efficiently separated from other charged hadrons (protons and pions). The consequence is that upstream detectors, placed along the beam line, are exposed to a particle flux much larger (about 17×) than the kaon component.
Muons originating from the decays of the kaon and pion components of the beam give a significant contribution to the single-particle flux to which the detectors outside the beam are exposed. A detailed study of this particle flux component, called muon *halo*, is reported in chapter 4 where its effect on the trigger is evaluated.
After the beryllium target, the beam optics is composed of quadrupole magnets to focus hadrons towards a beam dump element consisting of a momentum-defining slit. This is enclosed in an achromatic corrector composed of four dipole magnets, thus allowing to

select a narrow momentum band ($\Delta p/p \lesssim 1\%$). After the momentum selection, additional quadrupoles focus the beam towards two collimators in the vertical and horizontal planes and align the beam to the axis of a Čerenkov differential counter (CEDAR, see section 2.1.2) which is used to tag kaons. The following stage is a beam tracking system composed of a second achromatic corrector, four dipole magnets and three stations of a spectrometer (GigaTracker or GTK, see section 2.1.3).
Table 2.1 summarises the most relevant NA62 beam properties.

SPS proton rate on target		1.1×10^{12} Hz
Fluxes at production	p	171 MHz
	K^+	53 MHz
	π^+	532 MHz
Fluxes at beginning	p	173 MHz
of fiducial region	K^+	45 MHz
	π^+	525 MHz
	e^+	0.3 MHz
	μ^+	6 MHz
Mean K^+ momentum		75 GeV/c
Momentum band r.m.s.	$\Delta p/p$	1%
Beam size 2 r.m.s.	x	$\pm$27.5 mm
	y	$\pm$11.4 mm
Decay fiducial length		60 m
K^+ lifetime	$\gamma c\tau$	564 m
Decay fraction		0.101
K^+ decays in fiducial length	per year	4.5×10^{12}

Table 2.1: Most relevant properties of the NA62 beam. The μ^+ flux at the beginning of the fiducial region refers to the beam component only, and does not take into account the halo.

2.1.2 CEDAR

The kaon component in the beam is about 6% out of the total 750 MHz rate, as can be seen in table 2.1.
A critical aspect is therefore to positively identify the minority particles of interest, kaons, in a high rate environment. This is achieved by placing in the incoming beam a differential Čerenkov counter, the CEDAR, filled with hydrogen gas.
This detector is an upgrade of the CEDAR built for the SPS secondary beams. It is designed to identify particles of a specific mass by making the detector blind to the Čerenkov light produced by particles of different mass. For a given beam momentum, the Čerenkov angle of the light emitted by a particle traversing a gas of a given refraction index n and

pressure is a unique function of the mass of the particle. In addition, the chromatic dispersion of the gas gives a dependence of the angle on the wavelength of the emitted light. A schematic view of a standard CERN SPS CEDAR is shown in figure 2.3.

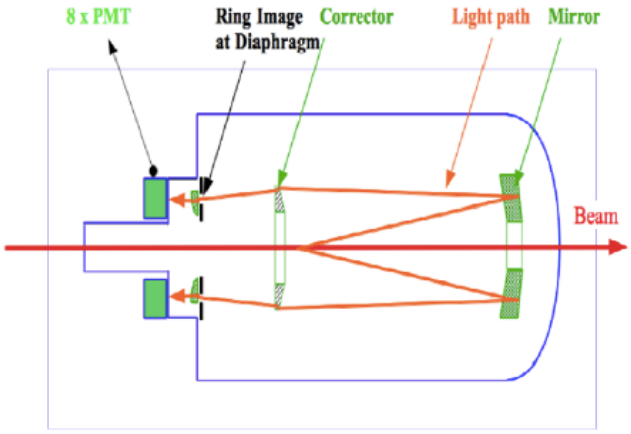

Figure 2.3: Schematic layout of a standard CERN SPS CEDAR.

The CEDAR consists of a pressure vessel filled with hydrogen at a pressure of 3.85 bar. At the end of the vessel, the Čerenkov light is reflected by a spherical mirror onto a ring-shaped diaphragm of 100 mm radius with adjustable aperture width, located at the beginning of the vessel. A chromatic corrector lens, designed to match the dispersion curve of the gas and positioned in between the mirror and the diaphragm, ensures that the light of all wavelengths arrives at the same radius on the diaphragm plane. The advantage of this design is that light from unwanted particles hits the diaphragm plane at a different radius, it therefore does not pass through the aperture and does not contribute to the rate. This only works if all rings are concentric, which requires all beam particles to be parallel to each other and consequently imposes constraints on the beam optics.

The KTAG upgrade of NA62 acts in the Čerenkov light detection phase: to cope with the expected 45 MHz kaon rate, 384 photomultipliers (PMTs) divided in 8 light boxes called octants (48 PMTs per octant), and replacing the original 8 PMTs, are placed behind the 8 annular slits. As a consequence, an average rate of about 4 MHz is foreseen on a single PMT.

The required performances of the CEDAR+KTAG system are an efficiency in kaon tagging above 95% with a kaon time resolution of the order of 100 ps. In addition, the pion mis-identification probability must be kept under 1×10^{-3}.

The front-end system is based on 8 boards (one per light box) housing 8 ultra fast NINO amplifier/discriminator chips [28], to benefit from the fast PMT response.

The CEDAR uses the common TDC-based readout system TDCB+TEL62 described in

detail in chapter 3.

2.1.3 GigaTracker

The GigaTracker (GTK) is a core detector in the NA62 experimental strategy for the tracking of kaons, needed for the missing mass based kinematic rejection of the background kaon decays.
It is a spectrometer composed of three stations mounted in between four achromat magnets as shown in figure 2.4. The detector is placed along the beam line, just before the fiducial region in the decay vacuum pipe.

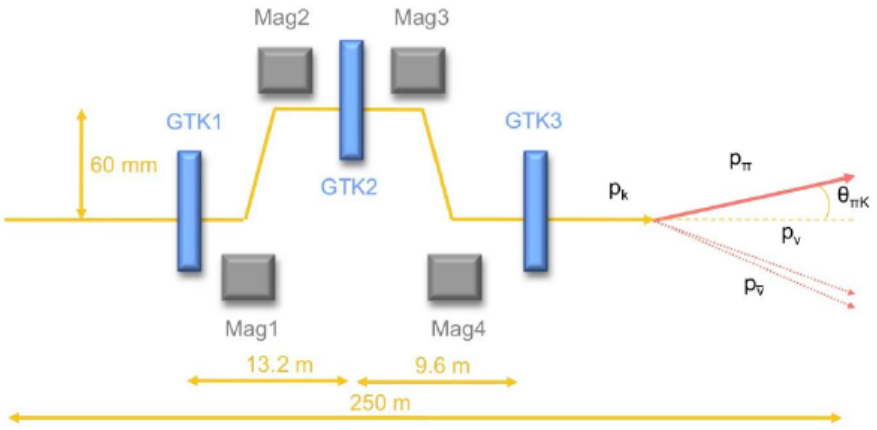

Figure 2.4: Layout of the GigaTracker stations.

The measurement of the particle momentum and direction is obtained through a magnetic field: the path of the particle is bent depending on its momentum. As indicated in figure 2.4, the second station is displaced by 60 mm from the beam axis.
Each GTK station is a hybrid silicon pixel detector with a total size of 63.1 mm × 29.3 mm, thus matching the expected beam dimensions (table 2.1). The pixel size is (300×300) µm^2. A total number of 18 000 pixels, arranged in a matrix of 90×200 elements, make one station. The pixel thickness is 200 µm and corresponds to 0.22% X_0: a minimal amount of material is in fact required not to spoil the beam divergence and limit the rate of beam hadronic interactions. Including the material budget for the pixel readout and cooling, the total amount per station remains below 0.5% X_0.
The expected beam rate of 750 MHz is not uniform over the detector area, and presents a peak value over 1.4 MHz/mm^2. The beam intensity distribution over the GTK station 3 is shown in figure 2.5.

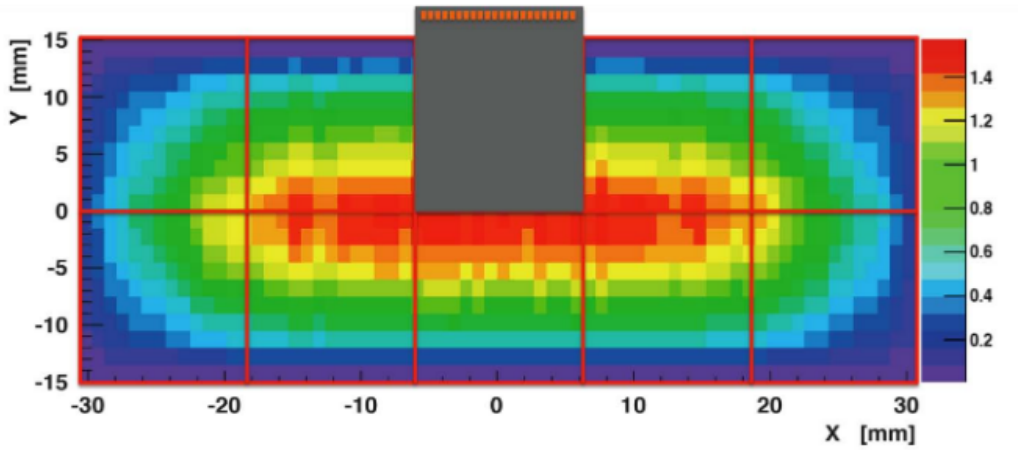

Figure 2.5: Beam intensity distribution over GTK3 (MHz/mm^2). In grey one of the 2×5 readout chips.

The pixel dimension choice has been driven by the required momentum and angle resolution of the detector. A Monte Carlo simulation of the apparatus, taking into account the expected tracking resolution for the decay products (see section 2.2.1) indicated that the GigaTracker has to measure the momentum with a relative resolution of $\sigma(p)/p \sim 0.2\%$ and the direction with a resolution of 16 µrad.
Due to the high intensity environment the required time resolution on a single reconstructed track using all three stations must be 150 ps.
In order to achieve this performance, the active silicon sensor is bump-bonded to 2×5 TDC based read-out ASICs, called TDCPix [29], each delivering a time resolution of better than 200 ps for each pixel hit and working at an operational rate up to 210 MHits/s, allowing to reach the above mentioned characteristics.

2.2 Particle tracking, identification and timing

In this section the spectrometer tracking system for the decay products is described, together with detectors needed to achieve the required timing and the essential pion identification to provide the additional background suppression factor.

2.2.1 STRAW spectrometer

The primary purpose of the STRAW magnetic spectrometer is the measurement of the direction and momentum of secondary charged particles originating from the decay region. In addition it will enter in the high level trigger (see section 3.1.1) for the rejection of

multiple-track events.
A schematic view of the detector is shown in figure 2.6. It is composed of four chambers with a high aperture dipole magnet in the middle. The detector operates in vacuum in order to minimise multiple scattering effects.

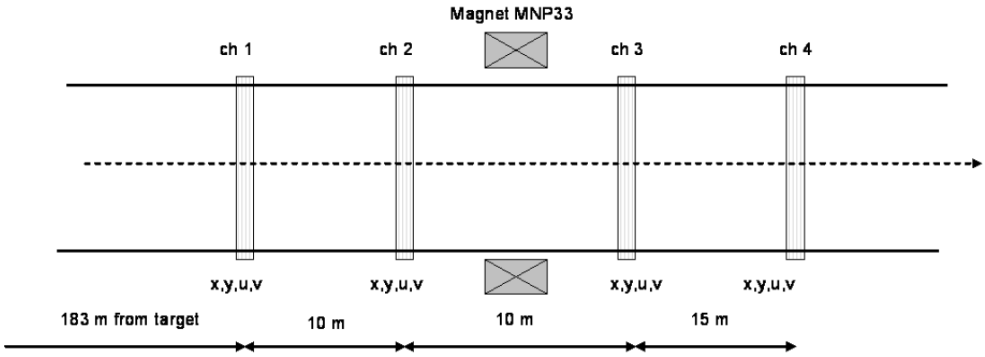

Figure 2.6: Schematic view of the magnetic spectrometer

Each chamber is equipped with 1792 straw tubes which are arranged in four "views" providing measurements of four coordinates x, y, u, v (figure 2.7).
Figure 2.8 shows the layout of a single view of one chamber, which contains four layers of tubes to solve the left-right ambiguity. There are 112 straws in each layer and the distance between the straws in one layer is 17.6 mm, thus at least two hits per view are always present.

The main building block of the detector is the ultra-light straw tube. It is 2.1 m long and has a diameter of 9.8 mm. The tubes are manufactured from 36 µm thin PET foils, coated inside with two thin metal layers (0.05 µm of Cu and 0.02 µm of Au) to provide electrical conductance on the cathode. The anode wire has a diameter of 30 µm and is made of gold-plated tungsten. The very low total amount of material ($< 0.5\%\ X_0$ for each chamber) guarantees minimum multiple Coulomb scattering along the particle trajectory.
After the second chamber the magnet used by the NA48 experiment is present. It is 1.3 m long and has an integrated field of 0.858 T m; the resulting applied transverse momentum is 257.4 MeV/c.
The requirements for the detector performances are a relative momentum resolution of 1%, a spatial resolution of 130 µm per coordinate needed to precisely reconstruct the decay vertex, and a very low track reconstruction inefficiency.
The front-end electronics used to detect the straw signals is the 8-channel CARIOCA chip which was developed for LHCb [30].

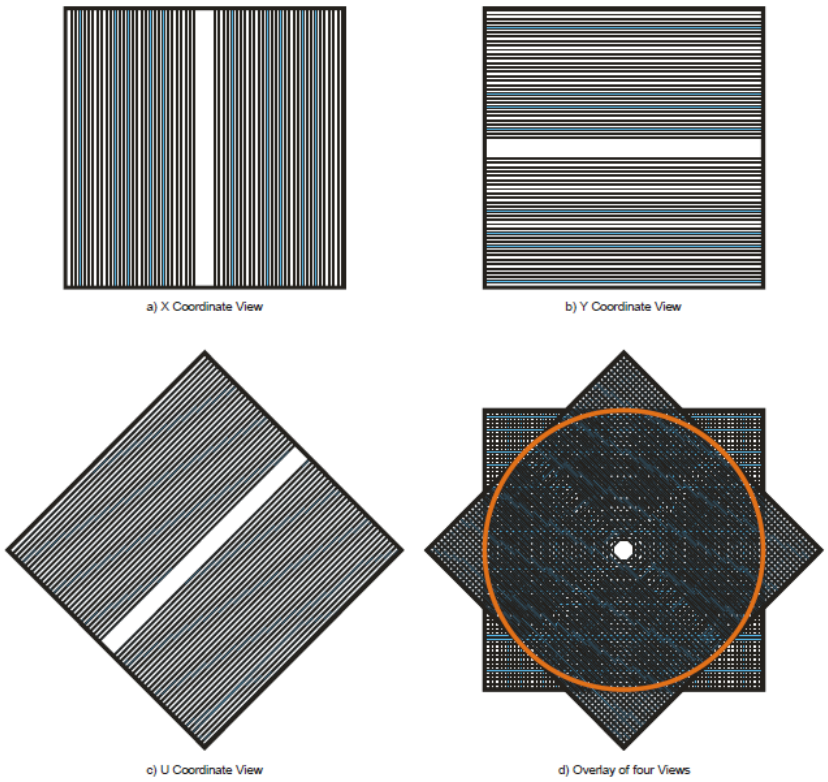

Figure 2.7: Drawing of the four views of each straw chamber: a) vertical straws for the x-coordinate; b) horizontal straws for the y-coordinate; c) 45° oriented straws for the u-coordinate (the v-coordinate is obtained from straws perpendicular to c); d) full chambers with all four views.

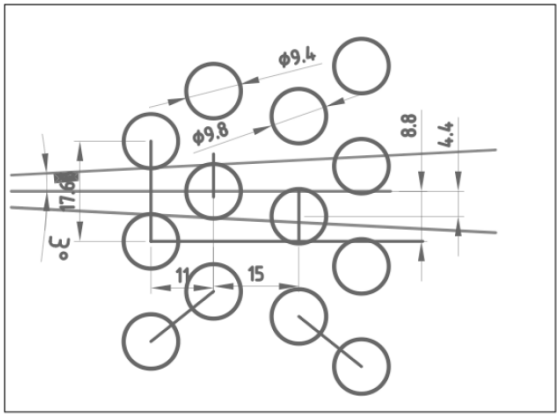

Figure 2.8: Straw layout in one view.

2.2.2 RICH

The Ring Imaging Cherenkov (RICH) is the main particle identification detector in NA62. Its principal purpose is a further rejection of the muon background component by means of identification and separation of π^+ and μ^+ particles. At the lowest trigger level it will be one of the reference detectors, tagging the passage of a charged particle and partially vetoing multi-track events (see chapter 4).
The particle identification exploits the formation of light cones due to the Čerenkov effect. A charged particle traversing a medium of refraction index n with a velocity β higher than the speed of light in the medium, emits a radiation at an angle $\cos\theta_c = 1/(n\beta)$. The light cone is reflected by the mirrors and the photon detectors are placed on the mirror focal plane: here the cone image is a ring of radius $r = f\tan\theta_c \sim f\theta_c$ where f is the focal length of the mirror. The radius depends only on the particle velocity and this means that for a given value of the momentum of a particle, the ring radius depends only on its mass.
The NA62 RICH is required to provide a pion-muon separation in the momentum range between 15 GeV/c and 35 GeV/c. Given that the radius of the cone is $r \propto \theta_c$ and the number of emitted photons through a radiator thickness per unit of photon energy is $\frac{d^2N}{dxdE} \propto \sin^2\theta_c$, the momentum threshold $p_t = m/\sqrt{n^2-1}$ below which no Čerenkov light is emitted for particles of mass m must be about 20% smaller than the particle momentum p, in order to be fully efficient in the detection and reconstruction of the rings (for $p = p_t$ follows that $\theta_c = 0$, so $r = 0$ and $N = 0$). Assuming a momentum threshold of 12.5 GeV/c for pions leads to the choice of Neon at atmospheric pressure corresponding to $(n-1) = 62 \times 10^{-6}$.
The NA62 RICH is placed right after the fourth straw chamber and is followed by the CHOD (section 2.2.4). It is composed of a 17 m long cylindrical tank, with a diameter of 2.8 m, filled with Neon at atmospheric pressure, which corresponds to 5.6% of a radiation length. A beam pipe with three sections respectively of external diameter 20 cm, 22 cm and 24 cm allows the beam to pass through; it has an inclination of 2.4 mrad with respect to the axis of neutral particles not deviated by the magnetic field. A schematic view of the detector is shown in figure 2.9.

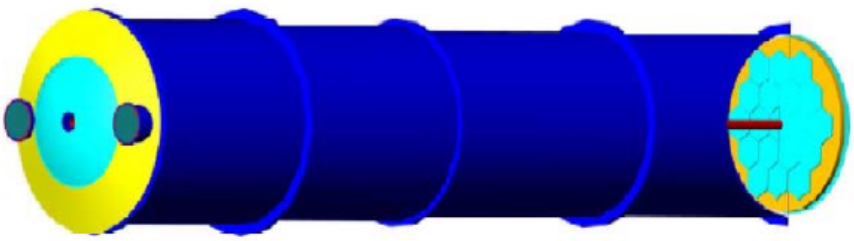

Figure 2.9: Schematic layout of the NA62 RICH detector.

The Čerenkov light is reflected by a system of hexagonal spherical mirrors placed at the downstream end of the tank, and is convoyed towards the upstream part of the detector. In order to avoid absorption of reflected light on the beam pipe the mirrors are divided into two spherical surfaces, one with the center of curvature to the left and one to the right of the beam pipe. Two flanges equipped each one with 960 photomultipliers are located in the upstream end of the detector. The centre of each flange is at a distance of 1.2 m from the beam pipe axis. The design of the mirror system and an image of one of the PMT flanges can be seen in figure 2.10. The active area of each PMT has a diameter of 8 mm, and a Winston cone is used to collect the light from a pixel of 18 mm of diameter.

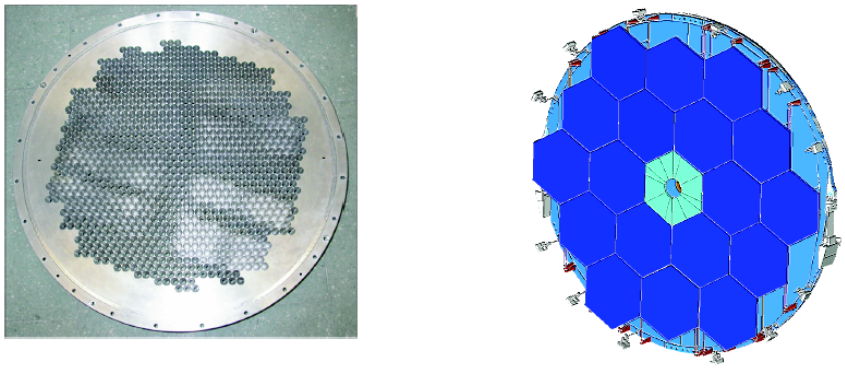

Figure 2.10: PMT flange (left) and design of the hexagonal mirror system of the RICH detector.

In 2009 a test beam was performed with a RICH prototype equipped with 414 PMTs [31]. The π/μ separation was investigated in the range from 15 GeV/c to 35 GeV/c. The μ suppression factor was estimated to be 10^{-2} averaged over the momentum range of interest, in line with the requirements of the experiment. In this test a time resolution of 65 ps was measured, and this performance strengthens the choice of the RICH as reference positive detector in the design of the L0 trigger described in chapter 4.
For what concerns the front-end electronics, PMT signals are processed by the same NINO chip [28] as for the CEDAR PMTs.
The readout of the about 2000 channels is done through the TDC based common system TDCB+TEL62 described in chapter 3.

2.2.3 MUV1-2

A further reduction of the background coming from the most frequent kaon decay, the $K_{\mu 2}$, is achieved by means of the MUV1 and MUV2 detectors. The name derives from the fact that they are part of the muon veto system, nevertheless they are hadronic calorimeters

located after the LKr electromagnetic calorimeter, used for the measurement of deposited energies and shower shapes of incident particles.
A number of events in which muons from kaon decays undergo catastrophic Bremsstrahlung or direct pair production and deposit a major fraction of their energy in the calorimeter, must be identified and vetoed, to ensure the S/B ratio required by the experiment. To reject these events, electromagnetic muon showers must be distinguished from hadronic pion showers by measurements of the shower shape.

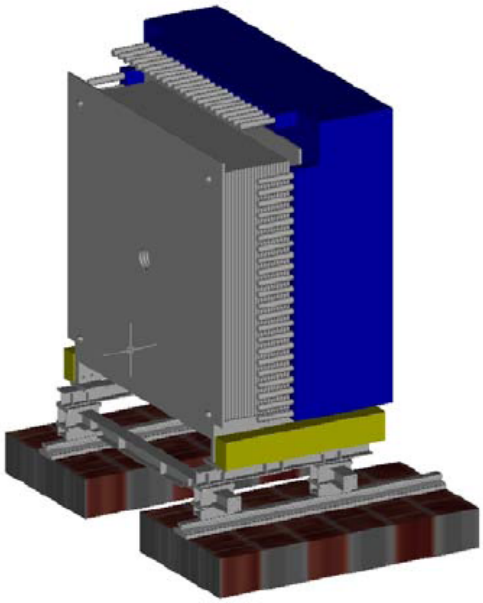

Figure 2.11: View of the MUV1 (grey) and MUV2 (blue) modules.

The two modules are shown in figure 2.11. The MUV1 is a new detector, while the MUV2 is the front module of the old NA48 hadron calorimeter (HAC) turned by 180°.
Both modules are classic iron-scintillator sandwich calorimeters with 24 (MUV1) and 22 (MUV2) layers of scintillator strips, which are alternately oriented in the horizontal and vertical directions in both detectors.
In the MUV1, the steel layers have a dimension of $2700 \times 2600 \times 25$ mm^3 with 12 mm spacing between plates, and a central hole of 212 mm diameter to allow the passage of beam particles. In the MUV2, the steel layers have a similar dimension of $2600 \times 2600 \times 25$ mm^3 with the same 12 mm spacing for the scintillator and the same 212 mm diameter central hole.
For what concerns the scintillators, the MUV1 layers contain each one a total of 48 strips of about 6 cm width, for a total of $48 \times 24 = 1152$ strips. The choice of the width is the result of a compromise between the need of high granularity and the number of PMTs and

readout channels. The readout is made by two wavelength-shifting fibres per scintillator strip. The fibres of one longitudinal row of scintillators are bundled together to direct the light to one single PMT, therefore no longitudinal segmentation exists.
The MUV2 scintillator planes consist of 44 strips of about 11 cm width, each one spanning only half of the transverse size of the detector, so that each plane is made of two half-planes. Consecutive strips with an identical x/y position and alignment are coupled to the same photomultiplier using Plexiglas light-guides.
The described layout of the scintillator strips is shown in figure 2.12.
MUV1 and MUV2 detectors will be readout with the same ADC-based CREAM module used by the LKr calorimeter [32].

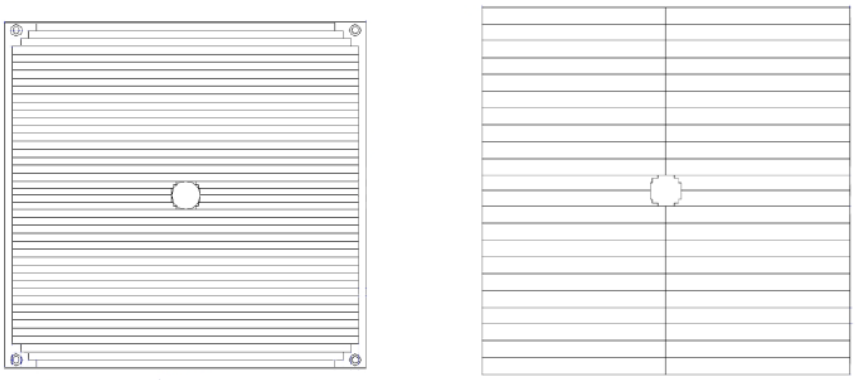

Figure 2.12: Layout of one scintillator layer of the MUV1 (left) and of the MUV2 (right)

2.2.4 CHOD

NA48 CHOD

For the first phase of the data taking, NA62 will reuse the charged hodoscope (CHOD) of the NA48 experiment [33].
The charged hodoscope is placed right after the RICH tank and before the LKr calorimeter, with the main purpose of detecting possible photo-nuclear reactions in the RICH mirror plane. The RICH mirror system amounts to about 20% of radiation length and photons from π^0 decays can undergo photonuclear interactions producing low energy hadrons. This effect can weaken the photon veto function of the LKr. In order to re-establish the veto sensitivity to the required level a detector for low momentum charged track after the RICH is needed. This function can be fulfilled by the CHOD.
It is composed of two planes made of BC408 plastic scintillators, one with vertical and one with horizontal slabs. A layout of the CHOD detector is shown in figure 2.13.

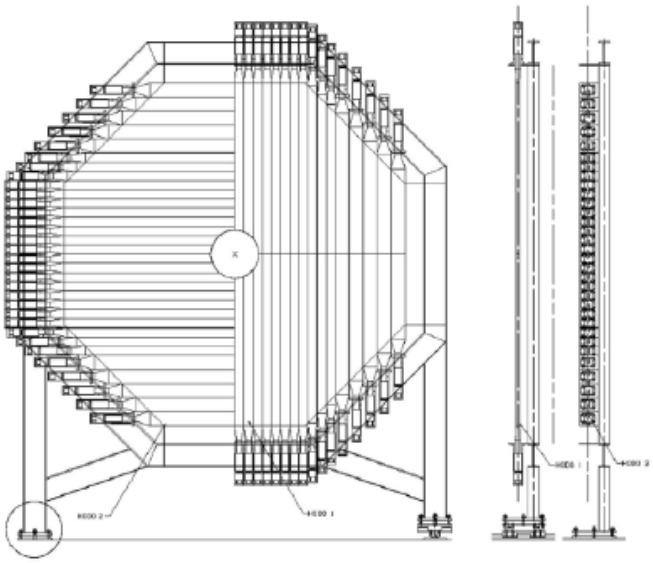

Figure 2.13: Sketch of the horizontal and vertical planes of the CHOD.

Each plane consists of 64 scintillator slabs of different length and width, divided in 4 quadrants containing 16 counters. The length varies from 60 cm to 121 cm and the width from 6.5 cm (in the region close to the beam pipe) to 9.9 cm. The thickness is the same for each slab and is equal to 2 cm, corresponding to 0.05 radiation lengths.
The central hole, in which the beam pipe passes through, has a radius of 10.8 cm.
The scintillation light produced at the passage of a charged particle is collected at the edge of a counter from a Plexiglas fishtail shaped light guide connected to a photomultiplier.
The particle is identified through a time matching between hits in slabs of corresponding quadrants of the two planes.
The distance between the two planes is $\sim$ 30 cm. The different timing related to this distance will be used to tag fake coincidences due to the back-splash coming from the calorimeter surface, i.e. particles of the electromagnetic shower going back to the hodoscope.
The CHOD can provide the timing of charged decay products with a resolution of about 200 ps. In order to achieve this resolution, an impact point correction must be applied to avoid the effect due to the propagation time of the light inside the scintillator slabs towards the PMT. The timing capability of the CHOD is useful to complement the RICH detector in the L0 trigger selecting charged tracks (see chapter 4).
The detector makes use of the LAV front-end electronics [34], and is read out with the common TDCB+TEL62 system (see chapter 3).

NEW CHOD

A new charged hodoscope is being developed and will be used in the second phase of the experiment.
The main reason for replacing the old NA48 detector is the high hit rate at which the meter long slabs are exposed. The intrinsic dead time and the light transit time inside the scintillator are not compatible with the expected overall rate on the detector above 10 MHz.
The proposed layout of the new CHOD is shown in figure 2.14.

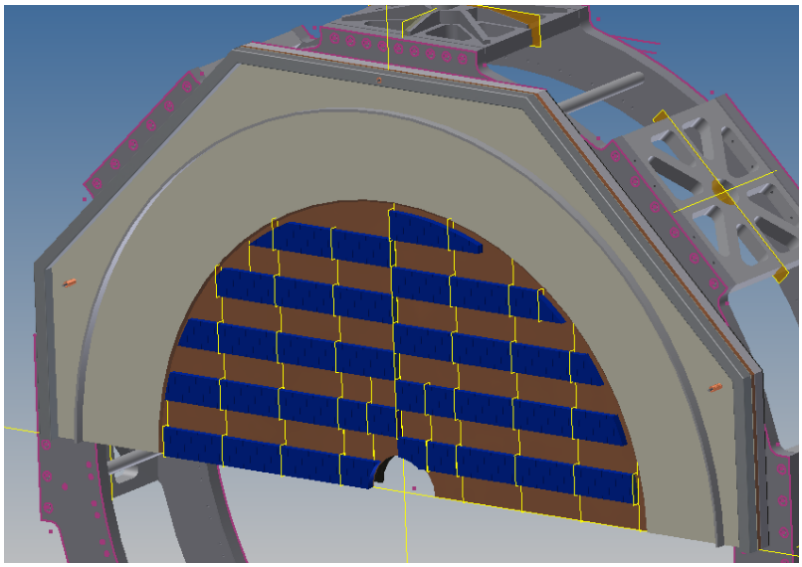

Figure 2.14: Proposed layout of the new charged hodoscope.

The transverse size will be reduced to 107 cm of radius, not overlapping anymore with the 12th station of the large angle veto (section 2.3.2).
The detector will be made of a single plane of scintillator tiles of 30 mm thickness, 107 mm height and 265 mm width. The light will be collected by two sets of wavelength-shifting fibres linked to silicon photomultipliers (SiPM). A total number of 148 tiles and 296 SiPM are foreseen.
With this design the expected maximum rate over a single tile close to the beam pipe is of the order of 500 kHz.

2.3 Veto system

This last section covers the detectors mainly used as vetoes in order to reject background events coming from kaon decays and kaon interactions before the decay region.

Before the beginning of the fiducial region, a number of guard-ring counters reduce critical background from inelastic interactions of beam particles in the last GTK station. The photon veto system is designed for the suppression of the $K_{\pi 2}$ channel with an overall inefficiency of about 10^{-8} for π^0 detection; it covers an acceptance from 0 mrad to 50 mrad in the polar angle with respect to the beam line. The highest rejection factor for $K_{\mu 2}$ decays is ensured by a fast muon veto detector to be used also at trigger level.

2.3.1 CHANTI

Beam particles can undergo inelastic interactions in the GTK material. The most critical events take place in GTK3: the scattered particles, pions or muons, if emitted within the straw acceptance, can mimic a kaon decay in the fiducial region. If no other track is detected these events lead to a $\pi\nu\bar{\nu}$ signature. The probability of kaon inelastic scattering is about 10^{-3}: thus, to achieve the required S/B ratio, the combined rejection factors from analysis cuts and veto efficiency must reach a level of 10^{-8}.

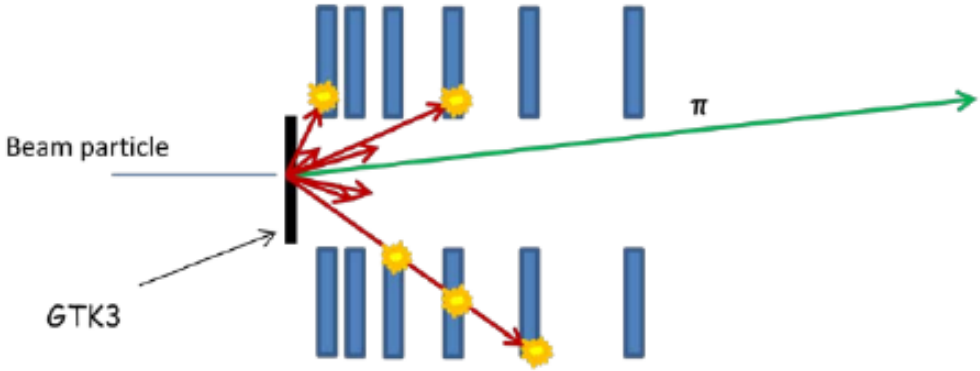

Figure 2.15: Beam particles can create accidental background if they undergo inelastic interaction in the GTK material. The scattered particles are revealed in the CHANTI stations (blue).

The CHANTI detector is used for this purpose (see figure 2.15): it consists of six stations of scintillator bars surrounding the beam and placed inside a single vacuum tight vessel together with the GTK3 station.
The stations are placed respectively at 27 mm, 77 mm, 177 mm, 377 mm, 777 mm and 1577 mm from the GTK3. They have an outer square side length of 300 mm and a rectangular hole of 90 mm × 50 mm for the passage of beam particles. The angular coverage for particles originating in the centre of GTK3 is between 34 mrad and 1.38 rad.
Each station is made of two layers in the x and y direction, with 22 and 24 parallel triangular prism bars. Light is collected by means of one wavelength-shifting fibre placed

inside each bar. The fibre is then coupled to a silicon photomultiplier device for photon detection.
The CHANTI will be sensitive to inelastic interactions in GTK3 as well as to the muon halo component near the beam axis: the expected rate of particles that release enough energy to be detected is around 2 MHz, so a time resolution below 2 ns is required to keep the random veto at an acceptable level.
The CHANTI is able to veto about 95% of kaon inelastic interactions in GTK3. This vetoing efficiency reaches almost 99% if one restricts to potentially signal-like events, namely those where the kaon either does not survive the inelastic interaction or does not decay in the fiducial volume and one track is reconstructed by the STRAW tracker at the same time.
The LAV front-end electronics board [34] is used to produce a Time-over-Threshold (ToT) signal output which is then sent to the common TDCB+TEL62 readout system described in chapter 3.

2.3.2 LAV

The Large Angle Veto system provides full coverage for decay photons with polar angles from 8.5 mrad to 50 mrad. Together with the electromagnetic calorimeter it will participate in the L0 trigger chain to further suppress $K_{\pi 2}$ events with one (or both) photons from π^0 at large angle.
The NA62 LAV detectors make creative reuse of lead glass blocks recycled from the OPAL electromagnetic calorimeter barrel [35]. Other solutions considered included a lead/scintillating tile design, and a lead/scintillating-fibre design based on the electromagnetic calorimeter for the KLOE experiment. Prototypes based on each of the three technologies were built, and tested with the electron beam at the Frascati Beam-Test Facility. These tests demonstrated that all three technologies are suitable for use in NA62. In particular, the inefficiency for the detection of single, tagged electrons with the OPAL lead glass modules was measured to be $1.2^{+0.9}_{-0.8} \times 10^{-4}$ at 203 MeV and $1.1^{+1.9}_{-0.7} \times 10^{-5}$ at 483 MeV. Basing the construction of the LAV system on the OPAL lead glass modules provides significant economic advantages.
The modules from the central part of the OPAL electromagnetic calorimeter barrel consist of blocks of lead glass. This material is about 75% lead oxide by weight and has a density $\rho = 5.5\,\mathrm{g\,cm^{-3}}$ and a radiation length $X_0 = 1.50$ cm; its index of refraction is $n \approx 1.85$ at $\lambda = 550$ nm and $n \approx 1.91$ at $\lambda = 400$ nm. Electromagnetic showers in the lead glass are detected by virtue of the Čerenkov light produced; measurements indicate that, averaged over modules, minimum ionising particles produce about 0.34 photoelectrons per MeV of deposited energy.
The front and rear faces of the blocks measure about 10×10 cm^2 and 11×11 cm^2, re-

spectively; the blocks are 37 cm in length. Each block is read out at the back side by a photomultiplier, which is optically coupled via a 4 cm long cylindrical light guide of the same diameter as the PMT. A complete module (block plus PMT, see figure 2.16) is a common assembly; the block and PMT cannot be independently replaced.

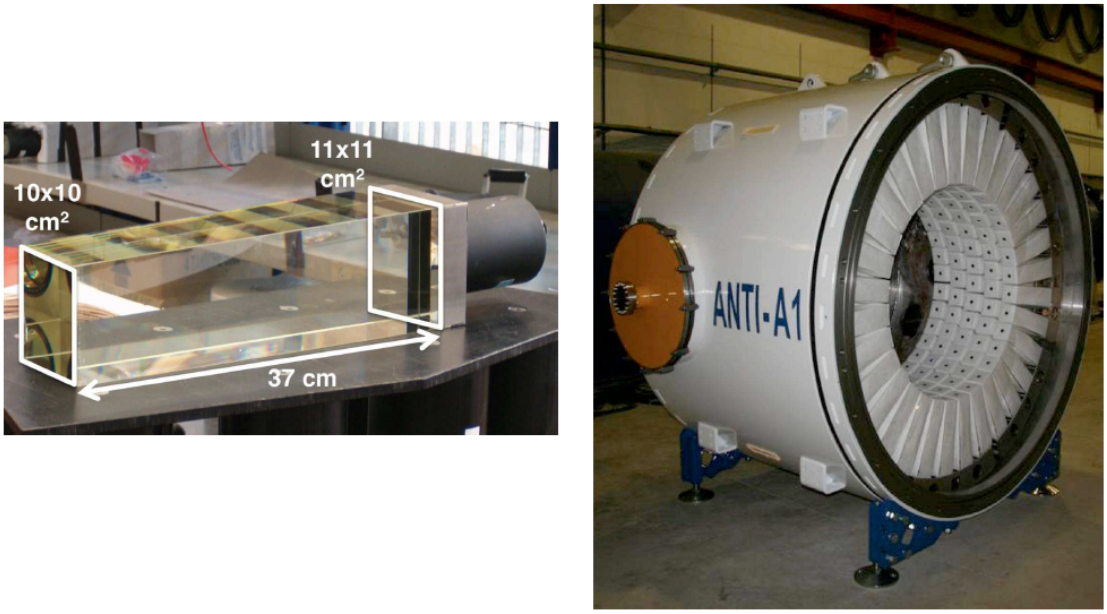

Figure 2.16: A module from the OPAL calorimeter (left). The 1st LAV station with 32×5 wrapped OPAL lead glass calorimeter elements (right).

A LAV station is made by arranging these blocks around the inside of a segment of vacuum tank, with the blocks aligned radially to form an inward-facing ring. Multiple rings are used in each station in order to provide the desired depth for incident particles. The blocks in successive rings are staggered in azimuth; the rings are spaced longitudinally by about 1 cm. Figure 2.16 shows the completed first station of the LAV system.
The LAV system consists of a total of 12 stations, the diameter of which increases with distance from the target. The geometry of the LAV stations is summarised in table 2.2. As a result of the staggering scheme, particles incident on any station are intercepted by blocks in at least three rings, for a total minimum effective depth of 21 radiation lengths. The vast majority of incident particles are intercepted by four or more blocks (27 X_0). The stations with five layers (A1-A8) are 1.55 m in length, while those with four layers (A9-12) are 1.43 m in length.

The LAV provide time and energy measurements with a readout scheme based on the time-over-threshold (ToT) technique. This is implemented using a dedicated front-end discriminator board [34] which converts the analog signals to low-voltage differential sig-

Station	Diameter (mm) outer wall	Block radius (mm) Inner - Outer	Layers	Blocks
A1-A5	2168	537 - 907	5	160
A6-A8	2662	767 - 1137	5	240
A9-A11	3060	980 - 1350	4	240
A12	3250	1072 - 1442	4	256

Table 2.2: Parameters of LAV stations.

nals (LVDS). The common TDCB+TEL62 system (see chapter 3) is used for the readout and for trigger generation.
Results from a test beam performed on LAV stations showed a single block time resolution of

$$\sigma_t = \frac{220\,\text{ps}}{\sqrt{E(\text{GeV})}} \oplus 140\,\text{ps}$$

and an energy resolution obtained with the ToT technique of

$$\frac{\sigma(E)}{E} = \frac{9.2\%}{\sqrt{E(\text{GeV})}} \oplus \frac{5\%}{E(\text{GeV})} \oplus 2.5\%$$

2.3.3 LKr

The NA48 Liquid Krypton electromagnetic calorimeter has the main purpose of rejecting background events with photons at an intermediate angle between 1 mrad and 8.5 mrad. In addition, it enters the L0 trigger as a fundamental block for the first stage reduction of $K_{\pi 2}$ decays (see chapter 4).
For the study of direct CP violation with the required precision, the NA48 experiment needed an electromagnetic calorimeter with good energy, position and time resolution, precise charge calibration, long-term stability and a fast read-out. In order to meet these requirements a liquid Krypton calorimeter (LKr) was built, an almost homogeneous ionisation chamber with a tower structure geometry [33]. A photon or an electron entering the active volume of the calorimeter produces an electromagnetic shower via repeated pair production and Bremsstrahlung processes until the energy of the particles is below the critical energy. The low energy charged particles in the shower can then ionise the Krypton atoms producing a certain numbers of electron-ion pairs, proportional to the deposited energy.
The calorimeter works as an ionisation chamber: all the electrons produced and accelerated towards the anode are collected before they can recombine, but the electrons do not get enough energy to produce secondary ionisation. The choice of a liquefied noble gas is due to the good resolution and linearity response in energy, the absence of ageing problems

and the relative short radiation length which allows a compact design without the need of heavy passive parts, typical of sampling calorimeters. The homogeneity ensures a good energy resolution, the granularity improves the spatial resolution and allows to separate showers close to each other. Radioactivity of the Krypton is negligible with respect to electronic noise and has therefore no effect on the resolution, but, due to the low boiling temperature of Krypton at 120 K, the whole detector has to be kept inside a cryostat where only temperature variations of few per mille are allowed, since the drift velocity of the electrons depends strongly on the temperature ($\Delta v_d/v_d \propto \Delta T/T$). Working at cryogenic temperature greatly increases the stability of the detector response and accuracy of its calibration.
The LKr is octagonal, containing a circle of 128 cm radius, 127 cm thick, corresponding to about 27 radiation lengths, and has a hole at the centre of 9 cm radius for the beam pipe. The total active volume of about 7 m^3 liquid Krypton is divided into 13248 cells (towers) by 18 mm wide, 40 µm thick copper-beryllium ribbons at a distance of 1 cm from each other and with no longitudinal segmentation. The ribbons are used as electrodes to collect the ionisation signal. A cell consists of a central anode, to which is applied a voltage of 3 kV, and two cathodes, one at each side, so that each cathode is in common between two cells. The separation between two cell layers is 2 mm. The cells define a projective geometry of the calorimeter pointing at about 90 m in front of it, inside the decay region. This particular geometry was chosen in order to achieve the best possible accuracy in the measurement of the angle between the flight path of photons and the beam direction. To avoid response variations depending on the lateral distance between the shower core and the anode, the cells are not straight along the flight path of the original particles but follow a "zig-zag" shape or an "accordion geometry". The LKr electrode structure and the detail of the cell structure is shown in figure 2.17 (left).

The energy resolution of the calorimeter, measured using an electron beam of different momenta (15 GeV/c, 25 GeV/c, 50 GeV/c and 100 GeV/c) and 0.1% momentum bite, can be parametrised as

$$\frac{\sigma(E)}{E} = \frac{3.2\%}{\sqrt{E(\mathrm{GeV})}} \oplus \frac{9\%}{E(\mathrm{GeV})} \oplus 0.42\%$$

where the first contribution is the Poisson term from stochastic fluctuations, the second is mainly due to electronic noise and Krypton radioactivity, and the last one comes from the non perfect inter-calibration of the cells. For a 20 GeV particle the energy resolution is about 1%.
Space resolution was measured by comparing the extrapolated track impact point of electrons from calibration runs with the reconstructed centre of energy deposition, yielding

the following result:

$$\sigma_{x,y} = \left(\frac{0.42}{\sqrt{E(\text{GeV})}} \oplus 0.06 \right) \text{cm}$$

where the first term is due to by the statistical fluctuation of the particles in the shower and the second one is due to the size of the cells. For a typical energy of 20 GeV, the space resolution is 1.1 mm in each coordinate.

The time resolution on a single shower is at the level of 500 ps.

The readout of the LKr calorimeter works in a current-sensitive mode using the initial induced current, proportional to the ionisation generated in the LKr by the shower and proportional to the energy of the incoming particle. The sampling and the digitization of the signal is performed every 25 ns by a new flash ADC-based calorimeter readout module (CREAM) [32]. A zero suppression is applied to the cells below a certain threshold, in this way the number of read cells is reduced to about 100 per shower.

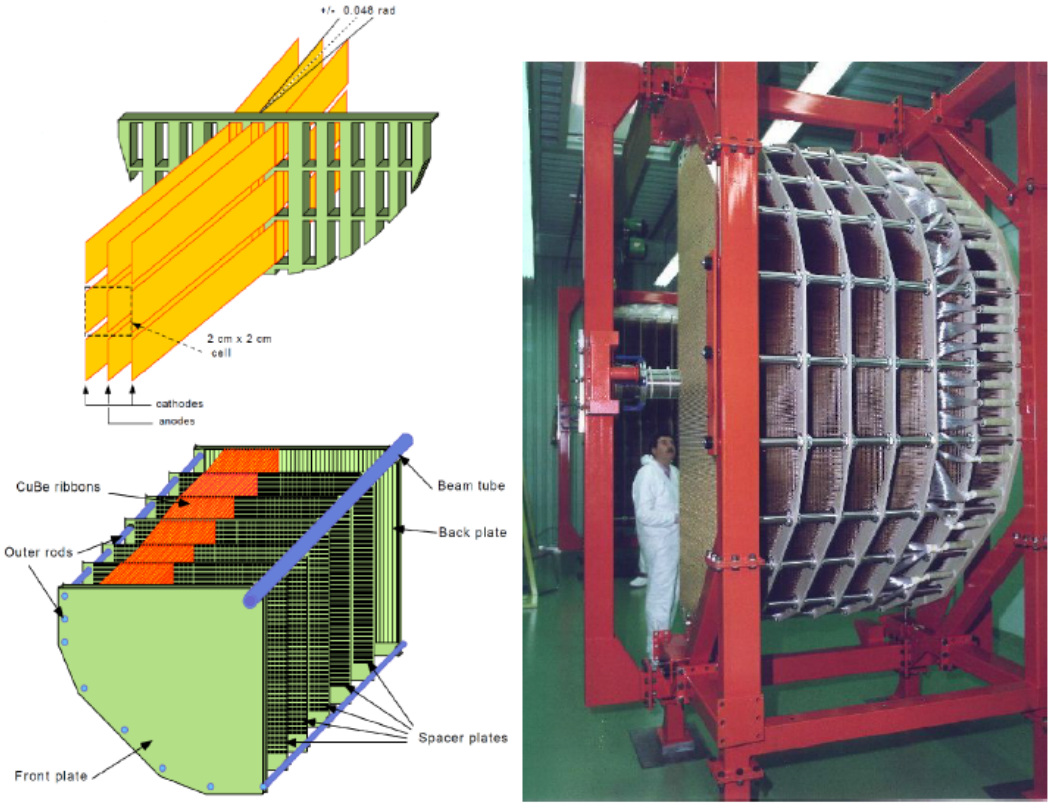

Figure 2.17: The LKr electrode structure and a detail of the LKr cell structure showing the "accordion geometry" structure of the ribbons (left). A picture of the LKr (right).

2.3.4 SAV

The Small Angle Vetoes provide hermeticity for photons at polar angles below 1 mrad with respect to the kaon flight direction. This system is composed of two detectors: the Inner Ring Calorimeter (IRC) and the Small Angle Calorimeter (SAC).
These detectors are both exposed to photons with energies higher than 5 GeV, and have to provide detection inefficiency better than 10^{-4}.
Furthermore they are sensitive to the muon halo component of the beam.
Both detectors makes use of the Shashlyk technology: it is based on consecutive lead and plastic scintillator plates as in figure 2.19 (left). The incoming photon interacts with the lead and develops an electromagnetic shower, and its products produce scintillation lights inside the plastic material. The light is taken out by wavelength-shifting fibres to a photomultiplier. A single module is also a single channel detector: the attenuation length of the emitted scintillation light in the scintillator is much longer than the actual transverse size of the module which leads to light in all the fibres.
The photomultipliers of both detectors are read out by the GANDALF board [36] equipped with ADC-based mezzanines.

IRC

The IRC is placed in front of the LKr electromagnetic calorimeter, right after the two CHOD planes. It is situated around the beam pipe, as close as possible to the undecayed beam but at the same time far enough away so that the beam halo does not generate a too high rate in the detector. Its main purpose is the rejection of photons travelling towards the inactive annular central region of the LKr around the beam pipe.
The photon component from the $K_{\pi 2}$ decay gives a rate of about few hundreds of kHz, which is a small fraction of the total rate of about 6 MHz to which the detector is exposed due to the beam halo component.
Figure 2.18 shows the layout of the IRC. The detector is made as a cylindrical tube with two active regions: the first with 25 layers and the second with 45 layers. The outer radius is centred at the z axis, while the inner radius is centred at the beam axis which is displaced 1 cm in the x direction. The detector is segmented into 4 parts each representing a 90° sector, thus resulting in 4 channels.

SAC

The SAC is located at the end of the experimental hall and is the last detector in longitudinal order. It has the purpose of covering the small angle region not covered by the IRC and the LKr.

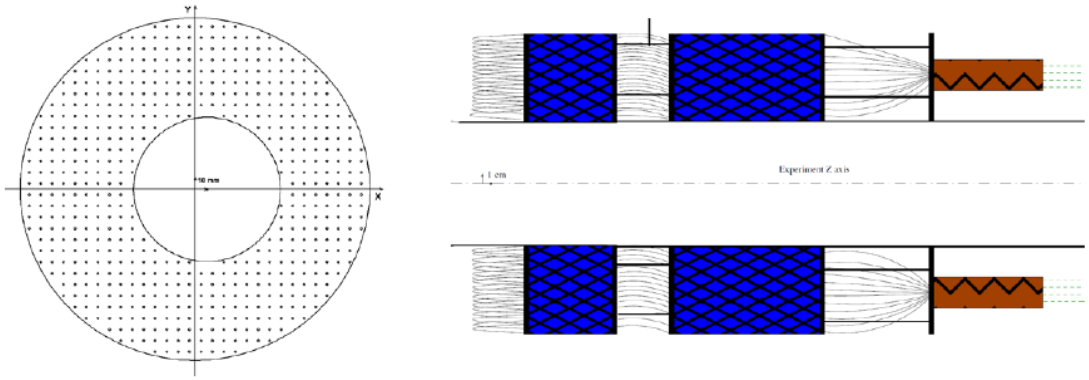

Figure 2.18: Layout of the IRC detector. The distribution of the fibre holes can be seen in the frontal view (left).

A sweeping magnet is present after the experimental setup and before the SAC to deflect the charged component of the beam. The SAC detects the remaining undeflected photons. It must be small enough not to interact with the undecayed deflected beam.
The rate on the detector is of the order of 100 kHz and is due to the remaining $K_{\pi 2}$ decays. Figure 2.19 (right) shows the SAC prototype. It is assembled from 70 lead plates of 1.5 mm with 1.5 mm scintillator in between, for a total of 21 cm and about 17 radiation lengths in order to keep the punch through probability below 10^{-5}. The 480 WLS fibres are divided into four channels and read by four photomultipliers.

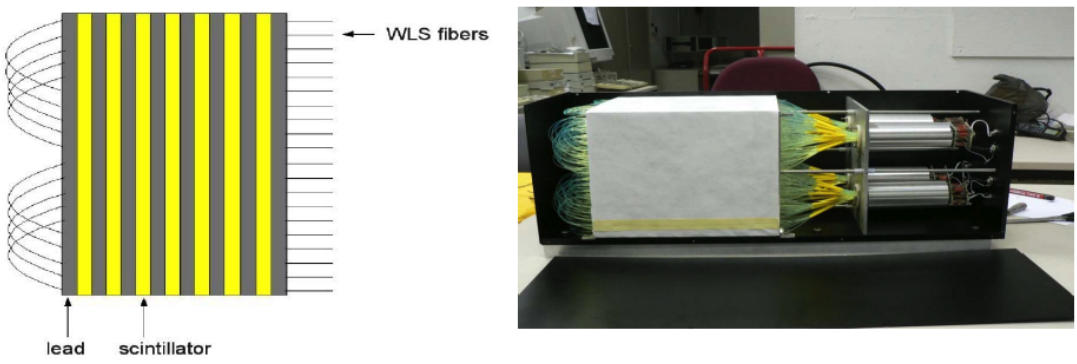

Figure 2.19: Shashlyk technology with lead and scintillator plates (left). The SAC prototype (right).

2.3.5 MUV3

The third station of the muon veto system is located after the first two stations and an additional muon filter, an iron wall of 80 cm depth, in order to detect non-showering muons;

it also acts as muon veto detector at the lowest trigger level to suppress the high rate of $K_{\mu 2}$ decays.

The detector consists of an array of 12×12 5 cm thick scintillator tiles, with a transverse area of 22×22 cm^2. The light produced by traversing charged particles is collected by photomultipliers positioned about 20 cm downstream. Due to this geometry the maximum time jitter between photons from particles hitting different parts of the scintillator tiles is less than 250 ps, thus preserving the required time resolution of this detector.

The time resolution may be spoilt by Čerenkov photons that are produced by particles traversing the PMT windows. These Čerenkov photons arrive earlier than photons produced in the scintillators, whose typical decay time is about 2 ns. To overcome this problem, each scintillator tile is read out by two PMTs. The output time of the coincidence of the two PMT signals, corresponds to the time defined by the PMT which is unaffected by the Čerenkov photons.

Figure 2.20 shows the layout of the MUV3 module and a detail of a single tile counter from a side view. As can be seen from the left, in the central region near the beam pipe, 8 smaller tiles around the hole replace 4 standard tiles, in order to better cope with the expected high rate of that region.

The PMT output signals are sent to constant fraction discriminators (CFD) which are then readout through the common TDC-based system TDCB+TEL62 (see chapter 3).

A number of test beams and data from the initial calibration phase of the NA62 run show a time resolution below 500 ps, in agreement with the requirements of the experiment in order to keep the random veto probability at an adequate low level.

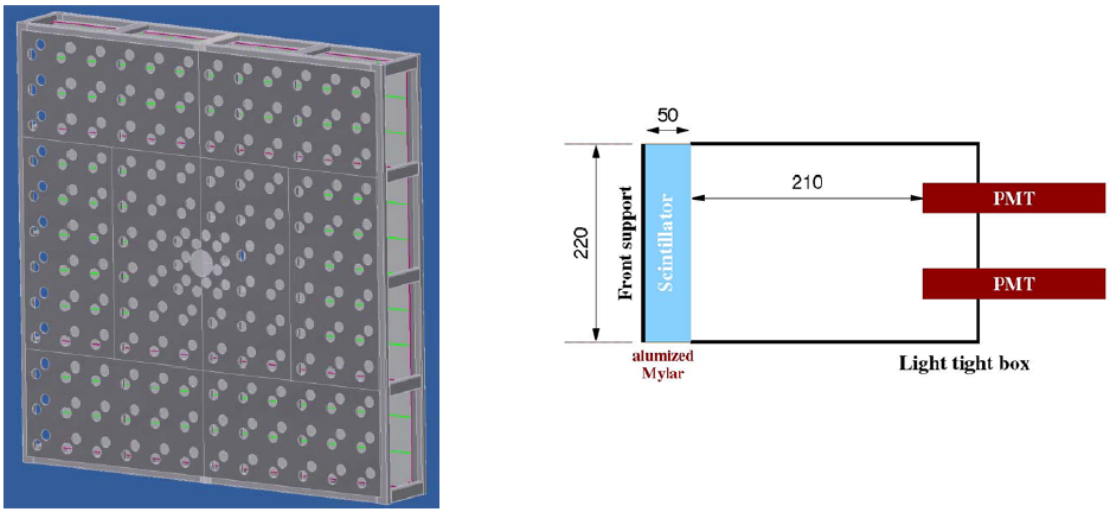

Figure 2.20: Layout of the MUV3 module (left). Detail of a single tile counter from a side view (right), with particles coming from left.

Chapter 3

The TDAQ system: development of the TDCB and TEL62 common boards

After an introduction about the NA62 Trigger and Data Acquisition system in section 3.1, this chapter will focus on the design, development and testing of the TDCB (section 3.2) and TEL62 (section 3.3) electronic boards, which was the main task of the first half of this work.
A significant contribution was given in the evolution of the firmware of both TDCB and TEL62's Field Programmable Gate Arrays (FPGAs): this work is described in sections 3.2.2, 3.3.2 and 3.3.3.

3.1 Introduction: the NA62 Trigger and Data Acquisition system

The intense beam flux of the experiment requires an high performance trigger and data acquisition (TDAQ) system, which must minimize dead time and random veto effects, and maximize the efficiency in data collection at high rates, because of the very sizeable background, keeping a time resolution as high as possible.
NA62 has a unified trigger and data acquisition system: the trigger primitive generation process is integrated inside the DAQ system and the low-level selection is done digitally using the data itself, with just a single digitization, thus allowing an accurate offline monitoring.
A schematic view of the NA62 TDAQ system is shown in figure 3.1. The trigger logic is made of three levels: an hardware lowest-level trigger (L0) followed by software high-level triggers (L1 and L2) implemented in dedicated PCs. A full description of the trigger sys-

tem is provided in section 3.1.1. The L0 trigger primitives coming from subdetectors are managed by the L0 Trigger Processor (L0TP), which combines them following pre-defined schemes and subsequently delivers a L0 trigger signal if a number of conditions are satisfied. The trigger request is sent back to all subdetector readout systems, where data are stored in buffers waiting for the trigger decision. Following a trigger request, data corresponding to the trigger time are extracted and sent to the readout PC farm for L1 and L2 processing. A description of the NA62 readout and data acquisition systems is given in section 3.1.2. The communication of timing, triggers and backpressure between the trigger system and the data acquisition devices is guaranteed by the Timing, Trigger and Control (TTC) common system, described in detail in section 3.1.3.

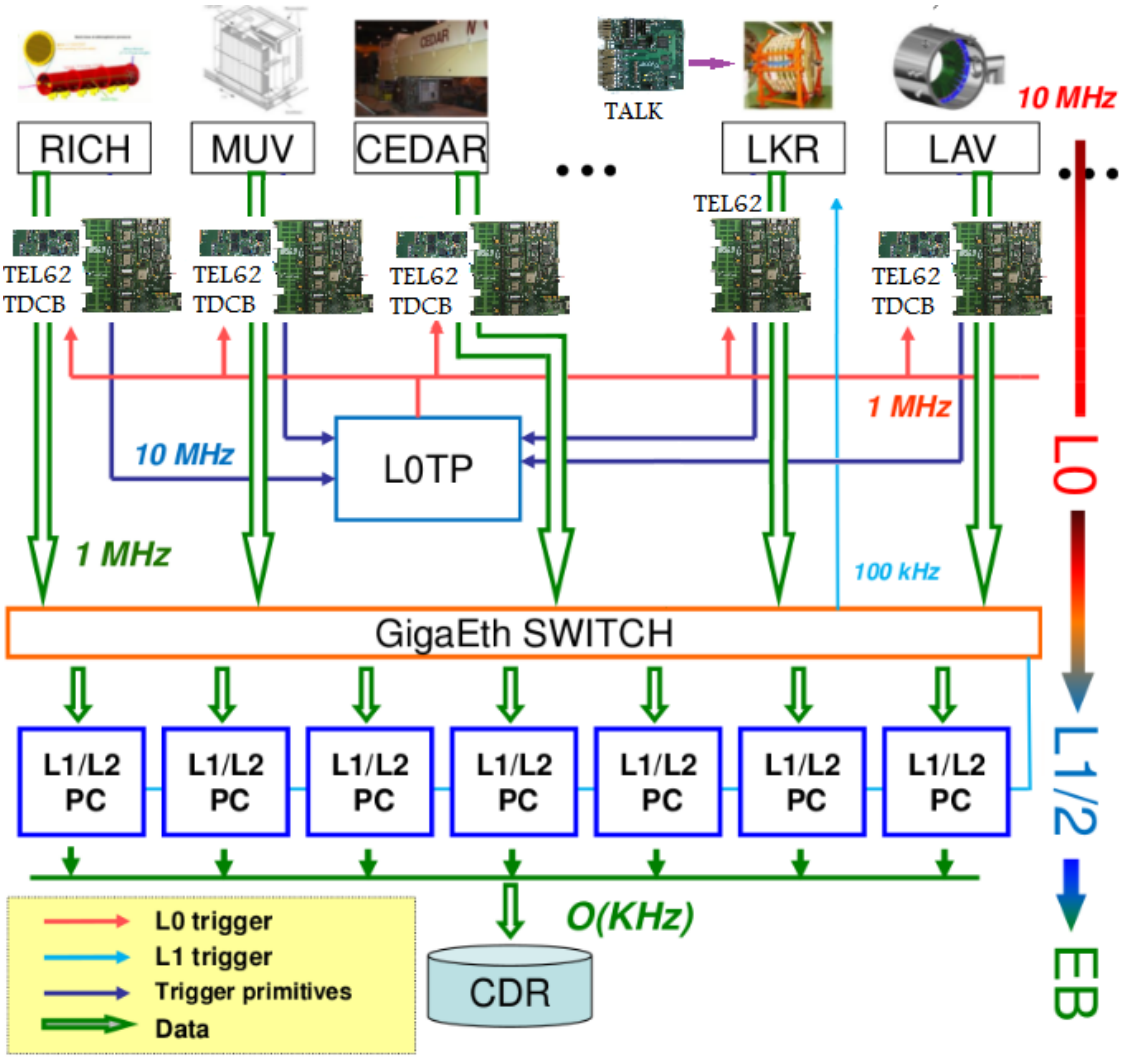

Figure 3.1: Schematic view of the NA62 TDAQ system.

3.1.1 Trigger hierarchy

The trigger logic is composed of three levels: the rates and the number of channels of the experiment (see section 3.1.2) have driven the choice of NA62 for an hardware lowest-level trigger, called L0; after a L0 trigger, subdetectors will transfer data to dedicated PCs where software L1 and L2 trigger will be implemented, respectively based on information computed by each complete sub-system, and on assembled and partially reconstructed events with the possibility to use correlations between different subdetectors. A schematic view of NA62 trigger hierarchy can be seen in figure 3.1.

The L0 will be fully digitally implemented on hardware in the common TEL62 board (see section 3.3). It is based on inputs from the RICH, the CHOD, the MUV (in particular the fast muon veto plane MUV3), the LKr and the LAV, both for the main trigger and for other physics selections. The default L0 trigger algorithm will require the presence of a single charged track in the RICH and the CHOD, nothing in the MUV and in the LAV, and no more than one single cluster in the LKr. This lowest trigger level has the purpose to reduce the event rate from the starting value of about 10 MHz to 1 MHz, which corresponds to the data bandwidth available to the experiment for event storage in the PC farm.
The CHOD is the positive element to tag a charged particle within the detector acceptance, reducing the rate due to K decays downstream of the final collimator. The multiplicity could be also used to select multi-track events.
A contribution from the RICH is hits multiplicity, for the reduction of the background due to multi-track events; particle identification cannot be exploited at this early level of triggering since it would require correlation of information from different subdetectors, in particular the momentum measurement from the slow magnetic spectrometer.
For what concerns the MUV, the third fast station (MUV3) will be used to veto the high rate of muon events due to the main background from $K_{\mu 2}$ and to the muon halo components from decays upstream of the final collimator. This element will provide the largest rate reduction factor, and its efficiency drives the overall L0 trigger rate. This feature leads to the requirements for the MUV3: the geometrical acceptance must exceed that of the positive elements (CHOD and RICH in this case), and the online time resolution should be good enough to keep random vetoing to an acceptable level.
The LKr in the L0 trigger will be useful to suppress the rate due to the other background decay $K^+ \to \pi^+\pi^0$, requiring no more than one cluster (corresponding to a showering charged pion) electromagnetic shower. An online cluster counting with a time resolution of the order of 1 ns will lead to a good rejection and also to several other physics triggers.
The LAV gives further reduction for events with photons at high angles and also for the halo component far from the beam axis.
A detailed simulation of this low-level trigger to study its performances in terms of effi-

ciency and output rate has been one of the major efforts of my work and will be described in chapter 4.
The subdetectors involved in this hardware level will produce trigger primitives with timestamp and fine time, to provide a complete time information needed for the time matching. The time matching of L0 trigger primitives will be done asynchronously by a central L0 Trigger Processor. An FPGA based prototype of the L0TP has been developed and will be used in the first run of NA62. It makes use of the Altera® development DE4 board [37] which accommodates a Stratix® IV FPGA [38], plus a TTC interface card and daughtercards for 8 Gigabit ports used for trigger primitives reception.
The firmware of the L0TP is organized in such a way that the received primitives are stored in RAMs implemented in the FPGA, with a RAM address depending on the time of the primitive. The timestamps of a reference (positive element) detector are stored in a FIFO, and subsequently read to search for matching times from other detectors; different trigger chains will coexist for different physics goals, and a look up table is implemented inside the FPGA for this multiple matching purpose. After matching the primitives from subdetector trigger electronics the trigger processor will generate after a fixed latency a synchronous trigger signal followed by a trigger type; these signals will be dispatched by the TTC system back to all detectors, that consequently will readout data corresponding to a programmable number of time windows (25 ns) around the central trigger time, possibly depending also on the received trigger type.
During L0 trigger evaluation data are stored into the buffers on-board the TEL62 and the other readout systems, for a time up to a defined maximum L0 trigger latency, currently set to 1 ms. This value is actually limited by the buffer size in the detector with the highest rate, i.e. the GTK, while the DDR2 buffers on the TEL62 can currently store data for about 50 ms.

L1 and L2 triggers are implemented at software level in the readout PC farm.
After subdetector data is sent to the PC farm following a L0 trigger signal, the L1 algorithms will check data quality conditions and then require simple correlations between conditions computed by single subdetectors: a single charged pion in the detector with the accepted momentum (main trigger), an equal odd number of tracks in the front and back of the STRAW, hit patterns in the RICH, further rejection from SAV calorimeters and MUV1-2 hadronic calorimeters. A further factor 10 in events reduction is expected from the L1 conditions, to achieve an overall trigger rate below 100 kHz.
In case of a positive L1 decision, a complete event reconstruction at L2 will be done, accepting as the main trigger events with a single identified charged pion.
Both these trigger levels are implemented inside the same PCs, to avoid data transfers.
All data satisfying the L2 trigger conditions are finally logged to tape. A final output trigger rate of about 10 kHz must be achieved in order to match the available bandwidth

of about 100 MB/s for data storage.
A parallel fast online triggering system using commercial graphic processors (GPUs) is being developed by the NA62 Pisa group [39]. It will support the standard software L1 and L2 triggers, and in some cases it could represent a Level 0.5 between the hardware level and the software levels on the PC farm. Some examples of low latency applications under evaluation at NA62 are the RICH online ring-finding as well as an online reconstruction of tracks in the STRAW spectrometer.

3.1.2 Data acquisition

From the data acquisition point of view, the detectors have the number of channels and the typical hit rates presented in table 3.1 (total rates are displayed for detectors with more than one station). The total number of channels of the experiment is about 80 000: considering the rates in table and the expected event size of each subdetector, the entire DAQ system produces about 2 TB/s of raw data bandwidth.

Subdetector	**Total channels**	**Hit rate (MHz)**
CEDAR	384	50
GTK	54000	2700
LAV	4992	11
CHANTI	276	2
STRAW	7168	240
RICH	1920	11
CHOD	128	12
IRC	4	6
LKr	13248	40
MUV	576	30
SAC	4	2

Table 3.1: Number of channels and typical rates of NA62 subdetectors.

The need for a good time resolution in a high-rate environment, coupled with the need to have manageable data rates, naturally leads to the use of a TDC-based system, where pulse-height information can also be obtained by using a time-over-threshold approach if both leading and trailing edges of a pulse are measured. For these reasons most of the detectors in NA62 adopted the common readout system based on the TEL62 carrier board and on the high performance TDCB daughter-card: it is the case of CEDAR, LAV, CHANTI, RICH, CHOD and MUV3. The development of these devices was the core of the first half of my work and are described in detail in sections 3.3 and 3.2 respectively.
The remaining detectors either adopted a custom TDC approach or an ADC based readout. The GigaTracker readout is based on the TDCPix chip [29]. It provides pre-amplification

and discrimination of the signal, and a time-over-threshold self-triggered measurement for 360 channels, with a TDC bin size of about 100 ps, at an expected rate of 210 MHits/s; the output is given by 4×3.2 Gbit/s. The resolution of the chip's TDCs is ~ 60 ps; if the propagation of the signal through the chip and the relative time correction are taken into account, the whole chip resolution is ~ 70 ps. 4 output serial links sends data to a carrier GTK-RO VME 6U board where the full data-flow is stored while waiting for a L0 trigger decision: upon reception of a L0 trigger a data slice of 75 ns is sent to the readout PC farm. The GTK-RO board hosts also the TTC interface to send the clock to the TDCpix and to receive triggers from the central L0 Trigger Processor.
The STRAW tubes are read out by the CARIOCA chip [30]. This chip is integrated in a custom COVER board together with an Altera® Cyclone® III FPGA [40]: it houses 16 pairs of sub-nanosecond resolution TDCs with de-randomizers and an output link serializer [41]. The full system is composed of 14236 TDCs creating a bulk of data of the order of 2 GB/s. The back-end VME 9U Straw Readout Board (SRB) receives data from TDCs for processing (by means of an FPGA) and storage in DDR3 memories. A TTC interface is also present, to optically receive the clock and the triggers. After receiving a L0 trigger, data are extracted from the buffers and sent to the PC farm.
The IRC and SAC small angle photon veto detectors adopted the existing solution of the GANDALF board [36], developed for the CERN COMPASS experiment. This VME 6U board is equipped with ADC-based mezzanine daughter-cards, providing a 12-bit sampling of 8 channels with a rate of 500 MHz. In addition, monitoring tools like scaler channels for rate measurements are present. Data are stored in DDR2 buffers accessed by an on-board FPGA; after receiving a L0 trigger, a dedicated readout PC will read, format and subsequently send data to the PC farm.
The LKr electromagnetic calorimeter has a flash ADC (FADC) based readout. The same system has been adopted for the readout of the MUV1 and MUV2 hadronic calorimeters. The readout of these systems is performed by the Calorimeter Readout Module (CREAM) [32] developed by CAEN (see figure 3.2). It is a VME 6U board able to digitise 32 LKr channels at 40 MHz using four 8-channel, 14-bit ADCs. 414 such boards are needed to read out the 13248 calorimeter cells. After signal digitisation, samples are stored in a circular buffer built inside a DDR3 module, waiting for the L0 trigger signal. Upon its reception through a custom backplane, data is moved to the L0 buffer, also built in the same DDR3 module, where it waits for a L1 trigger signal. This is one main difference with respect to other detectors: due to the high data rate, the LKr is only read out at the reduced L1 trigger rate (below 100 kHz). When such signal is received, the corresponding data is sent to the PC farm. The CREAM module also computes digital sums of 4×4 channels, called SuperCells (see section 4.3.1), for trigger purposes: two SuperCells are read out by each CREAM, and digital sums are sent every 25 ns to a system based on 36 TEL62s and custom interface mezzanine boards, where LKr L0 trigger primitives, based on energy

deposits and cluster identification, are generated.

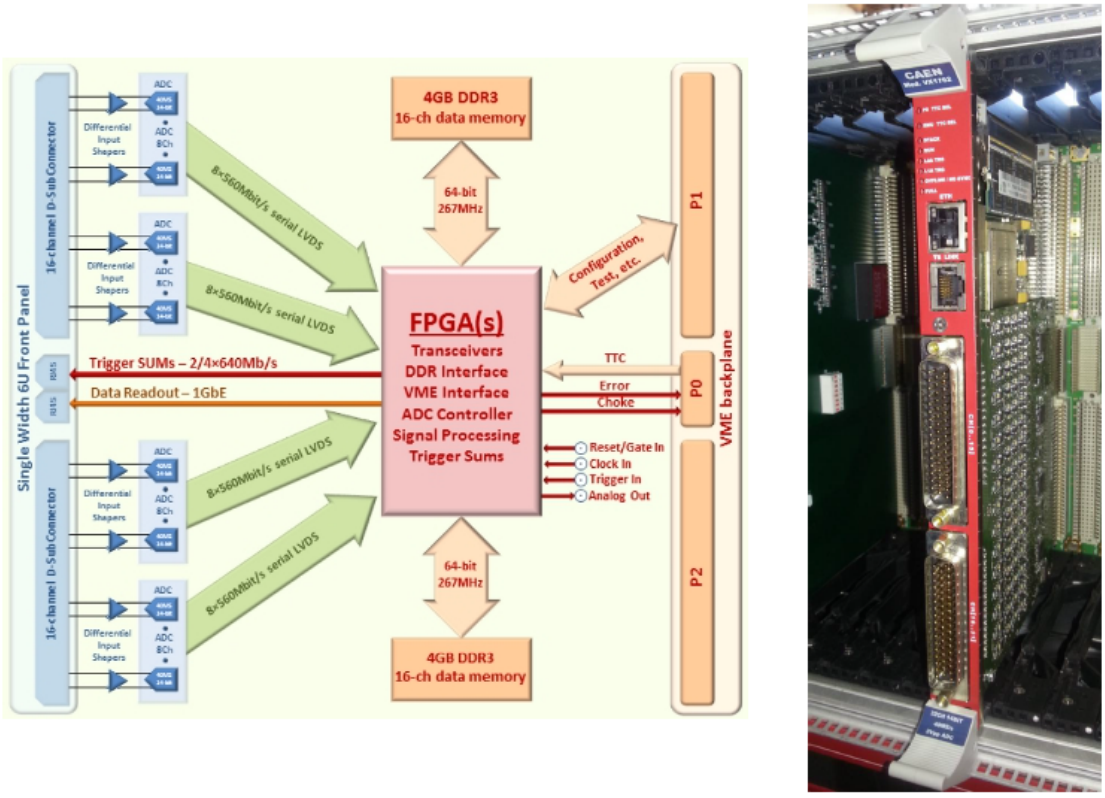

Figure 3.2: Logical scheme and picture of a Calorimeter Readout Module.

3.1.3 Timing and Trigger distribution

The timing of the experiment is provided by the Timing, Trigger and Control (TTC) system developed for the LHC experiments [42].
The TTC provides a common, centrally generated, free-running synchronous 40.079 MHz clock which is the unity reference for time measurements. This frequency is the one of the LHC bunch clock, the period being the bunch crossing time. In NA62 the situation is different: the kaon beam is unbunched, and this is just the reference clock frequency of a free running clock. The clock is distributed throughout the experiment by means of optical fibres: while in LHC the clock comes from radio-frequency timing generators towards the experiment areas, in NA62 it is generated by a clock reference source and is then propagated to detectors' DAQ and the L0 trigger processor.
The scheme of the NA62 TTC system is shown in figure 3.3. A central source dispatches the clock to multiple instances of the fundamental block: the LTU + TTCex partition. These two modules encode and send clock and triggers to the readout electronics of the detectors. The L0TP is the trigger source, as it combines the single trigger primitives

received by subdetectors themselves (for details see section 3.1.1). A backpressure system with CHOKE and ERROR signals is also implemented: they are received from data acquisition boards and the LTU propagates them to the L0TP to momentarily stop triggers in case of exceedingly high rate or errors.

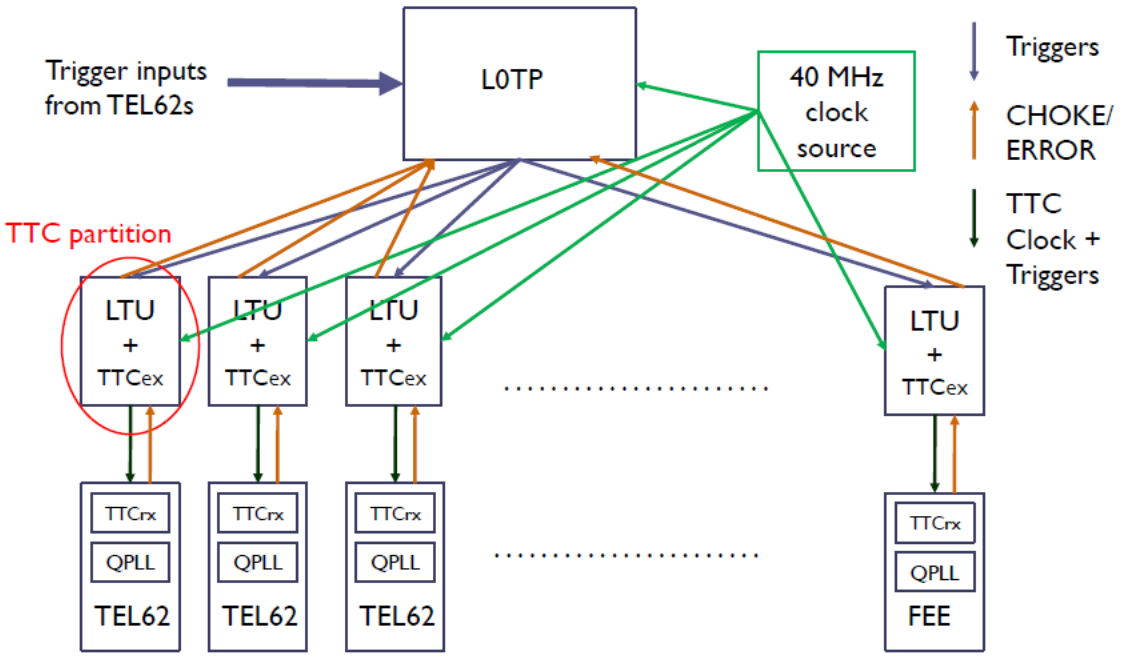

Figure 3.3: The NA62 Timing and Trigger Control system.

The TTCex module [43] is a 6U board: it receives the main clock source which drives an internal QPLL, and is linked to the LTU to receive trigger signals and trigger information messages. The module provides several optical fibre outputs in which clock, trigger signals and trigger messages are encoded together.
The LTU [44] is a 6U VME module, first developed as Local Trigger Unit for the ALICE experiment. NA62 uses an updated version. An on-board FPGA receives the clock from the TTCex and is programmed to perform the following tasks: triggers received from the L0TP are convoyed to the TTCex for optical encoding, in the form of a trigger signal and a trigger message containing 8 serial bits; propagates the backpressure CHOKE and ERROR signals to the L0TP; delivers synchronously to the readout systems the start of burst (SOB) and end of burst (EOB) signals, received from the SPS, as special trigger messages: these signals respectively start and end the data acquisition operations inside a single burst synchronously throughout the entire system.
All the subdetectors front-end subsystems are endowed with a TTC interface containing an optoelectronic receiver and a TTCrx chip [45] which decodes the clock timing and the trigger information.

The time scale of the experiment is defined by a 32-bit timestamp with 25 ns least significant bit (LSB), covering the duration of an entire burst (which is of the order of 10 s), plus 8 bit of fine time with 100 ps LSB.
Trigger messages contain 8 bits: the lowest two LSBs are reserved to encode SOB and EOB signals, the remaining 6 bits represent the Level 0 trigger word (up to 64 different trigger types). The trigger word can encode several physics triggers belonging to different conditions and subdetectors, as well as some service triggers, e.g. synchronization, calibration, monitoring, error on/off and choke on/off.

3.2 The TDC Board

3.2.1 TDCB architecture

The TDC Board (TDCB) is a high-density mezzanine daughter-card for the TEL62 (section 3.3) carrier motherboard, designed in Pisa for precision time measurements.
A fully assembled TDCB can be seen in figure 3.4.
The board design was driven by the desire to integrate a high number of channels within the same processing board, in order to ease triggering issues. The desire for a compact and common electronics and the short distance (order of meters) between subdetectors and readout electronics, with no space constraints, led to the choice of having digitizers on the readout board rather than on the detector thus leaving only analog front-end electronics on each individual subdetector in a potentially higher radiation environment and making all digital electronics common and located on the same boards, at the price of having to transmit analog pulses on the 5 m LVDS cables between the two.

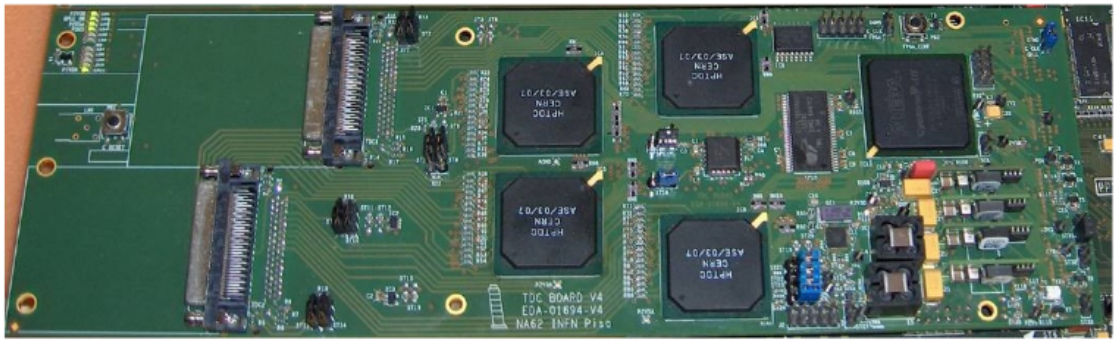

Figure 3.4: The TDCB daughter-board.

HPTDC

The requirements of a good time resolution and high channel integration led to the choice of the CERN High Performance Time to Digital Converter (HPTDC or TDC chip) as time digitizers [46]. The HPTDC can work in an un-triggered mode, in which all available data is delivered at every readout request, or in a trigger-matching mode, in which a readout request follows a trigger pulse, and the TDC only delivers the data which matches in time the trigger occurrence, within some programmable time windows. Trigger-matching mode was implemented to allow HPTDCs to work as front-end buffers, storing data in the so called L1 buffer (see figure 3.5) while a trigger signal was generated; however, in a modern experiment such as NA62, the latency of the lowest trigger level (1 ms) is much longer than the typical time it takes to fill TDCs' buffers (order of tens of µs in our experiment). The TDCBs therefore use TDCs in trigger-matching mode just as a way of obtaining properly time-framed data, but triggers are actually sent to HPTDCs in a continuous periodic stream, with no relation whatsoever to the trigger of the experiment (data storage during trigger latency being actually provided on the carrier board with much larger buffers).
The time-matching parameters in the TDCs have to be properly set in order to allow readout of all hits which occurred since the previous trigger (time-matching window set equal to the trigger period): in this way the TDCs are periodically triggered and readout, receiving all hits corresponding to a time frame of length equal to the triggering period, in a continuous sequence. Since the range of time measurement within the TDC chips is limited (up to a maximum of 51.2 µs), and therefore a roll-over of the TDC time word periodically occurs, only by exploiting this working mode one can be guaranteed that all the data are being read.
A scheme of the HPTDC architecture is shown in figure 3.5.

Each HPTDC provides 32 TDC channels when operated in fully digital mode at 98 ps LSB resolution, with some internal buffering for multi-hit capability and a trigger-matching logic allowing the extraction of hits in selected time windows. Four such chips, for a total of 128 channels, are mounted on each TDCB, resulting in a grand total of 512 TDC channels per fully-equipped TEL62 carrier-board; as an example, the entire RICH detector can be handled by 4 TEL62 boards only, while most small subdetectors only require a single TEL62 board.
With a fast front-end electronics providing adequately time-stretched LVDS discriminated pulses, the measurement of both the leading and trailing edge times allows obtaining analog pulse-height information by the time-over-threshold method: HPTDCs can indeed digitize the time of occurrence of both signal edges, provided they are separated by a minimum time (about 7 ns); the resulting time measurements (made with respect to clock edges) can be combined into a single word to reduce the required data bandwidth.

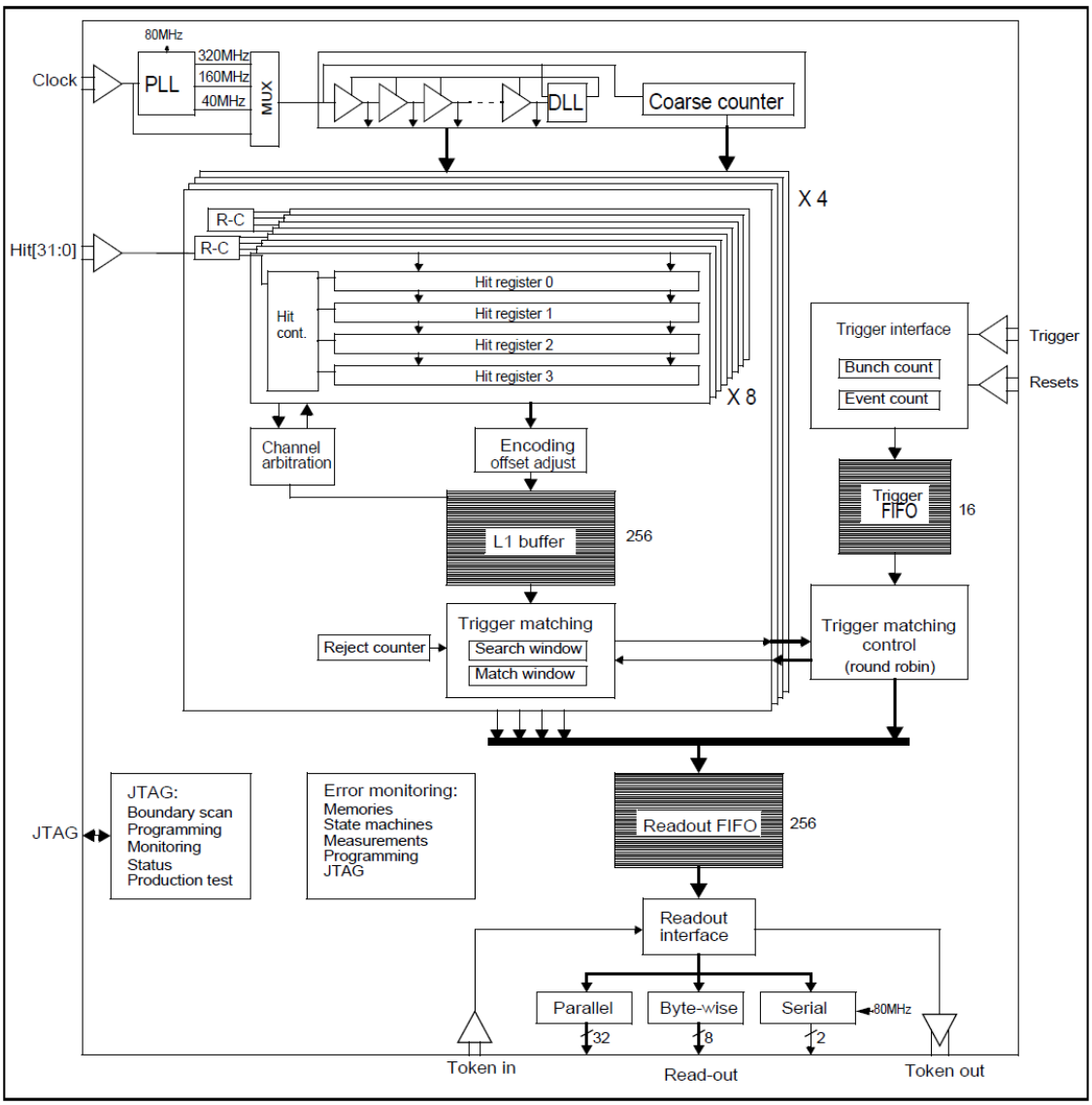

Figure 3.5: Schematic view of the HPTDC architecture. The connections with the subdetector front-end electronics providing the input for the TDC are at top left. The link with the TDCC-FPGA which represents the next step of the data flow is at bottom.

TDC Board

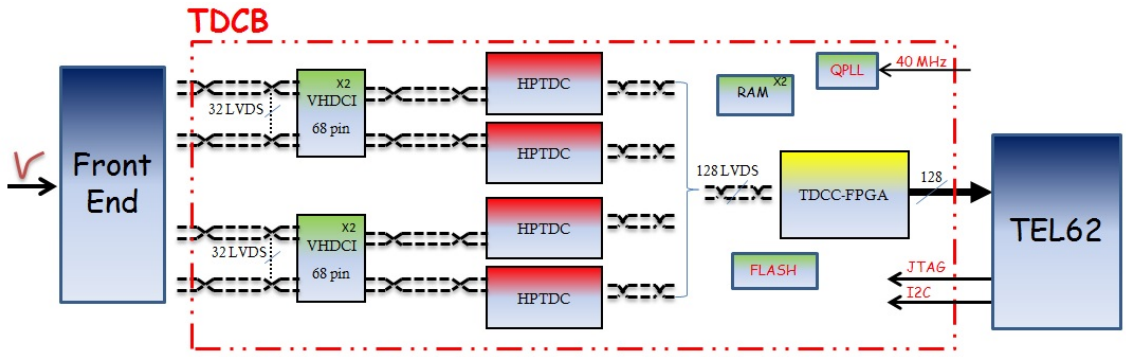

Figure 3.6: Schematic view of the TDCB architecture.

Figure 3.6 shows a schematic view of the TDCB architecture. The printed circuit is made of 10 layers. The board houses four 68-pin VHDCI connectors for input signals, each of them delivering 32 LVDS signals to one HPTDC, with two spare pairs being used to provide additional grounding (one pair) and to allow user-defined back communication from the TDCB to the front-end electronics (one pair). This latter feature can be used to trigger the injection of calibration pulses in the subdetector or calibration patterns in the front-end (as two single-ended lines allowing bidirectional communication, or as a LVDS pair towards the front-end). This choice allows in principle the use of high-performance cables, if required by the intrinsic resolution of a subdetector, as well as cheaper solutions.
The TDCB houses a dedicated Altera® Cyclone® III EP3C120 FPGA [40], named TDC Controller (TDCC-FPGA) which can handle the configuration of the four HPTDCs via JTAG, read the data they collect, and possibly pre-process it. A 2 MB external static RAM block is also available and will be used for online data monitoring purposes and low-level checks on data quality.
The TDCC-FPGA can be configured from an on-board flash memory (Altera® EPCS64 [47]), which can be loaded using an external programmer via an on-board connector or through JTAG, either using a JTAG port on the TEL62 board, or through its Credit Card PC (CCPC). Communication between each TEL62 FPGA and the corresponding TDCC-FPGA on the daughter-board proceeds through a 200-pin connector with 4 independent 32-bit single-ended LVTTL parallel data buses (one for each TDC, running at 40 MHz, for a total bandwidth of about 5 Gbit/s) and a few dedicated lines for synchronous commands and resets. The TDCC-FPGA on the TDC daughter-card can also be accessed from the TEL62 CCPC card via a dedicated I2C connection for slow operations.
The individual TDCs are configured via JTAG, with the TDCC-FPGA acting as the JTAG master: the configuration bits are sent to the TDCC-FPGA from the TEL62 CCPC card via I2C, and are then uploaded to the TDCs. A second working mode allows inserting both the TDCC-FPGA and the four HPTDCs into a global JTAG chain which also includes all

the TEL62's devices, and which can be driven by the TEL62 CCPC card.
The contribution of the digitizing system to the time resolution ultimately depends on the random jitter of the reference clock against which the measurement is performed. The 40.079 MHz clock is optically distributed by the TTC system to each TEL62 board, where it is cleaned by the on-board QPLL [48] to reduce the jitter below 50 ps. This clock signal drives the internal logic and is distributed to each TDCB, where it can be configured to go through two more jitter-cleaning stages: these are the internal PLL of the TDCC-FPGA and a second on-board QPLL.

3.2.2 TDCC-FPGA firmware

A firmware for the TDC board's TDCC-FPGA has been developed with the software tools HDL Designer® and Modelsim® (from Mentor Graphics®), and Quartus® II (from Altera®).
A schematic view representing the main firmware functionalities in a block diagram is shown in figure 3.7.
In the configuration chosen by NA62, each channel within the TDCs will produce two 32 bit-long words for each LVDS signal, one word for the leading and one for the trailing edge. 19 bits out of 32 are dedicated to time measurement, while the other bits identify the channel (5 bits), the TDC inside the board (4 bits) and the type of data sent (4 bits), i.e. leading or trailing edge, error words and TDC frame timestamps and word counters. Through a 32-bit parallel block writing protocol the TDCC-FPGA receives the data sent by the HPTDCs and performs several other operations:

- **Packing the data stream from the TDCs appending a time stamp and a word counter**.
  The TDC data format is such that the time measurement rolls over every 51.2 µs; therefore a timestamp should be added to data in such a way that the TDC time measurement is unambiguously associated to an "absolute" time which can cover a whole SPS spill (up to a few seconds). This is achieved by periodically triggering the TDCs with a period shorter than the TDC's roll-over (presently a trigger is sent by the TDCC-FPGA every 6.4 µs) and adding a frame timestamp at the beginning of the data stream associated with each trigger. A word counter, indicating the number of words received by the TDC plus the frame timestamp itself, is also appended at the end of the frame data stream. 28 out of the 32 bits of a single word are reserved for the timestamp and the counter, while the 4 most significant bits (MSBs) encode a flag indicating the type of word. The roll-over of the frame timestamp (whose LSB corresponds to 400 ns) is at $2^{28} \times 400\,\text{ns} \approx 107\,\text{s}$, much greater than the foreseen spill

duration.

- **Configuring TDCs and communicating with the CCPC on the motherboard**.
  As mentioned before, configuration data is sent to the TDCB through I2C. An I2C slave controller has been implemented in the firmware, through which internal registers are both written and read and a JTAG master controller is implemented in the TDCC-FPGA. Data to/from the TDCs are transmitted/received through the JTAG protocol, to which the I2C controller interfaces.

- **HPTDC emulator**.
  Two different HPTDC emulators are contained in the TDCB firmware: one suited to send some simple repeating pattern on selected TDC channels (single-channel TDC emulator), and one which allows to fully specify some amount of data words which are loaded from a file into memory and repeatedly sent (data emulator).
  In particular the data emulator generates data packets containing a variable number of words per frame as required by the user, sending one data packet for each frame to which the header (timestamp) and trailer (word count) are automatically added; these data words are inserted in the output FIFO directly. The data words are read from a 32-bit wide and 1k deep pattern memory, and modified so that the upper bits of the TDC time field do match the current frame timestamp (otherwise the words might be rejected in later stages of the processing): this means that the data words will not repeat exactly and will not be exactly as loaded in the pattern memory. The number of words to be put in each frame are read from each line of a 9-bit wide and 1k deep count memory: a 0 value will generate an empty frame (only header and trailer), while other numbers will generate a frame with that number of data words (as read from the pattern memory); note that there is a limit on the number of words per frame, which should not exceed 250, and a frame must be completed before a new trigger comes (with real TDC data this is not a strict requirement and it can happen that an outstanding frame will take longer than the inter-trigger period to be transferred, but this is not currently implemented in the data emulator). When the last address of the counter memory is reached the first one is read again, repeating the same sequence. The upper bit in the count memory forces a rewind so that the next event will be as the first one. In order to fill the pattern and count memories some suitable I2C registers are used to implement indirect memory addressing.

- **Enabling RAM reading/writing**.
  During the acquisition, the data stream can be optionally split and sent to the TDCB's on-board RAM. The RAM space is equally subdivided among the four TDCs. In the final implementation, it will be possible to choose between filling the RAM space with the first data of the spill or collecting only the most relevant data,

for example that corresponding to events where one or more TDCs sent an error word. This data can be then analysed off-line to better study some fine details of the data for debugging or monitoring purposes.

- **Front-end pulser**.
  The TDCC-FPGA can drive a spare output LVDS pair of the TDC connector, that allows to trigger the front-end boards for subdetectors' calibration. This can be done periodically by setting a mask register which is compared with a timestamp counter. An alternative way is to generate the signal to be sent to the front-end upon reception of a special trigger from the motherboard.

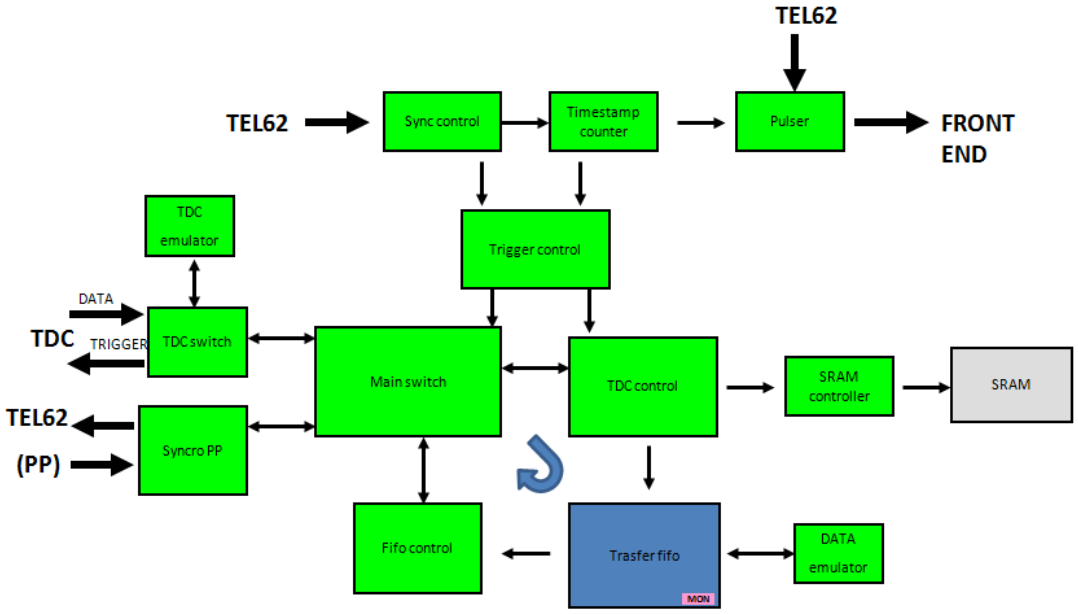

Figure 3.7: Block diagram of the TDCC-FPGA firmware.

3.2.3 TDCB tests

Once the TDCB design was finalized various tests were performed in order to verify that the system complies with the experiment's requirements. Some of such tests were performed in laboratory using a test setup which may reproduce conditions similar to the experiment environment, others were performed at CERN during a test beam.

Time Resolution and Cross-Talk

A measurement of the intrinsic contribution of the board to the time resolution was evaluated in the laboratory by pulsing TDC channels with signals of fixed duration generated by an FPGA-based test board working on the same clock used by the TDCB, and measuring the time difference between the trailing and leading times of a LVDS pulse with nominal

25 ns duration.
When pulsing 32 TDC channels at a time, the observed RMS of the measured pulse width on a single channel was 61 ps (figure 3.8 left), with an average of 25.18 ns, for 10^5 pulses. The values are comparable when only 1 every 4 TDC channels (8 in total) is pulsed simultaneously with the same signals of the previous case (figure 3.8 right).

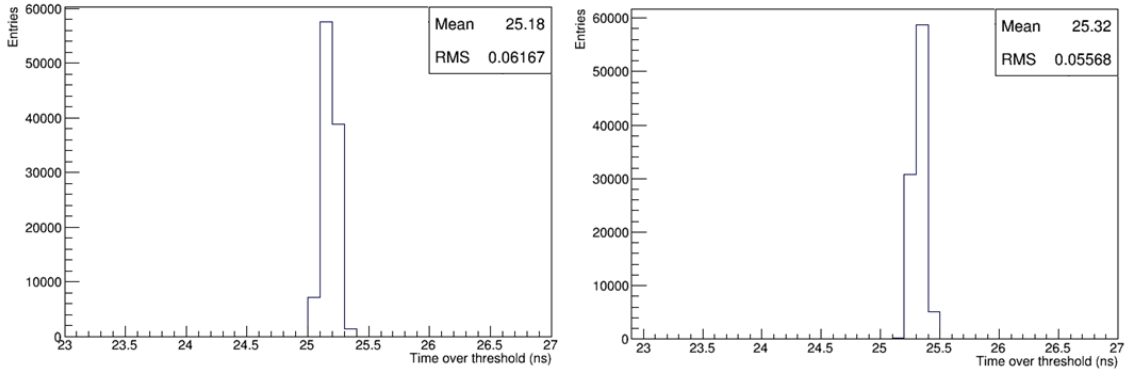

Figure 3.8: Distribution of times-over-threshold for digital 25 ns wide signals as measured by the TDCB, with 32 channels pulsed (left) and 8 channels pulsed (right).

No spurious hits were detected on channels which were not pulsed, over a sample of 10^7 events, but other possible cross-talk effects were checked by comparing a channel time resolution into 2 different cases: all the 32 TDC channels pulsed with signals of constant width (25 ns) or pulsing only 8 TDC channels (1 every 4); since no differences were observed in the time resolution (see figure 3.8) this is a indication that no significant effect of cross talk is present.

Channel efficiency
The data transfer efficiency (ϵ) is defined as the ratio between the number of hits delivered by the system and the number of input pulses, and was measured in the laboratory both on a single channel (1 of every group of 8 for a total of 4 TDC channels) and on two neighbouring ones (channels 0 and 1 of every group of 8 for a total of 8 TDC channels). Results are shown in figure 3.9.

No data losses were observed for input rates below 17.5 MHz in the first case (single channel). In the case of two adjacent channels being pulsed, no data losses were observed for input rates below 8.5 MHz per channel; above such value data losses start to appear at slightly different levels depending on the pulsed channel.
Hit losses are expected at high rates due to the limited amount of buffering present in the HPTDC. In the HPTDC the 32 channels are divided in four independent groups of 8 chan-

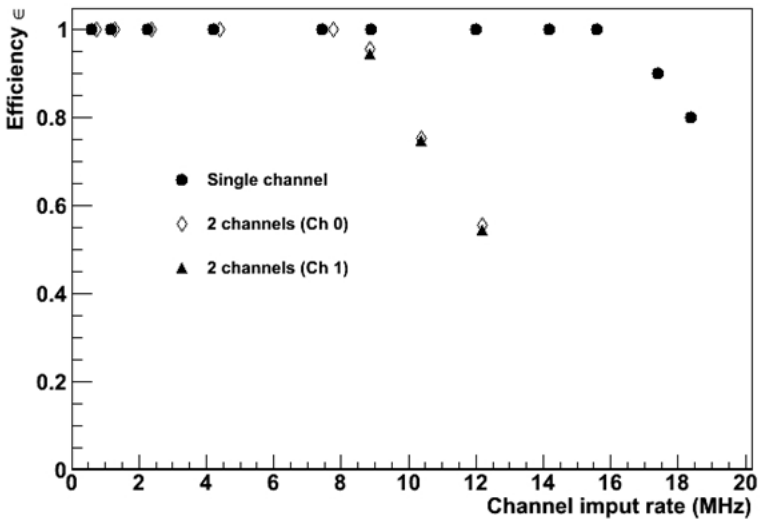

Figure 3.9: TDCB hits efficiency pulsing one and two channels.

nels each, and hits are buffered at different stages: per channel, per group of 8 channels, per full chip (respectively Hit registers, L1 buffer and Readout FIFO in figure 3.5); apart from the first buffering stage, the other ones are monitored for overflow conditions.
The first channels in each group of 8 are serviced faster than the last ones due to the simple fixed-priority arbitration scheme adopted. At high rates this gives an advantage to the low-numbered high-priority channels which can use their channel de-randomizers more efficiently, while in such conditions lower-priority channels appear like they have smaller de-randomizing capability and therefore slightly higher data losses.

Test beam results

In November and December 2012 a test run with beam was performed at the CERN SPS. The response of the detector, the time and space correlations between the detectors, the rates and efficiencies of the detectors and the TDAQ system were the main measurements performed during of this test.
The experimental setup in the test beam was similar to the experiment, with the secondary kaon beam of 75 GeV/c produced by protons from the SPS. The test was carried out with a much reduced intensity (1/50 of nominal rate foreseen for NA62).
Figure 3.10 shows the event time difference distribution between the fast and high-resolution detectors CHOD and CEDAR, which had a fitted standard deviation of 410 ps, a value which is compatible with the intrinsic detector resolutions, thus confirming a negligible contribution from the electronics.

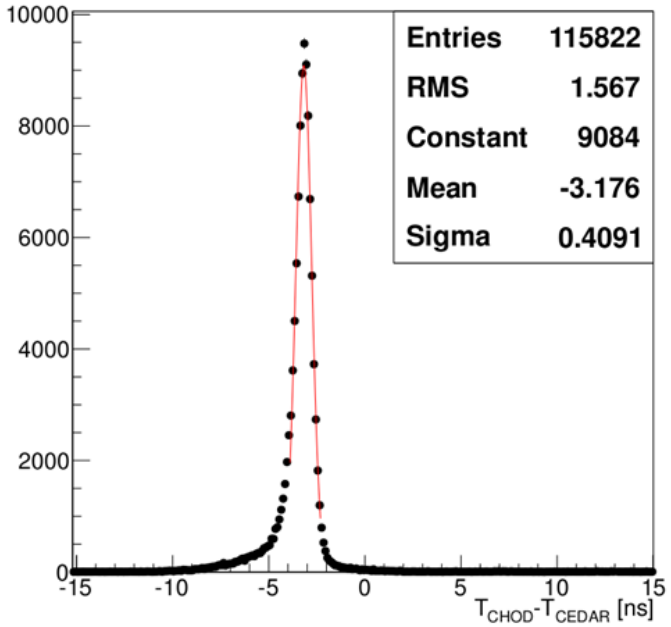

Figure 3.10: Distribution of event time difference between CHOD and CEDAR detectors (test beam).

3.3 The TEL62 multi-purpose board

The TEL62 board is the common FPGA-based motherboard for trigger generation and data acquisition of the NA62 experiment [49]: about 100 cards will be installed on the experiment. It has been developed in Pisa, and represents a major redesign of the TELL1 board designed by EPFL Lausanne for the LHCb experiment at CERN [50].
The overall architecture of the TEL62 is similar to the TELL1's, but the board is based on much more powerful and modern devices, resulting in 8 times the computing power and about 20 times the buffer memory. Figure 3.11 shows a picture of the TEL62 motherboard.

The TEL62 handles up to 4 TDCB mezzanines, for a total of 512 input TDC channels. The amount of data arriving from the TDCs can be up to a few tens of MB/s per channel, depending on the subdetector. Data are organized in packets, each one related to time frames of defined duration. A first set of four FPGAs (PP-FPGAs, see the architecture in section 3.3.1) has the duty of collecting and merging the data and then of organizing them on the fly in a 2 GB DDR2 memory, where each "page" is related to a well defined 25 ns time window. Whenever a L0 trigger request arrives the data within a programmable number of 25 ns time windows around the trigger timestamp are collected and sent to the central FPGA (SL-FPGA, see section 3.3.1). Here data are merged and synchronized, pre-processed and sent in packets through 4 Gigabit Ethernet links hosted on a custom daughter-card to a computer farm that performs additional cuts (software trigger levels)

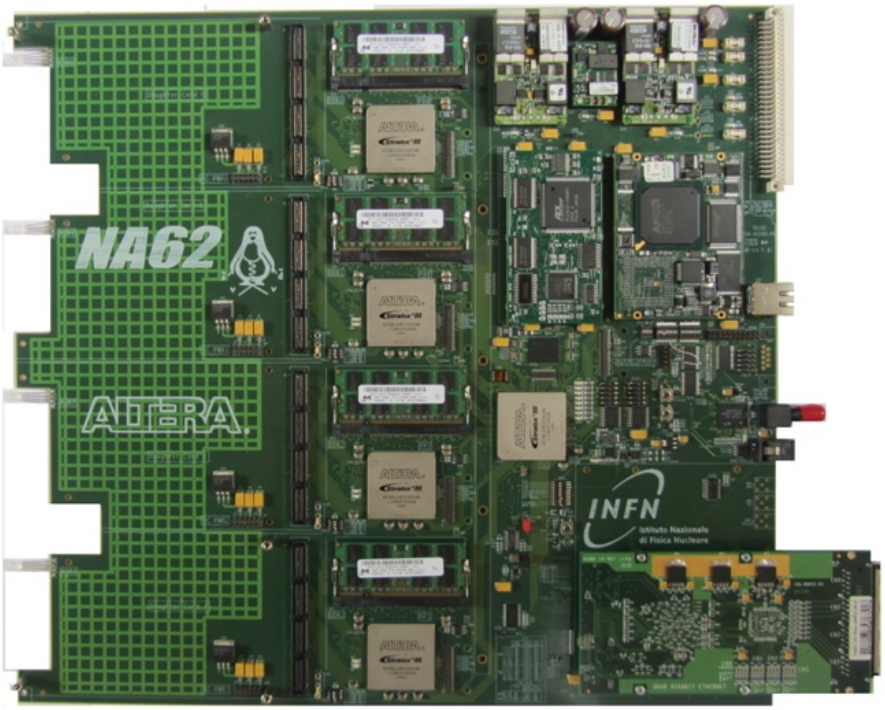

Figure 3.11: The TEL62 multi-purpose motherboard.

and eventually writes events to permanent storage.
A detail of the TEL62 architecture and the description of the firmware of the on-board FPGAs is given in following sections.

3.3.1 TEL62 architecture

The board size complies with the 9U Eurocard standard. The printed circuit is made of 16 layers, with all lines controlled in impedance (50 Ω). Special care has been used for the clock tree routing, to avoid introducing further signal jitter.
A scheme of the TEL62 architecture is shown in figure 3.12. The board is composed of the following parts:

- 4 Altera® Stratix® III FPGAs EP3SL200F1152 [51] (called Pre-Processing or PP-FPGAs), each one containing an embedded memory of 9396 kbit and 198 900 equivalent logic elements. Each PP-FPGA handles the data from one TDCB (see section 3.2) mezzanine daughter-card providing digitized words; the mezzanine is connected through a 200-pin connector, containing 4 data buses 32-bit wide, one for each HPTDC, running at 40 MHz, for a total bandwidth of about 5 Gbit/s. Each PP-FPGA is also connected to a 2 GB DDR2 memory buffer: the communication bus has 64 bits and is used at a clock frequency of 640 MHz, resulting in $\sim$ 41 Gbit/s.

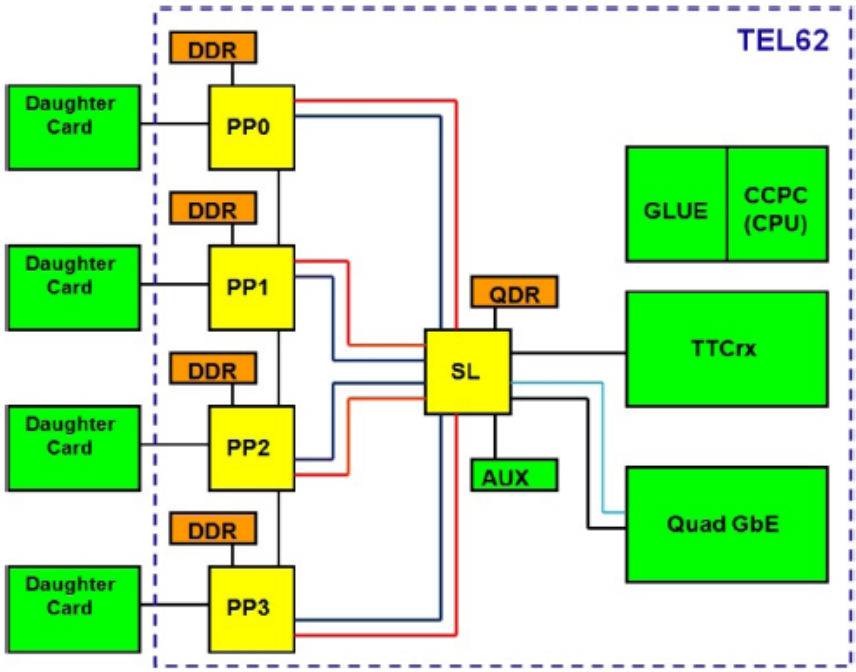

Figure 3.12: Layout of the TEL62 board architecture. FPGAs are in yellow, memory buffers in orange, other chip and daughter-card connectors are in green. Lines represent data bus links between devices.

A connection between PPs is implemented on the board: 2×16 bit buses (input and output) connect pairs of adjacent PPs (as can be seen in figure 3.12 PP1 and PP2 have two such connections, while PP0 and PP3 have only one).

- 1 Altera® Stratix® III FPGA EP3SL200F1152 [51] (called Sync-Link or SL-FPGA, with the same characteristics mentioned for the PP-FPGAs), connected to all the four PPs through independent data and trigger primitives flow buses, 32 bits each one operating at a clock frequency of 160 MHz, with a total bandwidth of about 10 Gbit/s per PP-FPGA connection, equally divided between data flow and trigger flow. All signal lines have been properly terminated and equalized in length to handle this clock speed; in addition, a proper set of time constraints has been set up during the firmware development stage, in order to keep all signal edges within few nanoseconds, to guarantee the functionalities of the board. The SL-FPGA is also connected to the output mezzanine Gigabit Ethernet (GbE). An external 1 Mbit Quad Data Rate (QDR) Synchronous Pipelined Burst SRAM is used as intermediate buffer, allowing simultaneous read and write operations at a clock frequency of 120 MHz.

- The custom output mezzanine card is a Quad GbE [52] (same daughter-card as in the TELL1 design), which implements four 1 Gbit copper Ethernet channels, used to connect the TEL62 to the L0 Trigger Processor (L0TP), to other TEL62s in daisy

chain, or to send the main data flow to the PC farm.

- The slow control, monitoring and configuration of the board is handled by two other mezzanine cards: a commercial Credit Card PC (CCPC) running a Linux kernel (the operating system is Scientific Linux, mounted through a dedicated Ethernet link from an external CCPC boot server) and a custom input/output interface card named Glue card [53], also identical to those on the TELL1 board; the connection of these daughter-cards to the TEL62 is made through PCI buses.
  Three different communication protocols are implemented in the Glue Card and distributed to all devices and connectors on the TEL62: JTAG to remotely configure and program the FPGA devices on the motherboard and on the daughter-boards loading the firmware on the respective EEPROMs, I2C mainly used for slow communication with the TDCB daughter-card, and ECS (a custom parallel bus used to quickly access the TEL62 FPGA's internal registers, control and monitor the board functionalities).

- Clock and L0 triggers are distributed through a standard optical TTC link, a CERN-developed optical time-multiplexed connection which distributes the main 40 MHz clock with triggers and timing signals encoded in it; a TTCrx chip [45] is used to decode this information. After being decoded, the clock signal passes through an on-board QPLL [48] in order to reduce signal jitter to few tens of ps.

- The FPGA configuration data is stored in two 64 Mbit EEPROMs (Altera® EPCS64 [47]), a common one for the 4 PPs and one for the SL. The 4 PP-FPGAs are programmed with the same code.

- Dedicated auxiliary connectors (two independent 16-bit buses) on the board allow daisy chaining of several TEL62 boards, in order to collect L0 trigger primitives from all the boards of a single subdetector without giving up one or more of the Quad Gigabit links.

A picture of the TEL62 board without mezzanine daughter-cards plugged in and indicating the above described components is shown in figure 3.13.

3.3.2 PP-FPGA firmware

The same software tools already mentioned in section 3.2.2 have been used to develop the firmware of the PP-FPGAs and the SL-FPGA.
The firmware of the PP-FPGA, which is the same for all the four PP-FGPA devices on-board the TEL62, can be divided in five main areas: three are related to the input flow of the board, one concerns the output of the PP-FPGA, the remaining one is about the

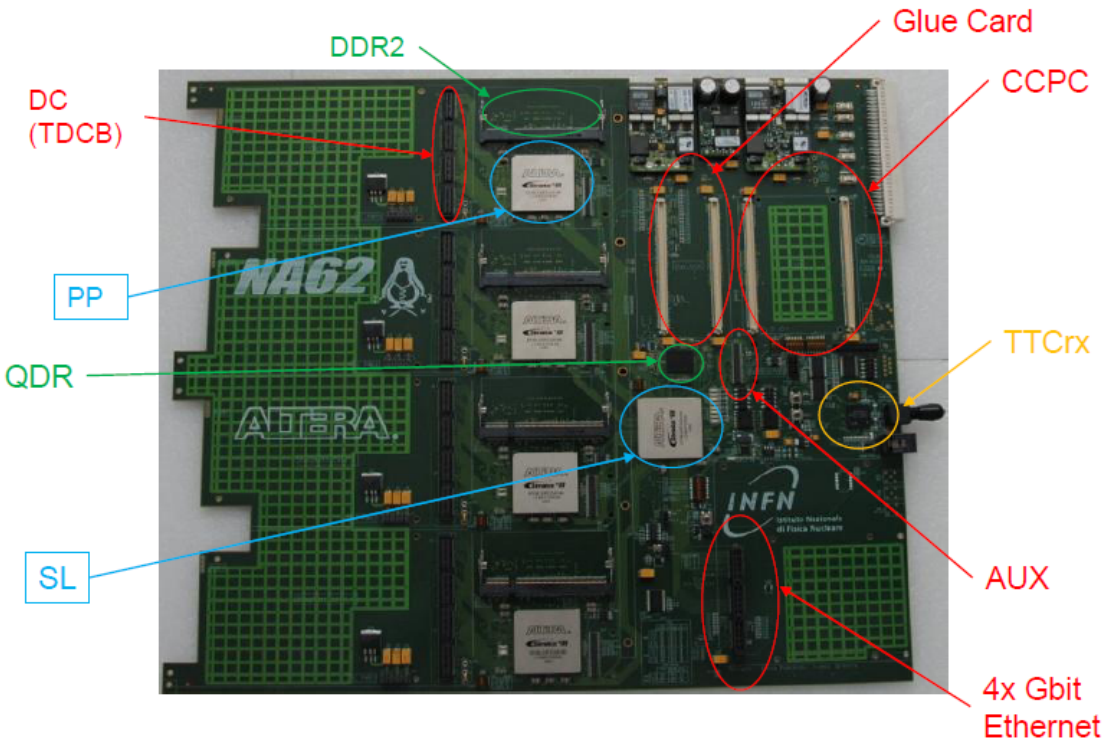

Figure 3.13: TEL62 board architecture. FPGAs are indicated in blue, memory buffers in green, connectors for daughter-cards are in red and the TTCrx chip is in orange.

testing of the FPGA.
A block diagram layout of the PP-FPGA firmware is represented in figure 3.14, where these components can be identified.

- **Incoming data buffering**
  The PP-FPGA receives the data flow from four different buses coming from the TDCB mezzanine card (see the left part of figure 3.14). A first group of four de-randomizer FIFOs (Input Buffer or IB FIFOs), one per TDC, is filled at a clock frequency of 40 MHz with incoming data, packed in 6.4 µs data frames by the TDCC-FPGA firmware. A merging stage (OB) running at 160 MHz puts together data belonging to same frames, identified by the timestamp, to build a bigger frame with all hits coming from the associated mezzanine, which is stored in three copies of the Output Buffer (OB) FIFO.
  The following stage of the data buffering concerns the on-the-fly storage inside the external DDR2 memory (left-upper part of figure 3.14). This represent the most challenging part of the PP-FPGA firmware, and has been the subject of an important revision during the evolution of the firmware itself.
  Data must be organized in proper memory structures in order to maximize the time

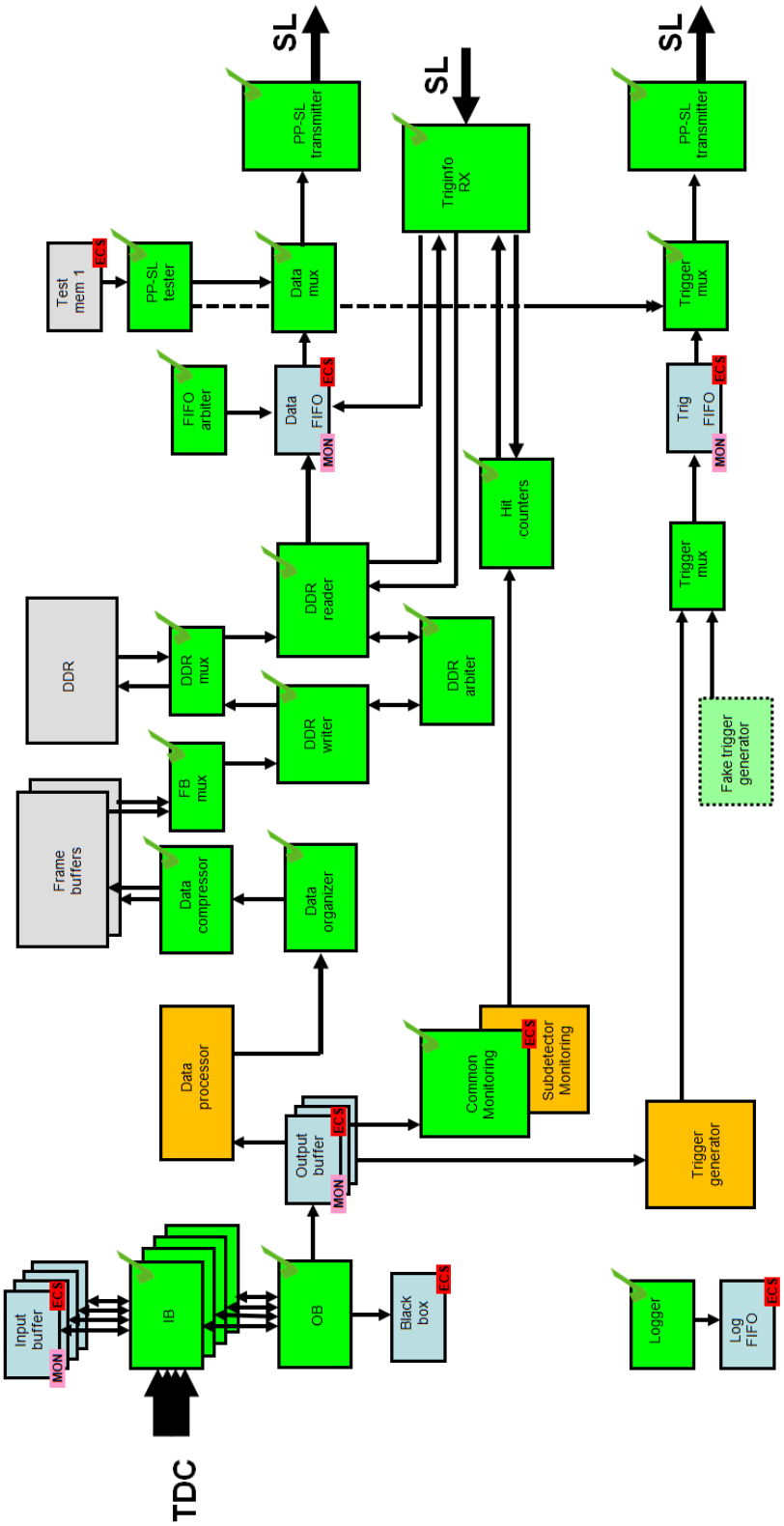

Figure 3.14: Block diagram of the PP-FPGA firmware. Version 2 of the firmware is represented.

efficiency of DDR2 writing and reading operations. The DDR2 interface plays a crucial role: it performs memory accesses with a so called *burst* structure, with a minimum of 256 bit written or read in a 160 MHz clock cycle.
The first version was based on organizing data of the same 6.4 µs frame in fixed 25 ns time slots: a total of 256 slots are needed to cover the entire frame. Each time slot was reserved a memory amount equal to 128×32-bit words: consequently a 6.4 µs frame corresponds to a 1 Mbit memory; two of these memories are implemented inside the FPGA for time optimization: while one memory is written by the Data Organizer, the other is read by the DDR writer. The number of words reserved to one 25 ns time slot is a trade-off between the need to sustain high instantaneous rates and the memory of the FPGA: two 1 Mbit memories actually are equal to a quarter of the internal FPGA memory.
One half of the 2 GB DDR2 is reserved for data storage, while the other one is filled with 8-bit counters. These represent each one the data word counter of one 25 ns time slot: this is mandatory since the DDR2, used as a circular buffer, is not entirely overwritten, and only actual data are stored to optimize DDR2 writing times. Counters are therefore used by the DDR2 reader module to put in the data flow only the relevant part of each 25 ns time slot.
The resulting capacity of the DDR2 in terms of latency for the trigger is

$$\frac{8\,\text{Gbit}}{1\,\text{Mbit}/6.4\,\mu\text{s}} = 51.2\,\text{ms}$$

This way of organizing data presents some problems when increasing the trigger rate. The DDR2 reading module has to perform several memory accesses, and most of the read locations are empty (the average expected rate on detectors is well under the instantaneous rate which would fill the 128 locations of a 25 ns slot). The arbitration of the DDR2 accesses suffers from these accesses from the DDR reader: with a trigger rate of 1 MHz, an average of more than 6 reading accesses must be performed per each writing access.
A second version improved the organization of data, with the introduction of a data compressor stage. Inside the same 1 Mbit allocated for a 6.4 µs frame, data are written in adjacent locations, without a pre-defined space for each 25 ns time slot. The DDR2 half with counters now contains 8-bit addresses, representing the starting address of a non-empty time slot in the DDR2 data part. This improvement provides a reduction of the number of accesses and of the time needed to read data, thus allowing to reach the required rate.

- **Incoming data monitoring**
  A second identical copy of the OB FIFO containing packed data in 6.4 µs frames is used for monitoring purposes (left-central part of figure 3.14). A number of actions

can be performed on data, e.g. the logging of errors or the detection of noisy or dead channels. This part is divided between a common and a subdetector specific monitoring. For what concerns the common monitoring part, it actually implements some scalers counting the number of words for each channel during a burst; 128 × 32-bit counters are stored in a memory, and read out upon the signal of end of burst; the information is then provided as part of the payload of the end of burst data packet (the last data packet of the burst sent from the TEL62 to the PC farm).

- **Trigger primitives generation**
  The third copy of the OB FIFO is reserved for the subdetector specific part responsible for the L0 trigger primitives generation (bottom of figure 3.14). Only detectors involved in the L0 trigger developed this part of the firmware: the RICH and CHOD as positive elements, the LAV and MUV3 as vetoes (see chapter 4).
  One example is the LAV firmware [54]. Here first of all data is corrected with a channel specific offset, then a sort of event reconstruction is performed, identifying a pair of low and high threshold signals belonging to the same LAV block. To obtain the required resolution, a time slewing correction is performed in order to account for the dependence of the hit leading time on the time-over-threshold (see section 4.3.1). Threshold values as well as time offsets for each channel are stored in internal FPGA memories. After building the primitive following a defined data format, this is sent to the SL-FPGA for further processing. A further intermediate stage using PP interconnections could be introduced to evaluate conditions on partial subdetectors (e.g. 2 layers of a LAV station) before the full stage inside the SL-FPGA.

- **Trigger decoding and data output**
  This part of the firmware takes care of receiving as input the trigger requests from the SL-FPGA and redirecting the request to the DDR2 reader in order to retrieve data (right part of figure 3.14). The Trigger Receiver (TrigRX) has the task of decoding the trigger type: it could be a physics trigger, and in this case a request will be forwarded to the DDR2 reader, or it could be a special purpose trigger, e.g. a synchronization or calibration trigger, or it could also be an error/choke trigger, which represents a warning telling the board to stop the data acquisition.
  In case of a physics trigger (up to 32 different physics trigger types can be accommodated by the firmware), the DDR reader is activated in order to read a pre-defined number of 25 ns time slots around the timestamp associated to the trigger. With the introduction of the version 2 of the PP-FPGA firmware, this number can be up to 32, corresponding to a time window of 800 ns. Furthermore, the centring of this window around the trigger timestamp can be selected as well.
  Data extracted from the DDR, together with data belonging to the above mentioned special triggers (a special arbitration module regulates both the input flows), are

stored in a Data output FIFO, from which they are transferred to the SL-FPGA.

- **Firmware testing and monitoring tools**
  Several monitoring and debugging tools have been implemented to check firmware performances during the data acquisition. The FPGA is accessed from the CCPC via the custom fast access ECS bus, allowing the possibility to read internal registers and monitoring FIFOs and memories status. An important debugging feature is a Logger system, which stores in a memory a number of informations (timestamp and source) related to specific error conditions, for later checking from the slow control CCPC.
  Additional firmware has been developed for the PP-related testing of the board. The main test concerns the bus links between the PP and the mezzanine on one side, the PP and the SL on the other side. A typical implementation foresees the use of memories filled with random words (from the software CCPC side): the communication with the other device is subsequently started, and the receiving memory is finally read out by the CCPC to check the consistency of the performed operation.

3.3.3 SL-FPGA firmware

The SL-FPGA firmware is represented in figure 3.15 and can be divided in five main parts. The first two core blocks are related to the data flow, respectively before and after the temporary storage of data inside the external QDR buffer. Another important section handles the communication with the TTC system. A piece of firmware dedicated to testing and monitoring is present, as in the PP-FPGAs. Finally, a trigger primitives flow is implemented (shown in figure 3.16), similar to that of data.

- **Data merging and MEP assembling**
  The first step of the data flow inside the SL-FPGA is the merging from the 4 PP sources (left part of figure 3.15). Similarly to what happens in the PP-FPGA, data for triggered events coming from 4 different buses are stored in 4 de-randomizing input FIFOs. The Event Merger acts like the OB stage of the PP, and merges data belonging to the same event (same trigger) from the four buffers with a round-robin architecture, storing the resulting global event in the Event Data FIFO.
  Multiple events can be packed together in a custom defined Multi-Event Packet (MEP), which is used in case of events with an expected small size (order of 100 B) to avoid that the available output bandwidth could be dominated by packet header (42 B in total) rather than payload. After MEP assembly, the packet is stored in the external QDR memory. This buffer is written in a circular way, so that at each moment it contains previous data for a total amount of 1 Mbit.

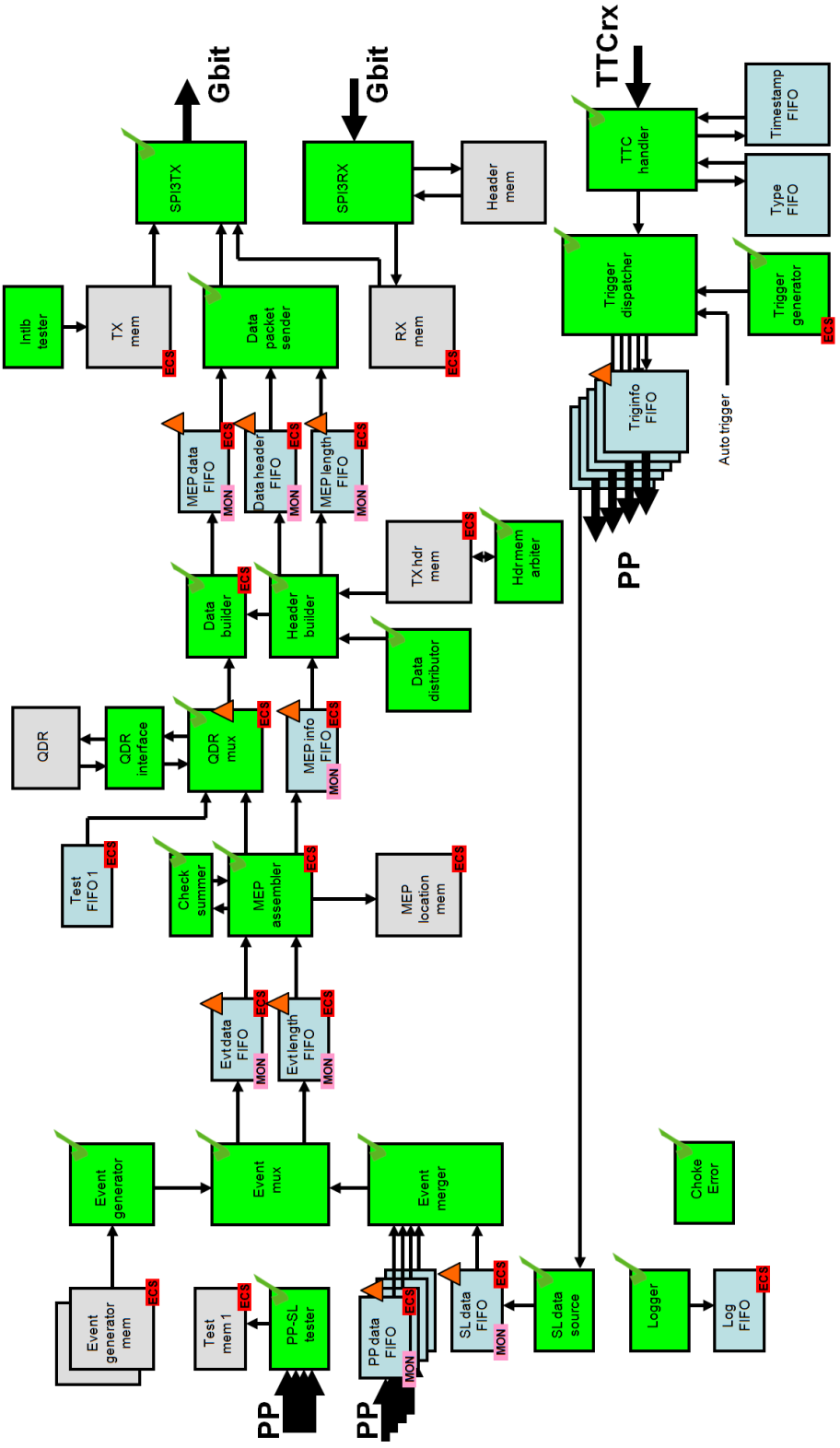

Figure 3.15: Block diagram of the SL-FPGA firmware (data and trigger flows).

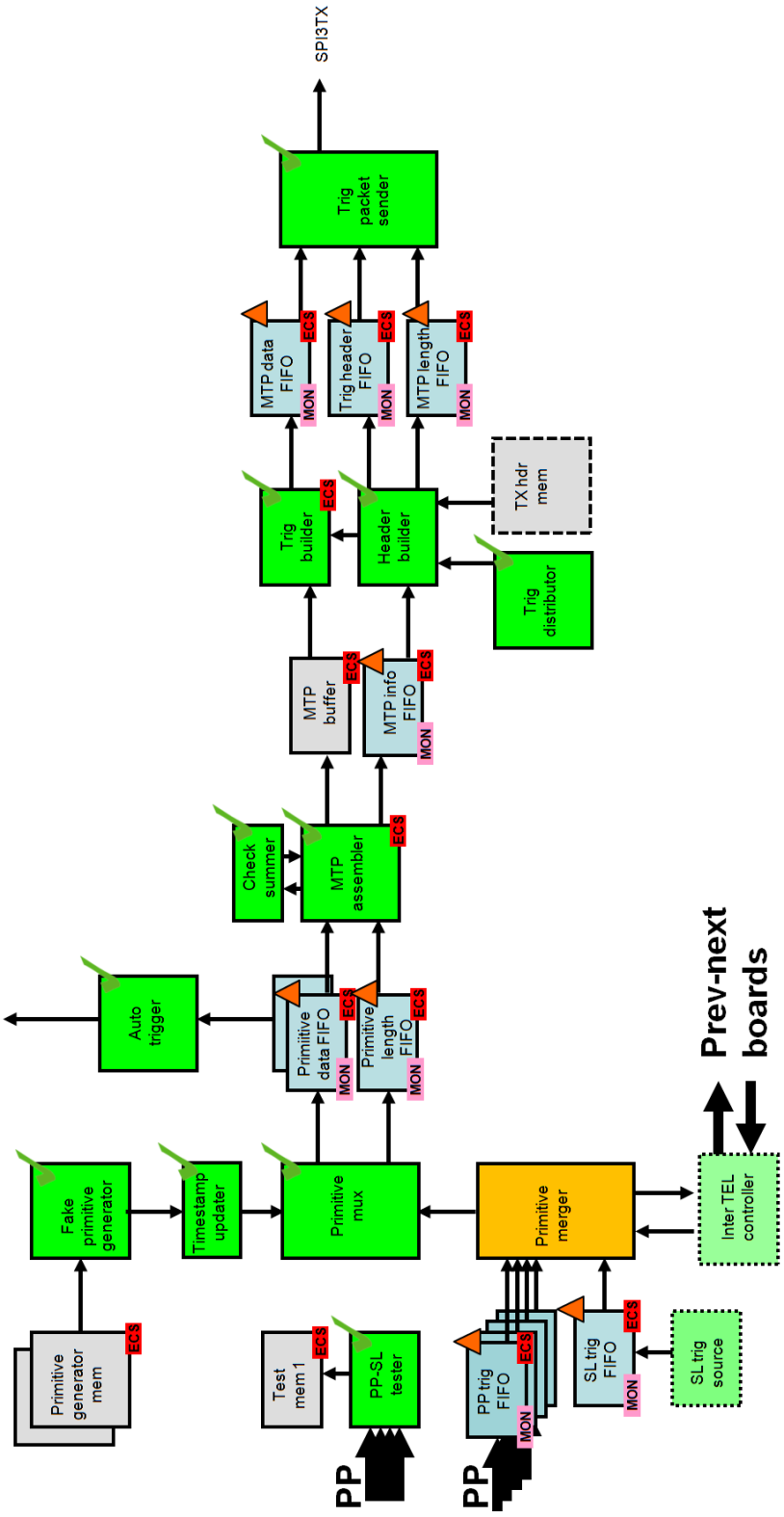

Figure 3.16: Block diagram of the SL-FPGA firmware (trigger primitive flow).

- **Data output**
  To complete the data flow, the packet is extracted from the QDR and is formatted in a UDP packet. All the information needed to build the UDP packet is stored in three FIFOs, containing the data, the header and the information about the length of the packet. Finally packets pass to the SPI3 interface, the module which implements the communication with the GbE output mezzanine (right-top of figure 3.15).

- **TTC interface**
  The TTC interface (right-bottom part of figure 3.15) takes care of the communication with the on-board TTCrx chip. First of all it decodes the start of burst (SOB) and end of burst (EOB) signals which respectively start and end the acquisition phase of the board during a burst. The other tasks of this core block is the decoding of triggers arriving from the TTC system. Each trigger is assigned a timestamp: in NA62 this is not explicitly propagated with the trigger through the TTC, and an internal "timer" can be safely used since all subsystems are synchronously reset via the SOB signal. Following the timestamp assignment, triggers are processed for dispatching towards the PP-FPGAs where the corresponding data will be read out.
  A number of parallel trigger systems have been implemented for testing purposes, e.g. an auto-trigger mode as well as the possibility to produce trigger patterns via ECS control.

- **Trigger primitives flow**
  Figure 3.16 shows the trigger primitives flow, which follows a similar path to that described for data. After the merging from the 4 PPs, primitives could undergo further processing stages, e.g. the cluster identification in the case of LAV firmware [54], or a global TEL62 (512 channels) multiplicity counting for the case of RICH. In addition, an interface with other TEL62 boards will be implemented for detectors using more than one TEL62 for the readout and the generation of trigger primitives (RICH and LAV in case of more than one station).
  An internal memory acts as the storage buffer: here Multi-Trigger Packets (MTPs) are stored. Following is an analogous extraction of primitives which are sent as UDP packets via dedicated Ethernet ports of the GbE to the L0 Trigger Processor.

- **Testing and monitoring tools**
  Like the case of the PP-FPGA, the SL-FPGA has a number of firmware modules dedicated to the monitoring of the FPGA during the data acquisition and to the testing of the board interconnections. In addition to what has been already mentioned for the PP, in the SL a loop-back test concerning the GbE mezzanine has been implemented, which exploits the possibility to write/receive data to/from the output mezzanine. The possibility to generate fake trigger primitives, overriding the primitive generation in the PP-FPGA, is also present, and has been extensively used

for the development and testing of the L0 Trigger Processor.

3.3.4 TEL62 tests

The performances of the TEL62 were tested at the end of 2013 during one of the TDAQ commissioning phases.
Some results concerning the output data bandwidth of the board are shown in figure 3.17. These results have been obtained with a standalone data acquisition, including the use of the TDC emulators implemented inside the TDCC firmware (see section 3.2.2) as input and the LTU in standalone mode as trigger source.
The top plot shows the bandwidth as a function of the number of used Gigabit ports. The blue line indicates the expected upper limit value (1 Gbit/s = 125 MB/s per port), while red points refers to the measured values. The results are rather in agreement with expectations: the slight gap indicates that the firmware could be further optimized for what concerns the data transmission section; however some limitations are introduced by firmware operations like the data formatting, which prevents to reach the theoretical bandwidth.
The bottom plot was obtained using 4 Ethernet ports and shows the maximum data payload (without including the IP and UDP packet headers) for a given trigger rate, assuming one data packet for each incoming trigger. As expected, measured values are along a hyperbola where the product between the trigger rate and the payload represents the effective data output bandwidth.

The TDCB+TEL62 system has been extensively tested during 2012 and 2013 TDAQ commissioning runs, and 2012 NA62 Technical Run. The system proved to match the requirements of the experiment in terms of performances: the time resolution is compatible with the intrinsic detector resolutions, with a negligible contribution from the TDCB; the TEL62 stores data in DDR2 buffers and extract them at a trigger rate above 1 MHz. The system is currently being used for data acquisition during the 2014 NA62 Pilot Run, in which the validation of the subdetectors trigger primitives generation will be performed.

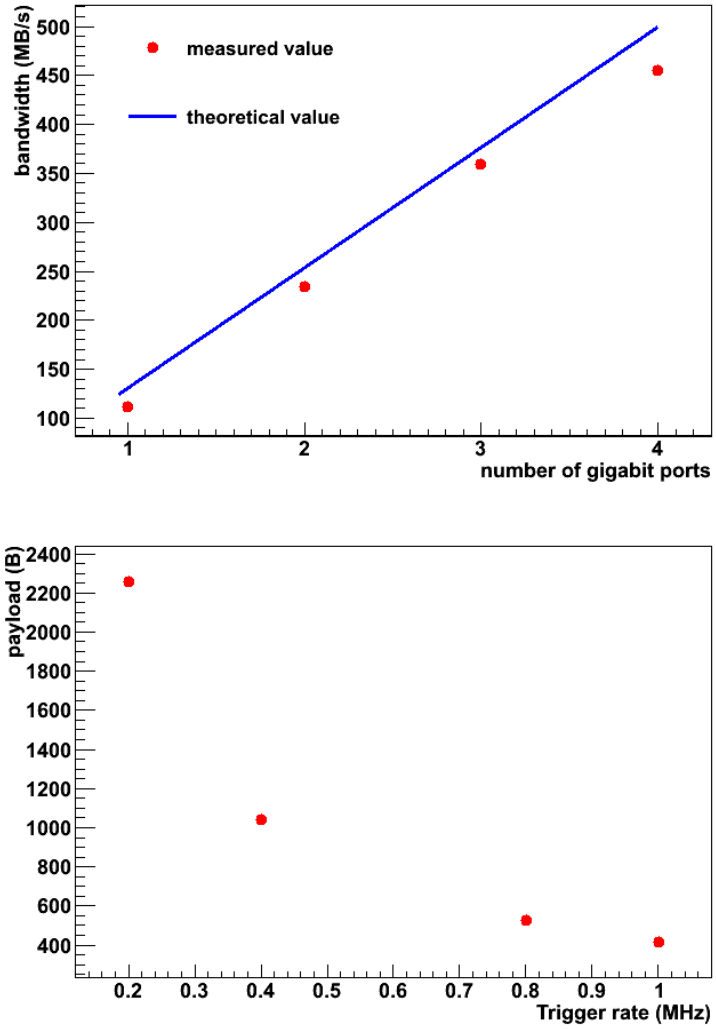

Figure 3.17: TEL62 firmware performances in terms of output bandwidth as a function of the number of used Gigabit ports (top), and data packet maximum payload as a function of the trigger rate using 4 ports (bottom).

Chapter 4

MC studies of the NA62 hardware L0 trigger

4.1 Introduction

The intense beam flux of the NA62 experiment requires a high performance trigger system, which should maximize the collection efficiency for events under study and the rejection power against background events.
The trigger logic of the experiment is made of three levels: the rates and the number of channels of the experiment have driven the choice of NA62 for an hardware lowest-level trigger (L0) to be implemented in the firmware of the common readout boards; in response to a L0 request, coming from a L0 Trigger Processor (L0TP) which puts together the informations from different subdetectors, data is transferred to a farm of dedicated PCs where L1 and L2 high-level trigger algorithms are applied.
The rate on main detectors is expected to be of the order of 10 MHz, while, given the available bandwidth and the average event size, the current accepted L0 trigger rate must not exceed 1 MHz [55]. This overall rate should include the main data stream for the $K^+ \to \pi^+\nu\bar{\nu}$ analysis, but also secondary triggers for control samples and different physics goals, such as the search for other rare or forbidden decays of the K^+ [56] and the π^0 (see chapter 5). Hence the L0 should possibly reduce the background by a factor greater than 20.
In this chapter a L0 trigger scheme for the selection of the $K^+ \to \pi^+\nu\bar{\nu}$ is simulated and studied, making use of the subdetectors which are expected to have L0 trigger primitive firmware ready for use during the first phase of the data taking starting in fall 2014. The focus is on the effect of the variation of crucial parameters on the signal trigger efficiency and the total trigger rate, which leads to a set of optimized values.
After a description of the software used in section 4.2, the L0 trigger primitives generation simulation is presented in section 4.3.1; section 4.4 shows how the rates and the efficiency

are computed and their values for every parameter under study; in sections 4.5 the generation of muon halo and beam pions as accidentals is described; final results are presented in section 4.7 which summarizes the total L0 trigger output rate and the trigger efficiency of the designed trigger chain.

4.2 Simulation

4.2.1 Generated samples

The NA62MC software [57] has been used to generate kaon decays and halo events needed for the study.

A first production with the software version (rev.) 301 not including the generation of accidentals was made with 100k events generated for each of the 6 main K^+ decays modes covering the 99.98% of the kaon's BR, later referred to as $K_{2\pi}$, $K_{3\pi}$, $K^{00}_{3\pi}$, $K_{\mu 2}$, $K_{\mu 3}$, K_{e3}. Each sample is made of events in which the kaon is forced to decay in the region between the GTK3 ($z = 102.4\,\text{m}$) and $z = 300\,\text{m}$. For signal efficiency evaluation 100k $\pi\nu\bar{\nu}$ events were generated, with the kaon forced to decay between $z = 104\,\text{m}$ and $z = 180\,\text{m}$. In addition to these, 5 classes of beam halo events have been taken into account: beam pions (π^+) and muons generated "upstream", i.e. originating in the decay of beam kaons and pions before the GTK3 plane, coming from 4 different sources (μ_{K^+}, μ_{π^+}, μ_{K^-}, μ_{π^-}, where μ_{K^+} stands for positive muons originating from K decays, etc.). The beam protons component has not been considered in this study.

NA62MC makes use of the TURTLE program [58] for the propagation of beam particles along the beam line (from particle generation at the position of the production target $z = 0\,\text{m}$ to the beginning of CEDAR region at $z = 69.165\,\text{m}$), then GEANT4 [59] simulates the propagation along the downstream region up to $z = 300\,\text{m}$ and the interactions of all particles with detectors.

Halo events are obtained from the HALO program [60] providing muons' and beam pions' position and momentum at GTK3 as input files [61] for GEANT4. These samples have a fixed number of events, being equal to the expected rate in kHz of each component: 526562 beam pions, 99144 μ_{π^+}, 21375 μ_{π^-}, 11792 μ_{K^+}, 3035 μ_{K^-}.

A second production (rev. 314) was used for the generation of accidental events to be superimposed on 10k "central" events of the above mentioned 6 main kaon decays and $\pi\nu\bar{\nu}$: accidental kaon decays are simulated over a window of $\pm 150\,\text{ns}$ around the central decay (figure 4.1b).

This second set of samples has been obtained with some changes in the generator of NA62MC. Additional beam kaons are produced with a generation time given by the exponential distribution of times between two consecutive beam particles. The rate at generation point (beginning of the CEDAR) is 50 MHz, thus resulting in 15 superimposed

kaons in average in the whole time window (figure 4.1a). Differently from the kaon in the "central" event, which is forced to a defined decay mode, accidental beam particles are allowed to decay according to their Branching Ratio and are not forced to decay in any specific region.
A third production (rev. 342 with some changes) introducing the generation of accidentals with halo particles has been used after the L0 study for a correct computation of the absolute values of the L0 trigger efficiency and output rate. A detailed description can be found in section 4.5.

4.2.2 Reconstruction

The software NA62Reconstruction [57] (rev. 315) simulates the digitization of signals coming from NA62MC hits in subdetectors, and subsequently performs the reconstruction of events in the detector. This step has been applied because the output of the digitization is expected to reproduce the data we find at hardware level after each detector's front end, which will be the basis for trigger primitives generation (section 4.3.1).
Following is the list of subdetectors used for this analysis and the description of signals coming from NA62Reconstruction and feeding the trigger primitives production:

- **RICH**: after applying the quantum efficiency of the photocathodes, PM signals are digitized simulating the response of a TDC, obtaining a pair of leading and trailing times with a precision of about 100 ps [62] (1/256 of the 40.079 MHz clock period) and a single channel resolution below 300 ps.
- **CHOD**: the used revision doesn't include the digitization, so a custom algorithm has been applied on MC hits. An energy deposit of at least 1 MeV in a single scintillator is required to produce leading and trailing times; Time over Threshold (ToT) information is generated from a Gaussian distribution with fixed mean (25 ns) and standard deviation (1 ns); a fixed dead time (10 ns) after each hit has been simulated too. The single channel time resolution used for this custom digitization is equal to 500 ps.
- **MUV3**: the used digitization reproduces the time evolution of signals and simulates the response of the mean timer and the TDC; each hit results in two pairs of leading and trailing times as coming from the two PMs of each scintillator pad [63]. The single channel time resolution is about 200 ps.
- **LKr**: the energy deposition in each cell is digitized simulating the response of a 40 MHz flash ADC. The energy value is reconstructed from the ADC counts using a

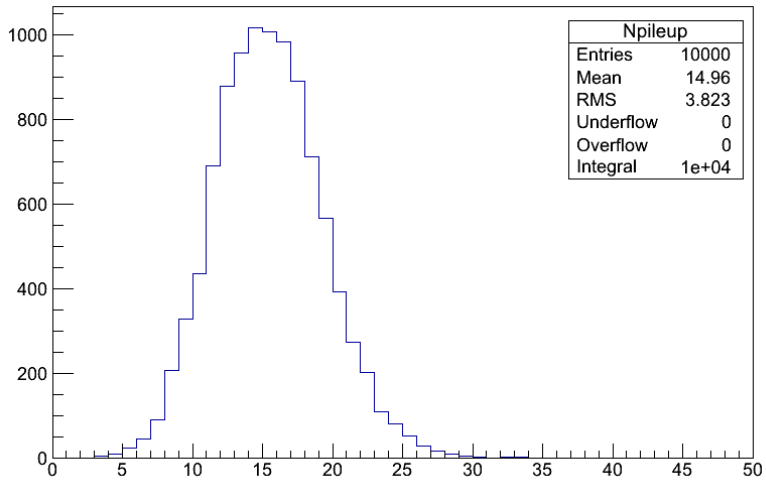

(a) Distribution of the number of pile up kaons per event

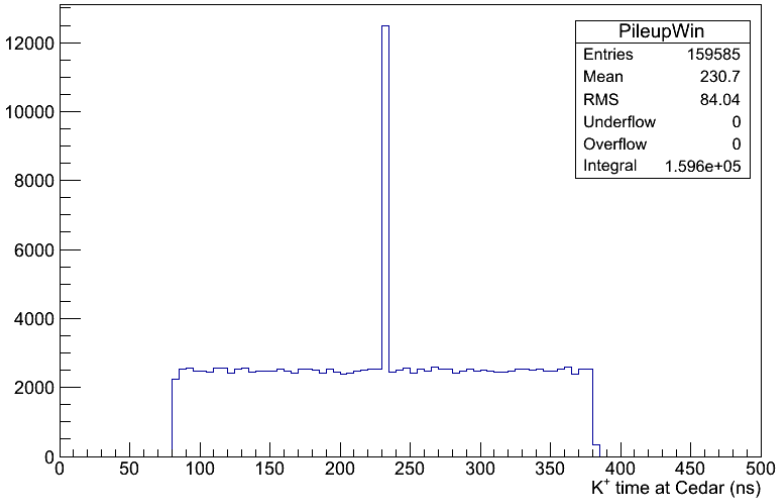

(b) Time distribution of the events in the pile up time window

Figure 4.1: Poissonian distribution of the number of generated beam kaons (a) in a $\pm 150\,\mathrm{ns}$ time window around the central event corresponding to the peak (b). The zero reference time is taken at the target at $z = 0\,\mathrm{m}$, and the peak value is the time of flight from the target to the beginning of the CEDAR region at $z = 69.165\,\mathrm{m}$.

digital filter method [64]. For this study the time of the hit is the true time inherited from NA62MC hits.

- **LAV**: the software includes a full digitization simulating the output of the LAV FE modules, with low threshold and high threshold (if the case) leading and trailing edges [65]. The used default values are 6 mV for low and 39 mV for high threshold. The raw (without slewing correction) single channel time resolution is of the order of 2 ns.

4.2.3 L0 simulation

The NA62Analysis framework [57] (rev. 319) has been used for the L0 simulation. A unique analyzer routine encloses the algorithms for the generation of primitives for events satisfying a set of conditions, reproducing the firmware at hardware level, together with the simulation of the L0TP performing the time matching of received primitives.
The following section describes the required conditions for each subdetector, and the parameters on which the simulated L0 trigger depends.

4.3 L0 trigger

4.3.1 Primitives

RICH

The production of primitives for the RICH detector is based only on the multiplicity of leading times coming from all the 1952 PMTs. All leading times for an event are partitioned in several time bins of equal adjustable width, in order to count for the hits multiplicity of each bin, thus generating an histogram whose bin contents are the multiplicities of each time interval. Edge effects, for which two hits arbitrarily close in time could belong to adjacent bins, are not taken into account in the generation of primitives.
A maximum of one primitive is generated out of each time bin if the multiplicity satisfies the condition to be between a low and a high threshold value. The time of the primitive is obtained as the average time of all hits in the time bin.
In figure 4.2 a detail of RICH hit leading times and primitive times is shown: as expected for an average value the distribution for primitives is narrower and shows a resolution of about 100 ps.

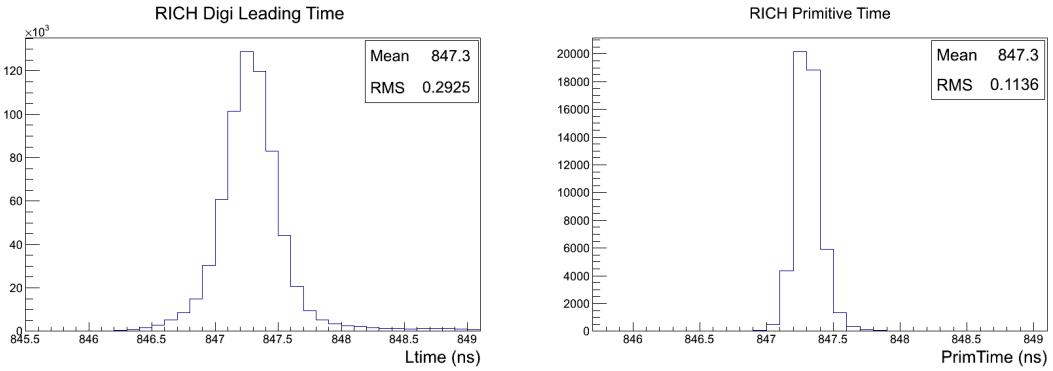

(a) (b)

Figure 4.2: Distribution of leading times (a) and primitive times (b) for events occurring always at the same time.

NA48 CHOD

Leading times from the NA48 CHOD custom digitization are first divided between the two planes of the detector, then all analysed pairwise to search for coincidences in space and time.

There is a coincidence in space if the channels belong to the same quadrants of the horizontal and vertical planes.

The condition on the time coincidence has been deduced from the distribution of time differences between hits in two planes (figure 4.3). The plot refers to the "cleanest" events ($K_{\mu 2}$) requiring only 2 hits in the CHOD, one on each plane. The chosen interval defining a time coincidence is $-0.9\,\text{ns} < \Delta t_{12} < 3.3\,\text{ns}$, corresponding to 3 times the RMS of the observed time difference distribution.

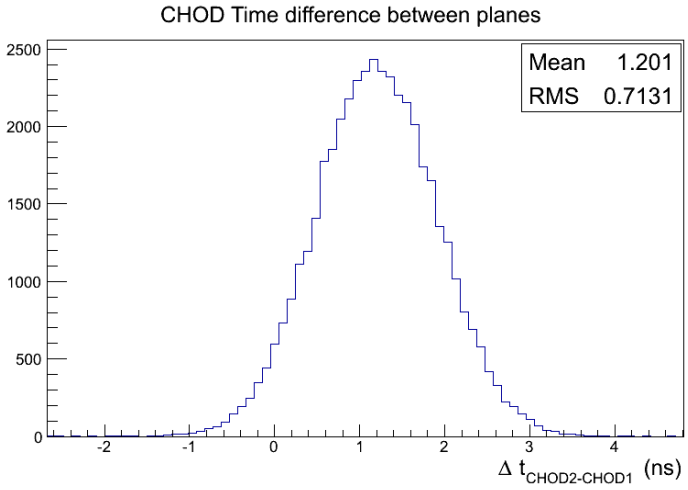

Figure 4.3: Distribution of hit time differences between two CHOD planes

Coincidences within the same time interval are then grouped into the same primitive. The information on hits multiplicity and quadrants multiplicity is also stored. This is a "maximum" multiplicity: a blind sum of crossing points is performed at this level, so that two slabs firing in the first plane and two other slabs firing in the correspondent quadrant of the second plane correspond to a multiplicity of four. As for the RICH, the primitive time is the average time of all coincidences in the same time interval (each coincidence is assigned the time of the hit on the first CHOD plane).
For the primitive to be sent to the L0TP, both the hit and the quadrant multiplicities have to be below an adjustable maximum value. The use of a cut in CHOD multiplicity can be explained through figure 4.4 showing the CHOD primitive multiplicity as a function of the pion interaction point, for $\pi\nu\nu$ events satisfying the signal conditions (see section 4.4). The multiplicity is 1 in most cases as expected, and it's greater in some other events like backsplashes from LKr (multiplicity below 5) or pion interacting in RICH flanges and mirror and in the CHOD itself (multiplicity up to 50, about 1% of the events).

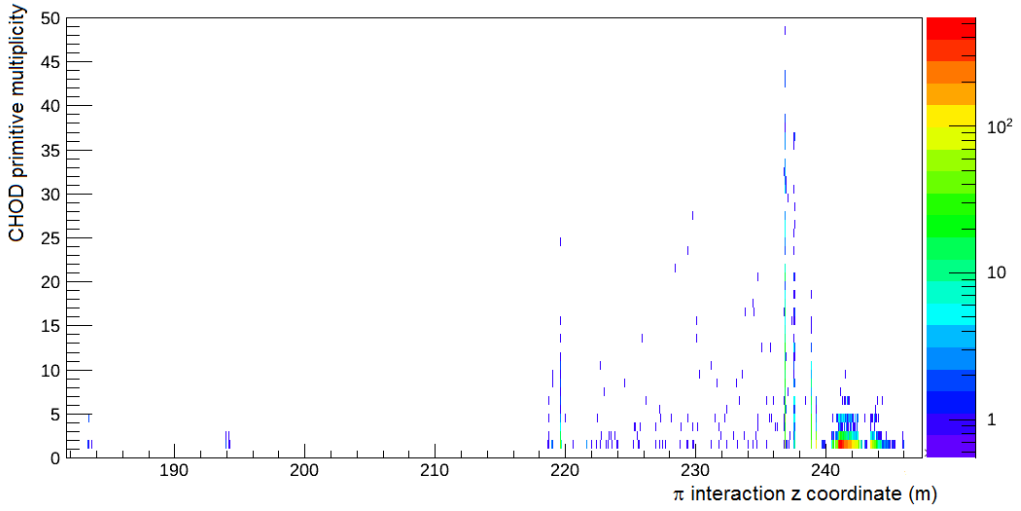

Figure 4.4: CHOD primitive hit multiplicity as a function of the pion interaction point, for signal events. The main vertical bands correspond respectively to RICH initial flange, RICH mirror, RICH final flange, CHOD planes, from left to right; the bump at the right end corresponds to pions interacting in LKr and MUV1.

MUV3

MUV3 primitive generation is based on leading hit times from both PMs belonging to the same scintillator pad. A time coincidence is required to build the primitive.
Like the case of the CHOD, the distribution of PMs time difference in the same pad (figure 4.5) drives the choice of a ± 0.4 ns coincidence time window. This distribution was obtained from $K_{\mu 2}$ events.

Coincidences from different pads within ±0.4 ns are then merged into the same primitive which is always sent to the L0TP, no matter what the multiplicity value is.

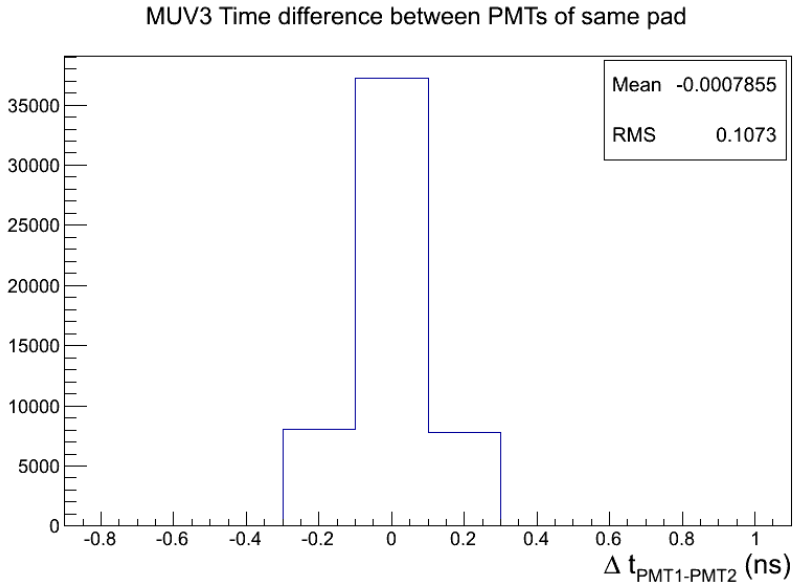

Figure 4.5: Distribution of differences between hit times of two PMs of the same MUV3 pad for $K_{\mu 2}$ events.

LKr

The described algorithm simulates what is done at hardware level, although implementations are deeply different [66] [67]. The main reason is the fact that the FADC-like 25 ns sampling is used on each single calorimeter cell to find cell's peak times and energies. The readout of the LKr instead will provide to the LKr L0 trigger system the ADC sampling of 4x4 SuperCells (SC), thus resulting in SuperCells' peak times and energies.
The time of cells above a certain energy threshold is evaluated to separate hits in several time bins of adjustable width; hits in the same time bin and belonging to the same 4x4 SC consequently form a SC hit, whose time is the energy weighted mean of the single cells' times, and whose energy is the sum of the cell energies.
From this point on the simulation matches the hardware. SC hits with energy above an adjustable threshold and adjacent in space and time are merged into clusters, keeping time and position informations as energy weighted mean of constituent SCs.
The clustering efficiency of this algorithm is showed in figure 4.6 together with its space resolution, for pion and photon clusters from $K_{\pi 2}$ events.
The LKr L0 primitive is then built requiring two or more clusters in time: the purpose is in fact to reject $K_{\pi 2}$, $K_{\pi 3}^{00}$, K_{e3}, $K_{\mu 3}$ events against signal which can have at most one cluster. Once again the primitive time is the energy-weighted average of the times of the

event clusters. The time resolution of the LKr L0 primitives is 1 ns.

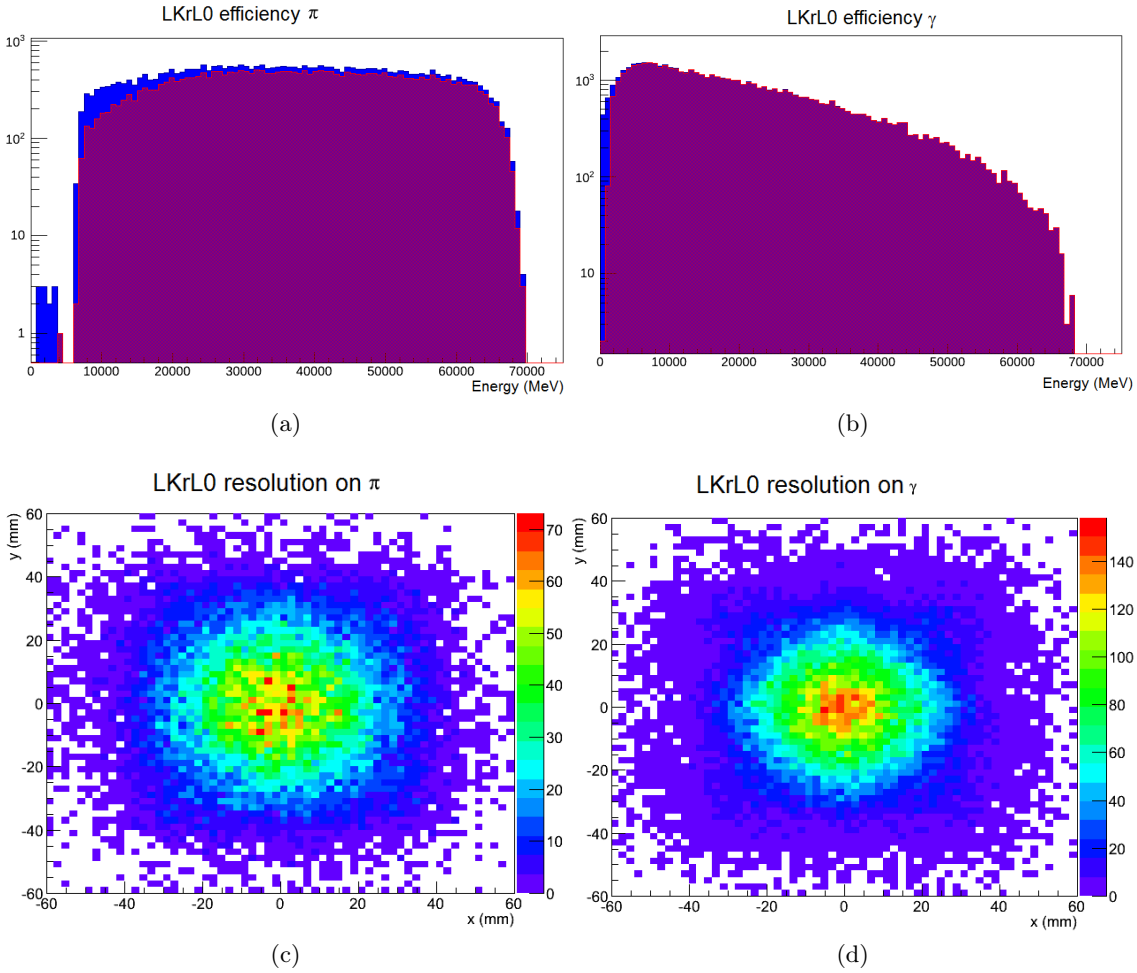

Figure 4.6: Energy distributions of generated (blue) and reconstructed (shaded red) pion clusters (a) and photon clusters (b), from the ratio of which the energy-dependent efficiencies of the LKr L0 clustering algorithm can be obtained. Distributions of differences between generated and reconstructed spatial positions of pion clusters (c) and photon clusters(d), which indicate the spatial resolution of the LKr L0 clustering algorithm. The distributions refer to $K_{\pi 2}$ events.

LAV

For this study only the last station (12) of LAVs has been used, as will be the case in the 2014 run.

The presence of both high and low threshold leading times is required, otherwise the hit is discarded. This is due to the fact that a slewing correction is mandatory to achieve an adequate time resolution of the primitive.

The slewing correction is performed using a linear approximation of the rising edge of the pulse and knowing the threshold values (LAV section in 4.2.2):

$$t_c = t_l - \frac{(t_h - t_l)V_l}{V_h - V_l}$$

where t_c is the corrected time, t_h and t_l are respectively the high and low threshold leading times, V_h and V_l the corresponding threshold values. The effect of this correction can be seen in figure 4.7.
Time offsets between 4 layers of the LAV12 station have been taken into account: for details see section 4.3.3.
For the primitive production, all corrected times from different channels are combined if within ± 0.5 ns; multiplicity is not considered. The obtained time resolution of the LAV primitives is 1 ns.
A detailed description of the hardware counterpart can be found in [54].

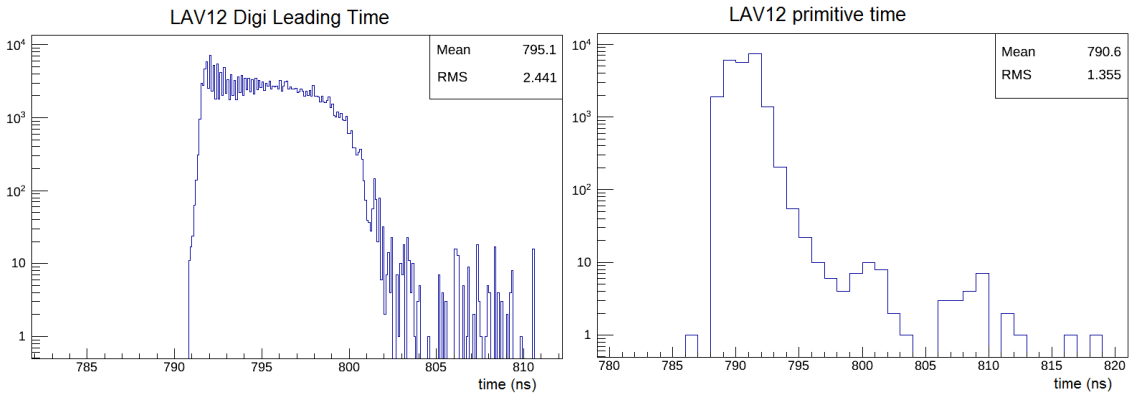

(a) (b)

Figure 4.7: Time distributions of high threshold leading times (a) and slewing corrected times (b) on LAV12 for $K_{\pi 2}$ events.

4.3.2 Parameters

In the above section not all the parameters entering the definition of the primitives were assigned a value. Rather they are variables on which rates and signal efficiency can depend. Following is the list of parameters under study divided by subdetector.

- RICH
  - Width of the time binning for multiplicity counting
  - Low multiplicity threshold

  - High multiplicity threshold

- CHOD
  - Width of the time binning for multiplicity counting
  - Maximum hit multiplicity
  - Maximum quadrant multiplicity

- LKr
  - Width of the time binning for cell hits
  - SCs and clusters matching time
  - Cell energy threshold
  - SC energy threshold

- L0TP
  - Primitive matching time

For what concerns the LKr, the first listed parameter doesn't exist in hardware: it is rather a way to study the systematic error that the LKr L0 simulation could introduce with respect to its hardware counterpart.
The L0TP matching time is discussed in section 4.3.3. The same value is used for the matching of all subdetectors primitives in this simulation, as is in the current implementation of the L0TP firmware [68].

4.3.3 L0TP simulation

The L0TP simulation algorithm has the task to match all the primitives coming from the detectors, as described in 4.3.1.
The L0TP doesn't evaluate complex trigger conditions, it just performs the time matching of primitives corresponding to same trigger words, following a scheme that implements several trigger conditions for different purposes.

Time alignment

A time alignment of all the subdetectors with the reference one is essential for the L0TP to be efficient, in the simulation as well as for the data taking.
In this study the RICH is considered as the reference subdetector: it enters as positive element in the main trigger chain and it has the best time resolution among L0 subdetectors.

The only required condition on RICH hits is that they must all be within 1 ns, to avoid introducing effects due to the reference detector time resolution in the time alignment.
$K_{\mu 2}$ events have been considered to study the time alignment of RICH with both CHOD and MUV3.
Concerning the CHOD, events with exactly 2 hits, one in each plane, have been selected for time alignment studies. Distributions are shown in figure 4.8: the widths reflect the resolution used for the digitization of CHOD, the difference between the mean values matches the time difference between planes as in figure 4.3. The chosen offset value is 50.4 ns (it refers to the first plane (a), which is the one used as reference time of CHOD primitives).

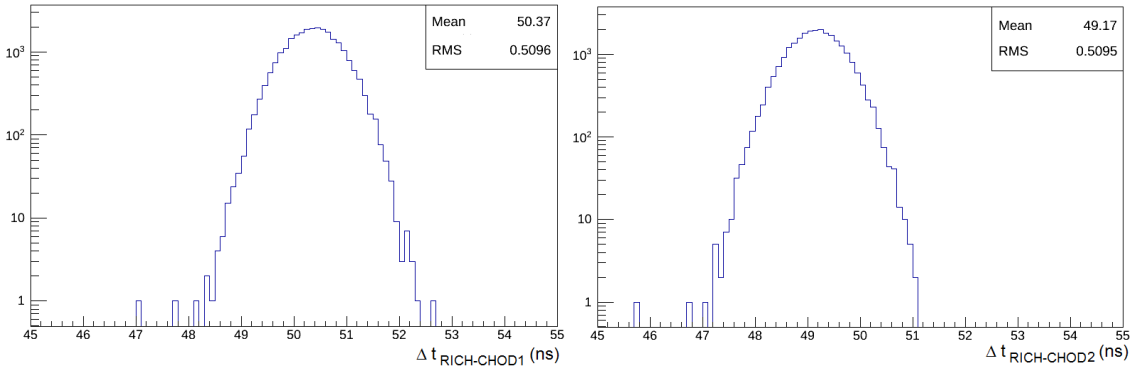

(a) (b)

Figure 4.8: Hit time difference distributions between RICH and CHOD plane 1 (a) and 2 (b). The positive sign of this difference is due to the fact that Čerenkov photons have to go back from the mirror to PMs, so that RICH hit times are greater even if the detector is placed upstream with respect to CHOD.

For MUV3 alignment a similar condition was applied requiring exactly 2 hits, one for each PM of the same pad. Figure 4.9 shows the time difference distribution. The used offset value is −96.2 ns, applied to the MUV3 trigger primitive time. The negative value indicates that the absolute time of MUV3 is greater than RICH.

$K_{\pi 2}$ events have been considered to study the time alignment of RICH with LKr and LAV. No selection has been applied over these events for LKr: the time distribution of all obtained cluster times is shown in figure 4.10. The large tail in the time difference distribution can be interpreted as due to additional clusters late in time. An offset of 42.1 ns was used, as obtained from the peak.

There is no event selection for the LAV alignment study: times in the distributions of figure 4.11 are slewing corrected and separated among the four station layers. The evidence of the peak gets worse for the downstream layers, due to less hits and mainly to the time

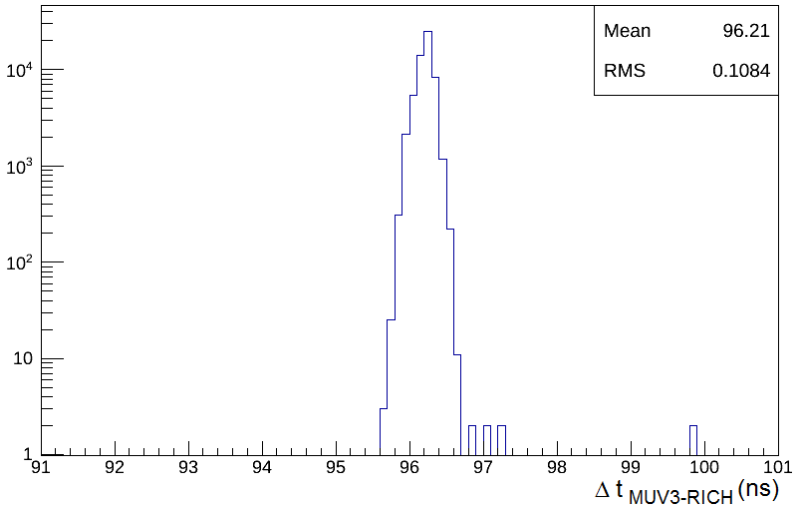

Figure 4.9: Hit time difference distribution between MUV3 and RICH.

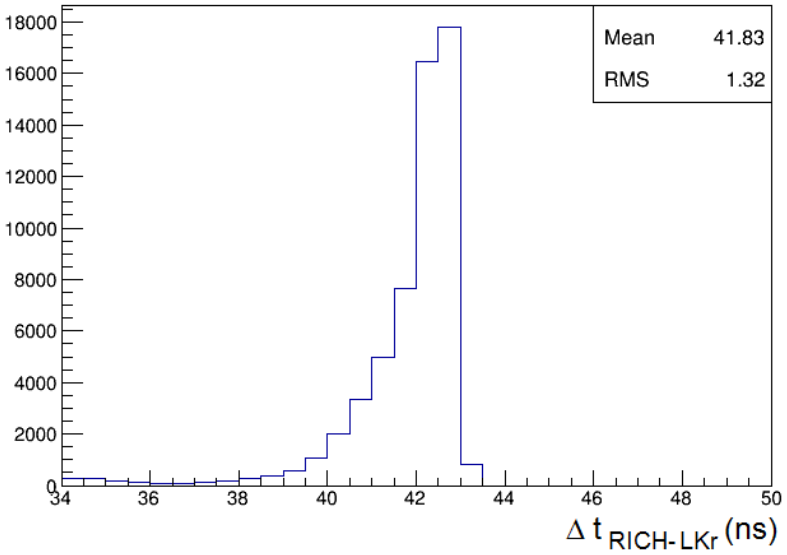

Figure 4.10: Time difference distribution between RICH and LKr clusters.

evolution of interactions inside LAV detectors. It is still possible to perform a peak fit, resulting in 58.2 ns for the first layer; relative offsets of other layers with respect to the first one are evaluated as 0.3 ns, 0.75 ns and 1.2 ns.

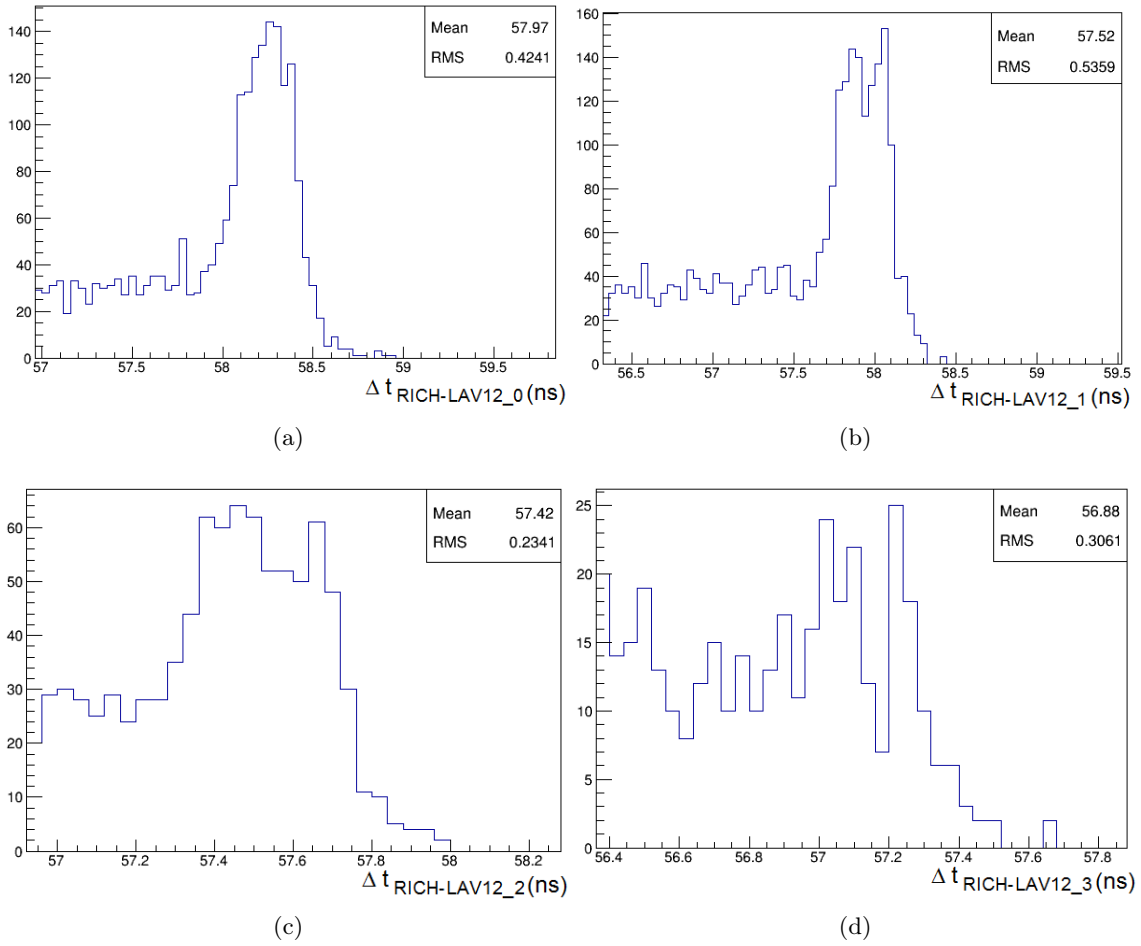

Figure 4.11: Hit time difference distributions between RICH and LAV12 for layers 0-3 (a-d).

4.4 L0 analysis

This study aims at the assessment of the L0 trigger rate for the $K^+ \to \pi^+\nu\bar{\nu}$ trigger chain described in section 4.3 and the trigger efficiency for selecting this channel, as obtained by varying the parameters under investigation presented in 4.3.2.

The total L0 trigger rate R is computed by summing the individual rates r_i of all the

processes (decay channels, muon halo, beam pions) under study:

$$R = \sum_i r_i, \quad r_i = \mathcal{R}_i f_i$$

where $\mathcal{R}_i$ is the total generated rate of the i-th process and works as normalization factor for the simulation, and f_i is the fraction of events belonging to the i-th process in the simulation which passes the L0 trigger conditions and produces a L0 signal.
The normalization factor for K^+ decay processes is derived from the known total kaon rate, 45 MHz at GTK3, the Branching Ratio of each channel, and the probability that the kaon decays in the region of interest for the simulation:

$$\mathcal{R}_i = 45\,\text{MHz} \times \text{BR}_i \times (1 - e^{\frac{\Delta z}{\gamma c \tau}})$$

In this simulation generated kaons are forced to decay between GTK3 ($z = 102.4\,\text{m}$) and $z = 300\,\text{m}$ which represents the longitudinal end of the simulated space, so $\Delta z = 197.6\,\text{m}$. Furthermore for K^+ at $75\,\text{GeV}/c$ we have $\gamma c\tau \simeq 564\,\text{m}$.
The normalization rates for each channel are listed in table 4.1, together with muon halo and beam pion rates.

Process	Rate $\mathcal{R}_i$ (kHz)
$K_{\mu 2}$	8452
$K_{\mu 3}$	446
K_{e3}	674
$K_{\pi 2}$	2748
$K_{\pi 3}$	743
$K_{\pi 3}^{00}$	234
μ_{π^+}	99144
μ_{K^+}	11792
μ_{π^-}	21375
μ_{K^-}	3035
π^+	526562

Table 4.1: Normalization rates $\mathcal{R}_i$ for each process involved in the simulation

The trigger efficiency is evaluated as the fraction of $K^+ \to \pi^+\nu\bar{\nu}$ events passing the L0 trigger conditions among those passing the analysis selection requirements.
The following preliminary conditions characterize the sample for trigger efficiency study:

- Pion momentum between $15\,\text{GeV}/c$ and $35\,\text{GeV}/c$
- Longitudinal position of kaon decay within the fiducial region between 105 m and

165 m

- Squared missing mass in region I ($0 < m^2_{\text{miss}}[\text{GeV}^2/c^4] < 0.01$) or region II ($0.026 < m^2_{\text{miss}}[\text{GeV}^2/c^4] < 0.068$)
- Pion in the CHOD acceptance
- Pion in the MUV3 acceptance
- Pion not in the LAVs acceptance
- No pion decay before LKr

The kinematic quantities entering these conditions are the generated ones, as obtained from NA62MC.
The remaining sample for the case without accidentals has 10624 events over the 100k generated; the sample with accidentals has instead 1048 events over 10k generated. This reduction to about 10% is in part due to the cut over the longitudinal position of the decay vertex, as the generated $\pi\nu\bar{\nu}$ events have a vertex between 104 and 180 m.

The analysis strategy is based on a starting set of values assigned to the L0 trigger parameters, as shown in table 4.2.

RICH time bin	3.125 ns
RICH low threshold	4
RICH high threshold	32
CHOD time bin	1 ns
CHOD max hit multiplicity	∞
CHOD max quadrant multiplicity	∞
LKr cell hit time bin	12.5 ns
LKr SC and cluster time	5 ns
LKr cell threshold	0.1 GeV
LKr SC threshold	0.7 GeV
L0TP matching time	3.125 ns

Table 4.2: Starting values of L0 parameters under study

The RICH time binning has been chosen as the value currently foreseen by the primitive generation firmware of the subdetector; low and high thresholds are the typical values in which the multiplicity distribution of $\pi\nu\bar{\nu}$ events is comprised.
The starting configuration of CHOD requires neither hit multiplicity nor quadrant multiplicity limits; the time binning is of the order of the resolution.
For what concerns the LKr, the software parameter on the cell hit time bin has been chosen

as half the ADC sampling period; the SC and cluster matching time are instead slightly greater than their expected time resolution.
The current design of the L0TP firmware has a matching time of $2 \times 3.125\,\text{ns}$ [68], being the same for all subdetectors, and this is the starting point for this simulation.

A set of simulations varying each parameter has been produced, keeping fixed all other ones to the values in table 4.2.
The scan of time parameters has been performed with time steps obtained by dividing the sampling period of 25 ns by powers of 2: this is the natural and simplest subdivision in the hardware, where all timers are binary counters based on the 40 MHz input clock.
For all parameters the comparison between simulation with and without accidentals is shown and discussed in figures from 4.12 to 4.22.
Reported error bars are statistical errors only. The rates are not to be compared with the final rate because in these figures the parameters are not set to their optimal values.

In figure 4.12 the dependence on the RICH time bin parameter is highlighted. The efficiency slightly diminishes for a tiny time bin of width comparable to the subdetector resolution, when multiplicity in a bin is reduced. On the other hand, for a large time bin, nothing happens as expected for events without accidentals, while both efficiency and rate fall down due to the multiplicity threshold being exceeded when including accidental hits.

There is no big difference between figures 4.13a and 4.13b, apart from the absolute value. In both cases the effect of low multiplicity threshold on the efficiency becomes relevant between the values 4 and 5.

No differences were expected also for the high multiplicity threshold behaviour. What can be observed in figure 4.14 is an effect due to the lack of statistics in the right tail of the multiplicity distribution for the case with accidentals.

For the CHOD time bin width study in figure 4.15, as there is yet no cut on CHOD multiplicity, the only effect on the total trigger rate for large time bins can be explained by delayed hits entering the bin and modifying the time of the primitive, which cannot be matched by L0TP causing the rejection of the event.

When applying CHOD hits multiplicity, the efficiency trend in figure 4.16 follows what can be deduced also from figure 4.4: about 1% of signal events are lost with a cut at 5 hits. The loss is negligible with a cut at 10, while there is still a remarkable rejection on the total rate.

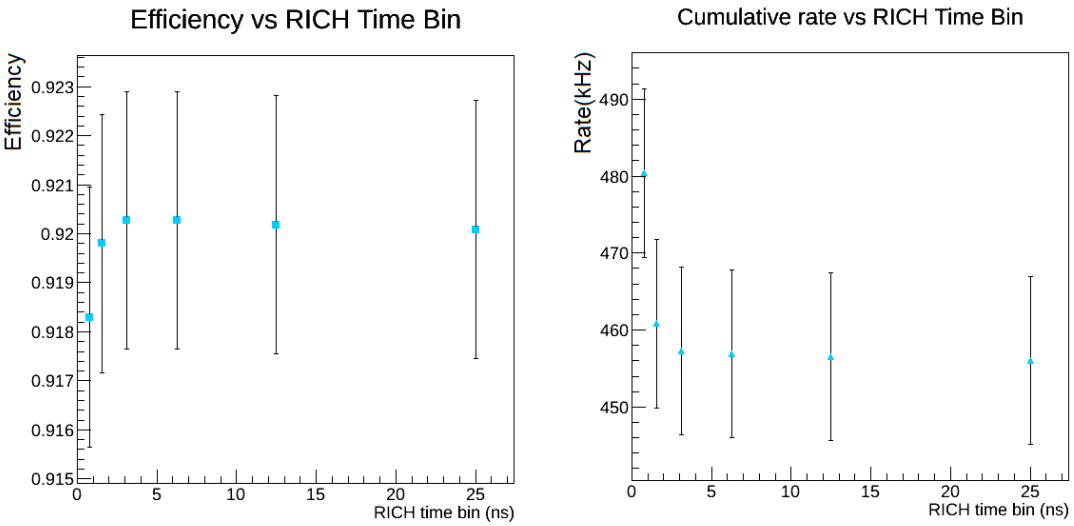

(a) Without accidentals

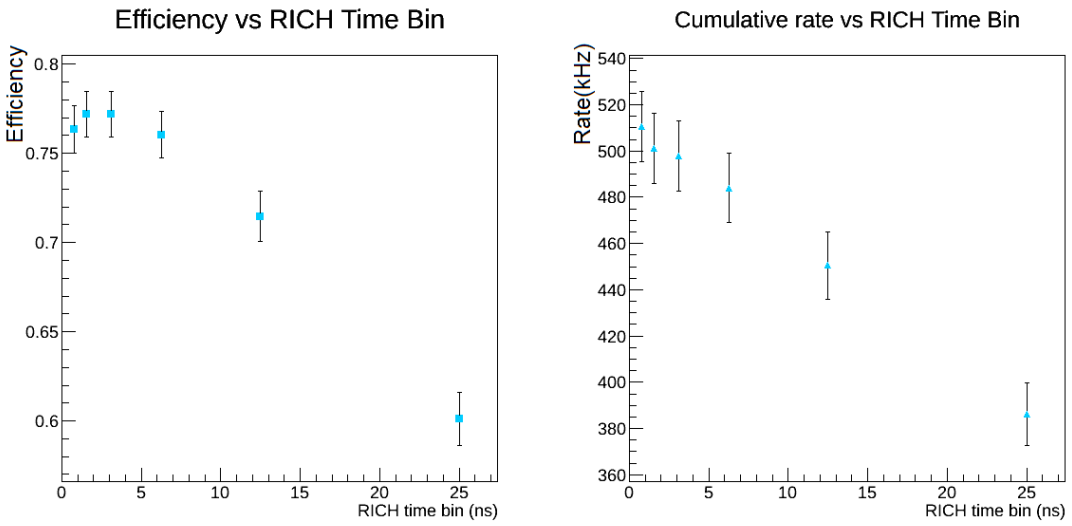

(b) With accidentals

Figure 4.12: Efficiency and rate dependence on RICH time bin width parameter.

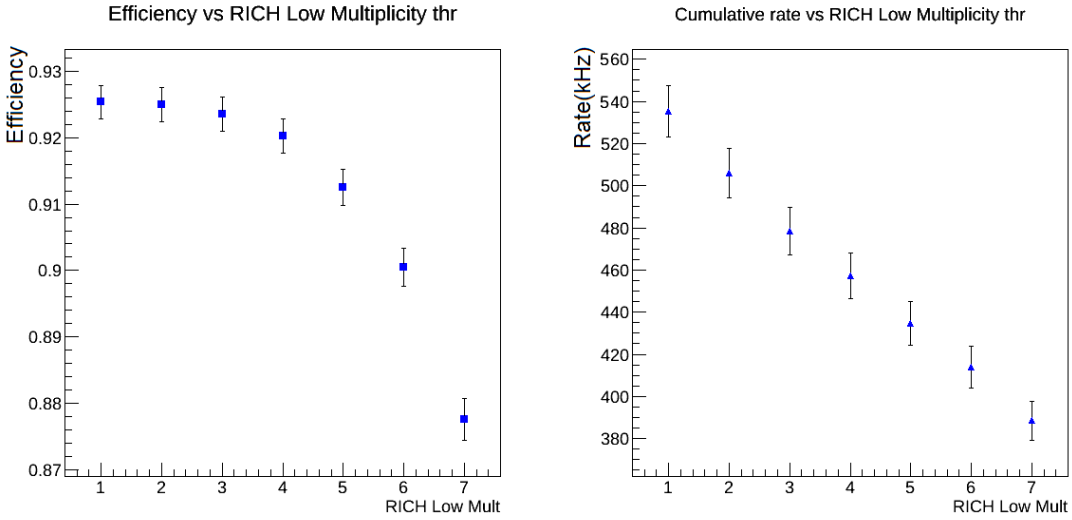

(a) Without accidentals

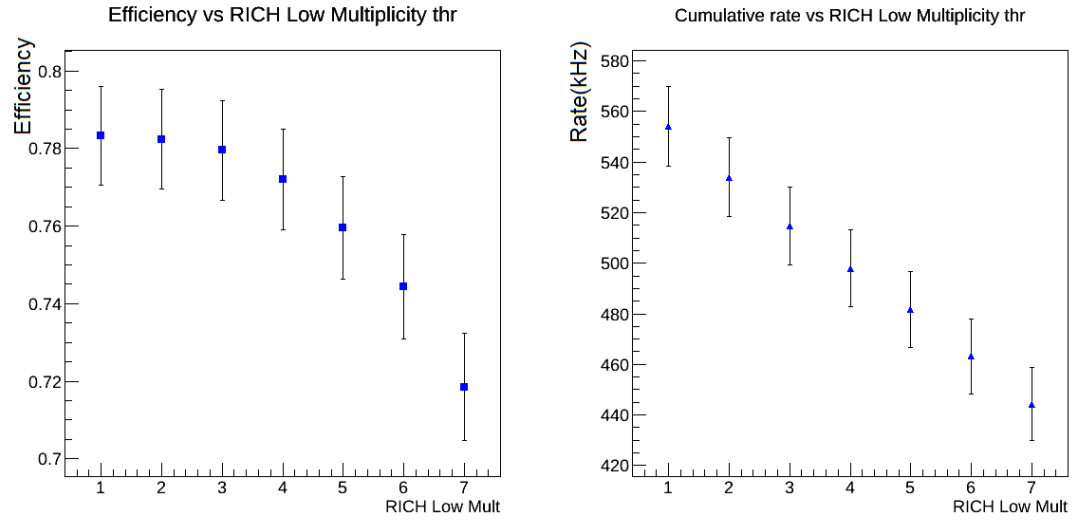

(b) With accidentals

Figure 4.13: Efficiency and rate dependence on RICH low multiplicity threshold parameter.

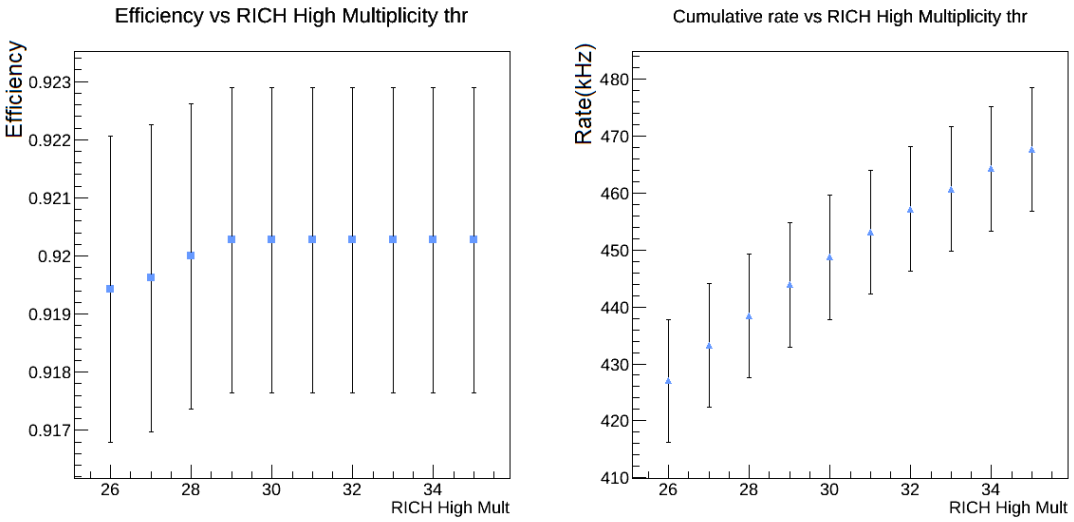

(a) Without accidentals

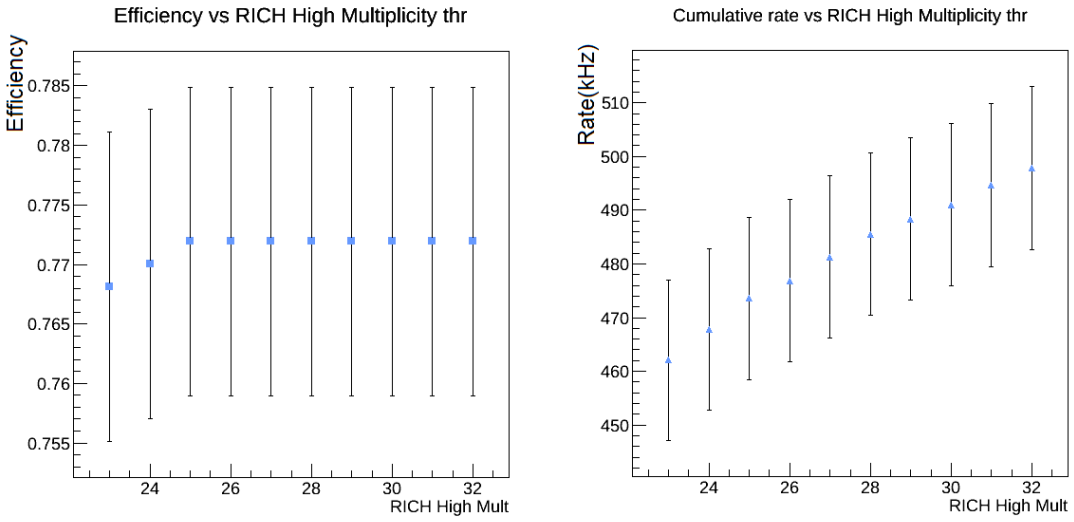

(b) With accidentals

Figure 4.14: Efficiency and rate dependence on RICH high multiplicity threshold parameter.

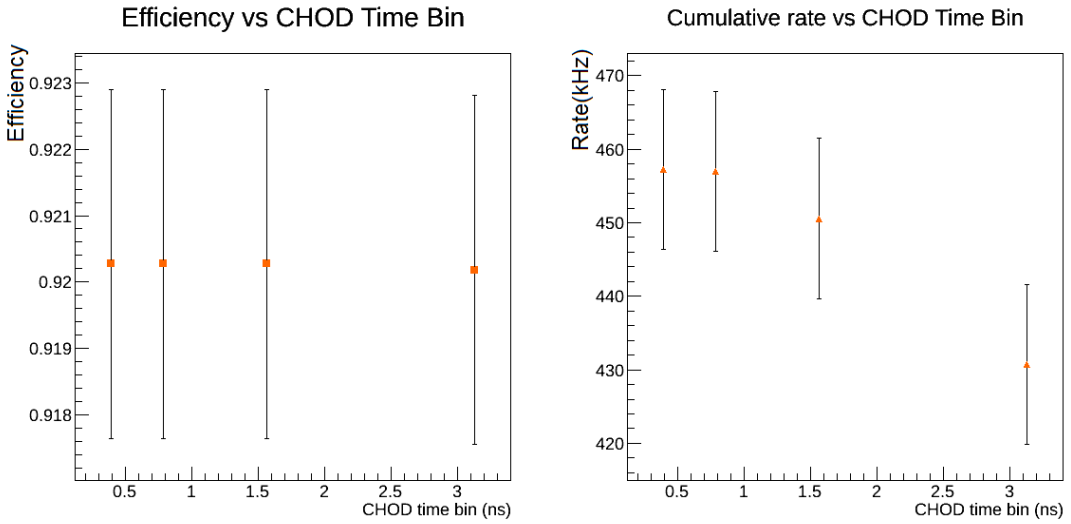

(a) Without accidentals

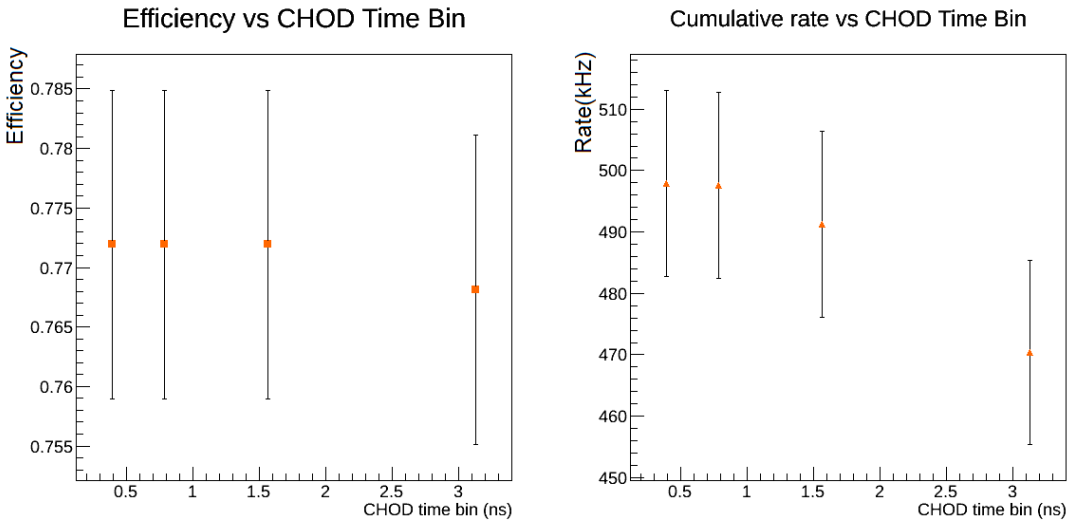

(b) With accidentals

Figure 4.15: Efficiency and rate dependence on CHOD time bin width parameter.

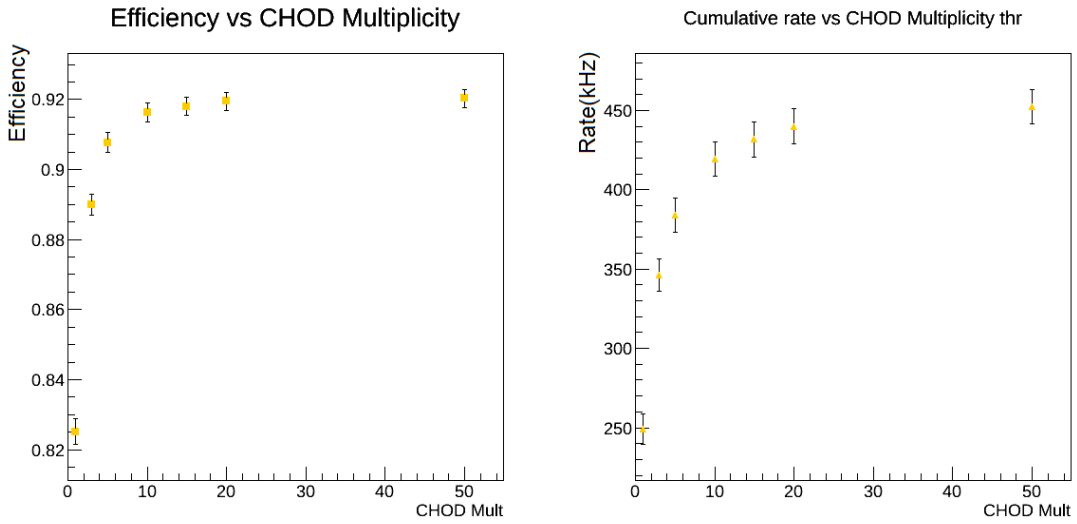

(a) Without accidentals

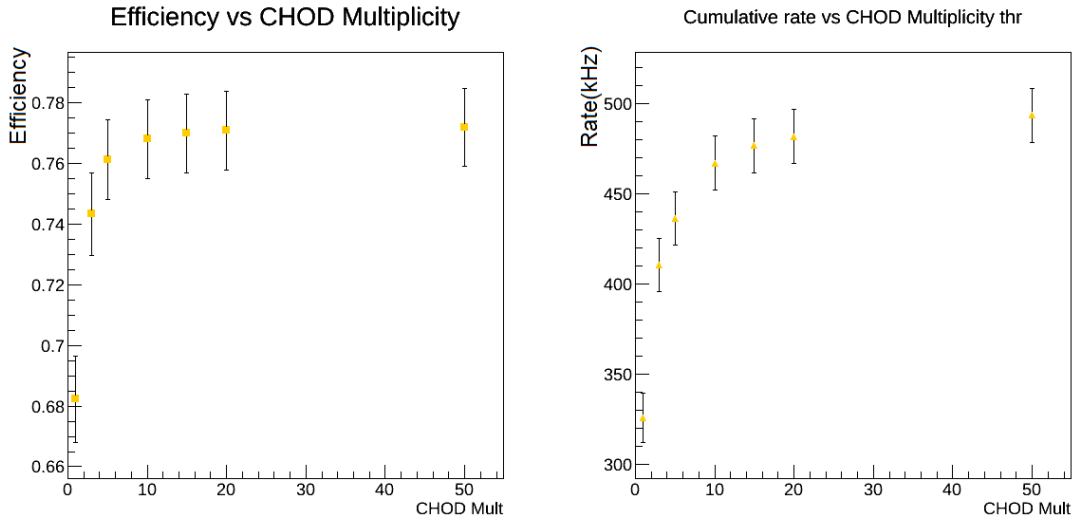

(b) With accidentals

Figure 4.16: Efficiency and rate dependence on CHOD max hit multiplicity threshold parameter.

This request relies upon a good simulation of particle interactions near the region of CHOD. The uncertainty is far from being just the statistical one showed in the plot, and is not evaluated here.

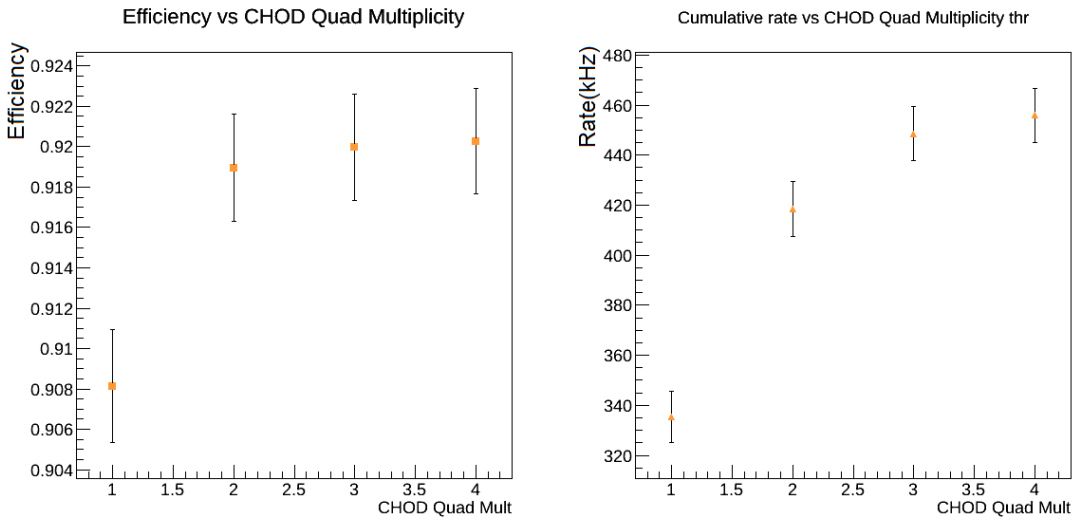

(a) Without accidentals

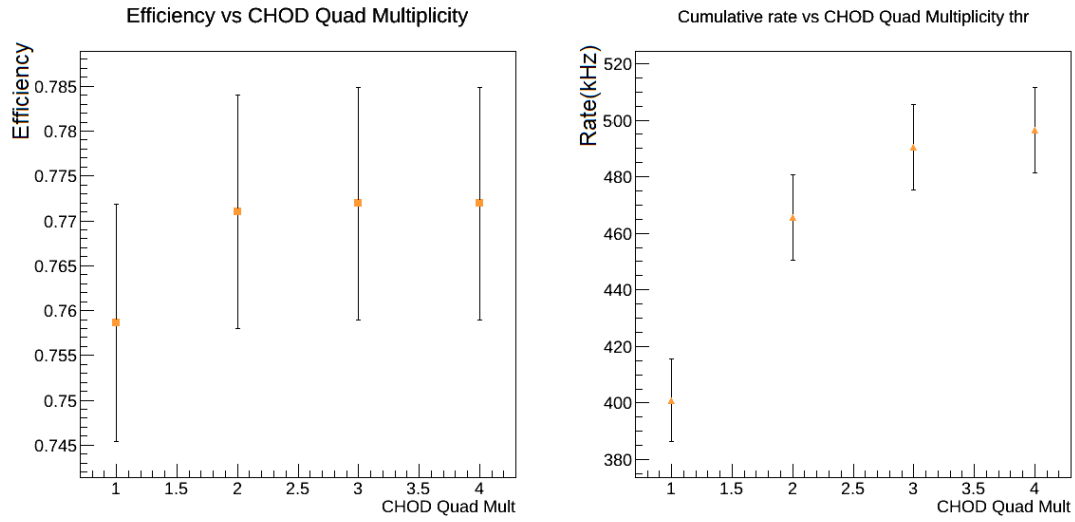

(b) With accidentals

Figure 4.17: Efficiency and rate dependence on CHOD quadrant multiplicity threshold parameter.

A similar behaviour appears in figure 4.17 for what concerns the CHOD quadrant multiplicity. This is mostly related to the spatial distribution of hits, and for signal events it is likely that no more than 2 quadrants fire, leaving rather unaltered the efficiency at this value.

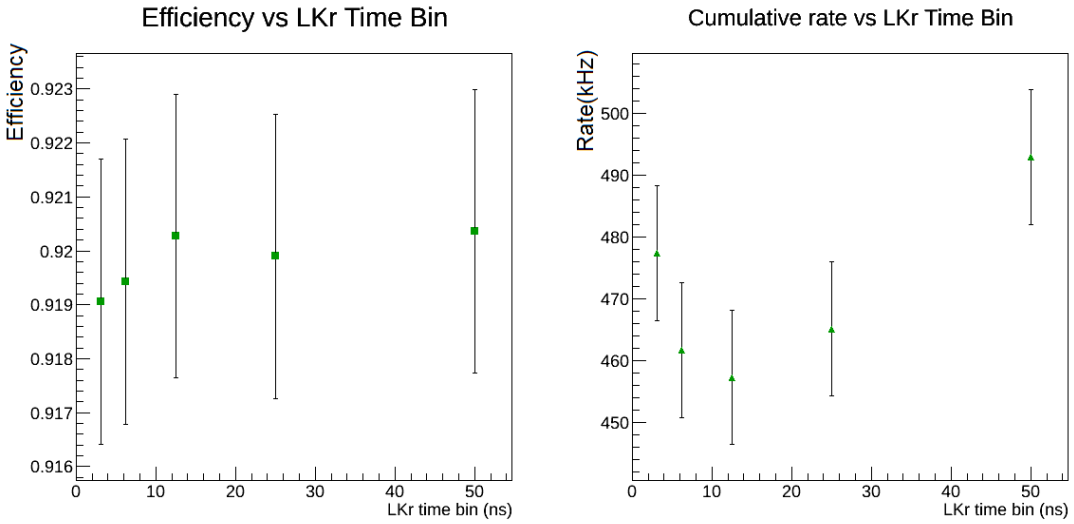

(a) Without accidentals

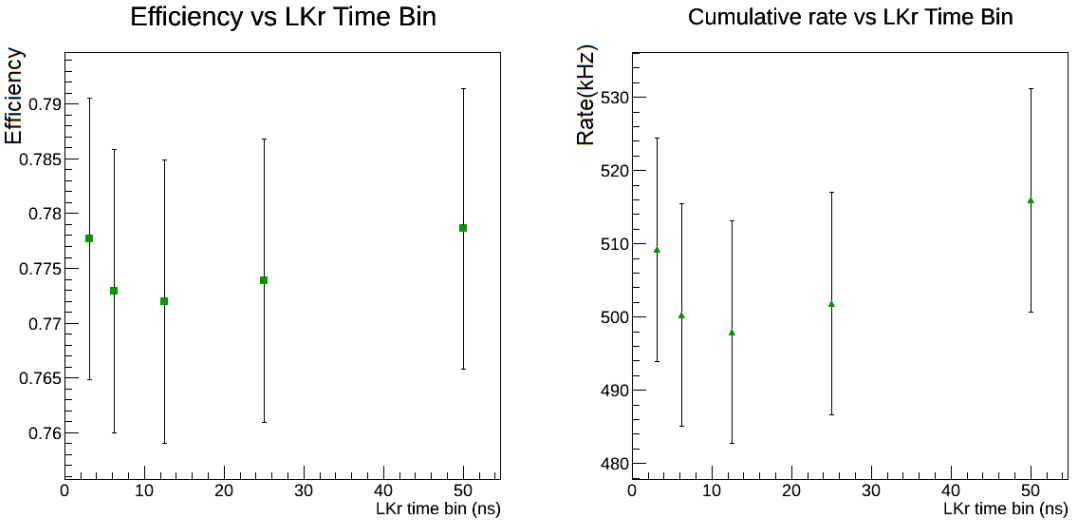

(b) With accidentals

Figure 4.18: Efficiency and rate dependence on LKr cell hit separation time parameter.

For the calorimeter simulation, figure 4.18 shows that, as expected, the time for cell hit separation must be kept of the order of the sampling time of 25 ns. The band between 6.25 ns and 25 ns presents almost no changes in rate and efficiency compared with the uncertainties.

The dependence on the LKr SCs and clusters matching time in figure 4.19 might be surprising for high values of this parameter. This is due to the interplay of two different effects: enlarging this time includes accidental clusters in the same primitive, giving a tiny

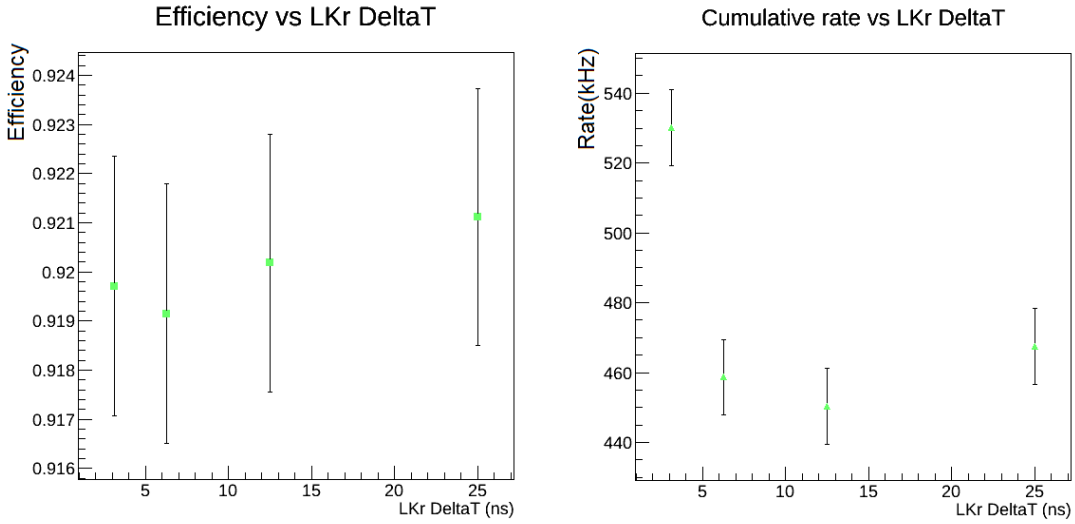

(a) Without accidentals

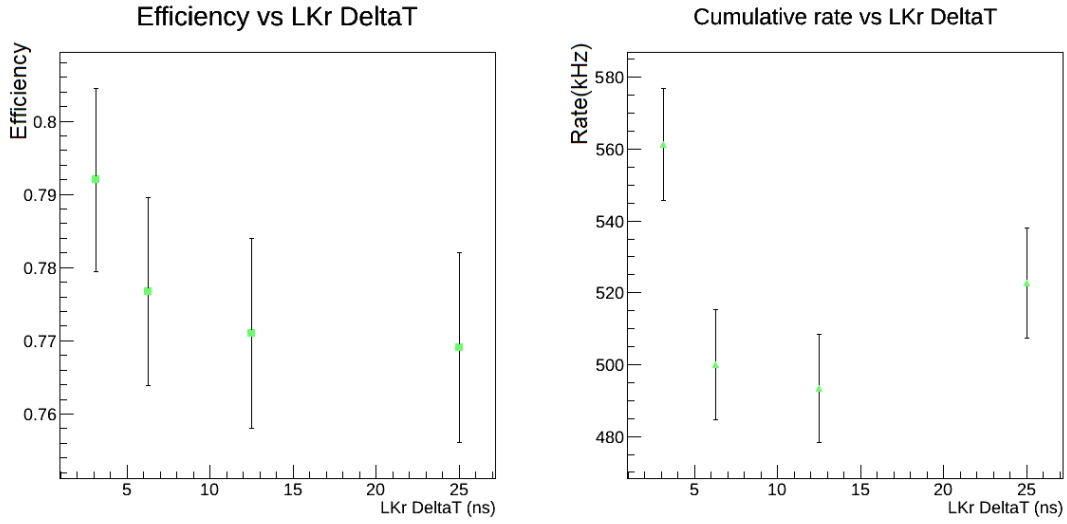

(b) With accidentals

Figure 4.19: Efficiency and rate dependence on LKr SC and cluster matching time parameter.

reduction in the efficiency (left plot of figure 4.19b); but it also modifies the primitive time (average of cluster times), and this parameter becomes very correlated with the L0TP primitive matching time: for high values of the analysed parameter (25 ns in right plots of figure 4.19) the probability that the LKrL0 primitive is not matched in the L0TP is higher and this causes an increase of the output rate since the LKr is a veto detector.

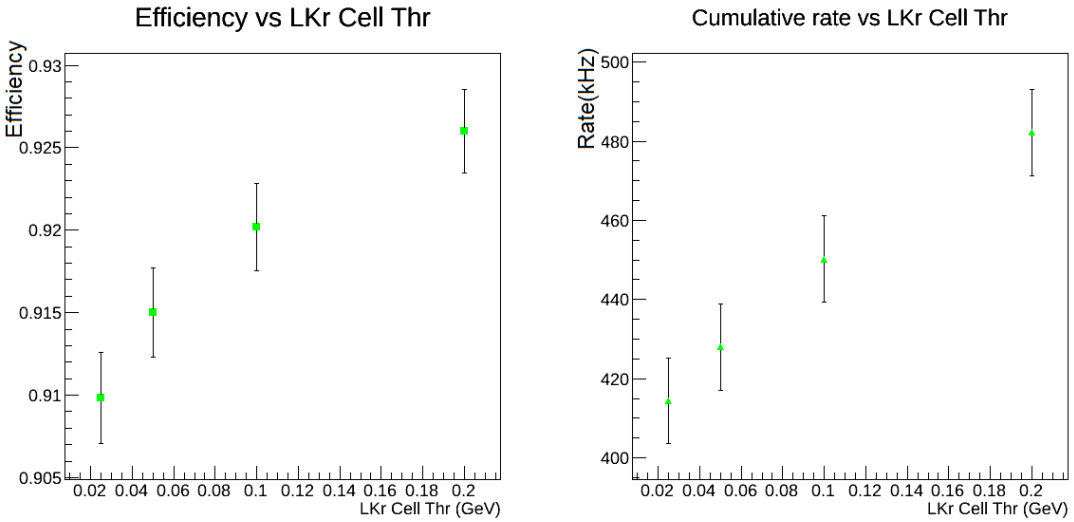

(a) Without accidentals

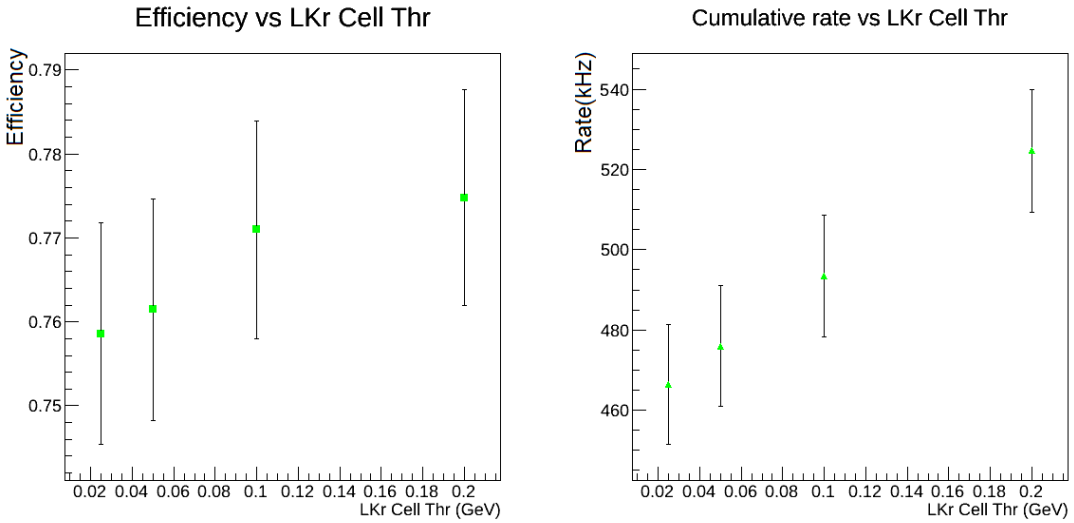

(b) With accidentals

Figure 4.20: Efficiency and rate dependence on LKr cell energy threshold parameter.

In figures 4.20 and 4.21 the rates scale quite linearly with the energy threshold; the efficiency for high thresholds tends to saturation towards the value corresponding to no cut on LKr primitives.

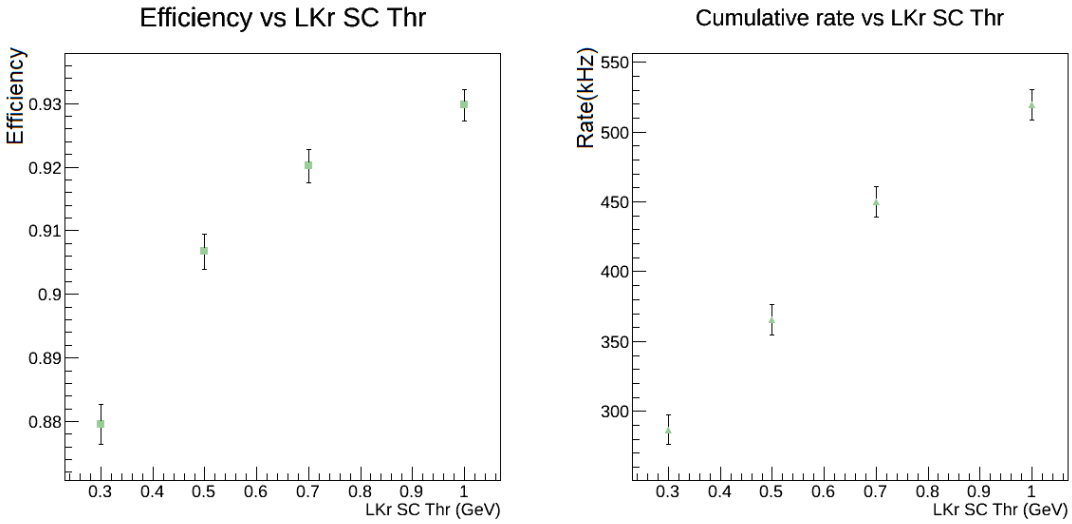

(a) Without accidentals

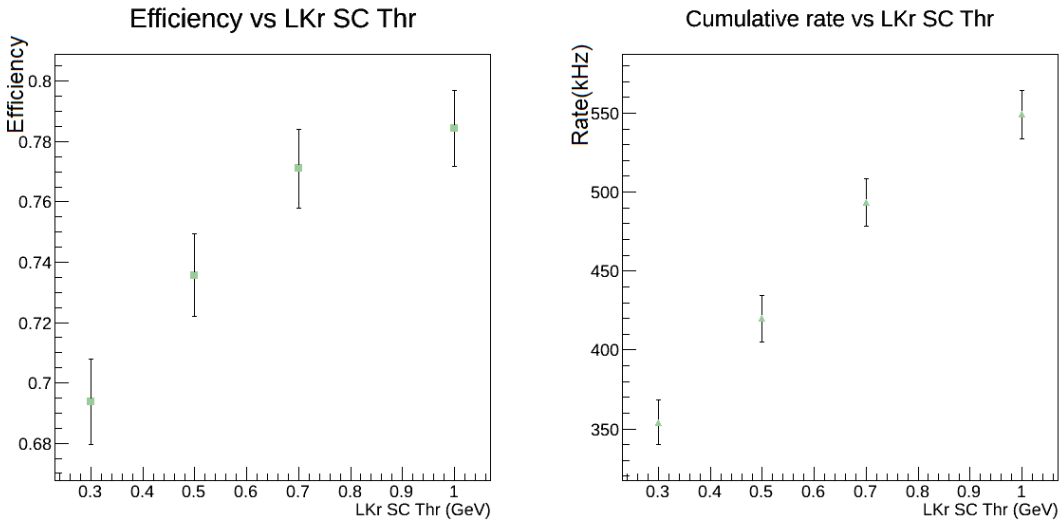

(b) With accidentals

Figure 4.21: Efficiency and rate dependence on LKr SC energy threshold parameter.

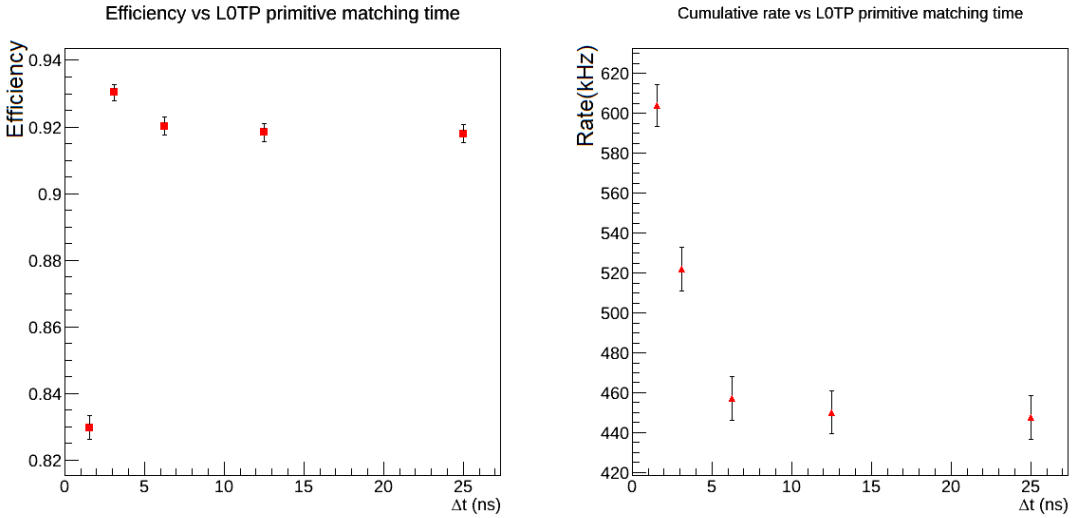

(a) Without accidentals

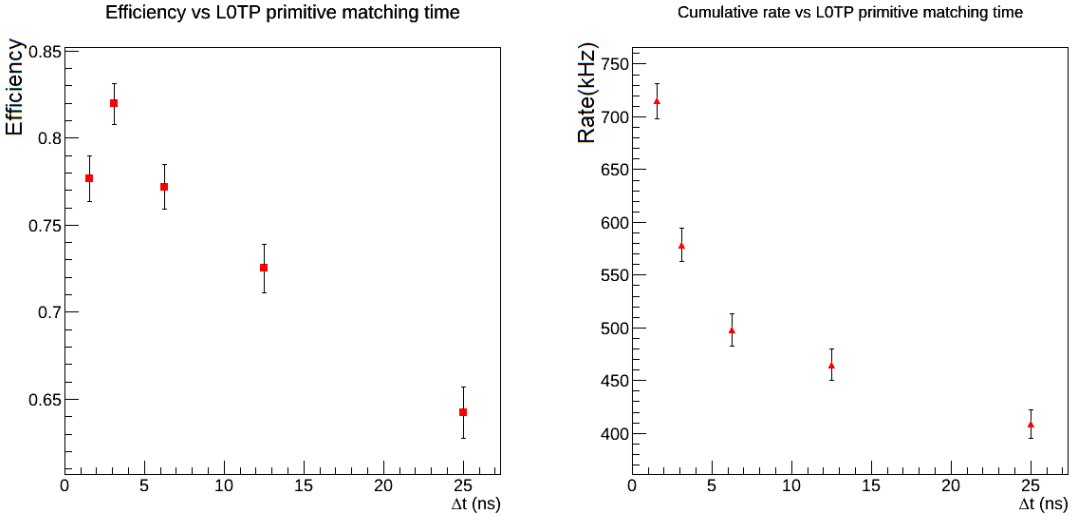

(b) With accidentals

Figure 4.22: Efficiency and rate dependence on L0TP matching time parameter.

The L0TP matching time in figure 4.22 plays a remarkable role in the design of the firmware. This number should not be too small to keep an adequate efficiency: in fact if this is comparable with the resolution of positive detectors (RICH, CHOD) this results in the loss of events due to a missed matching.

On the other end this time cannot be too large as this causes an efficiency decrease due to random veto coming from accidental $K_{\mu 2}$ and $K_{\pi 2}$ (effect that is absent without accidentals).

For what concerns the rate, the loss of veto events dominates on the effect of missed match-

ing of positive detectors for low L0TP matching times.

4.4.1 Results

Following the analysis presented in the previous section, a final set of parameters has been determined by trying to maximize the L0 trigger efficiency and at the same time minimize the total trigger rate.
This set is reported in table 4.3. The main changes with respect to the starting set are in the RICH high multiplicity threshold which has been lowered, and in the introduction of CHOD multiplicity limits (hits and quadrants multiplicities).

RICH time bin	3.125 ns
RICH low threshold	4
RICH high threshold	28
CHOD time bin	1.5625 ns
CHOD max hit multiplicity	10
CHOD max quadrant multiplicity	2
LKr cell hit time bin	12.5 ns
LKr SC and cluster time	6.25 ns
LKr cell threshold	0.1 GeV
LKr SC threshold	0.7 GeV
L0TP matching time	3.125 ns

Table 4.3: Optimized values of L0 parameters under study

Applying this choice a first estimate of the L0 trigger rate and of the L0 trigger efficiency is obtained.
Table 4.4 summarizes the effect of the above trigger selection on the different processes, with the comparison between events with and without simulated accidental activity. Here again the reported errors are statistical only.

The most relevant effect due to the accidentals is in the residual rate from the $K_{\mu 2}$ component: the presence of accidentals combined with the dead time of the MUV3 subdetector gives such enhancement.
Furthermore the presence of accidentals results in a decreased trigger efficiency caused mainly by the random veto due to the high rate in the MUV3 and also in the LKr.
The second most relevant component is in both cases the $K_{\pi 2}$: the majority of these events come from kaon decays downstream the fiducial region, for which the LKr has a large veto inefficiency.

Process	Rate(kHz)	L0 rate no acc. (kHz)	L0 rate with acc. (kHz)
$K_{\mu 2}$	8452	23.9 ± 1.4	216 ± 13
$K_{\mu 3}$	446	5.02 ± 0.15	8.0 ± 0.6
K_{e3}	674	25.7 ± 0.4	29.6 ± 1.4
$K_{\pi 2}$	2748	160 ± 2	142 ± 6
$K_{\pi 3}$	743	36.0 ± 0.5	26.0 ± 1.4
$K_{\pi 3}^{00}$	234	3.28 ± 0.09	2.9 ± 0.3
μ_{π^+}	99144	69 ± 8	-
μ_{K^+}	11792	5 ± 2	-
μ_{π^-}	21375	0 ± 0	-
μ_{K^-}	3035	0 ± 0	-
π^+	526562	33 ± 6	-
Total L0		360 ± 11	425 ± 15
		Efficiency no acc.	Efficiency with acc.
Signal $\pi\nu\bar{\nu}$		$(91.1 \pm 0.3)\%$	$(76.7 \pm 1.3)\%$

Table 4.4: L0 trigger rates for different channels and L0 trigger efficiency after applying the final set of L0 parameters

4.5 Adding halo to accidentals

After the determination of the L0 parameters the work focused on adding the beam halo particles to the generation of accidental events, with the purpose of obtaining a correct estimate of the absolute values of L0 trigger efficiency and output rate.
The software NA62MC at revision 342 has been used to generate samples with all kinds of accidental events. This required some modifications to the code of the generator. First of all the halo files obtained from the HALO program have been added as possible central events of the generation, in addition to the 6 main kaon decays and the signal; in this case halo files are read sequentially. Then a copy of these files is used as source for accidentals, following the same method described in section 4.2.1 based on the exponential distribution of times between two consecutive halo particles; in order to avoid halo accidentals repetition, a random number of particles in halo files is skipped for each simulation run.
10k "central" events have been generated for each one of the 6 main kaon decays and the signal $\pi\nu\bar{\nu}$, plus 10k "central" events of the beam pions component and μ_{K^+}, μ_{π^+}, μ_{π^-} halo components; 3k "central" events have been generated for μ_{K^-} halo (the maximum available number of particles). Accidental kaon decays and halo particles are generated over a window of ± 50 ns around the center.
The distributions of the total number of generated accidental particles and of the single accidental components per event window are shown in figure 4.23. The average values, in tens of MHz, are in agreement with the expectations from the rates: e.g. 50 MHz of generated kaons in a window of 100 ns results in 5 accidental kaons in average.

For what concerns the digitization, the NA62Reconstruction software has been updated to revision 342 too. The custom CHOD digitization described in 4.2.2 was still used to allow a more significant comparison of the results.

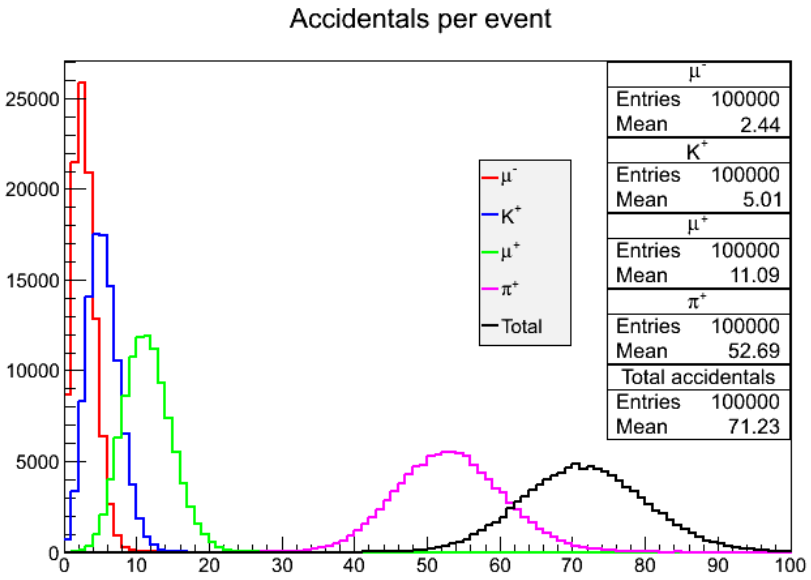

Figure 4.23: Distributions of the number of generated particles per event window (100 ns) for each single accidental component and in total.

The L0 analysis has been performed with the same requirements described in section 4.3 and using the set of parameters in table 4.3. This choice follows from the hypothesis that the introduction of halo particles in the generation of accidentals modifies the absolute values of trigger efficiency and output rate, but not the trend obtained by studying the variation of the parameters.
Table 4.5 summarizes the results obtained from the analysis, and the comparison with the results for accidental events without halo particles (right column of table 4.4).

The results point out that the beam pions and the μ_{π^+} halo component account for about 75% of the total rate, which is rather larger than the allowed limit of 1 MHz. Comparing the results for the halo components with the samples without accidentals of table 4.4, it can be seen that the partial output rates of these two channels are larger and have a larger statistical error.
The latter aspect is due to a lower number of generated events: 10k events with accidentals against 99k and 526k events respectively for the μ_{π^+} halo component and beam pions for the case without accidentals. This can be easily explained: in order to generate the same statistics, in the case of a ± 50 ns time window, the beam pions component requires about

Process	Rate(kHz)	L0 rate acc. halo (kHz)	L0 rate acc. no halo (kHz)
$K_{\mu 2}$	8452	152 ± 11	216 ± 13
$K_{\mu 3}$	446	7.8 ± 0.6	8.0 ± 0.6
K_{e3}	674	35.0 ± 1.5	29.6 ± 1.4
$K_{\pi 2}$	2748	165 ± 7	142 ± 6
$K_{\pi 3}$	743	35.1 ± 1.6	26.0 ± 1.4
$K_{\pi 3}^{00}$	234	2.8 ± 0.3	2.9 ± 0.3
μ_{π^+}	99144	280 ± 50	-
μ_{K^+}	11792	22 ± 5	-
μ_{π^-}	21375	21 ± 7	-
μ_{K^-}	3035	4 ± 2	-
π^+	526562	580 ± 170	-
Total L0		1300 ± 180	425 ± 15
		Efficiency acc. halo	Efficiency acc. no halo
Signal $\pi\nu\bar{\nu}$		$(78.0 \pm 1.1)\%$	$(76.7 \pm 1.3)\%$

Table 4.5: L0 trigger rates for different channels and L0 trigger efficiency after including the halo in accidental generation. The right column refers to accidentals without halo particles and is for comparison.

1250× CPU time and 300× memory while the μ_{π^+} halo component requires about 300× CPU times and 80× memory; in case of a ±150 ns time window, the numbers raise to 3500× CPU time and 850× memory for beam pions, 900× CPU time and 230× memory for μ_{π^+} halo.
The growth of absolute values of the output rates for the two mentioned halo processes can't be explained entirely by the dead time of MUV3 channels, which is the main effect affecting processes with a muon in the final state when accidentals are included in the simulation.

Figure 4.24 shows the rates of Monte Carlo hits on the 148 MUV3 channels, before the digitization and without dead time effects. Considering the ∼3 MHz rate of the hottest channel, which belongs to a pad near the beam pipe, and given an expected dead time of about 30 ns for the MUV3 front end, the Poissonian probability of having at least another hit inside the dead time on that hot channel is $1 - e^{-3 \cdot 10^6 \cdot 30 \cdot 10^{-9}} \simeq 8.6\%$. If this estimate is repeated for all the channels to compute the correct weights, it is evident that the dead time cannot justify the rate increase and the cause must be elsewhere.
An important aspect of the L0TP simulation that must be taken into account, not mentioned in section 4.3.3, is how to decide if the central event (in samples with accidentals generation) passes the L0 conditions. The reference detector is the RICH: the real time at RICH of the central event is known from the simulation, but the L0TP looks for a RICH primitive in a window of ±1 ns around the centre to avoid losing efficiency due to time

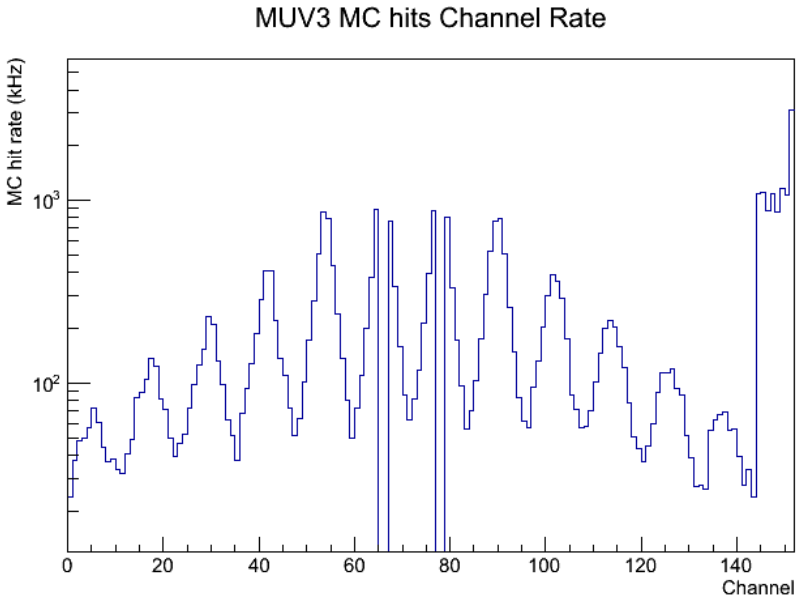

Figure 4.24: Rate of Monte Carlo hits on MUV3 channels. These rates are taken before the digitization process, so no dead time is present.

resolution effects. When analysing events with accidentals, there is a non-zero probability that a surrounding event satisfies the L0 conditions in that 2 ns wide time window. Despite the small probability, the number of such events can be relevant if compared with the similarly small amount of surviving halo events due to the low statistics. This effect biases the correct evaluation of the total rate, and a constant number must be subtracted from all channels to avoid multiple counting of those events.
A validation of what has been described comes from the results shown in table 4.6. The L0TP simulation has been repeated for each process, varying the time window around the center in which the L0TP looks for a RICH primitive. The table reports the number of events (out of 10k) passing the L0 selection for ± 0.5 ns, ± 1 ns and ± 2 ns time windows. The last five rows reveal that the effect is relevant for processes where the counting rate is comparable to that due to surrounding accidentals.

In order to evaluate this "background" to be subtracted, a sample of 10k accidental windows without central events has been generated. Running the L0 analysis on this sample gives a direct estimate of the number of accidental events inside the RICH primitive time window passing the L0. The results are reported in table 4.7.

Using the result in the last row, the number of "background" counting to be subtracted from the values of table 4.6 is 7.1 ± 0.8 (scaled to ± 1 ns and related to 10k events).
The L0 trigger output rates after the correction and the efficiency are presented in table

Process	$\Delta t = \pm 0.5\,\text{ns}$	$\Delta t = \pm 1\,\text{ns}$	$\Delta t = \pm 2\,\text{ns}$
$K_{\mu 2}$	173	180	181
$K_{\mu 3}$	165	175	178
K_{e3}	502	519	524
$K_{\pi 2}$	576	599	606
$K_{\pi 3}$	465	474	477
$K_{\pi 3}^{00}$	121	121	125
μ_{π^+}	19	28	36
μ_{K^+}	15	19	26
μ_{π^-}	4	10	14
μ_{K^-}	3	4	6
π^+	5	11	16

Table 4.6: Number of events passing the L0 selection for three different choices of the RICH primitive time window width parameter.

RICH primitive time window	♯ events passing L0
$\pm 0.5\,\text{ns}$	7
$\pm 1\,\text{ns}$	9
$\pm 2\,\text{ns}$	15
$\pm 10\,\text{ns}$	71

Table 4.7: Number of events passing the L0 selection for different RICH primitive time window widths (sample without central events).

4.8. Errors are statistical only; for the low counting cases of muon halo and beam pions processes the confidence intervals in presence of an uncertain background have been evaluated following [69], using the above mentioned estimated background and a confidence level of 68.27%.
The method described in [69] is an extension of [70], which concerns Poisson processes with known background. The prescription determines whether the confidence interval is one- or two-sided, avoiding negative values or null intervals in case of a number of observed event below the expected background. If the parameter estimate is sufficiently close to the boundary, the methods gives a one-sided limit: in the case of a Poisson variable in the presence of background this would occur if the number of observed events is compatible with the expected background. For parameter estimates increasingly far away from the boundary the interval makes a smooth transition from one- to two-sided, and far away from the boundary a central interval is obtained.

Process	Rate(kHz)	L0 rate (kHz) $\Delta t = \pm 0.5$ ns	L0 rate (kHz) $\Delta t = \pm 1$ ns	L0 rate (kHz) $\Delta t = \pm 2$ ns
$K_{\mu 2}$	8452	143 ± 11	146 ± 11	141 ± 11
$K_{\mu 3}$	446	7.2 ± 0.6	7.5 ± 0.6	7.3 ± 0.6
K_{e3}	674	33.6 ± 1.5	34.5 ± 1.5	34.3 ± 1.5
$K_{\pi 2}$	2748	157 ± 6	163 ± 7	163 ± 7
$K_{\pi 3}$	743	34.2 ± 1.6	34.7 ± 1.6	34.3 ± 1.6
$K_{\pi 3}^{00}$	234	2.7 ± 0.3	2.7 ± 0.3	2.6 ± 0.3
μ_{π^+}	99144	150^{+50}_{-40}	210^{+60}_{-50}	220^{+60}_{-60}
μ_{K^+}	11792	14^{+5}_{-4}	14^{+6}_{-5}	14^{+7}_{-6}
μ_{π^-}	21375	1^{+5}_{-1}	6^{+8}_{-6}	< 9
μ_{K^-}	3035	$2.0^{+2.1}_{-1.4}$	$1.9^{+2.4}_{-1.9}$	$1.8^{+2.9}_{-1.8}$
π^+	526562	80^{+140}_{-80}	210^{+200}_{-160}	90^{+240}_{-90}
Total L0		620 ± 150	820 ± 210	710 ± 250
		Efficiency $\Delta t = \pm 0.5$ ns	Efficiency $\Delta t = \pm 1$ ns	Efficiency $\Delta t = \pm 2$ ns
Signal $\pi\nu\bar{\nu}$		$(76.3 \pm 1.2)\%$	$(78.0 \pm 1.1)\%$	$(78.4 \pm 1.1)\%$

Table 4.8: L0 trigger rates for different channels and L0 trigger efficiency after the subtraction of background accidentals to avoid multiple counting of events. The three columns are for different RICH primitive central time windows. Results refer to accidentals generated in a ± 50 ns time window.

After the described correction the rates for different time windows are quite well in agreement for all the processes; a small decrease in rates and efficiency can be observed in the case of a ± 0.5 ns time window: while the values are still within the confidence intervals, the decrease can be ascribed to time resolution effects of the reference detector. As in table 4.5 the large uncertainty on the total rate comes from the small number of muon halo and

beam pion events passing the L0 selection.

4.6 Comparison between ±50 ns and ±150 ns accidental time windows: the MUV3 simulation

The results presented in table 4.8 underwent a further validation through a similar analysis of samples generated with accidentals (beam kaons, beam pions and muon halo) in a wider time window equal to ±150 ns.
The L0 trigger output rate and the efficiency are expected to be similar: the dead time of subdetectors' front end channels is below 50 ns, so the L0 selection on ±150 ns samples should not reveal any big difference.
Figure 4.25 shows the number of accidentals generated in the ±150 ns time windows: the average values for each channel are triple with respect to those in figure 4.23, as expected.

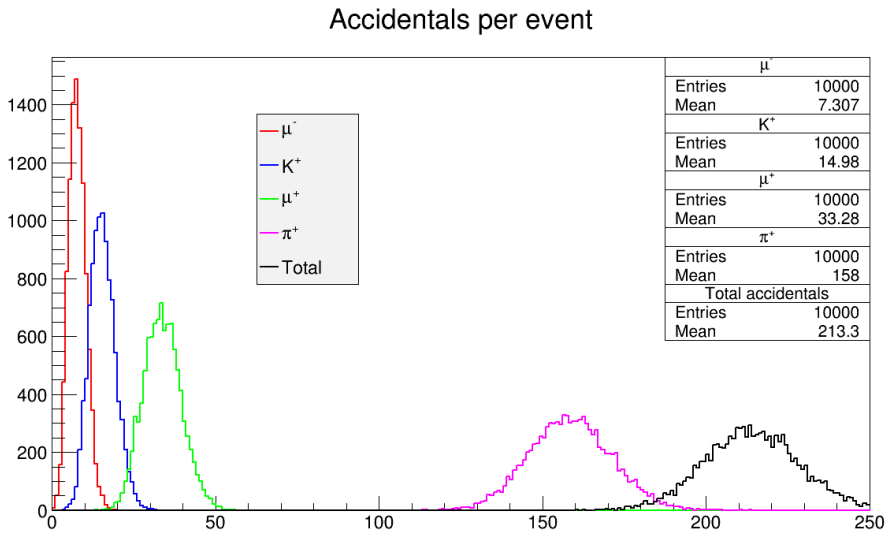

Figure 4.25: Distributions of the number of generated particle per event window (300 ns) for each single accidental component and in total.

The same L0 analysis and the corrections described in section 4.5 have been applied to these samples. The background estimate is the same too: at a first approximation this must be the same for all accidental generation time windows. Results from the L0 analysis are reported in table 4.9; the same considerations concerning the statistical errors as for table 4.8 are also valid.

A comparison of table 4.9 and table 4.8 highlights a remarkable increase of the output rate

Process	Rate(kHz)	L0 rate (kHz) $\Delta t = \pm 0.5\,\text{ns}$	L0 rate (kHz) $\Delta t = \pm 1\,\text{ns}$	L0 rate (kHz) $\Delta t = \pm 2\,\text{ns}$
$K_{\mu 2}$	8452	369 ± 17	381 ± 18	380 ± 18
$K_{\mu 3}$	446	5.6 ± 0.8	14.5 ± 0.8	14.6 ± 0.8
K_{e3}	674	15.2 ± 1.6	41.2 ± 1.6	41.7 ± 1.6
$K_{\pi 2}$	2748	156 ± 6	160 ± 6	160 ± 7
$K_{\pi 3}$	743	36.1 ± 1.6	37.2 ± 1.6	37.2 ± 1.6
$K_{\pi 3}^{00}$	234	3.8 ± 0.3	4.0 ± 0.3	4.0 ± 0.3
μ_{π^+}	99144	310^{+60}_{-50}	350^{+70}_{-60}	380^{+80}_{-70}
μ_{K^+}	11792	68^{+10}_{-9}	70^{+10}_{-9}	75^{+11}_{-10}
μ_{π^-}	21375	3^{+6}_{-3}	13^{+9}_{-7}	12^{+11}_{-10}
μ_{K^-}	3035	$3.0^{+2.4}_{-1.7}$	$2.9^{+2.6}_{-2.0}$	$0.7^{+2.7}_{-0.7}$
π^+	526562	130^{+150}_{-110}	150^{+190}_{-150}	< 220
Total L0		1100 ± 160	1220 ± 200	1110 ± 240
		Efficiency $\Delta t = \pm 0.5\,\text{ns}$	Efficiency $\Delta t = \pm 1\,\text{ns}$	Efficiency $\Delta t = \pm 2\,\text{ns}$
Signal $\pi\nu\bar{\nu}$		$(74.7 \pm 1.2)\%$	$(76.2 \pm 1.2)\%$	$(76.4 \pm 1.2)\%$

Table 4.9: L0 trigger rates for different channels and L0 trigger efficiency after the subtraction of background accidentals to avoid multiple counting of events. The three columns are for different RICH primitive central time windows. Results refer to accidentals generated in a $\pm 150\,\text{ns}$ time window.

that is due exclusively to channels with a muon in the final state, the largest contribution coming from $K_{\mu 2}$ and μ_{π^+}.

$K_{\mu 2}$ events passing the L0 analysis for the $\pm 150\,\text{ns}$ sample have been examined to discover a possible source of this unexpected disagreement.

The generated momentum and direction of the muon have been extracted from the Monte Carlo and the trajectory of the particle has been propagated through the experimental apparatus until the MUV3, taking into account the presence of the magnetic field of the spectrometer. A digitized hit from the MUV3 was obviously missing at the expected time, the event being not vetoed; a Monte Carlo hit at the right time was also absent, so the effect is not due to digitization inefficiencies. Looking at the MUV3 channel hit by the muon extrapolated trajectory, it has been found that the majority of the events had a previous hit in the same channel, coming from decays or halo from accidentals. Furthermore, a detailed analysis showed that all MUV3 channels had no more than 1 hit per event: the MUV3 simulation was summing the energies of all Monte Carlo hits of a channel within an event, but keeping only the time information of the first hit.

While this incorrect procedure is not relevant for the case in which no accidentals are generated, it greatly biases all the absolute values concerning the output rates of channels that are expected to be vetoed by the MUV3, introducing a "limitless" dead time for all channels of this detector, which become completely blind after the first hit in the event.

The reason why this effect affects mainly the ±150 ns samples is clear: the probability to have hits from accidentals on MUV3 is higher, and the corresponding channels are consequently prevented from vetoing the central event.
The simulation of the MUV3 has been changed to correct this effect which is inconsistent with the accidentals generation. New samples for both ±50 ns and ±150 ns accidentals generation time windows have been produced and the final results of the study described in this chapter are reported in the following section.

4.7 Final results

New samples with the correction to the MUV3 simulation have been generated to obtain the final results of the study object of this chapter. The number of events for each process and accidentals time window generation are listed in table 4.10.

Process	(±50 ns)	(±150 ns)
Signal $\pi\nu\bar{\nu}$	10k	10k
$K_{\mu 2}$	10k	10k
$K_{\mu 3}$	10k	10k
K_{e3}	10k	10k
$K_{\pi 2}$	10k	10k
$K_{\pi 3}$	10k	10k
$K_{\pi 3}^{00}$	10k	10k
μ_{π^+}	20k	10k
μ_{K^+}	11k	10k
μ_{π^-}	20k	10k
μ_{K^-}	3k	3k
π^+	20k	10k
Acc. only	100k	-

Table 4.10: Number of events of the samples generated to compute the final results.

The signal sample has been generated with a longitudinal position of the kaon decay vertex between $z = 105$ m and $z = 165$ m. After applying the signal cuts listed at the beginning of section 4.4, the acceptance is about 13% (1283 events for the ±50 ns sample, 1304 for the ±150 ns).
The sample without central events (last row of table 4.10) has been enlarged to reduce the statistical error on the background estimate. The L0 analysis, using a ±10 ns RICH primitive searching window, gives for the background counting due to accidentals a value of 8.0 ± 0.3 (for a RICH primitive searching window of ±1 ns and 10k events).
Table 4.11 shows the final results for the L0 output trigger rate and efficiency, with the

comparison between simulations with different accidentals generation time windows. The results are in agreement within the statistical errors. The same approach as in tables 4.8 and 4.9 has been used to compute the statistical errors of low counting processes.

Process	Rate(kHz)	L0 rate (kHz) ± 50 ns	L0 rate (kHz) ± 150 ns
$K_{\mu 2}$	8452	40 ± 6	34 ± 6
$K_{\mu 3}$	446	3.6 ± 0.4	4.3 ± 0.5
K_{e3}	674	25.6 ± 1.3	29.3 ± 1.4
$K_{\pi 2}$	2748	118 ± 6	126 ± 6
$K_{\pi 3}$	743	25.7 ± 1.4	24.4 ± 1.3
$K_{\pi 3}^{00}$	234	2.4 ± 0.2	3.6 ± 0.3
μ_{π^+}	99144	64^{+29}_{-25}	99^{+74}_{-68}
μ_{K^+}	11792	$2.4^{+3.9}_{-2.4}$	$9.4^{+5.1}_{-4.3}$
μ_{π^-}	21375	$6.4^{+5.4}_{-4.7}$	< 1.7
μ_{K^-}	3035	< 1.4	$0.6^{+2.1}_{-0.6}$
π^+	526562	230^{+140}_{-120}	110^{+170}_{-110}
Total L0		520 ± 140	440 ± 180
		Efficiency ± 50 ns	Efficiency ± 150 ns
Signal $\pi\nu\bar{\nu}$		$(77.9 \pm 1.2)\%$	$(74.0 \pm 1.2)\%$

Table 4.11: Final L0 trigger rates for different channels and L0 trigger efficiency. The two columns show the comparison of different accidentals generation time windows.

The rejection power of veto subdetectors has also been checked, for samples with and without accidentals generation. Results are shown as histograms in figure 4.26, in which each bin corresponds to one subdetector being eliminated from the L0 trigger.
This plot highlights that, as expected, the largest rejection is due to the MUV3 against all muon components, while the calorimeter and minimally the LAV act on π^0 channels. An important effect on the trigger efficiency is also due to the LKr veto in addition to the MUV3.

Finally, the samples without generation of central events have been studied to extrapolate the expected trigger primitive rates at L0TP coming from the involved L0 subdetectors. The distributions of primitive times within the simulation time window are reported in figure 4.27. The value on the vertical axis is the number of primitives per 100 ps bin, multiplied by 10^5 events of the sample. The rate in MHz is obtained dividing this number by 10. A fit with a constant value is performed to compute the primitive rates, which are summarized in table 4.12.

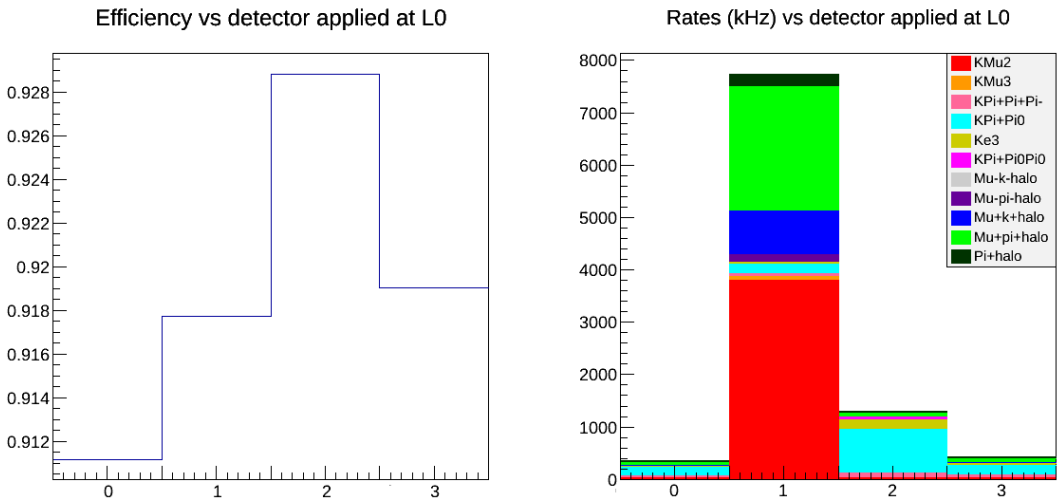

(a) Without accidentals

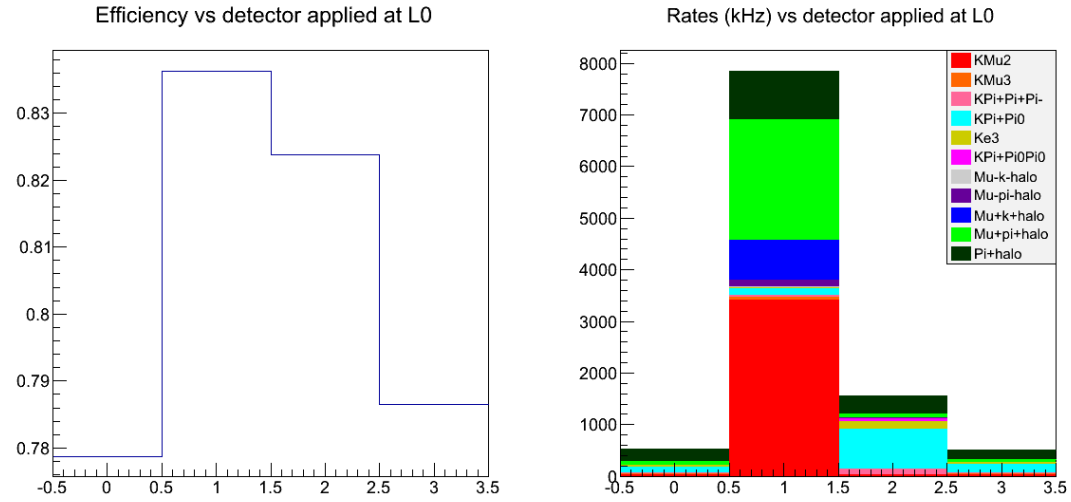

(b) With accidentals

Figure 4.26: Effects on trigger efficiency and rate removing one veto detector at a time:
0: complete trigger chain
1: MUV3 removed
2: LKr removed
3: LAV12 removed

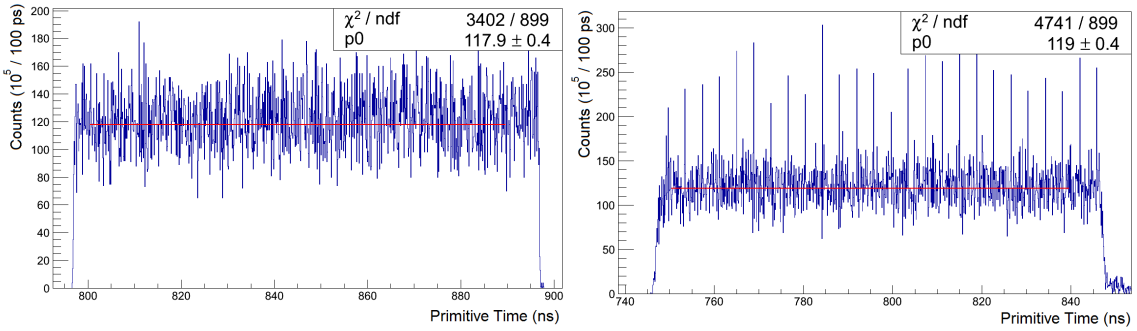

(a) RICH

(b) CHOD

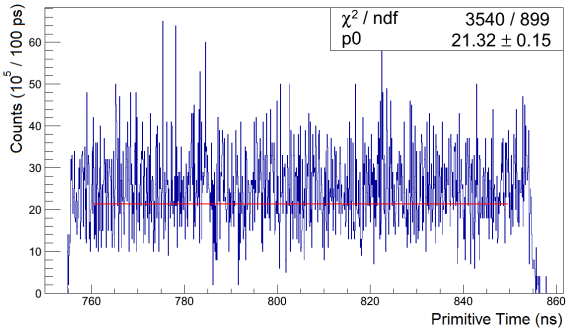

(c) LKr

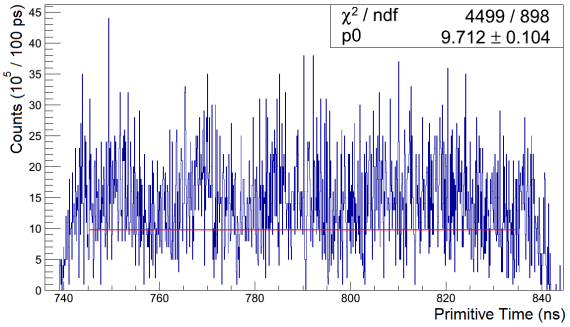

(d) LAV

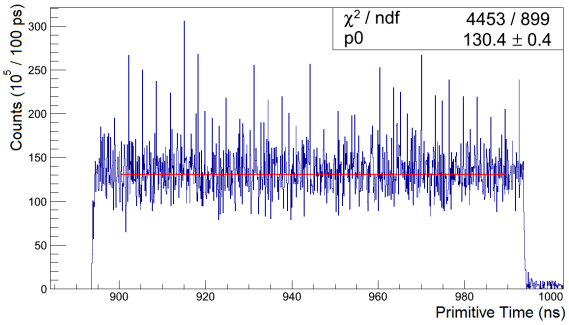

(e) MUV3

Figure 4.27: Distributions of primitive times per 100 ps from L0 subdetectors within the simulation time window of 100 ns for a sample without central event. The red line is the result of a constant fit.

	Primitive rate (MHz)
RICH	11.79 ± 0.04
CHOD	11.90 ± 0.04
MUV3	13.04 ± 0.04
LKr	2.132 ± 0.015
LAV	0.971 ± 0.010

Table 4.12: L0TP input trigger primitive rates.

Chapter 5

NA62 as π^0 factory: search for a dark photon in π^0 decays

5.1 Introduction: rare and forbidden decays at NA62

The Standard Model of particle physics explains with an elegant mathematical description almost all the observed interactions of the constituent elements of known matter. It was strengthened by several precision tests in many years of experiments; nevertheless it cannot provide a full description of subatomic physics, offering no explanation for several observed phenomena like fermion mass hierarchy, neutrino mixing, baryon asymmetry and the existence of dark matter and dark energy. During last decades the evidence of such phenomena pointed out the need for "new physics" beyond the SM, which could explain the disagreements between observations and SM predictions.

The search for new physics can follow two different approaches. The first one is based on achieving the highest possible energy in particle collisions, with the goal of direct observation of new particles. The other one is based on "precision" measurements, studying very rare processes. Here particle physicists pursue the intensity frontier, while the energy scale does not represent a technical limiting aspect. A deviation from expectations in a measurement related to a process described with a very low uncertainty by the Standard Model would suggest the existence of new phenomena. For what concerns the "precision" approach, the well known (from the Standard Model theoretical point of view) kaon and pion sectors are the field of interest for the NA62 experiment, exploiting an intense kaon beam provided by the CERN accelerator complex.

The unprecedented numbers of K^+ and π^+ decays expected to occur in the NA62 fiducial decay region over the full data taking ($N_K \sim N_\pi \sim 10^{13}$) potentially leads to record sensitivities for a wide range of rare and forbidden K^+ and π^+ decays. Moreover, the abundant $K^+ \to \pi^+\pi^0$ decay will provide a large number of tagged π^0 decays in vacuum, making the NA62 experiment a unique "π^0 factory".

The experiment will be able to improve the measurement of the Branching Ratios of rare kaon and pion decays, e.g. K_{e2} for a precision lepton universality test and an independent $|V_{us}/V_{ud}|^2$ measurement, $K_{\pi\gamma\gamma}$ sensitive to high order ChPT predictions, $K^+ \to \pi^+ l^+ l^-$, $K^+ \to \pi^+ \gamma l^+ l^-$, $K^+ \to \pi^+ \pi^0 e^+ e^-$, $K^+ \to 4l$, $\pi^+ \to 4l$.
Tables 5.1 and 5.2 show a list of kaon and pion rare and forbidden decays, in which the NA62 experiment could reach a higher sensitivity with respect to the present experimental results [7].

Process	Physics motivation	BR present result (experiment)	NA62 expected sensitivity
$K^+ \to \pi^+ \mu^+ e^-$	LFV	$< 1.3 \cdot 10^{-11}$ (E865)	$\lesssim 10^{-12}$
$K^+ \to \pi^+ \mu^- e^+$	LFV	$< 5.2 \cdot 10^{-10}$ (E865)	$\lesssim 10^{-12}$
$K^+ \to \pi^- \mu^+ e^+$	LNV, LFV	$< 5.0 \cdot 10^{-10}$ (E865)	$\lesssim 10^{-12}$
$K^+ \to \pi^- e^+ e^+$	LNV	$< 6.4 \cdot 10^{-10}$ (E865)	$\lesssim 10^{-12}$
$K^+ \to \pi^- \mu^+ \mu^+$	LNV	$< 1.1 \cdot 10^{-9}$ (NA48/2)	$\lesssim 10^{-12}$
$K^+ \to \mu^- \nu e^+ e^+$	LNV	$< 2.0 \cdot 10^{-8}$ (Geneva-Saclay)	$\lesssim 10^{-11}$
$K^+ \to e^- \nu \mu^+ \mu^+$	LNV	no data	$\lesssim 10^{-11}$
$K^+ \to \pi^+ \pi^+ e^- \bar{\nu}_e$	$\Delta S \neq \Delta Q$	$< 1.2 \cdot 10^{-8}$ (Geneva-Saclay)	$\lesssim 10^{-11}$
$K^+ \to \pi^+ \pi^+ \mu^- \bar{\nu}_\mu$	$\Delta S \neq \Delta Q$	$< 3.0 \cdot 10^{-6}$ (Birge et al. 1965)	$\lesssim 10^{-11}$
$K^+ \to \pi^+ \gamma$	Angular Mom.	$< 2.3 \cdot 10^{-9}$ (E949)	$\lesssim 10^{-12}$
$K^+ \to \pi^+ X^0$	NP: long-lived weakly int.	$< 5.9 \cdot 10^{-11}$,$m_{X^0} = 0$ (E787)	$\lesssim 10^{-12}$
$K^+ \to \pi^+ X^1 X^2$	NP: non-standard scalar and tensor int.	$< 2.7 \cdot 10^{-9}$ (scalar int.) $< 1.8 \cdot 10^{-9}$ (tensor int.) (E787)	$\lesssim 10^{-12}$

Table 5.1: List of kaon forbidden processes which could be studied by the NA62 experiment. Physics motivations, present results for the Branching Ratios and NA62 expected sensitivities are indicated. Acronyms and symbols in physics motivations indicate Lepton Flavour and Number Violation (LFV and LNV), $\Delta S = \Delta Q$ rule violation ($\Delta S \neq \Delta Q$), New Physics effects (NP).

The search for lepton number (LN) and flavour (LF) violation will be performed in both kaon and pion decays. It is already known that lepton number and flavour symmetries

Process	Physics motivation	BR present result (experiment)	NA62 expected sensitivity
$\pi^0 \to \mu^- e^+$	LFV	$< 3.4 \cdot 10^{-9}$ (KTeV)	$< 10^{-11}$
$\pi^0 \to \mu^+ e^-$	LFV	$< 3.8 \cdot 10^{-10}$ (KTeV)	$< 10^{-11}$
$\pi^+ \to \mu^- e^+ e^+ \nu$	LFV	$< 1.6 \cdot 10^{-6}$ (JINR-SPEC)	$< 10^{-11}$
$\pi^0 \to e^+ e^- \gamma$	see section 5.2	see section 5.3	see section 5.4
$\pi^0 \to e^+ e^-$	NP	$(6.46 \pm 0.33) \cdot 10^{-8}$ (KTeV)	2500 events
$\pi^0 \to e^+ e^- e^+ e^-$	Scalar contributions	$(3.46 \pm 0.19) \cdot 10^{-5}$ (KTeV)	10^6 events
$\pi^0 \to \gamma\gamma\gamma$	C violation	$< 3.1 \cdot 10^{-8}$ Crystal Box	$< 10^{-10}$
$\pi^0 \to \gamma\gamma\gamma\gamma$	Light scalar	$< 2 \cdot 10^{-8}$ Crystal Box	$< 10^{-10}$
$\pi^0 \to \nu\bar{\nu}$	RH neutrino	$< 2.7 \cdot 10^{-7}$ (E949)	$< 10^{-10}$

Table 5.2: List of pion rare and forbidden processes which could be studied by the NA62 experiment. Physics motivations, present limits and results for the Branching Ratios, NA62 expected sensitivities are indicated. Acronyms in physics motivations indicate: Lepton Flavour Violation (LFV), New Physics effects (NP), Charge conjugation symmetry (C) violation, Right-Handed (RH) neutrino.

cannot be exact: a prime example comes from the experimental discovery of neutrino oscillations. This also implies that neutrinos have non-zero masses, which opens the questions about the possible Majorana nature of the neutrino, as well as the origin of the sub-eV observed neutrino mass scale. As a consequence many SM extension theories foresee LN and/or LF violations. The search for such new physics effects has been pursuit worldwide since many years in several sectors of particle physics: B meson [71]:[75], but also τ [76]:[86] and μ [87] leptons. After setting an impressive number of very stringent limits in the past, the kaon sector suffered from the absence of dedicated experiments during last 2 decades: the current experimental limits date back to the 1990s and were set by experiments carried out at the Brookhaven Laboratory in the US [88]:[91]. NA62 is the only medium term experiment in this field. The foreseen sensitivity of NA62 will permit an improvement of two orders of magnitude on the upper limits on the Branching Ratios of LN and LF violating processes with respect to the best available experimental results.
The last rows of table 5.1 show possible processes to probe new hypothetical massless long-lived neutral particles through possible non-standard scalar and tensor interactions. An hypothetical long-lived weakly interacting particle or system of particles (X^0, X^1X^2) can be searched for in kaon decays in a mass spectrum between 0 and $M_K - M_\pi$.
For what concerns π^0 decays in table 5.2, in addition to the above mentioned LN and LF violations, we can distinguish between fully neutral final states and those with charged particles.
Among the neutral modes is the charge conjugation violating mode $\pi^0 \to 3\gamma$: it is forbidden by the invariance of the electromagnetic interaction under charge conjugation, therefore in the SM it might proceed only through weak interactions leading to an unobservable rate; the mere observation of this process would be a clear signal of new physics.
The $\pi^0 \to 4\gamma$ decay is allowed in the Standard Model and the main contribution is electromagnetic: the theoretical prediction for the Branching Ratio is of the order of 10^{-11} [92] and NA62 could obtain a first observation of the process. A deviation from the Standard Model Branching Ratio can be interpreted as a process mediated by possible light scalar S weakly coupled to the electromagnetic current ($\pi^0 \to SS$ followed by $S \to \gamma\gamma$).
The decay of the neutral pion into invisible particles ($\pi^0 \to \nu\bar{\nu}$) might have an important role in cosmological and astrophysical phenomena. In case of purely massless left-handed neutrinos, this decay would be forbidden by conservation of the total angular momentum. With a possible right-handed eigenstate of the neutrino the decay can instead occur through Z boson exchange and the Branching Ratio depends on neutrino masses [93]. Uncertainties on neutrino masses, coming from cosmological limits and direct experimental limits, reflect on the uncertainty of the Branching Ratio for this process and vice versa.
The allowed decays of the neutral pion with charged particles in the final state will be further investigated, searching for new physics effects in case of deviations from the Standard Model expectations. Furthermore, the double Dalitz decay is a probe for non-standard

scalar contributions to the process $\pi^0 \to \gamma^*\gamma^*$ [94].
The Dalitz decay is the main topic of this chapter of the thesis: physics interest, previous experimental results and NA62 expectations will be described in following sections.
Further exotic decay modes not included in the above tables can also be mentioned: the search for heavy neutral leptons in the process $N \to \mu^-\rho^+$, $\rho^+ \to \pi^+\pi^0$ and the search for axions from di-electron samples.
The exploitation of rare and forbidden decay physics beyond the flagship mode $K^+ \to \pi^+\nu\bar{\nu}$ in NA62 will rely on parallel and dedicated trigger chains: while trying to be as efficient as possible, they must coexist in terms of output rate with the primary trigger chain and with a number of control triggers.
The last section of this chapter focuses on designing a possible L0 trigger scheme, the first step in the general trigger chain, for the collection of a "di-electron" data sample searching for a dark photon in π^0 decays $\pi^0 \to \gamma U, U \to e^+e^-$.

5.2 Physics motivations

The strong, weak, and electromagnetic forces are mediated by vector bosons of the Standard Model. New forces could have escaped detection only if their mediators are either too massive ($\mathcal{O}$(TeV)) or quite weakly coupled.
An extra secluded $U(1)$ sector is postulated in most extensions of the Standard Model. Decays of neutral pseudoscalar mesons into a lepton-antilepton pair and a photon are among the processes to search for a new light vector gauge boson connected with dark forces [95]. Recent interest in searches of a light vector boson, in the $\mathcal{O}$(MeV-GeV) mass range, is motivated by astrophysics observations such as the positron (observed by PAMELA [96]) and electron+positron (observed by ATIC [97] and H.E.S.S. [98] which do not discriminate the charge) excesses, possible consequences of annihilation of dark matter into leptons, as well as the narrow 0.511 MeV γ-ray emission from the galactic bulge observed by INTEGRAL [99].
One of the simplest scenarios introduces a U(1) gauge boson and a single complex scalar Higgs' field responsible for spontaneous symmetry breaking. This new sector is not charged under the Standard Model, and the Standard Model degrees of freedom are uncharged under this secluded sector.
The U(1) gauge boson can communicate with the Standard Model photons through a small mixing in the kinetic term of the QED Lagrangian [100]. This mixing contribution can be written as

$$\mathcal{L}_{\text{mix}} = -\frac{\epsilon}{2} F^{\text{QED}}_{\mu\nu} F^{\mu\nu}_{\text{dark}} \tag{5.1}$$

where $F_{\mu\nu}^{\text{QED}}$ is the photon field strength, $F_{\text{dark}}^{\mu\nu}$ the analogous field for the U(1) gauge boson and ϵ is the mixing parameter.
The gauge boson (defined U in this chapter) is often called *dark photon* since it can mix with the photon in all processes, as the mediator of the interaction of dark matter with Standard Model matter.
One example is presented in figure 5.1, with a possible U contribution to the $\pi^0 \to e^+e^-\gamma$ decay.

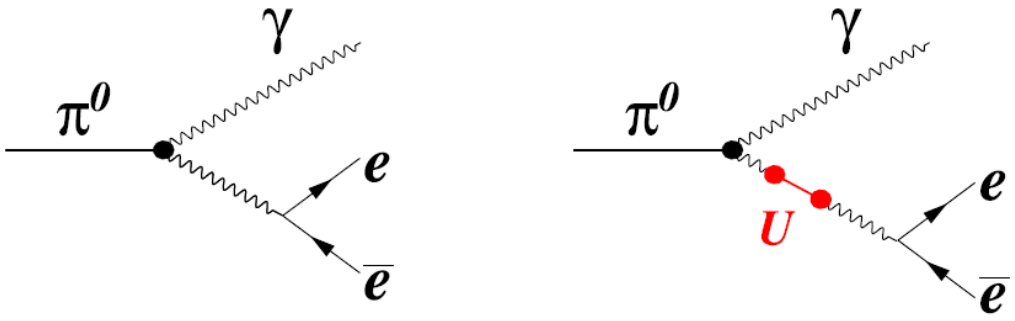

Figure 5.1: Feynman diagrams for the lowest order electromagnetic Dalitz decay $\pi^0 \to e^+e^-\gamma$ (left) and a possible contribution of the U vector boson (right).

The astrophysical observations suggest that the boson mass M_U must be below the GeV scale, due the excesses in electrons and positrons rather than in hadrons. Precision measurements such as the anomalous magnetic moments $(g-2)$ of muon and electron give a constraint on the mixing parameter, which must be of the order of 10^{-4} to 10^{-2} [101] (see section 5.3 for further details).

The Feynman diagram of the contribution of U to $(g-2)$ is shown in figure 5.2.
Calculation of this one-loop diagram produces the result for the additional contribution of U bosons to the anomalous magnetic moment of a lepton (electron, muon) [101] that can be conveniently expressed as:

$$\begin{aligned} a_l^U &= \frac{\alpha\epsilon^2}{2\pi}\int_0^1 dz \frac{2m_l^2 z(1-z)^2}{m_l^2(1-z)^2 + M_U^2 z} \\ &= \frac{\alpha\epsilon^2}{2\pi} \times \begin{cases} 1 & \text{for } m_l \gg M_U \\ 2m_l^2/(3M_U^2) & \text{for } m_l \ll M_U \end{cases} \end{aligned} \tag{5.2}$$

The precision measurement of $(g-2)_e$ currently surpasses the sensitivity of all other QED measurements, and is used for the extraction of the fine structure constant α. Equation

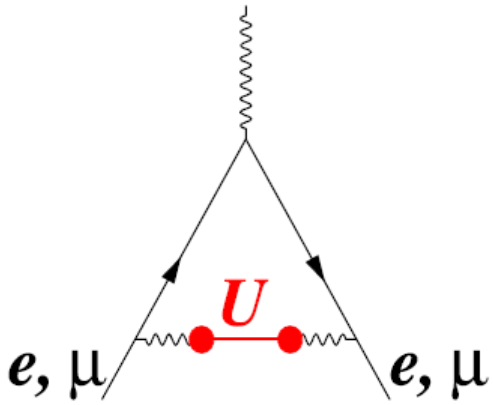

Figure 5.2: Feynman diagram of a possible U contribution to the lepton anomalous magnetic moments $g-2$.

5.2 can be reinterpreted as an effective shift of α by

$$\Delta\alpha = 2\pi a_e^U; \qquad \Delta\alpha^{-1} = -2\pi a_e^U/\alpha^2 \tag{5.3}$$

Another important constraint on the mass and mixing parameters comes from the measurement of the muon magnetic anomaly [102][103]. Investigations of these parameters corresponding to the experimentally preferred muon magnetic moment ($+3.3\,\sigma$ away from the Standard Model value) are therefore of great importance.

A minimal implementation of a secluded $U(1)$ is presented in [100]. Here it is assumed that any other states coupled to the boson are heavier (e.g. dark matter) so that all final states for the decay of the U boson consist of Standard Model particles.
Through mixing with the photon, U will decay to Standard Model leptons with partial width

$$\Gamma_{U\to\bar{l}l} = \frac{1}{3}\alpha\epsilon^2 M_U \sqrt{1-\frac{4m_l^2}{M_U^2}}\left(1+\frac{2m_l^2}{M_U^2}\right) \tag{5.4}$$

For masses $M_U > 2m_\pi$ the vector boson will decay also to hadrons:

$$\Gamma_{U\to\text{hadrons}} = \frac{1}{3}\alpha\epsilon^2 M_U \sqrt{1-\frac{4m_\mu^2}{M_U^2}}\left(1+\frac{2m_\mu^2}{M_U^2}\right) R(s=M_U^2) \tag{5.5}$$

where $R = \sigma_{e^+e^-\to\text{hadrons}}/\sigma_{e^+e^-\to\mu^+\mu^-}$. Since M_U may overlap with hadronic resonances, here it is used the fact that the total decay width of U to hadrons can be directly related

to the cross section $\sigma_{e^+e^-\to\text{hadrons}}$:

$$\frac{\Gamma_{U\to\text{hadrons}}}{\sigma_{e^+e^-\to\text{hadrons}}} = \frac{\Gamma_{U\to\mu^+\mu^-}}{\sigma_{e^+e^-\to\mu^+\mu^-}} \tag{5.6}$$

The total U decay width and the Branching Ratios computed from equations 5.4 and 5.5 are reported in figures 5.3 and 5.4.
For most values of M_U the vector boson has a significant branching to leptons, unless M_U happens to coincide with a hadronic resonance. It must be noted that it is also possible for the vector to decay to neutrinos due to kinetic mixing with the Z boson, but this is suppressed by a factor $M_U^2/M_Z^2 \sim 10^{-8}$ for a GeV-scale M_U and can safely be neglected.

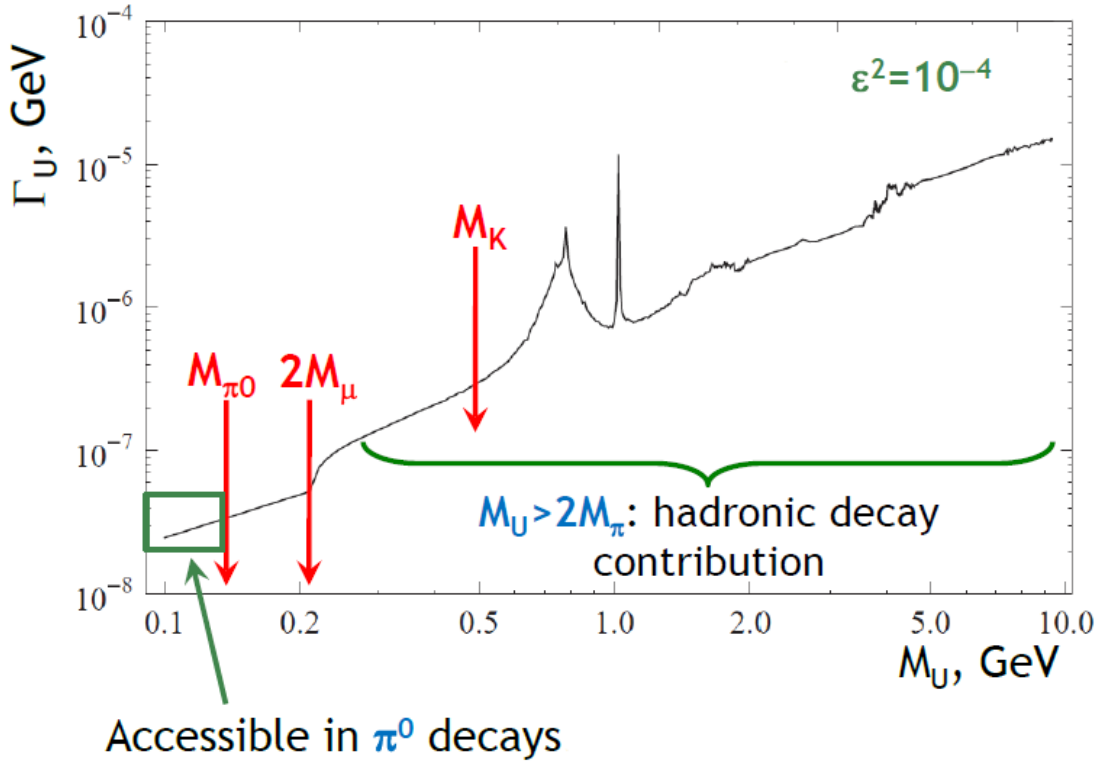

Figure 5.3: Total width Γ_U (GeV) for a choice of the mixing parameter $\epsilon = 10^{-2}$ [100].

For the case of a U boson with mass below the mass of the neutral pion, and neglecting the decay to a neutrino pair for the reason mentioned above, the total decay width is given by equation 5.4 for the electron:

$$\Gamma_{U\to\ e^+e^-} = \frac{1}{3}\alpha\epsilon^2 M_U \sqrt{1-\frac{4m_e^2}{M_U^2}}\left(1+\frac{2m_e^2}{M_U^2}\right) \tag{5.7}$$

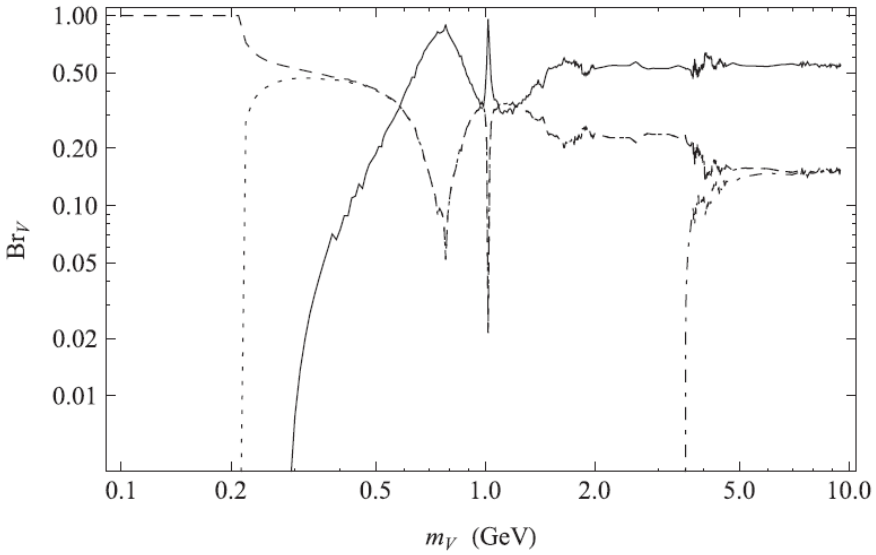

Figure 5.4: Branching Ratios for the U vector boson: $U \to e^+e^-$ (dashed), $U \to \mu^+\mu^-$ (dotted), $U \to \tau^+\tau^-$ (dotted-dashed) and $U \to$ hadrons (solid) [100].

Such a light and short-lived U boson (the proper lifetime is below 10^{-16} s for masses below M_{π^0}) can be searched for in the π^0 decay chain $\pi^0 \to \gamma U$, $U \to e^+e^-$, which has an experimental signature identical to the Dalitz decay.
The Branching Ratio of the $\pi^0 \to \gamma U$ process can be related to the well known amplitude $\Gamma(\pi^0 \to \gamma\gamma)$ through the mixing parameter [104]

$$\frac{\mathcal{B}(\pi^0 \to \gamma U)}{\mathcal{B}(\pi^0 \to \gamma\gamma)} = 2\epsilon^2 |F(M_U^2)|^2 \left(1 - \frac{M_U^2}{M_{\pi^0}^2}\right)^3 \tag{5.8}$$

where $F(M_U^2)$ is the value of the π^0 electromagnetic form factor for a squared momentum transfer equal to the U squared mass. This equation gives the evolution in figure 5.5 for the quantity $\frac{\mathcal{B}(\pi^0 \to \gamma U)}{\epsilon^2}$ as a function of the vector boson mass.

5.3 Experimental status

In recent years several experiments and measurements provided constraints on the ϵ^2 vs. M_U parameters space they probed.
A first kind of precision measurements concerns the anomalous magnetic moments $(g-2)$ of muon and electron to search for possible U contribution as shown in equations 5.2 and 5.3.
The current most precise determination of α comes from atomic physics results with Cs and Rb [105] [106]. This method is based on the extraction of α from precise measurement

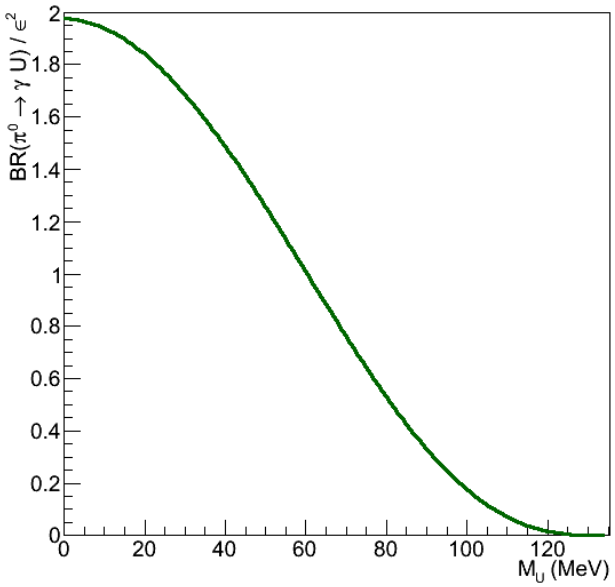

Figure 5.5: Ratio between the Branching Ratio of the decay of the neutral pion into one photon and the vector boson U and the square of the mixing parameter, as a function of the vector boson mass.

of the following parameters: the Rydberg constant, ratios of the total atomic mass (Re or Cs) to m_p, the m_e/m_p ratio, and the absolute value of the Planck constant to atomic mass ratio h/m_A. Any possible effect of a vector boson U on masses cancels in the ratio, and the only place where a vector contribution may affect α extracted that way is the Rydberg constant. The effect of the vector boson is in the shift of α due to a_e^U (equation 5.2). Measurements from [105] [106] show that the relative shift of $\Delta\alpha$ does not exceed 15×10^{-9}, which results in a constraint on the parameter of the model:

$$\epsilon^2 \times F(m_e^2/M_U^2) < 15 \times 10^{-9} \Rightarrow \epsilon^2 \times \left(\frac{100\,\mathrm{MeV}/c^2}{M_U}\right)^2 < 1.0 \times 10^{-3} \tag{5.9}$$

with the assumption that $M_U \gg m_e$. Here the function F is the integral of equation 5.2. Constraints imposed by primordial nucleosynthesis (BBN), in terms of equilibrium with the electromagnetic plasma through annihilation processes $U\bar{U} \leftrightarrow e^+e^-$, require $M_U \gtrsim 4\,\mathrm{MeV}/c^2$ to achieve the correct dark matter density and the observed light-element abundances [107]. If M_U is chosen right at such value then from equation 5.9 it follows that the mixing parameter ϵ^2 must be less then 10^{-6}, while this constraint weakens considerably for larger values of M_U.

The other important constraint comes from the measurement of the muon magnetic anomaly. The use of this constraint is not straightforward due to the need to deal with hadronic

uncertainties in extracting theoretical prediction for $(g-2)_\mu$. The determination based on lepton annihilation to hadrons points to a 3.3 σ discrepancy of $(g-2)_\mu^{\text{th}}$ relative to the experimental value measured at Brookhaven [102].
The positivity of the U-contribution a_μ^U improves the agreement between $(g-2)_\mu^{\text{th}}$ and $(g-2)_\mu^{\text{exp}}$, if one uses the $e^+e^- \to$ hadrons result.
A conservative limit for the value of a_μ^U is 5σ away from the discrepancy between $(g-2)_\mu^{\text{th}}$ and $(g-2)_\mu^{\text{exp}}$: such an additional contribution to the anomaly is excluded no matter which method of treating the hadronic contribution to $(g-2)_\mu^{\text{th}}$ one would like to choose.
Figure 5.6 shows the combination of these constraints. The muon measurement includes a forbidden region (at 5σ) as well as an allowed band of a_μ^U which puts the theoretical prediction based on $e^+e^- \to$ hadrons within 2 standard deviations from the experimental result of $(g-2)_\mu^{\text{exp}}$.

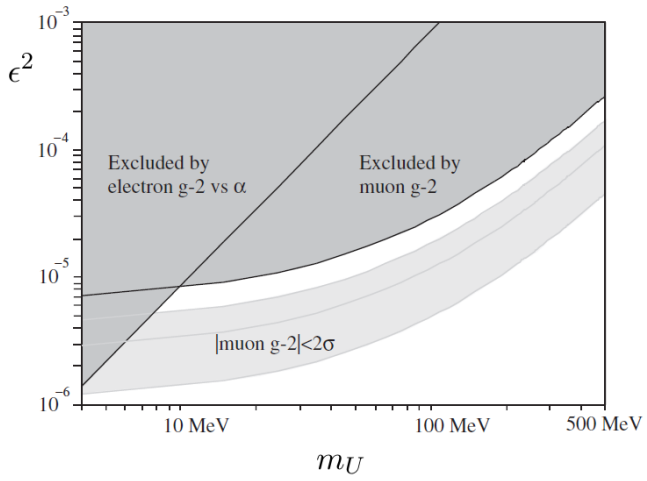

Figure 5.6: Muon $g-2$ and α measurement constraints on ϵ^2 vs. M_U parameter space [101]. The dark grey region is the excluded one. The light grey band around the line of the experimental value of $(g-2)_\mu$ indicates a consistency of theoretical and experimental values within 2σ.

Another way to search for such a light U boson is through direct production in particle accelerators. The idea is to search for narrow structures in the invariant mass spectrum of the lepton-antilepton pair.
For M_U above $100\,\text{MeV}/c^2$, the ϵ^2 vs. M_U region corresponding to the measured $(g-2)_\mu$ value $\pm 2\sigma$ is covered by the data from the BABAR [108], MAMI A1 [109], KLOE-2 [110] and APEX [111] experiments.

The A1 Collaboration set a new exclusion limit for the electromagnetic production of a light $U(1)$ gauge boson decaying to e^+e^- at the Mainz Microtron. They searched for a

narrow state coupling to e^+e^- in electron scattering from a heavy nucleus (the electron beam has an energy of 855 MeV), in a range of the lepton-pair mass between 210 MeV/c^2 and 300 MeV/c^2.
Figure 5.7 (a) shows the Feynman diagram of the process investigated by the A1 Collaboration. Since the coupling is small, the cross section for coherent electromagnetic production of the U boson can be enhanced by a factor Z^2 by choosing a heavy nucleus as the target (a tantalum foil, $Z = 73$, was the choice of the experiment); the subsequent decay of the U boson to a lepton pair would be the signature of the reaction. The experimental challenge is the suppression of the background which is dominated by radiative pair production (figure 5.7 (b)).
The result of the experiment is presented on the exclusion plot of figure 5.8 in terms of the ratio of the effective coupling to the fine structure constant $\alpha'/\alpha = \epsilon^2$. Also shown are the existing limits published by BABAR and the belt of the muon anomalous magnetic moment $a_\mu = g_\mu/2 - 1$.

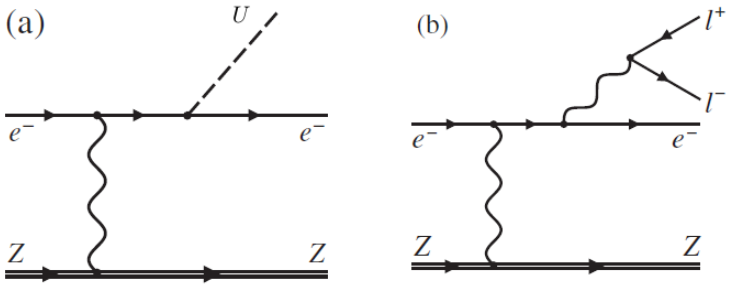

Figure 5.7: (a) Electromagnetic production of the U boson probed by the A1 collaboration at MAMI. (b) One of the dominant and irreducible background processes.

The BABAR experiment searched for evidence of a light scalar boson in the radiative decays of $\Upsilon(2S)$ and $\Upsilon(3S)$ resonances: $\Upsilon(2S, 3S) \to \gamma A^0, A^0 \to \mu^+\mu^-$. This particle can be interpreted as the Higgs' associated to the secluded U(1) symmetry, and the limit on its production can be related to exclusions in the ϵ^2 vs. M_U plane. The gauge boson mass region that this measurement probed is between 212 MeV/c^2 and 9.3 GeV/c^2. The empirical motivation of this search comes from the HyperCP experiment, which measured the Branching Ratio of $\Sigma^+ \to p\mu^+\mu^-$ observing three events: the masses of the three dimuons are within 1 MeV/c^2, and this might be interpreted as a production of a scalar boson with a mass of 214.3 MeV/c^2 [112].

The APEX experiment had an approach similar to the A1 Collaboration. They searched for new forces mediated by a vector boson with weak coupling to electrons, produced in

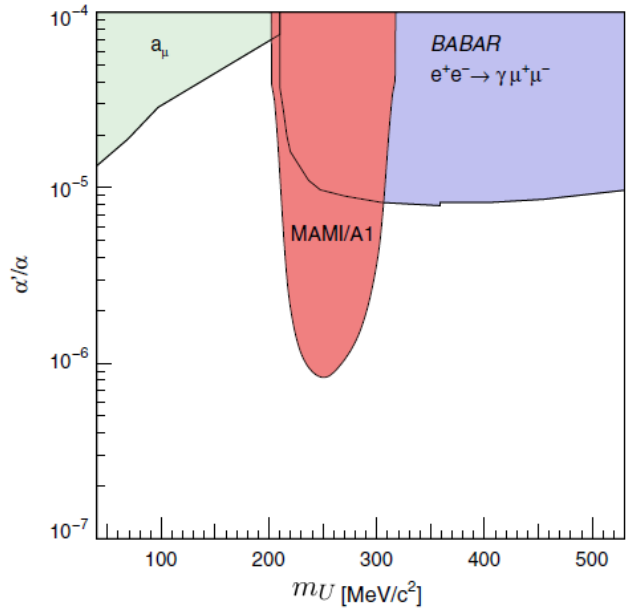

Figure 5.8: Exclusion limits at 90% confidence level in terms of relative coupling $\alpha'/\alpha = \epsilon^2$ from the MAMI A1 experiment [109]. Also shown are the previous limits by BABAR and for $a_\mu = g_\mu/2 - 1$.

electron-nucleus fixed-target scattering and decaying to an e^+e^- pair, producing a narrow resonance in the di-electron invariant mass spectrum. The experiment used a tantalum foil as target, with an electron beam energy of 2.26 GeV. The analysed lepton-pair mass spectrum ranges from 175 MeV to 250 MeV.
The process under analysis and a possible background are the same as shown in figure 5.7. No significant lepton-pair signal from electroproduction of a narrow resonance was detected, and the upper limit presented in the exclusion plot of figure 5.9 was established.

The KLOE-2 Collaboration at DAΦNE studied the possible production of a light U vector boson in the decay $\phi \to \eta U, U \to e^+e^-$.
The DAΦNE e^+e^- collider running at center-of-mass energy of $\sim$ 1020 MeV produces ϕ mesons nearly at rest. The η meson was tagged analysing the decays $\eta \to \pi^0\pi^0\pi^0$ and $\eta \to \pi^+\pi^-\pi^0$.
The main background component to the $\phi \to \eta e^+e^-$ decay comes from $\phi \to \eta\gamma$ events in which the photon converts to an electron-positron pair.
The exclusion plot in the $\alpha'/\alpha = \epsilon^2$ vs. M_U plane shown in figure 5.9, in the e^+e^- mass range between about 30 MeV/c^2 and 400 MeV/c^2, was derived from the relation between $\sigma(e^+e^- \to \phi \to \eta\gamma)$ and $\sigma(e^+e^- \to \phi \to \eta U)$, which involves the parametrisation of the $\phi\eta\gamma^*$ transition form factor.

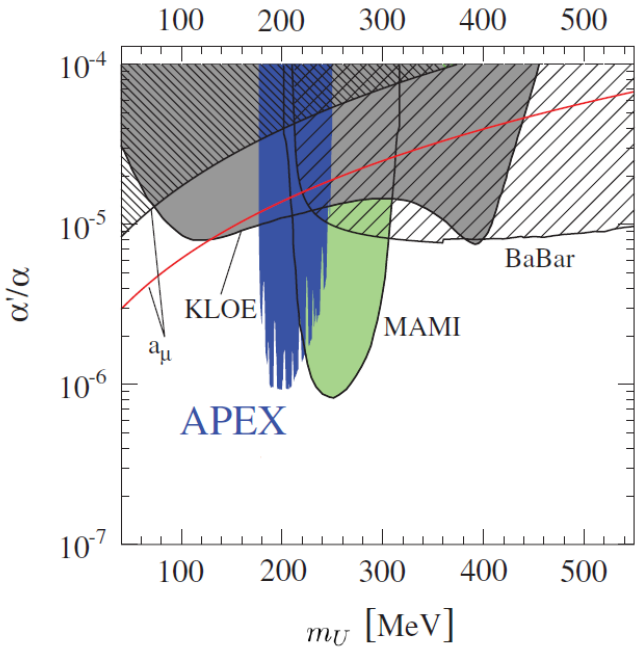

Figure 5.9: The 90% confidence upper limit on $\alpha'/\alpha = \epsilon^2$ versus the vector boson mass for the APEX experiment [111], compared with other 90% confidence level limits from the muon anomalous magnetic moment, KLOE, A1 at MAMI and BABAR.

In addition to KLOE-2, two other experiments investigated the U mass region under $135\,\mathrm{MeV}/c^2$, which corresponds to the mass of the neutral pion. At this value for the mass of the vector boson, the common feature of these experiments is the search of the U boson from π^0 decays. NA62 will also focus on this process and this mass range, as described in next section.

The first experiment in order of time was SINDRUM I running at PSI [113]. The purpose was to search for a peak in the continuous invariant mass spectrum of the lepton pair from the Dalitz decay $\pi^0 \to e^+e^-\gamma$, which represents a natural background to the U production and decay into e^+e^-.

The production of π^0 was done through the $\pi^-p \to \pi^0 n$ charge exchange interaction at rest, stopping a π^- beam with a momentum of $95\,\mathrm{MeV}/c$ in a small liquid-hydrogen target. Thus another way to search for the U boson was in the $\pi^-p \to Un$ reaction. The allowed electromagnetic process $\pi^-p \to e^+e^-n$ was the main background in this case.

The SINDRUM I experiment had a limit on the detectable lifetime of the vector boson: $10^{-23}\,\mathrm{s} < \tau_U < 10^{-11}\,\mathrm{s}$; for lower values the width of the particle would have been too high and the peak smeared out beyond recognition; for larger values the U particles would have decayed outside the target region, preventing the event to be triggered. The lower limit in the invariant mass of the lepton pair was of about $25\,\mathrm{MeV}/c^2$ due to a minimum opening angle between e^+ and e^- required by the trigger.

The experiment found no evidence for the existence of the boson and set the upper limits

for the two processes as shown in figure 5.10. The upper limits on $\Gamma(\pi^0 \to U\gamma, U \to e^+e^-)/\Gamma(\pi^0 \to \text{all})$ are 2×10^{-4} for $25\,\text{MeV}/c^2$ bosons and 4×10^{-6} for $100\,\text{MeV}/c^2$ bosons. The upper limits on the other process $\Gamma(\pi^- p \to Un, U \to e^+e^-)/\Gamma(\pi^- p \to \text{all})$ are 2.5×10^{-3} for $25\,\text{MeV}/c^2$ bosons, 1.0×10^{-5} for $100\,\text{MeV}/c^2$ bosons and of the order of 10^{-7} for the region around the mass of the neutral pion.

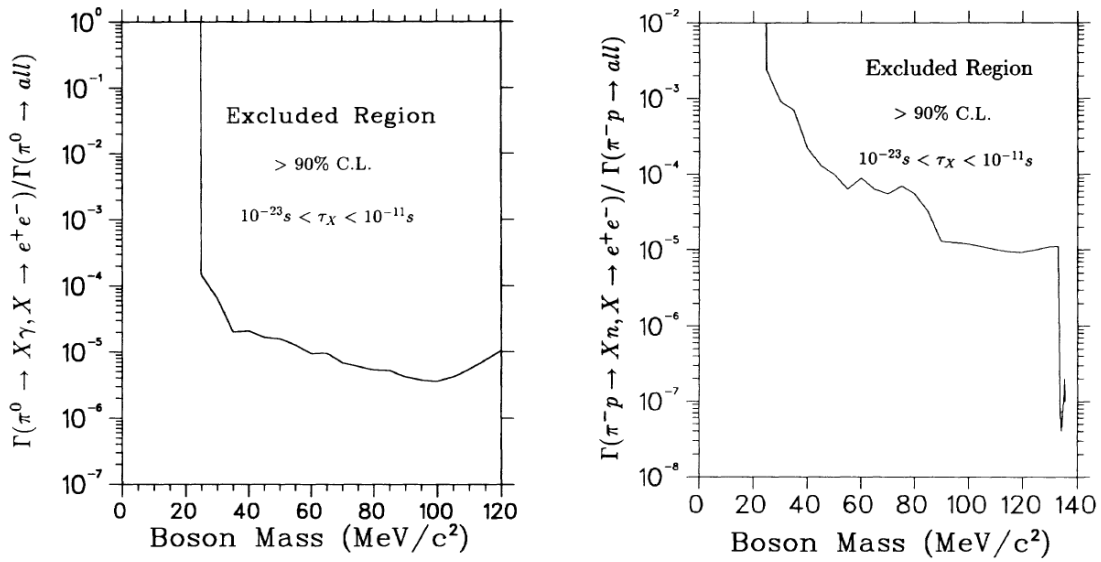

Figure 5.10: The 90% confidence level upper limits for the SINDRUM I experiment on $\Gamma(\pi^0 \to U\gamma, U \to e^+e^-)/\Gamma(\pi^0 \to \text{all})$ (left) and $\Gamma(\pi^- p \to Un, U \to e^+e^-)/\Gamma(\pi^- p \to \text{all})$ (right) versus the vector boson mass [113].

The recent WASA experiment [114] improved on the SINDRUM measurement in the mass range between $20\,\text{MeV}/c^2$ and $100\,\text{MeV}/c^2$. The approach was the same: the search for a short-lived U vector boson in the decay chain $\pi^0 \to U\gamma, U \to e^+e^-$, appearing as a narrow peak in the well-known e^+e^- invariant mass distribution of the background Dalitz decay. The detector was optimised for the production of low energy π^0 mesons through the reaction $pp \to pp\pi^0$. The proton beam had a kinetic energy of 550 MeV corresponding to a center-of-mass excess energy of 122 MeV, below the threshold for the production of two pions.

In addition to the Dalitz decay, another source of background comes from the standard decay of the neutral pion into two photons, where one photon converts in e^+e^- in the beam tube.

The obtained 90% confidence level upper limits for the Branching Ratio of the $\pi^0 \to U\gamma$ decay and for the mixing parameter ϵ^2 as a function of the vector boson mass are presented in figure 5.11, compared with SINDRUM and KLOE-2 results together with muon and electron $g-2$ measurements.

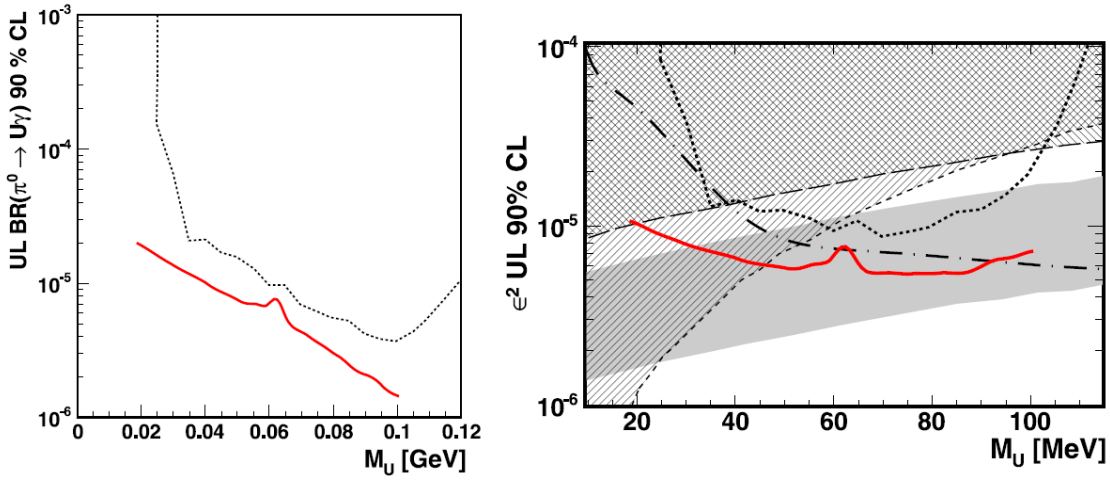

Figure 5.11: 90% confidence level upper limit for the Branching Ratio of $\pi^0 \to \gamma U$ from WASA [114] (solid red line) compared to SINDRUM (dotted line) (left). Summary of the 90% confidence level upper limits for the mixing parameter ϵ^2 versus the vector boson mass M_U from WASA [114] (solid red line) compared to SINDRUM (dotted line), KLOE (dashed dotted), the exclusion areas from electron and muon $(g-2)$ and the grey band corresponding to the present value of $(g-2)_\mu$ (right).

5.4 Search for the dark photon at NA62

The NA62 experiment will profit from the high flux of tagged π^0 to search for the $\pi^0 \to \gamma U$ decay, in a mass range for the vector boson up to the mass of the neutral pion.
In this section the kinematics of the decay and the rates of the experiment are evaluated, in order to obtain an estimate of the NA62 expected sensitivity together with the mass range that the experiment will be able to probe.

5.4.1 Kinematics of the $K^+ \to \pi^+\pi^0$, $\pi^0 \to \gamma U$, $U \to e^+e^-$ decay

The NA62 experiment will probe the same region of the vector boson mass spectrum as SINDRUM I and WASA, below the mass of the neutral pion, possibly improving the limits for the coupling constant of the U boson with the photon.
One important difference between NA62 and the above mentioned experiments is the in-flight decay technique: the hypothetical U boson originates from a neutral pion coming from the decay of charged kaons with a central momentum of 75 GeV/c.
A fundamental assumption for SINDRUM I and WASA was the fact that the decay vertex of the $U \to e^+e^-$ process was nearly corresponding with the interaction point within the

vertex reconstruction resolution of the tracking detectors.
The identification of the $K^+ \to \pi^+\pi^0$, $\pi^0 \to \gamma U$, $U \to e^+e^-$ decay chain in NA62 will be based on a three-track vertex reconstruction: the lepton pair together with the tagging π^+. The mean free path of the U boson must be evaluated in order to check the consistency of this condition.
The width of the particle can be extracted from equation 5.7, and is well approximated by $\Gamma_U \approx \alpha\epsilon^2 M_U/3$ for $m_e \ll M_U$. It is not a fixed value as it depends on the couple of free parameters ϵ^2 and M_U.
The proper lifetime of the vector boson is given by the inverse of the width:

$$\tau_U = \frac{\hbar}{\Gamma_U} \approx 3 \times 10^{-16}\,\mathrm{s} \times \frac{10^{-6}}{\epsilon^2} \times \left(\frac{M_U}{\mathrm{GeV}/c^2}\right)^{-1} \tag{5.10}$$

The mean free path in the laboratory reference frame depends also on the energy of the particle in that reference frame:

$$\lambda_U = \gamma c \tau_U = \frac{\gamma c \hbar}{\Gamma_U} \approx \frac{E_U}{M_U c^2} \times 80\,\mathrm{nm} \times \frac{10^{-6}}{\epsilon^2} \times \left(\frac{M_U}{\mathrm{GeV}/c^2}\right)^{-1} \tag{5.11}$$

Figure 5.12 shows the distribution of the values of the U boson energy in the laboratory reference frame as a function of the boson mass, as obtained from a Monte Carlo simulation of the $K^+ \to \pi^+\pi^0$, $\pi^0 \to \gamma U$ process. For details about the simulation see section 5.5.

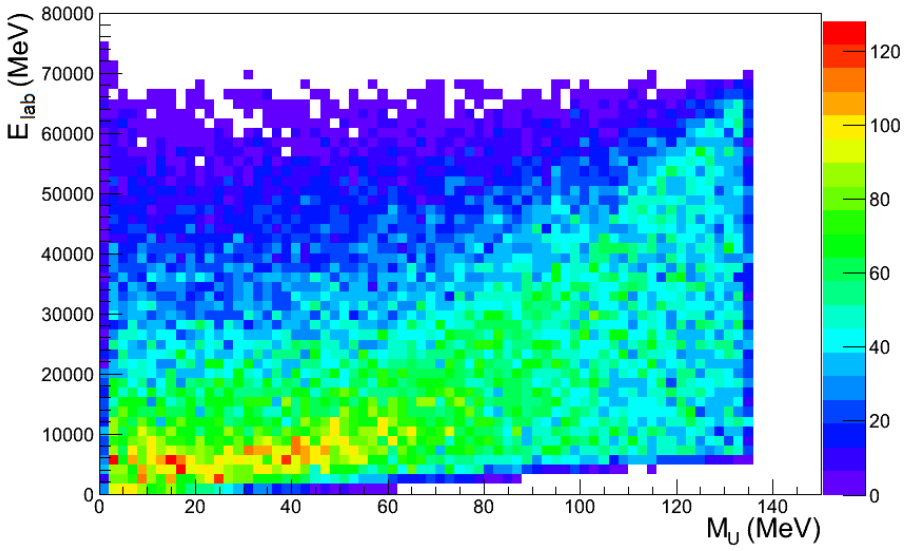

Figure 5.12: Distribution of the energy in the laboratory reference frame of the U boson produced in $K^+ \to \pi^+\pi^0$, $\pi^0 \to \gamma U$ as a function of its mass.

From equation 5.11 follows that the U mean free path decreases as the square of its mass. For U masses below $20\,\mathrm{MeV}/c^2$ figure 5.12 shows that the peak energy is below 10 GeV,

and in most cases the U energy is below 20 GeV. The trend of the mean free path as a function of the vector boson mass of figure 5.13 can be obtained by fixing the remaining two variables. In this plot a coupling constant $\epsilon^2 = 10^{-6}$ and an energy $E_U = 20$ GeV have been assumed (red line). The blue line refers to a mean free path $c\tau$ with $\gamma = 1$.
From the figure it can be seen that for low mass (below 10 MeV/c^2) and high energy (over 20 GeV) bosons there is a loss of acceptance due to a wrong three-track vertex identification. This will result in a lower sensitivity for the mixing parameter ϵ^2 for low mass bosons.

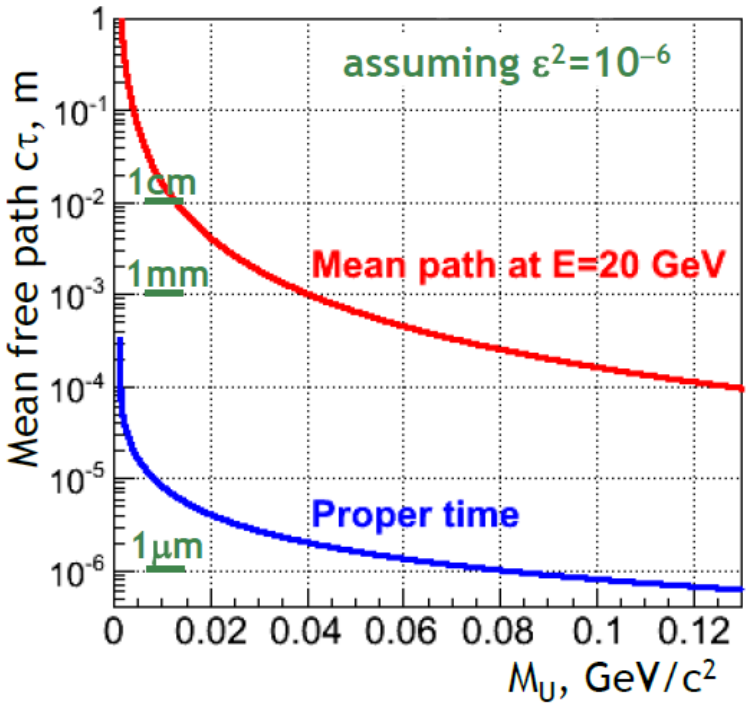

Figure 5.13: Mean free path in the laboratory reference frame of a U boson with an energy of 20 GeV as a function of its mass, assuming a mixing parameter $\epsilon^2 = 10^{-6}$.

5.4.2 Expected sensitivity

The expected single event sensitivity for the detection of the $\pi^0 \to \gamma U$ decay, with a vector boson mass equal to M_U, can be obtained from equation 5.12. It is defined as the measured value of the Branching Ratio of the process in case of observation of one event in absence of background.

$$U_{\mathrm{SES}}(M_U) = \frac{1}{\Phi_{\pi^0} A(M_U) \frac{\varepsilon(M_U)}{D}} \tag{5.12}$$

- Φ_{π^0} is the total flux of neutral pion decays under study (those coming from the $K_{\pi 2}$ process).

- $A(M_U)$ is the acceptance of the NA62 detector: it includes the geometric acceptance together with the efficiency of the cuts that will be performed during the analysis to select the sample for the measurement.
- $\varepsilon(M_U)$ represents the trigger efficiency for the collection of the data sample. Both the acceptance and the trigger efficiency depend on the boson mass, as a different mass results in a different kinematics of the lepton pair.
- D is the possible trigger downscaling factor that could be needed to reduce the output trigger rate and include the trigger in the data taking: its effect is a "blind" reduction of the trigger efficiency not dependent on the boson mass.

The total flux of neutral pion decays from $K_{\pi 2}$ can be evaluated from the beam particle rate of NA62 [55]. The nominal K^+ rate at GTK3 ($z = 102.4\,\mathrm{m}$) is 45 MHz. Then we consider the fraction of kaons decaying in the fiducial region between 105 m and 165 m, taking into account that kaons with a momentum of $75\,\mathrm{GeV}/c$ in the laboratory reference frame have a mean free path $\gamma c\tau \approx 564\,\mathrm{m}$:

$$f = e^{\frac{z_{\mathrm{GTK3}} - z_1}{\gamma c\tau}} - e^{\frac{z_{\mathrm{GTK3}} - z_2}{\gamma c\tau}} \simeq 10\%$$

We are selecting neutral pions from the $K_{\pi 2}$ decay, which has a Branching Ratio $\mathrm{BR}(K_{\pi 2}) \approx 20.6\%$ [7].
Other factors come from the integrated luminosity of NA62. The experiment will run for at least 3 years, corresponding roughly to 400 days. A weekly technical stop of the accelerator complex adds a factor 6/7. The data taking is foreseen to have an intrinsic efficiency of about 90% (based on 2007 data taking). The burst structure of the beam from the SPS has a duty cycle of about 25%.
Combining all these factors the final estimate for the total number of neutral pions is

$$\Phi_{\pi^0} = 45 \times 10^6\,\mathrm{s}^{-1} \times 10\% \times 20.6\% \times 400\,\mathrm{d} \times 86\,400\,\mathrm{s\,d}^{-1} \times 6/7 \times 90\% \times 25\% \approx 6 \times 10^{12}$$

In section 5.5 a possible implementation of a L0 trigger has been studied, together with an evaluation of the analysis acceptance based on a Monte Carlo simulation, to get the values for $A(M_U)$, $\varepsilon(M_U)$ and D.
In addition, in order to obtain the expected 90% confidence level upper limit as a function of the U boson mass, the presence of the background, mainly due to π^0 Dalitz decays, must be taken into account. A similar selection to that for signal events has been performed over simulated Dalitz decays to compute the expected background as a function of the lepton-pair invariant mass.
Using the prescriptions from [69] and assuming that the number of observed events for a given invariant mass will be equal to the expected background value, an upper limit N_{up}

for the counting of $\pi^0 \to \gamma U$ decays is obtained. The upper limit on the Branching Ratio as a function of the U boson mass is finally achieved multiplying $N_{\rm up}$ with the single event sensitivity $U_{\rm SES}(M_U)$, while the corresponding limits in the plane ϵ^2 vs. M_U are derived from equation 5.8.

5.5 Monte Carlo studies of a L0 trigger for the selection of $K^+ \to \pi^+\pi^0$ Dalitz decays

This section describes the implementation of a L0 trigger strategy for the selection of $K^+ \to \pi^+\pi^0, \pi^0 \to \gamma U, U \to e^+e^-$ decays. The acceptance of the signal has been evaluated using cuts based on the reconstruction of events. The trigger efficiency is computed for the signal, as well as for the main irreducible background of Dalitz decays, which has the same signature. Finally the expected sensitivity of the experiment after the full period of data taking in terms of upper limits for the Branching Ratio of the decay under investigation is extracted.

5.5.1 Generated samples

The same software described in section 4.2.1 has been used to generate the kaon decays of interest.

The evaluation of the output trigger rate made use of the sample described in chapter 4: 100k events of the six main K^+ decays ($K_{2\pi}$, $K_{3\pi}$, $K^{00}_{3\pi}$, $K_{\mu 2}$, $K_{\mu 3}$, K_{e3}), plus the five classes of beam halo events, where the number of events of the sample refers to the rate in kHz of that channel (526562 beam pions, 99144 μ_{π^+}, 21375 μ_{π^-}, 11792 μ_{K^+}, 3035 μ_{K^-}). The study reported in this chapter has been performed without considering the effects of accidentals.

To compute the acceptance and the trigger efficiency over the signal and the Dalitz events, 100k $K^+ \to \pi^+\pi^0, \pi^0 \to \gamma U, U \to e^+e^-$ and 500k $K^+ \to \pi^+\pi^0, \pi^0 \to \gamma e^+e^-$ have been generated, with the kaon forced to decay in the fiducial region between $z = 105\,\text{m}$ and $z = 165\,\text{m}$.

The generation of the Dalitz sample has been derived from the leading order amplitude corresponding to the $\mathcal{O}(e^3)$ one-photon reducible contribution [115] (Feynman diagram of figure 5.1).

The matrix element of the process can be expressed as a function of two independent

invariant kinematic variables:

$$\begin{aligned} x &= \frac{(p_+ + p_-)^2}{M_{\pi^0}^2}, \qquad & \frac{4m_e^2}{M_{\pi^0}^2} \leq x \leq 1 \\ y &= \frac{2P_{\pi^0} \cdot (p_+ - p_-)}{M_{\pi^0}^2(1-x)}, \qquad & -\sqrt{1 - \frac{4m_e^2}{xM_{\pi^0}^2}} \leq y \leq +\sqrt{1 - \frac{4m_e^2}{xM_{\pi^0}^2}} \end{aligned} \tag{5.13}$$

where p_- and p_+ are the four-momenta of the electron and positron respectively, P_{π^0} is the four-momentum of the neutral pion, m_e is the electron mass and M_{π^0} is the mass of the neutral pion.
Here x represents the square invariant mass of the lepton pair, normalized to the neutral pion square mass. y has been evaluated in the neutral pion rest frame:

$$y = \frac{E_+ - E_-}{\omega} \tag{5.14}$$

where E_- and E_+ are the energies of the electron and positron respectively, and ω is the energy of the photon. Thus y is related to the angle of e^+ in the di-lepton rest frame with respect to the di-lepton momentum in the π^0 rest system.
The simulation generates Dalitz decays with these two variables distributed according to the corresponding partial decay rates [115]:

$$\begin{aligned} \frac{d\Gamma}{dx} &\propto \frac{(1-x)^3}{x^2}\sqrt{1 - \frac{4m_e^2}{xM_{\pi^0}^2}}(xM_{\pi^0}^2 + 2m_e^2)|F(x)|^2 \\ \frac{d\Gamma}{dxdy} &\propto M_{\pi^0}^2 x(1+y^2) + 4m_e^2 \end{aligned} \tag{5.15}$$

where constant factors have been omitted as we are not interested in the total decay width but just its shape (the π^0 sample is forced to the Dalitz decay). $|F(x)|^2$ is the π^0 transition form factor, which is parametrised as a linear function of the x variable: $F(x) = 1 + ax$. The used value of the dimensionless linear coefficient of the form factor is $a = 0.032$ [7].
The simulation of the U boson decay is similar to the above.
The trigger efficiency study described in this chapter has the aim to evaluate the efficiency as a function of the U mass, which is not known. Thus a flat distribution of the U mass in the range between $2m_e$ and M_{π^0} has been used in the generation. The lepton angular distribution is the same as in the second line of equation 5.15. This is justified by the fact that the $\pi^0 \to \gamma U, U \to e^+e^-$ process has the same structure of $\pi^0 \to \gamma\gamma^*, \gamma^* \to e^+e^-$ in terms of spin.
Figure 5.14 shows the distributions of generated samples as a function of the lepton-pair invariant mass.

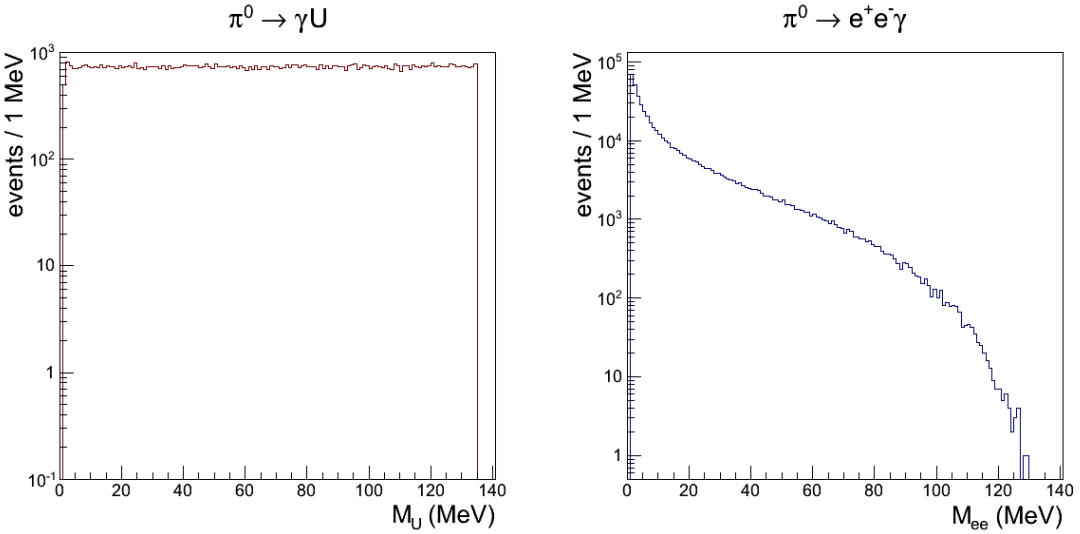

Figure 5.14: Distributions of the generated $\pi^0 \to \gamma U, U \to e^+e^-$ (left) and $\pi^0 \to \gamma e^+e^-$ (right) samples as a function of the lepton-pair invariant mass.

5.5.2 Acceptance

The first study on the produced $\pi^0 \to \gamma U, U \to e^+e^-$ and $\pi^0 \to \gamma e^+e^-$ Monte Carlo samples has the purpose to evaluate the $A(M_U)$ term in equation 5.12 for the signal, and is a first step towards an estimate of the total expected Dalitz background.
A selection has been performed over the samples to compute the acceptance of these two processes as a function of the lepton-pair invariant mass.
Following is a list of the cuts, which have been made on Monte Carlo generated kinematic quantities since not all of the detector reconstructions are available or fully tested in the current version of the software. Detectors acceptances have been evaluated with the propagation of particles from the generation position to the detector, taking into account the magnetic field at the center of the spectrometer.

- Kaon decay vertex between 105 m and 165 m. This condition has been imposed at generation level (since resolution effects due to the reconstruction are not taken into account) in order to avoid generating events which would have been rejected later;
- pion from the $K_{\pi 2}$ process not decaying before the LKr;
- pion from the $K_{\pi 2}$ in the CHOD acceptance;
- photon from the π^0 decay in the LKr acceptance and not in the LAV acceptance;
- electron and positron from the π^0 Dalitz (U boson) decay in the LKr acceptance and not in the LAV acceptance;
- pion momentum $> 5\,\mathrm{GeV}/c$;

- photon energy $> 3\,\text{GeV}$;
- electron and positron momenta $> 3\,\text{GeV}$;
- distance between tracks (π^+,e^+,e^-) at the first STRAW chamber $> 2\,\text{cm}$;
- distance between clusters (π^+,e^+,e^-,γ) at the LKr calorimeter $> 15\,\text{cm}$.

These conditions are driven by the characteristics of the NA62 detectors and the requests of the analysis. The charged pion will be reconstructed with the LKr calorimeter and MUV1-2 deposits, so no decay is requested. Dalitz decay products must be reconstructed in the LKr calorimeter: their position and energy resolutions are directly related to the resolution on the lepton-pair invariant mass, thus a minimum energy of the particles is required, as well as a minimum distance on the calorimeter surface to allow the identification of clusters. Similar conditions on momenta and track distances at the first STRAW chamber are imposed to ensure a good efficiency of the spectrometer in the evaluation of momenta and directions of charged particles.
5224 out of 100000 U boson events passed the described selection, while the number of surviving events is 8427 out of 500000 in the Dalitz case. The distributions of events passing the selection is shown in figure 5.15 by the shaded histograms, compared with the generated samples of figure 5.14.

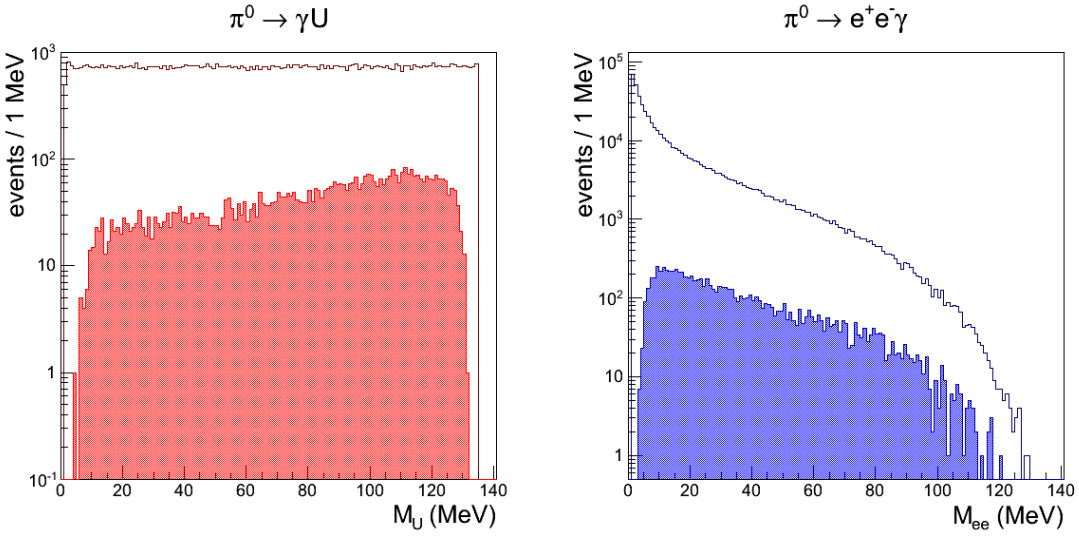

Figure 5.15: Invariant lepton-pair mass distributions of $\pi^0 \to \gamma U, U \to e^+e^-$ (left) and $\pi^0 \to \gamma e^+e^-$ (right) events passing the analysis-like selection (shaded histograms) compared with the distributions for generated events (solid line).

The fraction of remaining events is quite different between the two cases ($\sim 5\%$ for the U, $\sim 1.5\%$ for the Dalitz), and this is due to the Dalitz distribution in the lepton-pair

invariant mass, since the acceptance is lower for low invariant masses.
The ratios of the distributions of figure 5.15 are shown in figure 5.16. The trend of the acceptance is as expected (lower for low invariant masses), since a lepton-pair with a low invariant mass corresponds to a small angle between the electron and positron in the laboratory reference frame and these events are affected by cuts on track and cluster distances. Furthermore, the acceptances as a function of the lepton-pair invariant mass are in agreement within the statistical errors, meaning that the U boson decay and the Dalitz process are identical from the point of view of event reconstruction.

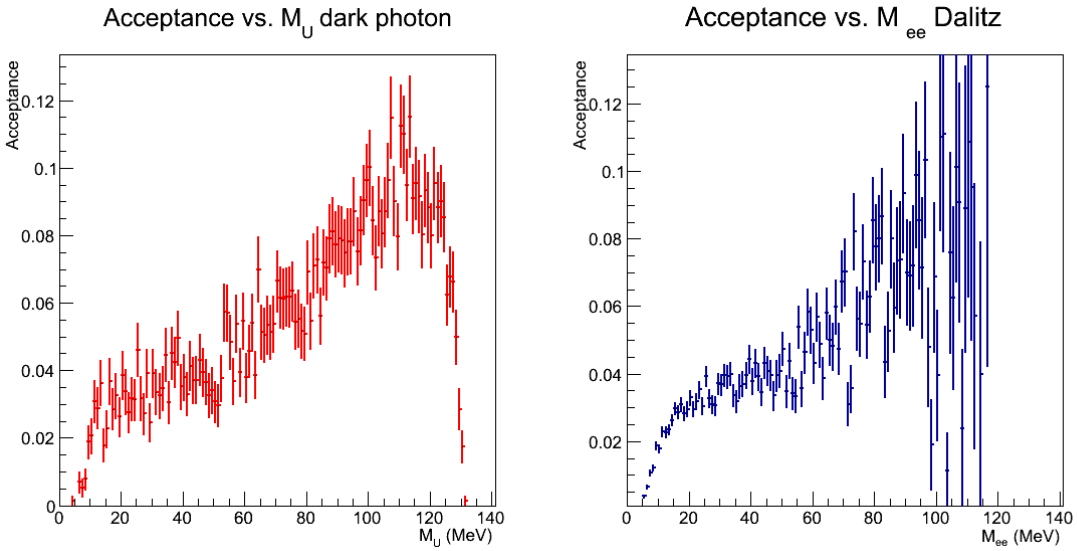

Figure 5.16: $\pi^0 \to \gamma U, U \to e^+e^-$ (left) and $\pi^0 \to \gamma e^+e^-$ (right) event acceptances as a function of the lepton-pair invariant mass.

5.5.3 L0 trigger

A trigger strategy to collect U decays into electron and positron (and the irreducible background of Dalitz decays) has been developed and is described in this section. The goal of the Monte Carlo study of the trigger is to achieve the highest possible efficiency in collecting the signal while keeping the trigger output rate as low as possible in order to fit within the maximum L0 rate of 1 MHz together with the main trigger, control triggers and triggers for other physics studies.
The generation of trigger primitives in the Monte Carlo simulation is described in detail in section 4.3.1.
The RICH as well as the CHOD are positive elements for the identification of charged particles belonging to the processes under study (π^+,e^+,e^-). The MUV3 is used as veto since no muons are expected in the final state. The last station of LAVs (LAV12) will be

used in veto as well: we are interested in events in which the decay products are detected in the LKr calorimeter, and this means that all LAVs will have no hits for good events. The main difference with respect to the L0 analysis of chapter 4 lies in the use of the LKr calorimeter: this detector is now used as positive element in the L0 Trigger Processor.
The parameters studied in chapter 4 and more strictly related to the firmware implementation, e.g. the time binning for multiplicity counting, are kept fixed to the values determined there. These are not expected to be related to the process under study, and the optimized values chosen during the parameter study is used also in the following analysis.
The primitive generation parameters which affect the trigger for the collection of U boson and Dalitz events are:

- RICH minimum multiplicity threshold
- RICH maximum multiplicity threshold
- CHOD minimum quadrants configuration
- LKr minimum number of clusters
- LKr minimum primitive total energy
- LAV12 in veto
- MUV3 in veto

The CHOD quadrants configuration is related to the number of firing quadrants: Q1 means that at least one quadrant is hit, Q2, Q3 and Q4 similarly, QX indicates that (at least) two opposite quadrants are crossed by charged particles (thus included in Q3 and Q4). The positive element LKr requires a minimum number of clusters, with a minimum sum of cluster energies. The presence of both veto detectors is studied as well.
The starting values for the listed parameters are shown in table 5.3. This represents the minimal configuration for the trigger RICH $\times$ CHOD $\times$ LKr ($\times$ NOT(MUV3) $\times$ NOT(LAV12) where the condition on LAV12 is optional). The 0.7 GeV value for the energy requirement in the LKr corresponds to the SuperCell energy threshold parameter (see section 4.4.1), and is the minimum value which allows to obtain a primitive from the LKr.

Similarly to the analysis of section 4.4, a set of simulations varying each parameter has been produced, keeping fixed all other ones to the minimal configuration of table 5.3.

The rates and the trigger efficiencies for U boson and Dalitz events have been evaluated using the same method of section 4.4. The reference samples for the computation of the efficiency are those obtained from the selection described in section 5.5.2 (shaded histograms of figure 5.15).

RICH min threshold	1
RICH max threshold	∞
CHOD quadrants	Q1
LKr min number of clusters	1
LKr total energy	0.7 GeV
LAV12	not used
MUV3	not used

Table 5.3: Starting minimal configuration of the L0 parameters under study.

The scan and the results for all parameters of table 5.3 are presented in figures from 5.17 to 5.23. In each figure, the left plot represents the trigger efficiency (integrated over the lepton-pair invariant mass range) for both U boson and Dalitz decays, while the right plot shows the cumulative rate due to the contributions from six main kaon decays and halo components. Reported error bars are statistical errors only. The rates are not to be compared with the final rate because for each parameter the other ones are not set to their optimised values but to the minimal configuration.

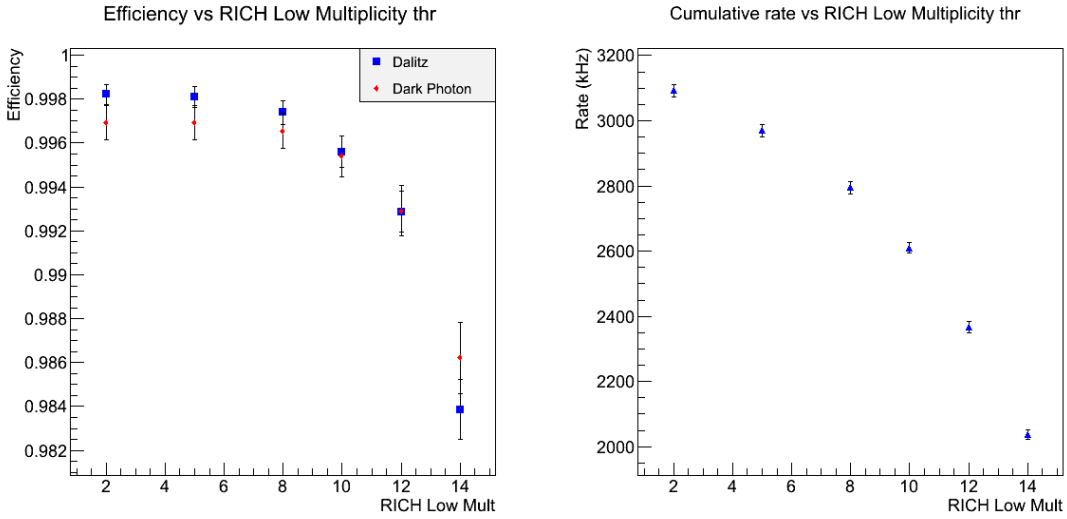

Figure 5.17: Efficiency and rate dependence on RICH minimum multiplicity threshold parameter.

Figure 5.17 shows the dependence on the RICH minimum multiplicity threshold parameter. As expected, the efficiency remains high (above 98%) also for the highest considered value (multiplicity threshold at 14). This is due to the fact that the three tracks of the final state are into the acceptance of RICH, the electron and positron being always above the Čerekonv threshold, so a multi-ring configuration with high multiplicity is present in the RICH. All kaon decay channels with one charged particle in the final state are suppressed by this condition, while the $K_{\pi 3}$ is not affected.

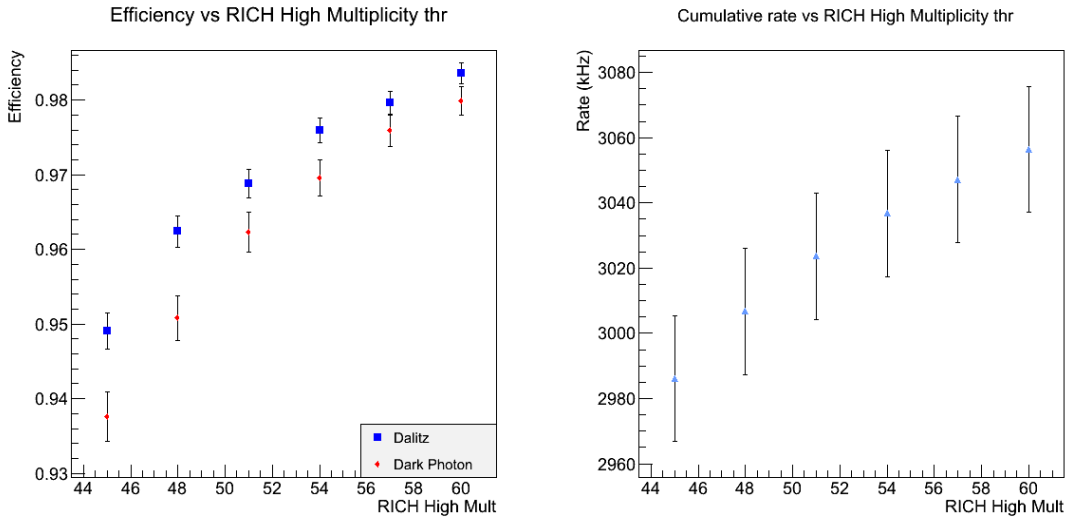

Figure 5.18: Efficiency and rate dependence on RICH maximum multiplicity threshold parameter.

The dependence on the RICH maximum multiplicity threshold is highlighted in figure 5.18. The loss of efficiency is of the order of 5% over the scanned range of maximum multiplicity, while the rate is slightly lowered by the changes in this parameter due to the fact that most of kaon decays have a lower RICH multiplicity.

For what concerns the dependence on the CHOD quadrant configuration (figure 5.19), at least a Q2 is expected for the signal. Requiring charged particles in opposite quadrants (QX, represented by the 2.5 value of the x axis) contributes with a rate reduction and a loss of about 10% efficiency. This loss increases to 20% for the case of Q3: this is mainly due to events with a low invariant mass of the lepton pair, corresponding to a small angle between the electron and positron in the laboratory reference frame, which consequently have in this case a good chance to hit the same CHOD quadrant (at high energies, when the deflection due to the magnet is small with respect to the CHOD quadrant transverse size).

Figure 5.20 shows the effects of varying the requested minimum number of clusters of the LKr trigger primitives. The efficiency is above 95% when requiring at least three clusters, and this condition turns out to be the most effective in terms of trigger output rate reduction. The remaining events are dominated by $K_{\pi 2}$, K_{e3} and $K_{\pi 3}^{00}$, while the $K_{\pi 3}$ component is negligible due to the low probability that the three pions, even if in the LKr acceptance, are all reconstructed by the LKr L0 trigger primitives generation algorithm; channels with muons in the final state are rejected by this condition.

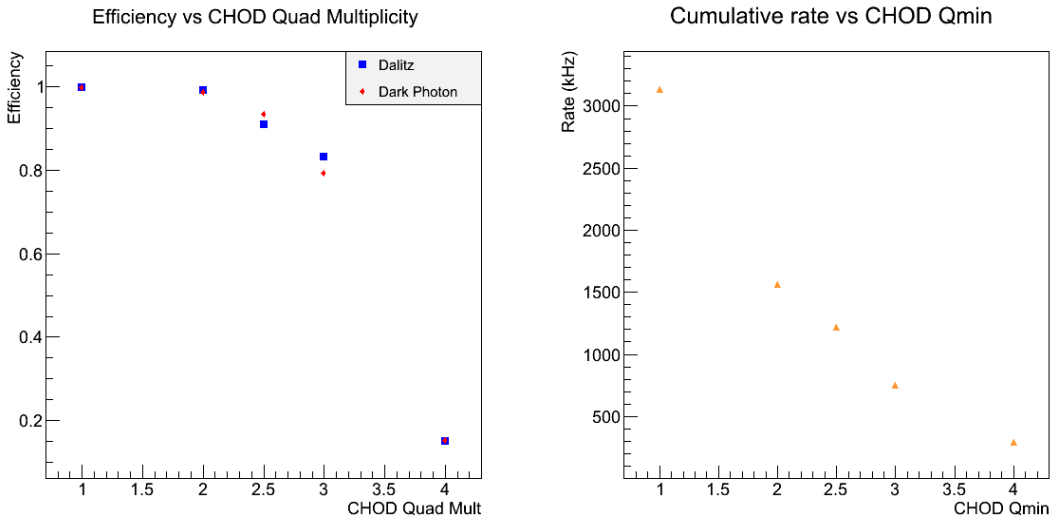

Figure 5.19: Efficiency and rate dependence on CHOD quadrant configuration parameter. The value 2.5 represents the QX condition, while an integer value n represents the Qn condition.

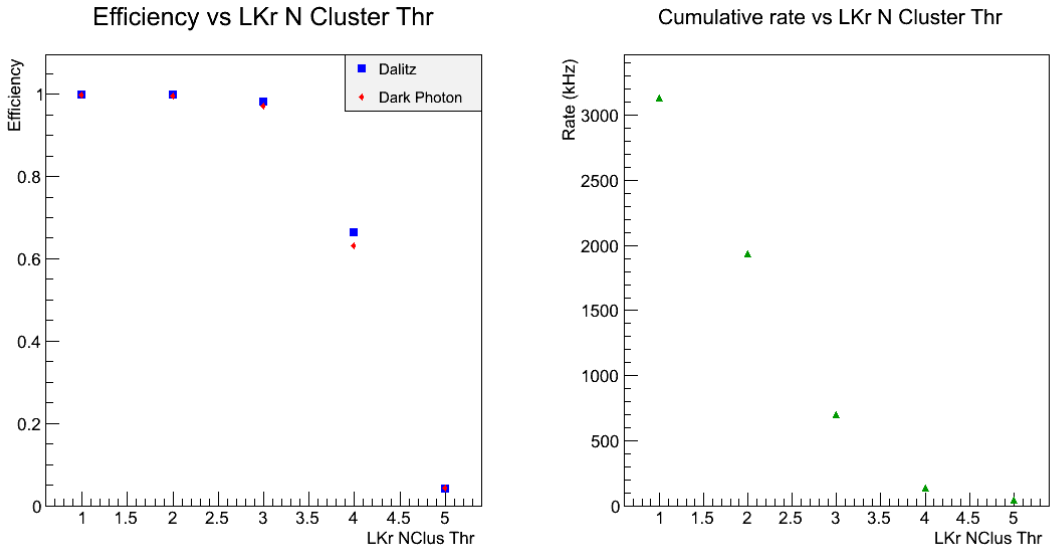

Figure 5.20: Efficiency and rate dependence on LKr minimum number of clusters parameter.

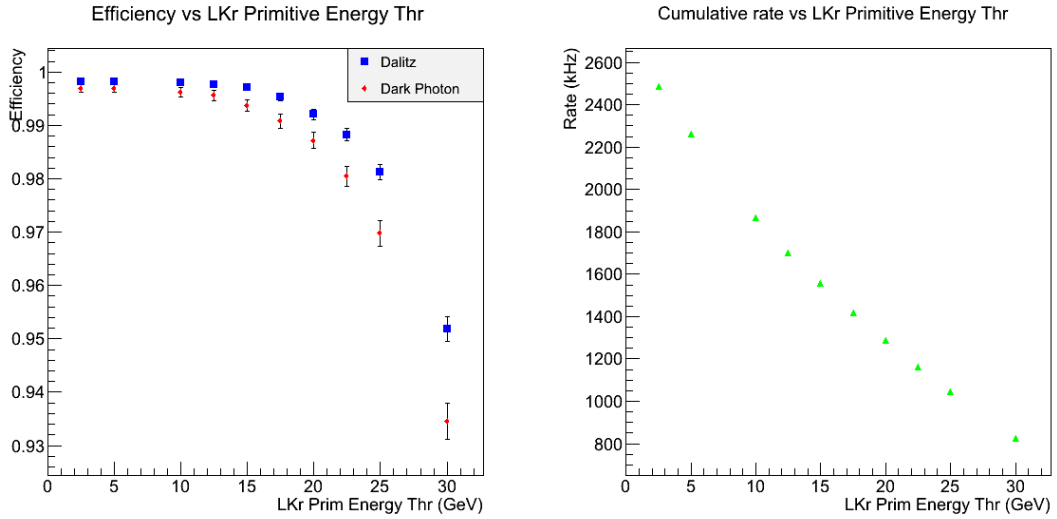

Figure 5.21: Efficiency and rate dependence on LKr primitive energy parameter.

A further reduction of the trigger output rate comes from the other parameter related to the LKr, the total energy of the primitive (sum of the clusters' energies), whose significance is shown in figure 5.21. For an energy threshold equal to 25 GeV the efficiency is above 97%. The effect on the rate follows the same reasoning as for the request on the number of clusters.

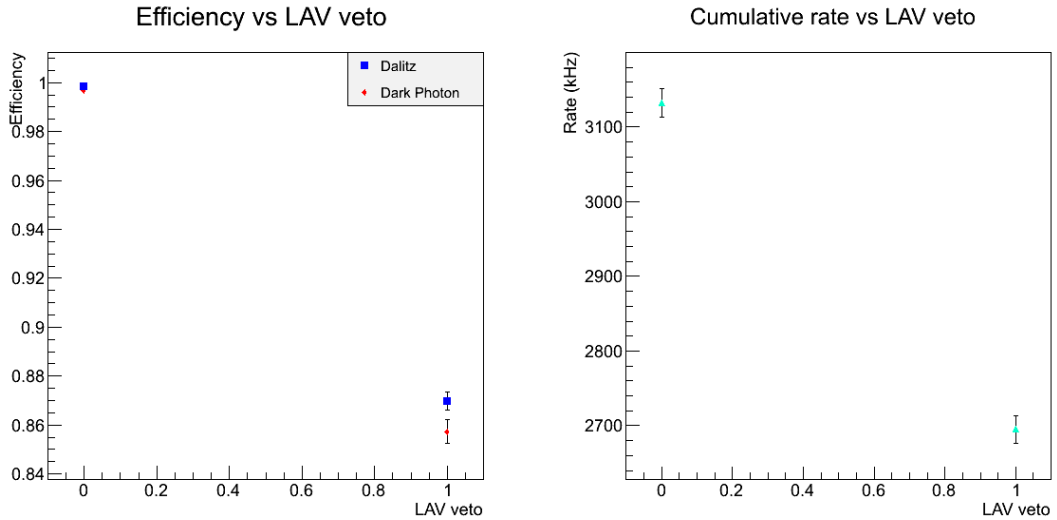

Figure 5.22: Efficiency and rate dependence on LAV12 veto condition in the L0 trigger.

The effectiveness of applying the LAV12 veto condition is evaluated in figure 5.22. The rate reduction is unsatisfactory if compared with the loss of efficiency, thus the LAV12 will

not be included in the L0 trigger for the assessment of the final results.

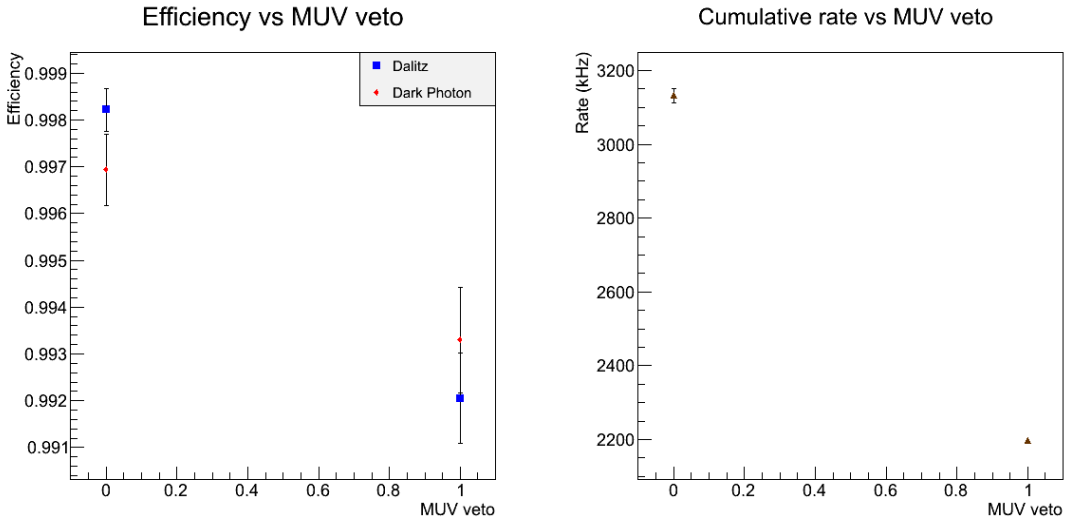

Figure 5.23: Efficiency and rate dependence on MUV3 veto condition in the L0 trigger.

Figure 5.23 shows that MUV3 does not affect the trigger efficiency. Its effect on rate reduction is highly correlated to the LKr conditions, which suppress kaon channels with muons in the final state and halo components, nevertheless including MUV3 in the trigger gives an additional attenuation.
The left plots in figures 5.17 to 5.23 show the efficiencies integrated over the lepton-pair invariant mass. The values for U boson decays and Dalitz decays are similar and in agreement in most cases, even if these numbers depends from the shape of the distributions of selected events (figure 5.15).
The trigger efficiencies for both processes as a function of the electron-positron pair invariant mass have been investigated for all the described sets of parameters. Figure 5.24 shows some of the results (for parameter values corresponding to the final choice of the L0 trigger, one at a time): RICH min (14) and max (60) multiplicity threshold at the top, LKr number of clusters (3) and energy threshold (25 GeV) at the center, CHOD quadrant configuration (QX) and MUV3 at the bottom. The general outline presents a similarity for the two processes within the statistical errors, with some deviation which can explain the slight differences in the integral efficiencies, e.g. in figure 5.21.

The final set of parameters in table 5.4 has been chosen to maximize the L0 trigger efficiency and minimize the total trigger output rate. This set corresponds to the expected configuration for a multi-track event with at least three clusters on the LKr calorimeter and no muons in the final state.

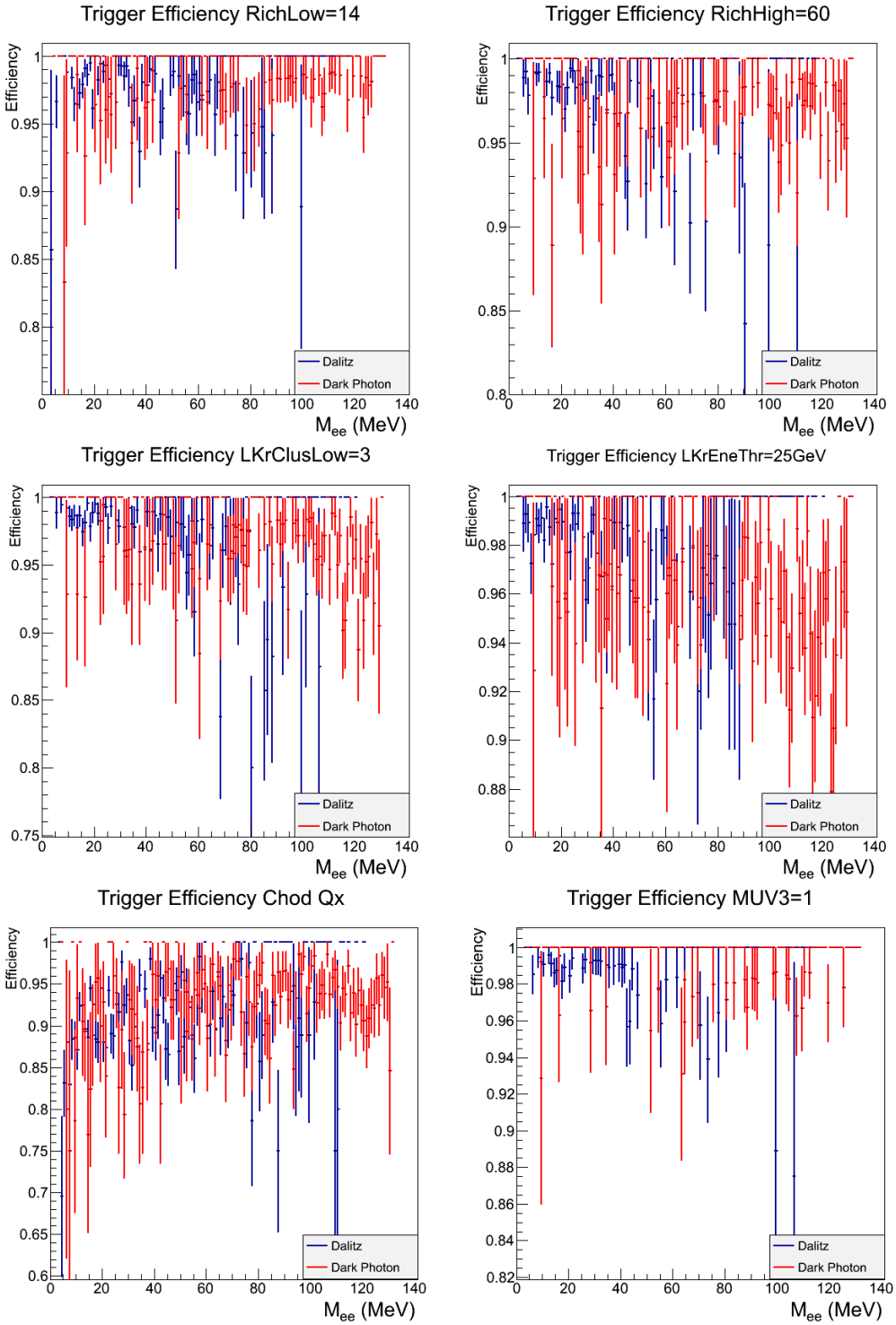

Figure 5.24: Trigger efficiencies for the different proposed L0 cuts as a function of the lepton-pair invariant mass. The value of each parameter corresponds to the final choice of its value.

RICH min threshold	14
RICH max threshold	60
CHOD quadrants	QX
LKr min number of clusters	3
LKr total energy	25 GeV
LAV12	not used
MUV3	used

Table 5.4: Optimized configuration of the L0 trigger parameters for the collection of U boson and Dalitz decays.

The values of table 5.4 have been used in a final simulation to compute the trigger output rate and the efficiencies for both $\pi^0 \to \gamma U, U \to e^+e^-$ and $\pi^0 \to \gamma e^+e^-$ events.
Table 5.5 summarizes the effect of the described trigger selection on the different kaon processes, muon halo and beam pions. Reported errors are statistical only. In case of no residual events, the 68.27% confidence level upper limits in absence of background [70] are reported.
The main contribution to the final rate comes from $K_{\pi 2}$ events, where a conversion of one of the two photons from the π^0 results in an additional track on the CHOD: these events will be rejected at analysis level using the spectrometer reconstruction. The same effect explains the other non-negligible contributions to the total rate coming from K_{e3} (the residual rate is proportional to the initial one as for $K_{\pi 2}$) and $K^{00}_{\pi 3}$ (rate proportional to the initial one with a factor 2 because of two π^0s in the final state).

Process	Rate(kHz)	L0 rate (kHz)
$K_{\mu 2}$	8452	< 0.11
$K_{\mu 3}$	446	0.045 ± 0.014
K_{e3}	674	23.1 ± 0.4
$K_{\pi 2}$	2748	82.2 ± 1.5
$K_{\pi 3}$	743	2.79 ± 0.14
$K^{00}_{\pi 3}$	234	16.37 ± 0.19
μ_{π^+}	99144	< 1.3
μ_{K^+}	11792	< 1.3
μ_{π^-}	21375	< 1.3
μ_{K^-}	3035	< 1.3
π^+	526562	< 1.3
Total L0		124 ± 3
		Efficiency
$\pi^0 \to \gamma U, U \to e^+e^-$		$(87.1 \pm 0.5)\%$
$\pi^0 \to \gamma e^+e^-$		$(85.8 \pm 0.4)\%$

Table 5.5: L0 trigger rates for different channels and L0 trigger efficiencies after applying the final set of L0 parameters.

The efficiencies reported in table 5.5 are integrated values over the whole spectrum of the invariant mass. The $\varepsilon(M_U)$ function of equation 5.12 must be extracted from the distribution of the U boson trigger efficiency as a function of the U boson mass, which is shown in figure 5.25 (right) together with the corresponding distribution for Dalitz events (left) to be used for the background estimate. The integral of the convolution between these functions and the shaded distributions of figure 5.15 gives the efficiencies of table 5.5.

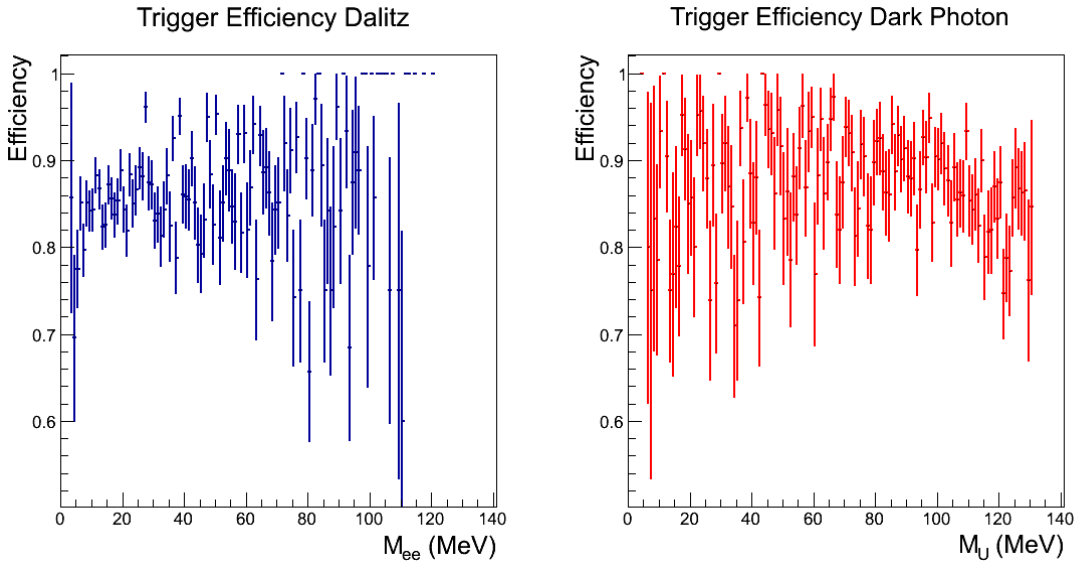

Figure 5.25: $\pi^0 \to \gamma e^+ e^-$ (left) and $\pi^0 \to \gamma U, U \to e^+ e^-$ (right) L0 trigger efficiencies as a function of the lepton-pair invariant mass after applying the final set of L0 parameters.

5.5.4 Expected upper limits

The last step towards the computation of the expected upper limit is the evaluation of the total Dalitz background, which is the limiting factor to the single event sensitivity for the detection of the $\pi^0 \to \gamma U, U \to e^+ e^-$ process.

The invariant mass distribution of the $\pi^0 \to \gamma e^+ e^-$ sample, obtained after the acceptance selection (section 5.5.2) and the trigger conditions (section 5.5.3), has been normalized to the expected total number of π^0 Dalitz decays ($\Phi_{\pi^0} \times \mathrm{BR}(\pi^0 \to \gamma e^+ e^-) = 6 \times 10^{12} \times 0.01174 \sim 7 \times 10^{10}$).

The Dalitz background distribution is shown in figure 5.26. The integral of the distribution attests that the reconstructed Dalitz sample at the end of the data taking period will be of the order of 10^9.

From the background distribution of figure 5.26, an upper limit N_{up} for the counting of $\pi^0 \to \gamma U$ events is extracted for each invariant mass bin.

This number has a strong dependence on the bin width, which must be large enough to

contain a possible U peak. The intrinsic width of the U boson is shown in figure 5.3, and is below 100 eV for the mass range under study. This value is negligible with respect to the expected mass invariant resolution: this cannot be estimated from Monte Carlo simulations due to the absence of a full detector reconstruction in the available software; nevertheless the mass invariant resolution of the NA48 experiment (the LKr calorimeter is the same) is of the order of $1\,\mathrm{MeV}/c^2$, and the expected improvement coming from new detectors like the GTK and the STRAW spectrometers drives the choice of a bin width equal to $1\,\mathrm{MeV}/c^2$. This rough estimate can be used to compute the expected upper limits for NA62, however a future measurement will rely on a precise evaluation of the resolution to obtain the right background distribution.
N_{up} for each bin has been computed according to the procedure described in [69], assuming that the number of observed events is equal to the expected Dalitz background. No uncertainty has been used for the background: we can safely assume that generating a large number of events can reduce the uncertainty to a negligible value. Furthermore, the theoretical uncertainties on the Dalitz distribution, from which the generation is derived, lie on high order radiative corrections [115]: this small effects are negligible for the purpose of this work.

The upper limit on the Branching Ratio is finally obtained multiplying N_{up} by the single event sensitivity $U_{\mathrm{SES}}(M_U)$ of equation 5.12. Figure 5.27 shows the expected upper limits at 90% confidence level for the Branching Ratio of $\pi^0 \to \gamma U$ (left) and for ε^2 as a function of the U boson mass, assuming no trigger downscaling. The chosen mass range is between $10\,\mathrm{MeV}/c^2$ and $105\,\mathrm{MeV}/c^2$, while outside this interval the lack of statistics causes the loss of significance (the obtained upper limits are above the current experimental excluded values).
The trigger output rate of about 120 kHz is probably too high to be included together with the main trigger (see results of chapter 4) and other control triggers for the NA62 experiment, given the limit of 1 MHz. Figure 5.28 shows the expected upper limit results in the same mass range, when applying a trigger downscaling factor $D = 10$ both to the background distribution of figure 5.26 and to the single event sensitivity in equation 5.12.

The comparison of these results with the exclusion plots in the same mass region obtained by the experiments described in section 5.3 is shown in figure 5.29. The described trigger strategy for the collection of π^0 Dalitz (and $\pi^0 \to \gamma U$) decays over the entire NA62 data taking period could result in an improvement of 2 orders of magnitude with respect to the current experimental limits in the mass region between $10\,\mathrm{MeV}/c^2$ and $105\,\mathrm{MeV}/c^2$, even with a trigger downscaling factor which would safely allow its inclusion in the NA62 trigger rate budget.
In addition to the improvement over the WASA experiment results, the proposed upper

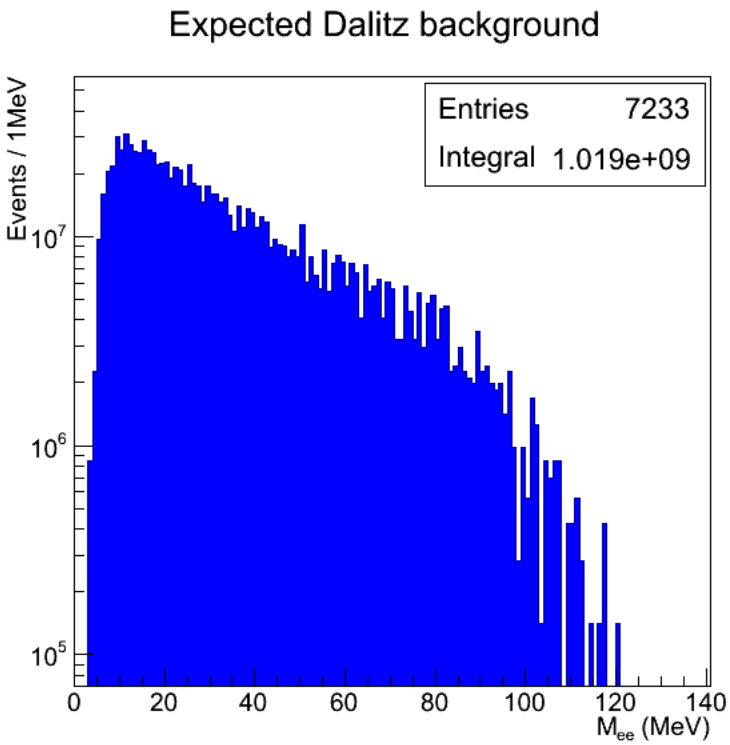

Figure 5.26: Dalitz background distribution as a function of the lepton-pair invariant mass. The number of entries indicates the number of events within the generated sample surviving acceptance and trigger selections, while the integral of bin contents has been obtained through normalization of the generated sample to the expected total number of Dalitz decays.

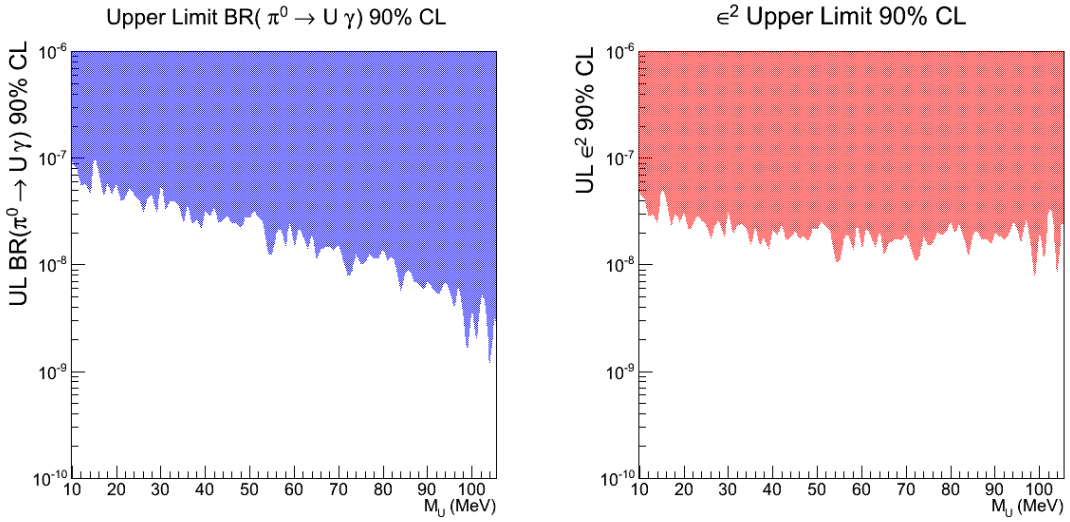

Figure 5.27: Expected NA62 upper limits at 90% confidence level for the Branching Ratio of $\pi^0 \to \gamma U$ (left) and for ε^2 as a function of the U boson mass, assuming no trigger downscaling.

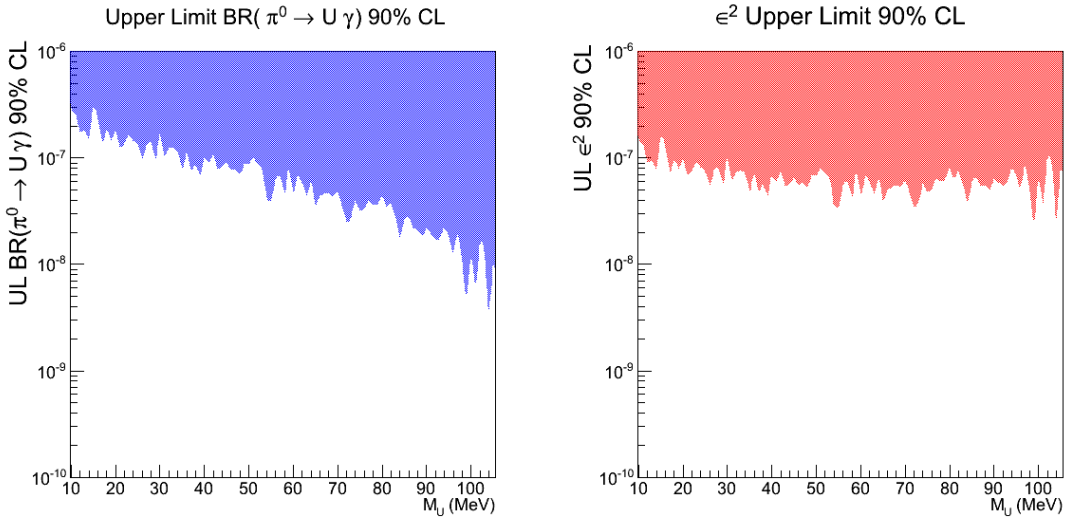

Figure 5.28: Expected NA62 upper limits at 90% confidence level for the Branching Ratio of $\pi^0 \to \gamma U$ (left) and for ε^2 as a function of the U boson mass, assuming a trigger downscaling factor $D = 10$.

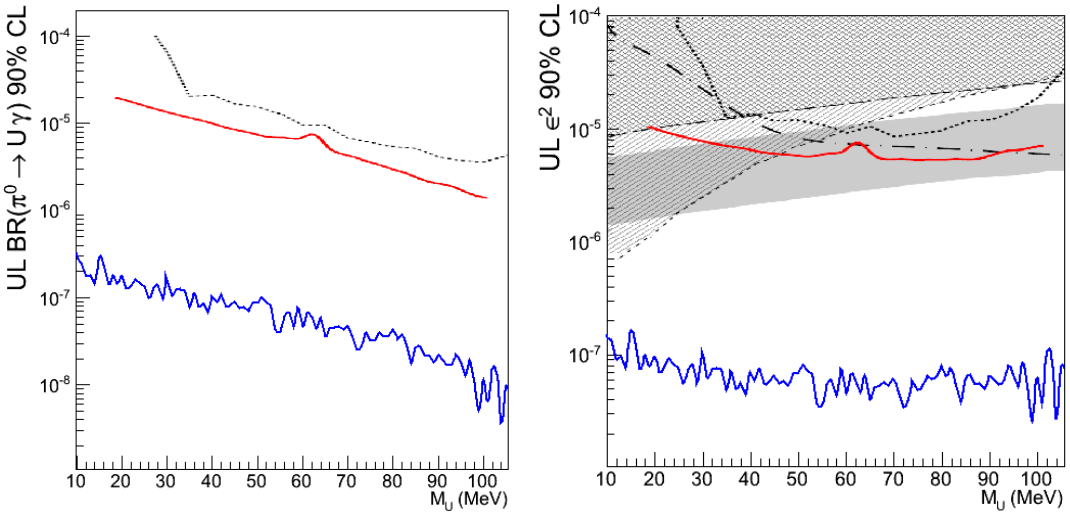

Figure 5.29: Comparison of the 90% confidence level upper limits obtained in this work (blue line) with WASA (red line) and SINDRUM (dotted line) results for the Branching Ratio of $\pi^0 \to \gamma U$ (left) and the mixing parameter ϵ^2 (right) versus the vector boson mass M_U. In the right plot KLOE results (dashed dotted), the exclusion areas from electron and muon $(g-2)$ and the grey band corresponding to the present experimental value of $(g-2)_\mu$ are also shown.

limits of figure 5.28 cover the present $(g-2)_\mu$ band: a negative result by NA62 would therefore rule out the U boson as an explanation of the experimental muon magnetic moment anomaly.

Conclusions

The work presented in this thesis focused on two aspects of the Trigger and Data Acquisition system of the NA62 experiment.
The main goal of the NA62 experiment at CERN is to measure the Branching Ratio of the ultra-rare $K^+ \to \pi^+\nu\bar{\nu}$ decay, collecting about 100 events to test the Standard Model of Particle Physics. Readout uniformity of subdetectors, scalability, efficient online selection and lossless high rate readout are key issues.
The first part of the work concerned the design, development and testing of the TDCB and TEL62 boards, which are the common blocks of the NA62 TDAQ system. TDCBs measure hit times from subdetectors, TEL62s process and store them in a buffer, extracting only those requested by the trigger system, which merges trigger primitives also produced by TEL62s.
A significant contribution was given in the evolution of the firmware of both TDCB and TEL62's FPGAs.
The system has been extensively tested at the end of 2012 during the NA62 Technical Run: time resolutions were found to be compatible with the intrinsic detector resolutions, thus confirming a negligible contribution from the electronics; the handled input trigger rate and the output data bandwidth of the system are in agreement with the requirements of the experiment; the integrated trigger primitives generation has been implemented and is being tested during the 2014 NA62 Pilot Run.
The second part of the work focused on the simulation of the hardware low-level trigger.
A minimal L0 trigger scheme for the collection of $K^+ \to \pi^+\nu\bar{\nu}$ decays has been discussed, focusing on subdetectors expected to be available in the first phase of the experiment data taking.
The scheme of L0 primitive production for each involved subdetector was described, pointing out some crucial parameters for the design of the L0 trigger which have been studied. The optimized set of parameters is shown in table 4.3 and will be used in the first phases of the 2014/15 NA62 physics run.
The Monte Carlo generation of events with accidentals has been implemented. After an upgrade of the MUV3 simulation the final trigger efficiency and L0 trigger rate have been evaluated and are listed in table 4.11; muon halo, beam pions, $K_{\mu 2}$ and $K_{\pi 2}$ are the main

surviving components after applying this trigger scheme.
The L0 trigger output rate is safely below the limit of 1 MHz and it allows the presence of additional control triggers as well as triggers for studying other rare and forbidden decays.
A L0 trigger selection for the search for a dark photon (U boson) in π^0 decays has been studied as well.
A Monte Carlo generator has been developed to simulate $K^+ \to \pi^+\pi^0, \pi^0 \to \gamma U, U \to e^+e^-$ decays. The acceptances of this process and the main background $\pi^0 \to \gamma e^+e^-$ (Dalitz decay) have been computed. The L0 trigger selection has been optimized to maximize the trigger efficiency and to reduce the trigger output rate: the results are shown in tables 5.4 and 5.5.
The presented study shows that a trigger downscaling factor 10 safely allows its inclusion in the NA62 trigger budget for the upcoming 2015 data taking phase.
The expected upper limits on the Branching Ratio of the $\pi^0 \to \gamma U, U \to e^+e^-$ decay and on the coupling of the U boson with the photon are reported in figure 5.29. An improvement of 2 orders of magnitude with respect to the current experimental limits in the mass region between $10\,\mathrm{MeV}/c^2$ and $105\,\mathrm{MeV}/c^2$ can be achieved in 3 years of data taking, fully covering the present experimental $(g-2)_\mu$ band and ruling out the U boson as an explanation of the experimental muon magnetic moment anomaly in case of no observation.

Bibliography

[1] J. Brod, M. Gorbahn, and E. Stamou, Phys. Rev. D **83**, 034030 (2011).

[2] G. Isidori, F. Mescia, P. Paradisi, C. Smith, and S. Trine, JHEP **0608**, 064 (2006).

[3] M. Blanke, A. J. Buras, B. Duling, S. Recksiegel, and C. Tarantino, Acta Phys. Polon. B **41**, 657 (2010).

[4] A. V. Artamonov et al., Phys. Rev. D **79**, (E949 collaboration), 092004 (2009).

[5] M. Kobayashi and T. Maskawa, Prog. Theor. Phys. **49**, 652 (1973).

[6] L. Wolfenstein, Phys. Rev. Lett. **51**, 1945 (1983).

[7] J. Beringer et al., Phys. Rev. D **86**, (Particle Data Group), 010001 (2012).

[8] A. J. Buras, M. Gorbahn, U. Haisch, and U. Nierste, Phys. Rev. Lett. **95**, 261805 (2005).

[9] A. Abulencia et al., Phys. Rev. Lett. **97**, 242003 (2006).

[10] R. Aaij et al., Phys. Lett. B **709**, 177 (2012).

[11] G. Buchalla and A. J. Buras, Nucl. Phys. B **548**, 309 (1999).

[12] W. J. Marciano and Z. Parsa, Phys. Rev. D **53**, R1 (1996).

[13] F. Mescia and C. Smith, Phys. Rev. D **76**, 034017 (2007).

[14] T. Inami and C. S. Lim, Prog. Theor. Phys. **65**, 1772(E) (1981).

[15] M. Misiak and J. Urban, Phys. Lett. B **451**, 161 (1999).

[16] J. R. Ellis and J. S. Hagelin, Nucl. Phys. B **217**, 189 (1983).

[17] J. Brod and M. Gorbahn, Phys. Rev, D **78**, 034006 (2008).

[18] G. Isidori, F. Mescia, and C. Smith, Nucl. Phys. B **718**, 319 (2005).

[19] U. Camerini et al., Phys. Rev. Lett. **23**, 326 (1969).

[20] G. D. Cable et al., Phys. Rev. D **8**, 3807 (1973).

[21] Y. Asano et al., Phys. Lett. B **107**, 159 (1981).

[22] S. Adler et al., Phys. Rev. Lett. **79**, (E787 Collaboration), 2204–2207 (1997).

[23] S. Adler et al., Phys. Rev. Lett. **88**, (E787 Collaboration), 041803 (2002).

[24] S. Adler et al., Phys. Lett. B **537**, (E787 Collaboration), 211 (2002).

[25] V. V. Anisimovsky et al., Hys. Rev. Lett. **93**, (E949 Collaboration), 031801 (2004).

[26] G. Ruggiero, PoS(KAON13), NA62 Collaboration, 032 (2013).

[27] H. W. Atherton et al., *Precise measurements of particle production by 400 GeV/c protons on beryllium targets*, tech. rep., CERN Yellow Report: CERN 80-07 (1980).

[28] F. Anghinolfi, P. Jarron, A. N. Martemiyanov, E. Usenko, H. Wenninger, M. C. S. Williams, and A. Zichichi, Nucl. Instrum. and Meth. A **533**, 183–187 (2004).

[29] A. Kluge et al., Nucl. Instrum. and Meth. A **732**, 511–514 (2013).

[30] D. Moraes et al., *Internal note LHCb-MUON 2003-009*, 2003.

[31] B. Angelucci et al., Nucl. Instrum. and Meth. A **621**, 205–211 (2010).

[32] A. Ceccucci, R. Fantechi, P. Farthouat, G. Lamanna, J. Rouet, V. Ryjov, and S. Venditti, JINST **9**, C01047 (2014).

[33] V. Fanti et al., Nucl. Instrum. and Meth. A **574**, NA48 Collaboration, 433–471 (2007).

[34] A. Antonelli et al., JINST **7**, C01097 (2012).

[35] K. Ahmet et al., Nucl. Instrum. and Meth. A **305**, OPAL Collaboration, 275 (1991).

[36] T. Baumann, M. Büchele, H. Fischer, M. Gorzellik, T. Grussenmeyer, F. Herrmann, P. Jörg, K. Königsmann, P. Kremser, T. Kunz, C. Michalski, C. Schill, S. Schopfere, and T. Szameitat, JINST **8**, C01016 (2013).

[37] Altera®, *DE4 board User Manual*, `ftp://ftp.altera.com/up/pub/Altera_Material/12.1/Boards/DE4/DE4_User_Manual.pdf`.

[38] Altera®, *Stratix IV Device Handbook*, `http://www.altera.com/literature/hb/stratix-iv/stratix4_handbook.pdf`.

[39] G. Collazuol, G. Lamanna, J. Pinzino, and M. S. Sozzi, Nucl. Instrum. and Meth. A **662**, 49–54 (2012).

[40] Altera®, *Cyclone III Device Handbook*, `http://www.altera.com/literature/hb/cyc3/cyclone3_handbook.pdf`.

[41] P. Lichard, G. Konstantinou, A. Villar Villanueva, and V. Palladino, JINST **9**, C03013 (2014).

[42] *TTC: timing, trigger and control systems for LHC detectors*, `http://ttc.web.cern.ch/ttc/intro.html`.

[43] B. G. Taylor, *TTC laser transmitter (TTCex, TTCtx, TTCmx) user manual*, RD12 working document, `http://ttc.web.cern.ch/TTC/TTCtxManual.pdf`.

[44] P. Jovanovic, *Preliminary Design Review Document, ALICE-INT-2003-056 LTU*, 2003.

[45] J. Christiansen et al., *TTCrx reference manual*, CERN-EP/MIC note, RD12 collaboration, (2004) http://ttc.web.cern.ch/TTC/TTCrx_manual3.9.pdf.

[46] J. Christiansen, *HPTDC, High Performance Time to Digital Converter*, CERN-EP/MIC, (2004) http://tdc.web.cern.ch/tdc/hptdc.htm.

[47] Altera®, *Serial Configuration (EPCS) Devices Datasheet*, http://www.altera.com/literature/hb/cfg/cyc_c51014.pdf.

[48] P. Moreira, *QPLL project*, (2005) http://proj-qpll.web.cern.ch/proj-qpll.

[49] B. Angelucci, E. Pedreschi, M. Sozzi, and F. Spinella, JINST **7**, C02046 (2012).

[50] G. Haefeli et al., Nucl. Instrum. and Meth. A **560**, 494 (2006).

[51] Altera®, *Stratix III Device Handbook*, http://www.altera.com/literature/hb/stx3/stratix3_handbook.pdf.

[52] H. Muller, A. Guirao, F. Bal, X. Tao, J. Christiansen, M. Muecke, N. Neufeld, and G. Haefeli, *Quad Gigabit Ethernet plug-in card*, Cern Electronic Document Server EDMS 520885, https://edms.cern.ch/file/520885/2/gbe_manual_ver2.pdf.

[53] F. Fontanelli, B. Jost, G. Mini, N. Neufeld, R. Abdel-Rahman, K. Rolli, and M. Sannino, *CC-PC Gluecard Application and User's Guide*, LHCb Technical Note LHCb 2003-098, (2003) https://edms.cern.ch/file/500461/1/lhcb-2003-098.pdf.

[54] F. Gonnella, TDAQ WG Meeting 18/12/2013, https://indico.cern.ch/event/286726/contribution/8/material/slides/1.pdf.

[55] *NA62 Technical Design*, (2010) https://na62.web.cern.ch/na62/Documents/TD_Full_doc_v10.pdf.

[56] E. Goudzovski and C. Parkinson, *Note NA62-14-07*, May 2014.

[57] *NA62 framework*, http://sergiant.web.cern.ch/sergiant/NA62FW/html/.

[58] K. L. Brown and C. Iselin, *Decay TURTLE*, (Feb. 1974) http://cds.cern.ch/record/186178/files/cern-74-02.pdf.

[59] S. Agostinelli et al., Nucl. Instrum. and Meth. A **506**, 250–303 (2003).

[60] C. Iselin, *HALO*, (Aug. 1974) http://cds.cern.ch/record/186209/files/CERN-74-17.pdf.

[61] S. Balev, Software WG Meeting 30/03/2011, https://indico.cern.ch/event/133194/contribution/4/material/slides/0.pdf.

[62] A. Cassese, Software WG Meeting 15/10/2013, https://indico.cern.ch/event/277982/contribution/0/material/slides/0.pdf.

[63] R. Fantechi, Software WG Meeting 17/12/2013, https://indico.cern.ch/event/289245/contribution/7/material/slides/1.pdf.

[64] G. Unal, *Reconstruction program for the LKr*, tech. rep., NA48 Note 98-1 (1998).

[65] V. Palladino and T. Spadaro, Software WG Meeting 25/05/2011, https://indico.cern.ch/event/140222/contribution/8/material/slides/1.pdf.

[66] N. De Simone, TDAQ WG Meeting 16/10/2013, https://indico.cern.ch/event/277269/contribution/5/material/slides/0.pdf.

[67] N. De Simone, TDAQ WG Meeting 12/02/2014, https://indico.cern.ch/event/299477/contribution/8/material/slides/0.pdf.

[68] D. Soldi, TDAQ WG Meeting 02/04/2014, https://indico.cern.ch/event/309052/contribution/7/material/slides/0.pdf.

[69] W. A. Rolke, A. M. López, and J. Conrad, Nucl. Instrum. and Meth. A **551**, 493–503 (2005).

[70] G. J. Feldman and R. D. Cousins, Phys. Rev. D **57**, 3873–3889 (1998).

[71] R. Aaij et al., Phys. Rev. D **85**, 112004 (2012).

[72] R. Aaij et al., Phys. Rev. Lett. **108**, 101601 (2012).

[73] O. Seon et al., Phys. Rev. D **84**, 071106 (2011).

[74] J. P. Lees et al., Phys. Rev. D **86**, 012004 (2012).

[75] J. P. Lees et al., Phys. Rev. D **85**, 071103 (2012).

[76] B. Aubert et al., Phys. Rev. Lett. **104**, 021802 (2010).

[77] B. Aubert et al., Phys. Rev. Lett. **98**, 061803 (2007).

[78] B. Aubert et al., Phys. Rev. Lett. **103**, 021801 (2009).

[79] Y. Nishio et al., Phys. Lett. B **664**, 35 (2008).

[80] K. Hayasaka et al., Phys. Lett. B **687**, 139 (2010).

[81] Y. Miyazaki et al., Phys. Lett. B **648**, 341 (2007).

[82] Y. Miyazaki et al., Phys. Lett. B **692**, 4 (2010).

[83] Y. Miyazaki et al., Phys. Lett. B **699**, 251 (2011).

[84] Y. Miyazaki et al., Phys. Lett. B **672**, 317 (2009).

[85] Y. Miyazaki et al., Phys. Lett. B **719**, 346 (2013).

[86] Y. Miyazaki et al., Phys. Lett. B **632**, 51 (2006).

[87] J. Adam et al., Phys. Rev. Lett. **107**, 171801 (2011).

[88] R. Appel et al., Phys. Rev. Lett. **85**, 2877 (2000).

[89] R. Appel et al., Phys. Rev. Lett. **85**, 2450 (2000).

[90] D. Ambrose et al., Phys. Rev. Lett. **81**, 5734 (1998).

[91] A. Sher et al., Phys. Rev. D **72**, 012005 (2005).

[92] R. L. Schult and B.-L. Young, Phys. Rev. D **6**, 1988 (1972).

[93] A. C. Kalloniatis, J. D. Carroll, and B.-Y. Park, Phys. Rev. D **71**, 114001 (2005).

[94] A. R. Barker, H. Huang, P. A. Toale, and J. Engle, Phys. Rev. D **67**, 033008 (2003).

[95] M. Dobroliubov and A. Y. Ignatiev, Phys. Lett. B **206**, 346 (1988).

[96] O. Adriani et al., Nature **458**, PAMELA Collaboration, 607 (2009).

[97] J. Chang et al., Nature **456**, 362 (2008).

[98] F. Aharonian et al., Phys. Rev. Lett. **101**, H.E.S.S. Collaboration, 261104 (2008).

[99] P. Jean et al., Astron. Astrophys. **407**, L55 (2003).

[100] B. Batell, M. Pospelov, and A. Ritz, Phys. Rev. D **79**, 115008 (2009).

[101] M. Pospelov, Phys. Rev. D **80**, 095002 (2009).

[102] G. Bennett, Phys. Rev. D **73**, Muon G-2 Collaboration, 072003 (2006).

[103] K. Hagiwara, J. Phys. G **38**, 085003 (2011).

[104] B. Batell, M. Pospelov, and A. Ritz, Phys. Rev. D **80**, 095024 (2009).

[105] P. Cladé et al., Phyd. Rev. Lett. **96**, 033001 (2006).

[106] V. Gerginov, Phys. Rev. A **73**, 032504 (2006).

[107] P. D. Serpico and G. G. Raffelt, Phys. Rev. D **70**, 043526 (2004).

[108] B. Aubert et al., Phys. Rev. Lett. **103**, BABAR Collaboration, 081803 (2009).

[109] H. Merkel et al., Phys. Rev. Lett. **106**, A1 Collaboration, 251802 (2011).

[110] D. Babusci et al., Phys. Lett. B **720**, KLOE-2 Collaboration, 111–115 (2013).

[111] S. Abrahamyan et al., Phys. Rev. Lett. **107**, 191804 (2011).

[112] H. Park et al., Phys. Rev. Lett. **94**, 021801 (2005).

[113] R. Meijer Drees et al., Phys. Rev. Lett. **68**, Sindrum I Collaboration, 3845–3848 (1992).

[114] P. Adlarson et al., Phys. Lett. B **726**, WASA-at-COSY Collaboration, 187–193 (2013).

[115] K. Kampf, M. Knecht, and J. Novotný, Eur. Phys. J. C **46**, 191–217 (2006).